UNIVERSITÀ DEGLI STUDI DI PAVIA
DOTTORATO DI RICERCA IN FISICA – XXI CICLO

Optical probes for inter-chain interactions in π-conjugated polymers

Valentina Morandi

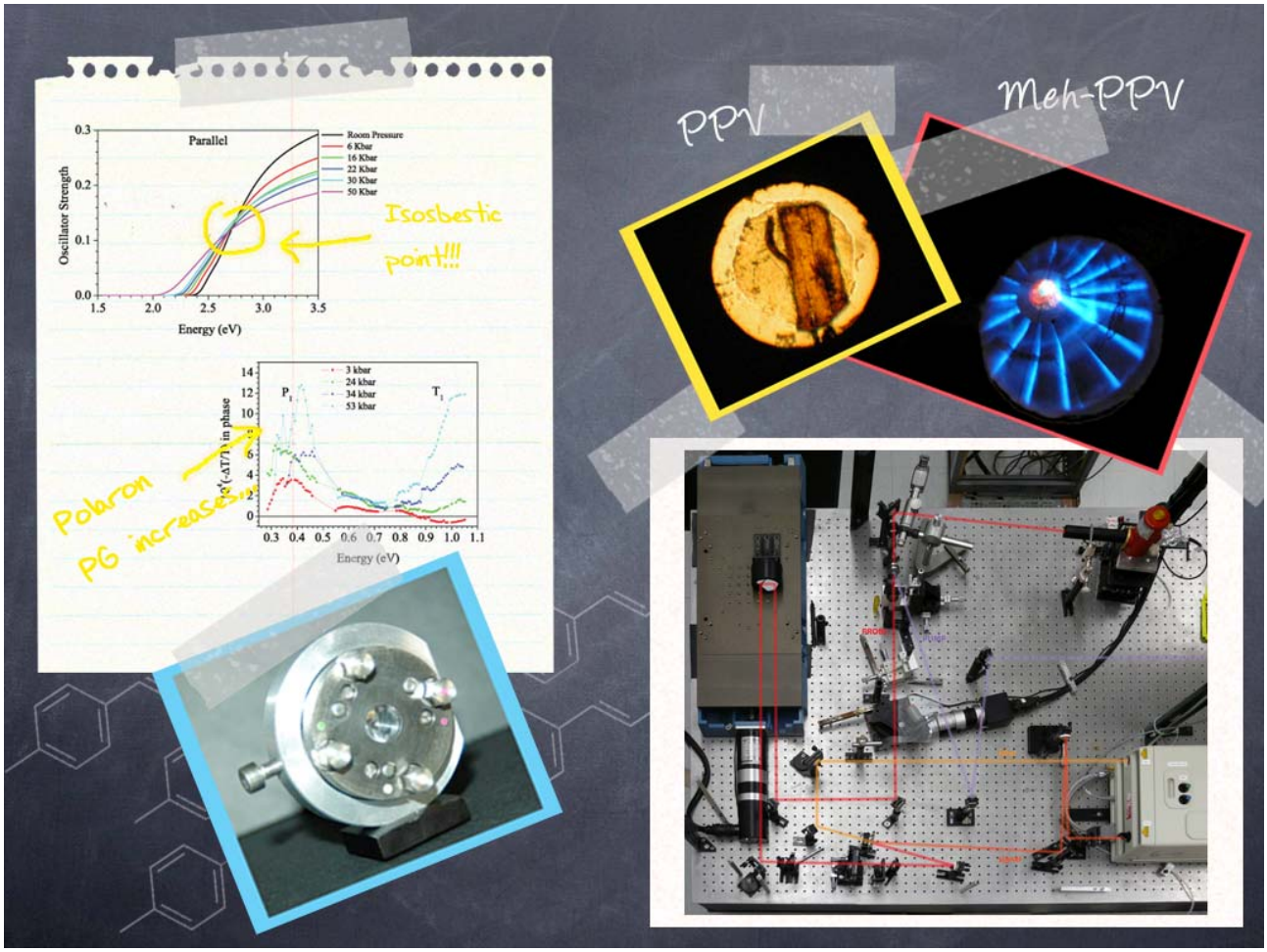

Tesi per il conseguimento del titolo

Università
degli Studi
di Pavia

Dipartimento
di Fisica
"A. Volta"

DOTTORATO DI RICERCA IN FISICA – XXI CICLO

Optical probes for inter-chain interactions in π-conjugated polymers

dissertation submitted by

Valentina Morandi

to obtain the degree of

DOTTORE DI RICERCA IN FISICA

Supervisors: Prof. F. Marabelli
Università degli Studi di Pavia
Dott. D. Comoretto
Università di Genova
Prof. Z. V. Vardeny
University of Utah

Referee: Prof. G. Bongiovanni
Università di Cagliari

Cover: Messy blackboard with sample pictures, set-up images (described in Chapter 3) and experimental results (discussed in Chapter 3 and 4).

Optical probes for inter-chain interactions in π-conjugated polymers
Valentina Morandi
PhD thesis – University of Pavia
Printed in Pavia, Italy, November 2008
ISBN 978-88-95767-22-2

'Begin at the beginning,' the King said, very gravely,
'and go on till you come to the end: then stop.'

Alice's adventures in Wonderland

Lewis Carroll
(1832-1898)

Just because something doesn't do what you planned it to do
doesn't mean it's useless.

Thomas A. Edison
(1847 - 1931)

Contents

Introduction **1**

1 Background **7**
1.1 π-conjugated polymers 7
1.2 Electronic and optical properties of π-conjugated polymers 9
1.2.1 Symmetry and ordering of the excited states 10
1.3 Non-interacting 1D models 12
1.3.1 Hückel model 14
1.3.2 SSH model 17
1.3.3 Photoexcitations 18
1.4 Correlated 1D models 20
1.4.1 Excitons 22
1.5 3D models: the role of inter-chain interactions 23
1.5.1 Inter-chain photoexcitations 24
1.5.2 Extended tight-binding model 24
1.5.3 Other 3D models 26
1.6 Optical processes 27
1.6.1 Interaction of light with the medium 27
1.6.2 Kramer-Kronig dispersion relations and sum rules 30
1.6.3 Reflection and transmission at normal incidence 31
1.6.4 Einstein coefficient for absorption and emission 33
1.6.5 Franck-Condon principle 34

2 Experimental methods **41**
2.1 Materials 41
2.2 Applying pressure: the diamond anvil cell 44
2.3 Optical probes 53
2.3.1 Raman scattering 53
2.3.2 Fourier transform spectroscopy 57
2.3.3 Pump/probe techniques 60

3 Inter- vs intra-chain interactions in highly oriented PPV 73
3.1 Introduction . . . 73
3.2 Pre-resonant Raman scattering . . . 75
3.3 Reflectance and transmittance . . . 80
3.3.1 Main features . . . 80
3.3.2 Reflectance under pressure: raw data . . . 82
3.3.3 Transmittance under pressure . . . 88
3.4 A model for data analysis: corrections to R spectra . . . 90
3.5 Corrected reflectance spectra . . . 96
3.6 A method to determine the dielectric constants . . . 98
3.7 Data analysis . . . 100
3.7.1 Anisotropic dielectric constants . . . 100
3.7.2 Analysis of the fit parameters . . . 109
3.7.3 Oscillator strength . . . 115
3.8 Conclusions . . . 117

4 Pump/probe spectroscopy on MEH-PPV under pressure 121
4.1 Introduction . . . 121
4.2 Steady state spectroscopy . . . 123
4.2.1 Photoluminescence . . . 123
4.2.2 Cw photoinduced absorption under pressure . . . 127
4.2.3 Frequency dependence response . . . 131
4.3 Ultrafast pump/probe spectroscopy . . . 133
4.3.1 Transient photoinduced absorption . . . 133
4.3.2 Dynamics . . . 136
4.3.3 Background . . . 139
4.4 Conclusions . . . 142

5 Conclusions and future perspectives 145

A Raman spectra of fluorinated Poly(p-phenylenevinylenes) 149
A.1 Introduction . . . 149
A.2 Experimental . . . 150
A.3 Results and discussion . . . 151
A.4 Conclusions . . . 155
A.5 Acknowledgments . . . 156

Acknowledgements 159

Bibliography 174

List of publications 175

Introduction

Research on π-conjugated polymer began in the early 1960s with studies on the electronic properties of small molecules [1]. Since then, the understanding of the physical processes underling their properties greatly improved while new capabilities, such as conductivities approaching that of copper [2] and electroluminescence [3], were discovered. Conducting and semiconducting polymers are nowadays available and capture the interest of electronic and optoelectronic industries. Most of the attractive features that make organic materials appealing for devices design are related to their mechanical properties and process-ability. Solubility in common solvents and tunability of light emission allowed the low-cost fabrication of bright light-emitting diodes [3, 4] large area flexible transistors [5, 6] and displays and photovoltaic devices with efficiencies approaching 5% [7–9].

Conjugated polymers owe their peculiar characteristics to the delocalization of π electrons along the chain backbone. Many of electronic and optical properties of these materials can thus be ascribed to their intrinsic 1D nature. Nonetheless, interactions between adjacent chains play a crucial role. Form a physical point of view, when chain proximity cannot be neglected, these low dimensionality systems (where only intra-chain interactions are relevant) are turned into a 3D solid, with dramatic consequences on their optical and charge transport properties. Indeed, inter-chain interactions can improve charge transport and charge generation efficiency, while, on the other hand, they might play a role in photoluminescence quenching of thin films with respect to solutions. It is thus obvious that the formation and nature of inter-chain species are critical issues for device design and optimization.

Nonetheless, a clear description of the role of inter-chain interaction on the primary photoexcitations of polymers in the solid state, such as aggregates formation, charge transport and exciton migration, is still lacking. A wide variety of possible species (labeled as excimers [10–12], aggregates [13, 14], polaron pairs [15, 16], and exciplexes [10]) has been proposed to explain the differences between the optical spectra of dilute solutions (where excitations are expected to have an intra-chain character) and thin films. However, despite the general consensus that the primary photoexcitations in dilute solutions are

intra-chain singlet excitons [17–20], the nature of the elementary species in films is still widely debated [21]. For instance, estimations of the fraction of photoexcitation that result in inter-chain species range from practically zero [22] to 90 % [23]. One controversy in particular, concerns the underlying mechanism of charge carrier photogeneration in MEH-PPV films, where, along with the photo-induced band of the singlet excitons, a relatively weak transient band in the mid-IR spectral range is instantaneously generated.

Many of the contradictions between literature data are originated by the strong dependence of the photo-generated species on the peculiar film morphology. Indeed, variations of the optical properties depending on the processing history (choice of the solvent or thermal annealing) of both the film and the solution from which it is cast do not allow a straightforward rationalization. A study of the influence of chain conformation and film morphology on inter-chain interactions, providing an interpretation that "heals" these discrepancies, is presented in [24].

Furthermore, el-ph coupling is not negligible in weakly ordered systems such as polymers [25], leading to an overall broadening of the electronic and vibronic transitions. The order of the system is a crucial parameter to disentangle between intra- and inter-molecular contribution. Single crystal represent the optimal system to investigate the role of inter-chain interactions but only a few molecular semiconductors are available in this form [26]. In general, disorder intrinsic to π-conjugated systems masks their fundamental properties, affecting the distribution of conjugation lengths and molecular weights, as well as the presence of unreacted monomers and catalyst residual. It is thus clear that a detailed study of inter-chain interactions requires a careful choice of the investigated system.

The ways of tuning inter-chain interactions are manifold. The distance between chains can be varied chemically, by substitution of the side groups, or with a control of the supra-molecular structure of the polymeric system, which gives rise to different physical-chemical properties related to the specific packing. A powerful tool to modulate intermolecular interactions in π conjugated systems without changing its chemical structure is the application of a hydrostatic pressure. This is done by means of a diamond anvil cell, which allows optical investigations of the pressure-induced changes in the material properties. When intermolecular distances are varied by an applied pressure, several effects occur simultaneously: the polymer chains are planarized, therefore increasing the conjugation length, and intra- and inter-molecular interactions are enhanced. Furthermore, due to disorder intrinsic to organic systems, the role of electron-phonon coupling cannot be discarded, and must be taken into account for a full understanding of inter-chain interactions.

The study of inter-chain interactions in PPV-based materials is particularly interesting both from a physical point of view, and for applications to device design. Two polymers belonging to this family were investigated in the present work, namely poly-p-phenylene vinylene (PPV) highly oriented

by tensile stretching, and its soluble derivative poly (2-methoxy, 5-(2'-ethyl)-hexyloxy) paraphenylene vinylene (MEH-PPV). Besides being a model system, the high crystallinity of stretch oriented PPV proves to be an ideal playground to unravel inter- and intra-molecular effects. On the other hand, MEH-PPV, is a well known material, widely used in organic optoelectronics due to its bright emission. Thus, the influence of inter-chain interaction on PL quantum yield and charge photogeneration efficiency is not only an academic issue, but has also implications on devices performances.

This thesis is organized as follows. Chapter 1 contains a general background on π-conjugated polymers. Their electronic properties are introduced and first discussed in the framework of 1D models. Intermolecular interactions are then included and a 3D model based on a tight binding approach is presented. Eventually, the optical processes occurring in π-conjugated systems are reported.

Chapter 2 illustrates the materials studied in this work and the experimental techniques used to characterize them. A brief introduction to diamond anvil cells is given, before the specifications of the two different cells used in this work are discussed. Raman, reflectance and transmittance spectroscopy, which were used to study highly oriented PPV are described. Steady state and transient pump/probe experiments for MEH-PPV are then presented. Each of the measurements here described was performed for different applied pressure, so the DAC was combined with every set up described.

Chapter 3 is devoted to the study of inter-chain interactions in thick, highly oriented poly(p-phenylene-vinylene) (PPV). Raman, reflectance and transmittance spectroscopy under applied hydrostatic pressure are presented and discussed. Raman spectra allow to infer important information on the geometrical changes of the polymer induced by pressure. These results, together with reflectance spectra, allow to clarify the role of inter-chain effects, though electron-phonon coupling cannot be discarded. Furthermore, R spectra are analyzed in the frame of an optical model developed to take into account diamond birefringence. The parallel and perpendicular components of the dielectric constant are also derived with a parametric procedure and their behavior as a function of pressure is studied. These findings are compared to the pressure dependence of the parameters used to obtain the anisotropic dielectric function. Finally, an analysis of the oscillator strengths for both polarizations is presented.

Chapter 4 deals with pump/probe spectroscopy of MEH-PPV under applied pressure. Room and low temperature steady-state spectra are presented and discussed. Continuous-wave photoinduced absorption spectra allow to probe the pressure dependence of long-lived species such as triplet exciton and trapped polarons. Information on the lifetime of the triplet excition as a function of pressure can also be gained by the frequency dependence response. Finally,the primary photoexcitation in MEH-PPV and their behavior as a function of pressure were recorded using an ultrafast two color laser system combined with a diamond anvil cell. Polaron generation and singlet exciton

transition were measured with a time resolution of 150 femtosecond in the IR spectral region with a probe energy ranging from 0.28 to 1.10 eV.

Finally, concluding remarks are given in the last Chapter, together with a hint for future work.

Chapter 1

Background

This Chapter is meant to be a general introduction on π-conjugated polymers. After a brief overview on their electronic and optical properties, a few theoretical models are discussed. 1D models based on a tight-binding approach are described starting with the simplest case of non interacting electrons in a fixed nuclear configuration. A model explicitly including electron-phonon coupling is then presented, which allow to introduce the elementary photoexcitations. Although 1D theories account for the major features of π-conjugated polymers, they fail to describe the complex interactions between chains in the solid state, where the effect of chain proximity has to be taken into account. Among the many 3D theories that have been developed, an extension of the tight-binding method is presented and the theoretical findings of recent 3D models are mentioned. Finally, optical processes occurring in π-conjugated polymers are described in the last section.

1.1 π-conjugated polymers

Since their discovery, conjugated polymers attracted much interest due to their peculiar electronic and mechanical properties. In their neutral form, these polymers are semiconducting, with a typical optical gap of about 2 eV. However, upon doping, they behave as metals, with electrical conductivities approaching that of copper. Conducting polymers were first demonstrated in 1977 by Heeger, McDiarmid, and Shirakawa [2, 27], who were awarded the Nobel prize in Chemistry in 2000. Light emitting properties of phenyl-based organic semiconductor, shown in the 90's [3], also contributed to the great attention towards the field of organic materials payed by physicists, chemists, and industries.

From a fundamental point of view, the unique properties of conjugated polymers rely on the π-electrons delocalization along the backbone chains. Thus, owing to the strong intra-molecular interactions, they behave as quasi-1D systems, with electronic wave function typically localized on a single chain.

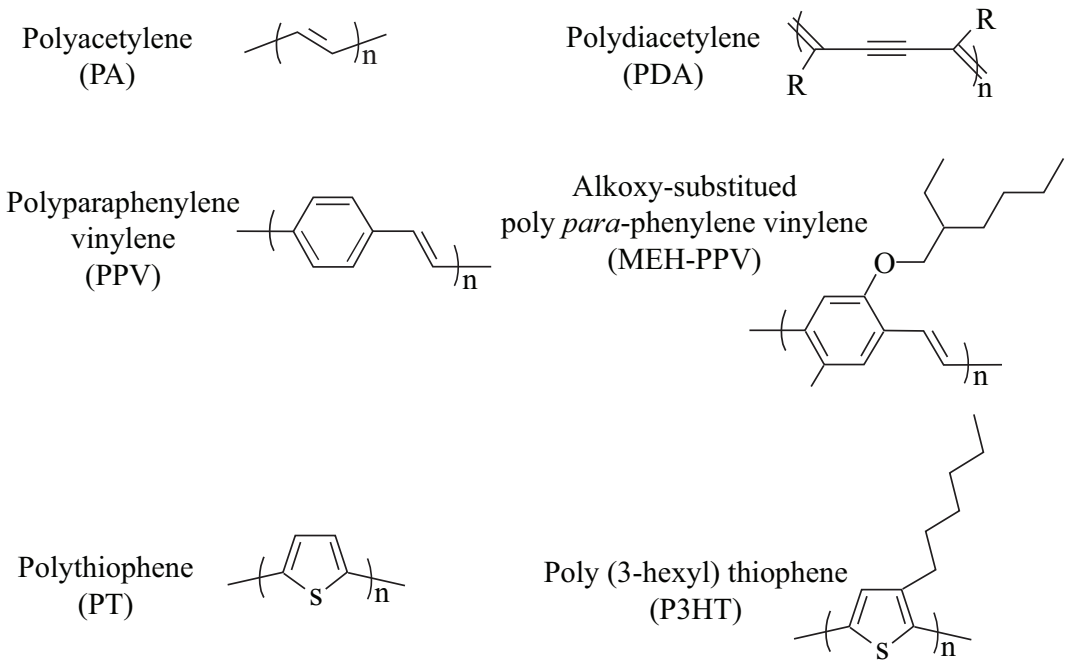

Figure 1.1: Chemical structure of common conjugated polymers.

This quasi-1- dimensionality implies that electron-electron interactions are weakly screened and as a consequence bound states between electrons and holes (excitions) are formed. Moreover, electron-lattice coupling is not negligible and also contributes to determine the character of the electronic states.

The processing advantages of this class of materials gave rise, over the past 30 years, to a huge variety of applications. Control on the chemical structure allows to include suitable functional side groups, obtaining materials that emit and absorb in a wide spectral range [28]. Besides tailoring the optical properties, side groups provide solubility, which is conveniently exploited in the fabrication of low cost and flexible large area devices, ranging form photovoltaic devices [9, 29, 30] to light emitting diodes [3, 4] and filed effect transistors [5, 6, 31].

The peculiar characteristics of organic materials are deeply related to their supramolecular structure [24]. Both the physical conformation of the chains and the way they pack together determine the optical and electronic properties of π-conjugated systems. The control of chain conformation (different morphologies can be obtained varying the procedure used for the synthesis) is thus a crucial issue not only for the design of efficient organic-based devices but also for a deep understanding of the photophysics of π-conjugated systems.

The chemical structure of the most common π-conjugated polymers is shown in Figure 1.1.

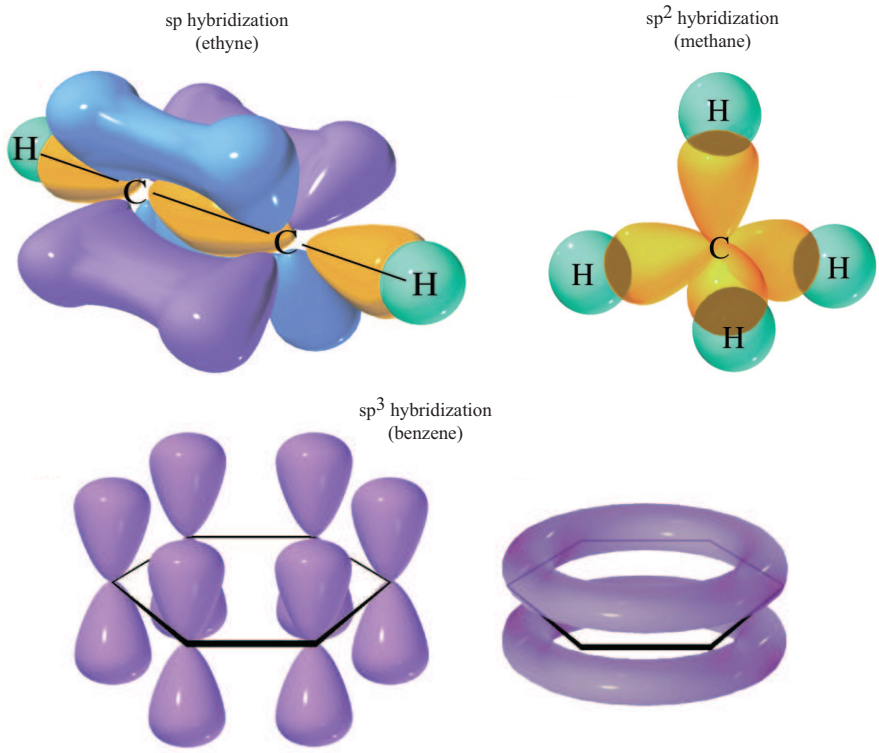

Figure 1.2: Hybrid molecular orbitals of acetylene (sp), benzene (sp^2), and methane (sp^3). Green: s atomic orbital; yellow: σ molecular orbital resulting from the mixing of 2s, $2p_x$, and $2p_y$; blue: π molecular orbital originating form the overlap between p_z orbitals. Adapted from [32].

1.2 Electronic and optical properties of π-conjugated polymers

Conjugated polymers are carbon-based macromolecules where valence electrons are delocalized along the backbone chains. Since these materials owe their peculiar properties to delocalization, we briefly review the types of bonding between C atoms.

In the ground state, carbon atoms have 4 electrons with configuration $2s^2 2p_x^1 2p_y^1$. In a bonding, these s and p atomic orbitals are hybridized to form sp^n orbitals. There are three types of sp^n hybridization: sp hybridization, found in linear molecules such as ethyne (Figure 1.2); sp^2 hybridization, typical of planar molecules such as ethylene, benzene (Figure 1.2) and graphite; and sp^3 hybridization, characteristic of three dimensional structures such as methane (Figure 1.2), ethane or diamond. Molecules with sp^3 orbitals are known as *saturated*, since every carbon is bond to 4 neighboring atoms.

Conjugated polymers are typically sp^2 hybridized (*unsaturated*). Three hybrid orbitals (σ orbitals) for each carbon atom originate form the mixing of 2s, $2p_x$, and $2p_y$, and lie in the plane of the molecule. The remaining $2p_z$ (or

π) orbitals accommodate the unpaired valence electrons. These orbitals are perpendicular to the molecule and overlap to form π bands. It is thus possible for the π-electrons to delocalize or *conjugate* throughout the molecule, as shown in Figure 1.2 for benzene. The different orientation between σ and π bonds can be exploited to separate the wavefunction describing their respective molecular orbitals. While the overall shape of the backbone is determined by σ bonds, the delocalization of π-electrons is responsible for the electronic properties of these materials, as we shall see in the following Sections.

1.2.1 Symmetry and ordering of the excited states

Optical properties of π-conjugated polymers such as fluorescence or electroluminescence are deeply related to the symmetry of the molecular wave functions. To illustrate this point, let us consider the simple example of polyenes [1].

Polyenes ($C_{2n}H_{2n+2}$) are linear chains of CH units with sp^2 hybridization of p_z atomic orbitals. The symmetry of such a polymer is described by the point group C_{2h} [33, 34] and the electronic wave functions are classified on the basis of their inversion and rotation properties. If the orbitals change (don't change) sign under inversion at the symmetry center they are dubbed as u (g); they are denoted with b (a) if they change (don't change) sign under 180° rotation around the symmetry axis. The atomic 2p-orbitals change sign under reflection in the symmetry plane, so p-electron orbitals are only a_u or b_g[1].

The wave function describing the electronic states of a polyene chain is still distinguished by its g or u character, but now the inversion properties are denoted with capitol letters A or B. The π-electron states in polyenes can then have either A_g or B_u symmetry according to:

$$\begin{aligned} a_u \otimes a_u = b_g \otimes b_g = A_g \\ a_u \otimes b_g = b_g \otimes a_u = B_u \end{aligned} \tag{1.1}$$

Polyenes have 2n electrons, so all π orbitals are fully occupied according to the Pauli exclusion principle and the ground state has A_g character. An excited state might be created promoting an electron from the highest occupied molecular orbital (HOMO) to the lowest unoccupied molecular orbital (LUMO), as depicted in Figure 1.3. In this case the character of the excited state is B_u. A higher energy excited state is crated either by moving two electrons move from the HOMO to the LUMO or one electron to the LUMO+1, and it will have A_g character.

It is useful to recall that many-body states are labeled as n^pX, where n is the overall quantum number, p is either 1 for singlet or 3 for triplet, and X is A_g or B_u.

Whenever electron-electron (el-el) and electron-phonon (el-ph) interactions can be neglected (non interacting models with and without electron lattice coupling are discussed in Section 2.4), the ordering of these excited states is:

[1] Wave functions have to be invariant with respect to every symmetry operation.

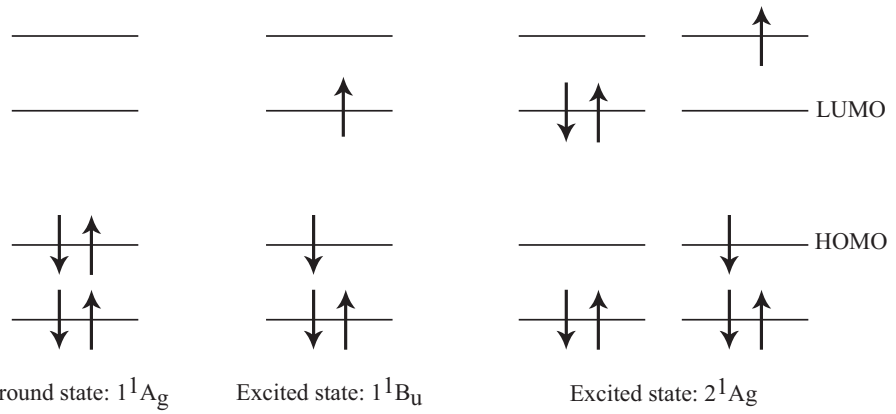

Figure 1.3: Symmetry of the ground and first excited states in polyenes.

$$1^1A_g < 1^1B_u < 2^1A_g. \tag{1.2}$$

The energies of these configurations can be regarded as approximately equal to the sum of the orbital energies. However, as a consequence of both el-el and el-ph interactions, the energetic ordering of the first excited states may be reversed:

$$1^1A_g < 2^1A_g < 1^1B_u \tag{1.3}$$

The ordering of the first excited states affects the optical properties of the material. When the B_u excited stated has lower energy than the A_g excited state (Figure 1.4), the material is expected to show fluorescence, since the $B_u \rightarrow A_g$ transition is dipole allowed. This is the case of polythiophene and poly (p-phenylenevenylene)s. Instead, if the B_u excited stated has higher energy than the A_g excited state, then the first excited state decays non radiatively to the ground state, due to the dipole forbidden $A_g \rightarrow A_g$ transition, and no fluorescence occurs. This happens for instance in the case of trans-polyacetylene and polydiacetylenes. A complete discussion about the interplay of el-el and el-ph coupling on state ordering is given in [25].

The emission properties of crystalline oligothiopenes (OT) with an odd (5T) or even (4T) number of rings have been recently related to the different point groups of their wavefunctions [35]. Selection rules imply that, for odd OT crystals (whose symmetry point group is C_{2v}), the transition moment of the lowest electronic transition is perfectly aligned along the molecular axis. In this structure, usually referred to as H-aggregate [1], the transition dipole moments cancel and, according to Kasha's rule, emission form the bottom of the exciton band is quenched . For even oligomers, the C_{2h} symmetry allows a component of the transition dipole perpendicular to the molecular axis, requiring only that the corresponding transition ($A_g \rightarrow B_u$) lies in the molecular plane. In a perfect crystal, the presence of a long-range orientational order produces a constructive interference of this off-axis component. This gives rise to and

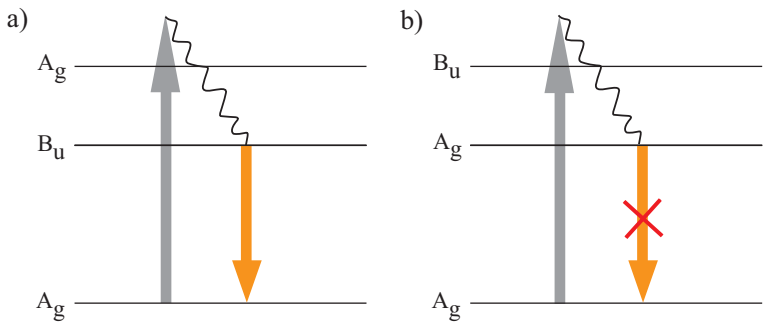

Figure 1.4: A different ordering of the first excited states gives rise to different optical properties. Upon absorption of a photon (gray arrow) the polymer fluoresces (yellow arrow) if $1^1A_g < 1^1B_u < 2^1A_g$.

array of head to tail transition dipoles typical of J-aggregates [1] and allows a low energy a_u transition polarized perpendicularly to the chains.

1.3 Non-interacting 1D models

Many of the properties of the electronic states in conjugated polymers can be accounted for by 1D models. In this section we will first illustrate the common approximations used to simplify the eigenvalue problem. We will then introduce the Hückel model, which is a tight binding approach where both el-el and el-ph interactions are disregarded. As a further degree of complication, the SSH model takes explicitly into account el-ph coupling. This description allows to introduced some of the main photoexcitations in π-conjugated systems. Furthermore, in this framework, the case of a linear chain will be discussed, to pave the way to the 3D treatment.

Let us consider the polymer as an infinite periodic structure, where every site is associated with an atomic wave function. The molecular wave functions[2] $\Psi(\mathbf{r}, \mathbf{R})$ must satisfy the Schrödinger equation:

$$H\Psi(\mathbf{r}, \mathbf{R}) = E\Psi(\mathbf{r}, \mathbf{R}) \tag{1.4}$$

where $\mathbf{r}$ and $\mathbf{R}$ are the set of electronic and nuclear coordinates, and E is the energy eigenvalue of the Hamiltonian. The many-body Hamiltonian H can be explicitly separated into three contributions:

$$H = H_{e-e}(\mathbf{r}) + H_{e-n}(\mathbf{r}, \mathbf{R}) + H_{n-n}(\mathbf{R}), \tag{1.5}$$

namely, the electronic part of the Hamiltonian including the electronic kinetic energy and Coulomb potential energy:

$$H_{e-e}(\mathbf{r}) = \sum_i \frac{\mathbf{p}_i^2}{2m_i} + \frac{1}{2}\sum_{i \neq j} \frac{e^2}{|\mathbf{r}_i - \mathbf{r}_j|}; \tag{1.6}$$

[2]In the following, for sake of simplicity we will neglect spin coordinates.

the nuclear Hamiltonian, also including a kinetic energy and a potential energy contribution,

$$H_{n-n}(\mathbf{R}) = \sum_{\alpha} \frac{P_{\alpha}^2}{2m_{\alpha}} + \frac{1}{2} \sum_{\alpha \neq \beta} \frac{Z_{\alpha} Z_{\beta} e^2}{|\mathbf{R}_{\alpha} - \mathbf{R}_{\beta}|}; \tag{1.7}$$

and the potential energy arising from the Coulomb interactions between the nuclei and electrons

$$H_{e-n}(\mathbf{r}, \mathbf{R}) = -\frac{1}{2} \sum_{\alpha, i} \frac{Z_{\alpha} e^2}{|\mathbf{R}_{\alpha} - \mathbf{r}_i|}. \tag{1.8}$$

Since the many-body Hamiltonian (1.5) can be solved exactly only for the hydrogen atom, approximations are required.

A first, important approximation is the so-called Born-Oppenheimer approximation. As a consequence of the large difference between the electrons and nuclei masses, the nuclear dynamics is expected to be slow compared to the electron dynamics. This can be exploited to factorize the many body state Ψ as the product of an electronic wave function ψ_e and a nuclear wave function ψ_n associated with the electronic state:

$$\Psi(\mathbf{r}; \mathbf{R}) = \psi_e(\mathbf{r}; \mathbf{R}) \psi_n(\mathbf{R}). \tag{1.9}$$

Decomposing H_{n-n} into its kinetic K_n and potential energy V_{n-n} components, the Schrödinger equation (1.4) becomes:

$$H\Psi(\mathbf{r}; \mathbf{R}) = (H_{BO} + K_n)\Psi(\mathbf{r}; \mathbf{R}), \tag{1.10}$$

where the Born-Oppenheimer Hamiltonian is:

$$H_{BO} = H_{e-e} + H_{e-n} + V_{n-n} \tag{1.11}$$

being:

$$V_{n-n} = \frac{1}{2} \sum_{\alpha \neq \beta} \frac{Z_{\alpha} Z_{\beta} e^2}{|R_{\alpha} - R_{\beta}|}. \tag{1.12}$$

The eigenvalue corresponding to an eigenstate of H_{BO}, also know as *adiabatic potential energy surface*, is the effective potential experienced by the nuclei and depends only parametrically from the nuclear coordinates $\mathbf{R}$.

For a given nuclear coordinate $\mathbf{R}$, the electron Hamiltonian is thus:

$$H_e = H_{e-e} + H_{e-n}(\mathbf{r}; \mathbf{R}). \tag{1.13}$$

It is convenient to write the Born-Oppenheimer Hamiltonian in second quantization [25]:

$$H_{BO} = \sum_{i,j} \tilde{t}_{ij} (c_i^{\dagger} c_j + c_j^{\dagger} c_i) + \frac{1}{2} \sum_{ijkl} \tilde{V}_{ijkl} c_i^{\dagger} c_k^{\dagger} c_l c_j + V_{n-n} \tag{1.14}$$

where

$$\tilde{t}_{ij} = \int \psi_i^*(\mathbf{r}) \left[\frac{\mathbf{p}^2}{2m} - \sum_\alpha \frac{Z_\alpha e^2}{|\mathbf{R}_\alpha - \mathbf{r}|} \right] \psi_j(\mathbf{r}) d\mathbf{r}^3 \tag{1.15}$$

is a one-electron integral representing the transfer integral of an electron from the orbital ψ_j to the orbital ψ_i. The second term in Equation (1.14) is a two-electron integral representing electron-electron interaction:

$$\tilde{V}_{ijkl} = \int \int \psi_i^*(\mathbf{r}) \psi_k^*(\mathbf{r}') \frac{e^2}{|\mathbf{r} - \mathbf{r}'|} \psi_l^*(\mathbf{r}) \psi_j^*(\mathbf{r}') d\mathbf{r}^3 d\mathbf{r}'^3 \tag{1.16}$$

Equation (1.14) represents all the electronic degrees of freedom. When considering low-energy processes it it indeed useful to introduce a further simplification. For carbon-based systems a common approximation is to consider π-electrons only (this corresponds to truncating the basis in (1.14)). This severe assumption is justified by the fact that $\sigma \rightarrow \sigma^*$ transitions lie at much higher energies than $\pi \rightarrow \pi^*$ excitations (10 eV versus 2-3 eV). The effect of σ electrons is a screening of the Coulomb interactions between π-electrons and nuclei, and of the mutual interactions of both nuclei and π-electrons. This screening, modeled by a static dielectric function, can be embedded in two pseudopotentials: V_p which describes the effective interactions between π-electrons and nuclei and V_{e-e}^{eff}, for the effective electron-electron interaction.

As a last simplification of the Born-Oppenheimer Hamiltonian, we will assume the integrals $\tilde{t}_{ij}$ to be non zero only for electrons on the same or neighboring orbital. Thus, we will assume:

$$\tilde{t}_{ii} = \varepsilon \quad \text{and} \quad \tilde{t}_{i,i+1} = t \tag{1.17}$$

To summarize, in the following we will derive the electronic properties of conjugated polymers taking into account π-electrons only, within the Born-Oppenheimer approximation, and assuming only nearest neighbors interactions are meaningful.

1.3.1 Hückel model

The simplest model to describe the electronic properties of π-conjugated systems is a tight-binding approach [33] neglecting electron-electron interactions and considering the nuclei as fixed. Ignoring el-el ($\mathrm{V}_{ijkl=0}$) and el-ph interactions, and setting the constant nuclear coordinates to zero (V_{n-n}=0), the Hamiltonian (1.14) reduces to:

$$H_{H\ddot{u}ckel} = \varepsilon + \sum_i t(c_{i+1}^\dagger c_i + c_i^\dagger c_{i+1}) \tag{1.18}$$

where t_i are the transfer integral between two neighboring sites and ϵ_i is the on-site energy.

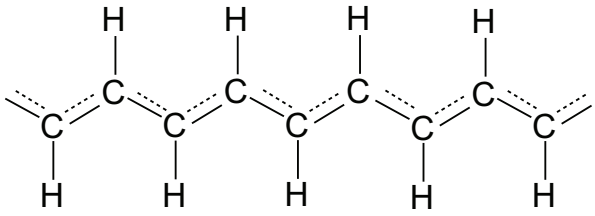

(a) Undimerized trans-CH

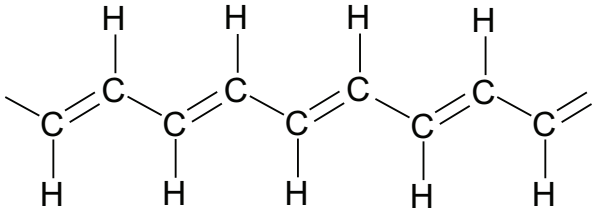

(b) Dimerized trans-CH

Figure 1.5: One dimensional chains of undimerized (a) and dimerized (b) polyacetylene

The many-body wave function $\phi(\mathbf{r}, \mathbf{R})$ describing π-electrons is a product of single-particle solutions ϕ, and it is made up by a linear combination of atomic orbitals that satisfy the Bloch theorem:

$$\psi(\mathbf{r}, \mathbf{R}) = \sum_{\mathbf{R}} \sum_{i} C_i e^{i\mathbf{k}\cdot\mathbf{R}} \phi_i(\mathbf{r} - \mathbf{R}) \tag{1.19}$$

where $\mathbf{R}$ is a Bravais lattice vector and C_i are the expansion coefficients for the i-th atom.

As an example let us consider a linear 1D chain of atoms with lattice constant a, as illustrated in Figure 1.5a for polyacetylene. The expectation values of the Hamiltonian for such a system are [36]:

$$E(k) = \varepsilon \pm t\sqrt{2 + 2\cos(ka)} \tag{1.20}$$

being

$$\varepsilon = \langle \phi_i | H_{H\ddot{u}ckel} | \phi_i \rangle \tag{1.21}$$

the on-site energy, and

$$t = \langle \phi_i | H_{H\ddot{u}ckel} | \phi_{i\pm1} \rangle. \tag{1.22}$$

the nearest neighbor interaction energy (transfer integral).

Since there is one π-electron for each carbon atom, the π-band is half-filled. The Fermi wave vector is $k = \pi/2a$, where a is the lattice constant, and the first Brillouin zone boundary is at $k = \pi/a$ where $E_{\pi/a}$. There is therefore no energy gap in the electronic band structure and the material is a 1D metal. Such a metal is, however, unstable. This instability, known as

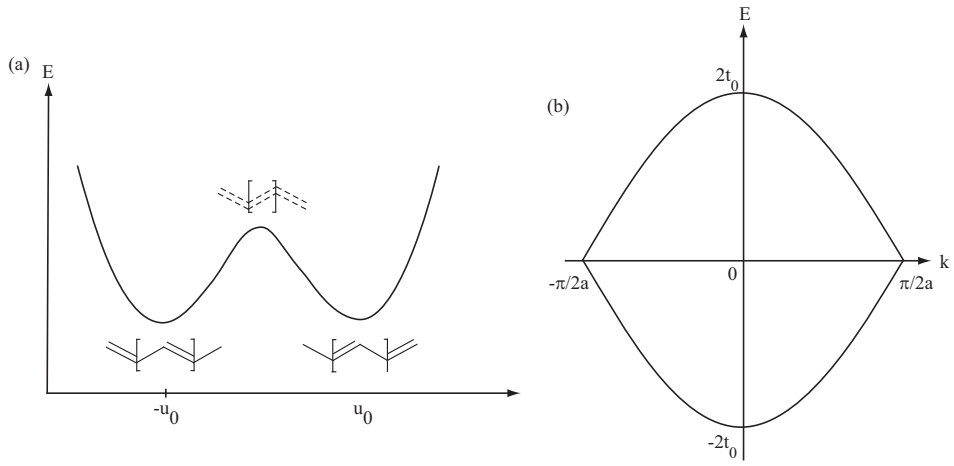

(a) Undimerized trans-CH

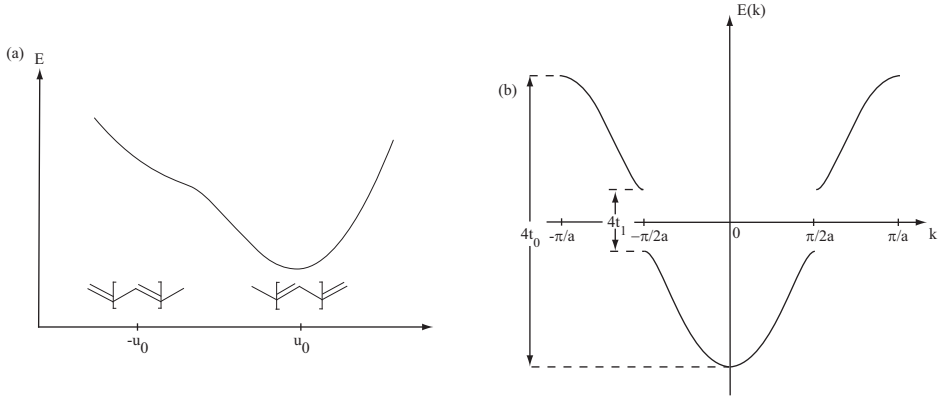

(b) Dimerized trans-CH

Figure 1.6: Energy versus dimerization coordinate for an undimerized (a) and dimerized (b) linear polymer chain and corresponding band structure [38, 39].

Peierls instability [37], gives rise to an alternating single and double bonds configuration (dimerization) which lowers the symmetry of the system. The double-well shape of the ground state energy E as a function of the dimerization coordinate and the corresponding band structure are shown in Figure 1.6(a).

We can now calculate the energy expectation values for the dimerized configuration (Figure 1.5(b)) [25, 36]. Here there are two bond lengths, single and double, hence two atoms per unit cell of length a. The solution of the Schrodinger equation reduces to an eigenvalue problem with a simple 2x2 matrix follows for the determination of the coefficients C_i. A non trivial solution is obtained only if

$$\begin{vmatrix} \varepsilon - E & t_1 + t_2 e^{-ika} \\ t_1 - t_2 e^{ika} & \varepsilon - E \end{vmatrix} = 0. \tag{1.23}$$

This matrix has on-site energies ε along the diagonal, and the transfer

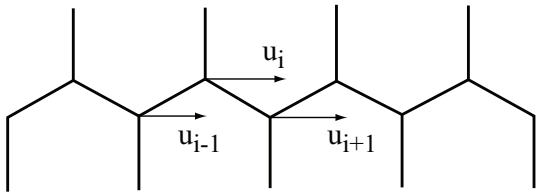

Figure 1.7: Dimerization coordinate defined for trans-CH.

integral t as off-diagonal elements.

The solution to (1.40) is [25, 36]:

$$E = \varepsilon \pm \sqrt{(t_1^2 + t_2^2 + 2t_1 t_2 \cos ka)} \tag{1.24}$$

Since there are two atoms per unit cell and one electron per atom, the lower band is completely filled, yielding a semiconductor with a band gap $\Delta = 2|t_1 - t_2|$ and with a total bandwidth $W = 2|t_1 + t_2|$, as shown in Figure 1.6(b).

1.3.2 SSH model

El-ph coupling plays a crucial role in one-dimensional systems. As we have seen when discussing the Hückel model, a linear undistorted polymer chain, such as trans-polyacetylene in Figure 1.5, is unstable with respect to a distorted structure [3]. El-ph interaction, responsible for bond alternation in π-conjugated polymers was first explicitly taken into account in the model developed by Su, Schriffer, and Heeger for trans-polyacetylene [40][4].

Let us consider the displacement u_i of the i-th CH group along the molecular symmetry axis of trans-polyacetylene, as depitctd in Figure 1.7. In the SSH model, the nearest neighbor transfer integral is expanded to first order about its non dimerized value[5]:

$$\tilde{t}_{i,i+1} = t_0 - \alpha(u_{i+1} - u_i) \tag{1.25}$$

where α is the el-ph coupling constant.

The SSH Hamiltonian is the Hückel Hamiltonian (1.18) with an additional term that takes into account lattice energy:

$$H_{SSH} = H_{e-e} + H_{n-n} + H_{e-n} \tag{1.26}$$

where:

[3]This is a consequence of the Peierls theorem which states that 1D metals are unstable with respect to a lattice distortion that opens a gap at the Fermi surface.

[4]In the absence of lattice dynamics the SSH model is known as Pierls model.

[5]This means that only the normal mode that predominantly couple to the π electrons, i.e. for polyacetylene C stretching, is considered.

$$H_{e-e} = -t_0 \sum_i (c_{i+1}^\dagger c_i + c_i^\dagger c_{i+1}) \tag{1.27}$$

describes the hopping of π-electrons to nearest neighbor sites along the chain,

$$H_{n-n} = \sum_i \left(\frac{P_i^2}{2M} + \frac{K}{2}(u_{i-1} - u_i) \right) \tag{1.28}$$

is the sum of the kinetic energy of the CH units of mass M and the elastic energy for small displacements of σ bonds with coefficient K, and

$$H_{e-n} = \alpha \sum_i (u_{i-1} - u_i)(c_{i+1}^\dagger c_i + c_i^\dagger c_{i+1}) \tag{1.29}$$

gives the el-ph interaction.

As a consequence of the broken symmetry of the ground state in dimerized polyene chains, boundaries between one phase of bond alternation and another occur (Figure 1.6(b)). These defects, known as solitons, are associated with mid-gap electronic states, as discussed in the next Section.

1.3.3 Photoexcitations

Despite the SSH Hamiltonian neglects electron-electron and 3D interactions, it allows to introduce some of the elementary photoexcitation in π-conjugated polymers.

In systems such as *trans*-$(CH)_x$ the Hamiltonian is invariant with respect to the exchange of single and double bond. The ground state energy per site as a function of the dimerization parameter has thus a double minima associated with the two possible phases of the system, as shown in Figure 1.6(a).

Domain boundaries between the two degenerate ground state configurations are topological excitations dubbed as *solitons* [38–40]. The existence of such defects, or kinks, on the chain implies an energy state in the middle of the gap (between the HOMO and LUMO levels), that can accommodate up to two electrons. Thus, a soliton can be either neutral or (positively or negatively) charged, as shown in Figure 1.8.

For a neutral soliton S^0, the state is singly occupied: the net charge is Q=0, but because of the unpaired electron, it has a spin 1/2. For a positive (negative) soliton S^+ (S^-), the mid-gap state is unoccupied (doubly occupied), due to the removal (introduction) of an electron from (in) the system. So the net charge of S^+ (S^-) is Q=+e (Q=-e). However, since the state is empty (full), the spin of S^+ (S^-) is zero. It follows that solitons are characterized by a reversed spin-charge as compared to electrons.

Trans-$(CH)_x$ is the only polymer that supports solitons. Instead, non degenerate ground state systems are characterized by bound-soliton-antisoliton

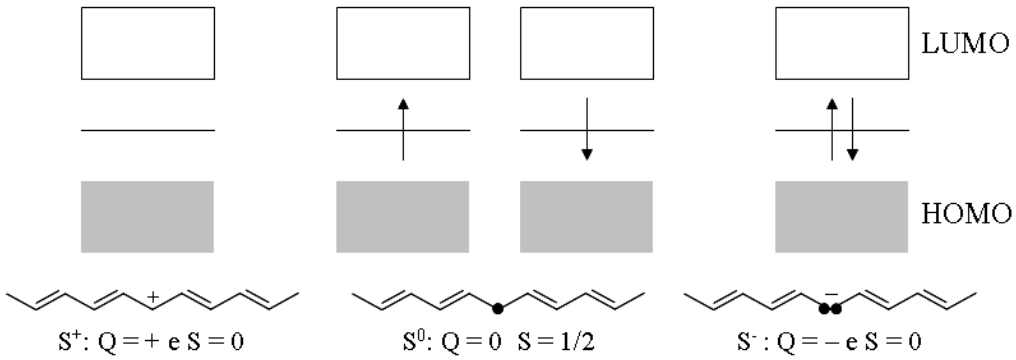

Figure 1.8: Band diagrams showing the mid-gap states associated with solitons and their occupation for neutral(S^0) or charged (S^+, S^- solitons. In the corresponding schematics, black dots represent spin while charge is indicated with + or -.

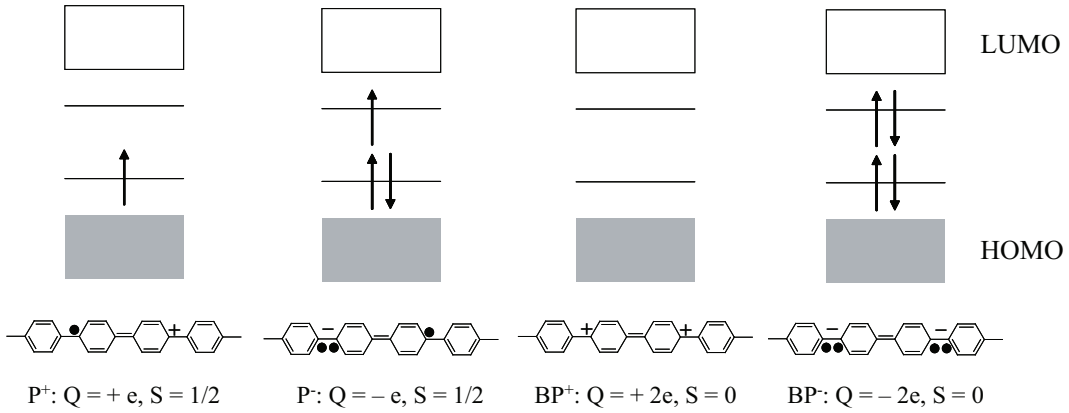

Figure 1.9: Band diagrams showing the mid-gap states associated with polaron and bipolarons and their occupation. In the corresponding schematics, black dots represent spin while charge is indicated with + or -.

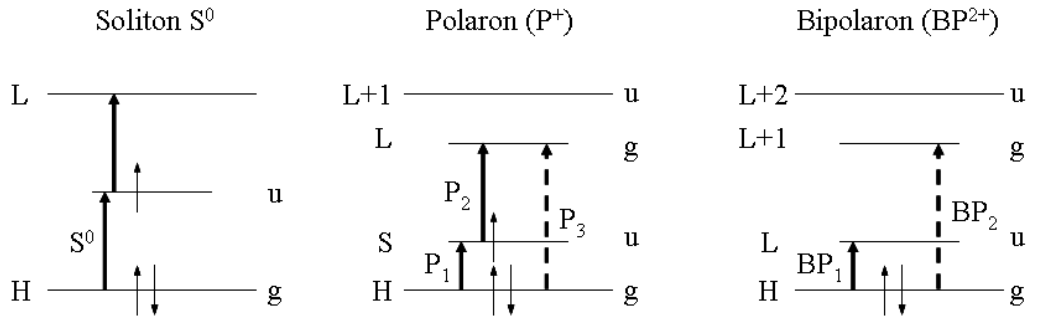

Figure 1.10: Energy levels and optical transitions of solitons, polarons, and bipolarons. The full and dashed arrow represent allowed and forbidden transition respectively. H, S, and L are the HOMO, SOMO, and LUMO levels, and u and g represent their symmetry.

pairs, referred as polarons and bipolarons. They are schematized for poly(paraphenylene) (PPP) in Figure 1.9 together with their band diagrams .

The formation of polarons gives rise to two levels symmetrically displaced about the midgap, as shown in Figure 1.9. Depending on their occupation, polarons can be either positive or negative polaron with the usual charge-spin relationship of Q = ±e and S = 1/2.

Similarly, a bipolaron is a bound state of two charged solitons of like charge (or two polarons whose neutral solitons annihilate each other) with two corresponding midgap levels. Since each charged soliton carries a single electronic charge and no spin, bipolarons has charge Q = 2e and zero spin. While polarons are possible in both degenerate and non degenerate ground state polymers, bipolarons can be formed only in non degenerate systems. The spin-charge relations of bipolaron are shown in Figure 1.9.

The photogeneration of solitons in degenerate ground state polymers and of polarons or bipolarons in non degenerate ground state polymers lead to the formation of electronic levels inside the gap. These in turn lead to the appearance of subgap photoinduced absorption in optical spectra. This transitions are schematically represented in Figure 1.10.

1.4 Correlated 1D models

Interacting electrons with fixed nuclei are described by the Pariser-Parr-Pople model, which is the most general approximation within π-electron theories. The Hamiltonian is given by the sum of three terms: the contribution due to the transfer of electrons form site to site, the Coulomb interaction between electron on the same site, and the Coulomb interaction of electrons on different sites. This last term is expressed as [25]:

$$V = \frac{1}{2}\sum_{i\neq j} V_{ij}(n_i - 1)(n_j - 1) \tag{1.30}$$

Electron-electron interactions are usually treated semi-empirically, parameterizing V_{ij} as[6]:

$$V_{ij} = \frac{U}{\sqrt{1 + (U\epsilon r_{ij}/14.397)^2}} \tag{1.31}$$

where ϵ is the dielectric function (usually set equal to unity), and U is taken to be the value of the ionization potential minus electron affinity ($\sim$ 11 eV in conjugated molecules).

Including el-el interaction has the important consequence of the creation of quasi-particles, formed by a bound electron-hole pair, as discussed in the next section.

Singlets and triplets

The wave function describing a two particle system such as an exciton (discussed in the next Paragraph) must be anti-symmetric in spin and electron coordinates. it is simply obtained from the Slater determinant:

$$\Psi = \frac{1}{\sqrt{2}}\begin{vmatrix} \psi_i(r)\chi_i(\sigma) & \psi_i(r')\chi_i(\sigma') \\ \psi_j(r)\chi_j(\sigma) & \psi_j(r')\chi_j(\sigma') \end{vmatrix} \tag{1.32}$$

where $\psi_(r)$ and $\chi_i(\sigma)$ are the electronic and spin part of the wave function, respectively. Indicating with α and β the spin up and down projection of χ, we can thus construct wave functions that have different total spin quantum number S

$$\begin{aligned} \Psi^{S=0} &= \frac{1}{2}[\psi_1(1)\psi_2(2) + \psi_2(1)\psi_1(2)][\alpha(1)\beta(2) - \alpha(2)\beta(1)] \\ \Psi^{S=1} &= \frac{1}{2}[\psi_1(1)\psi_2(2) - \psi_2(1)\psi_1(2)][\alpha(1)\beta(2) + \alpha(2)\beta(1)] \\ \Psi^{S=1} &= \frac{1}{2}[\psi_1(1)\psi_2(2) + \psi_2(1)\psi_1(2)][\alpha(1)\alpha(2)] \\ \Psi^{S=1} &= \frac{1}{2}[\psi_1(1)\psi_2(2) + \psi_2(1)\psi_1(2)][\beta(1)\beta(2)] \end{aligned} \tag{1.33}$$

In the non interacting limit, singlet (S=0) and triplet (S=1) states are degenerate, but including el-el correlation lowers the triplet energy. Selection rules determine which transitions are allowed. In particular, transitions might occur only between states of the same spin manifold. So, $A_g \rightarrow B_u$ is allowed but $A_g \rightarrow A_g$ is forbidden. Transition between singlet and triplet state become allowed only if spin-orbit coupling is not negligible.

[6]This parametric form of intra-chain inter-site Coulomb interaction is known as Ohno potential [25].

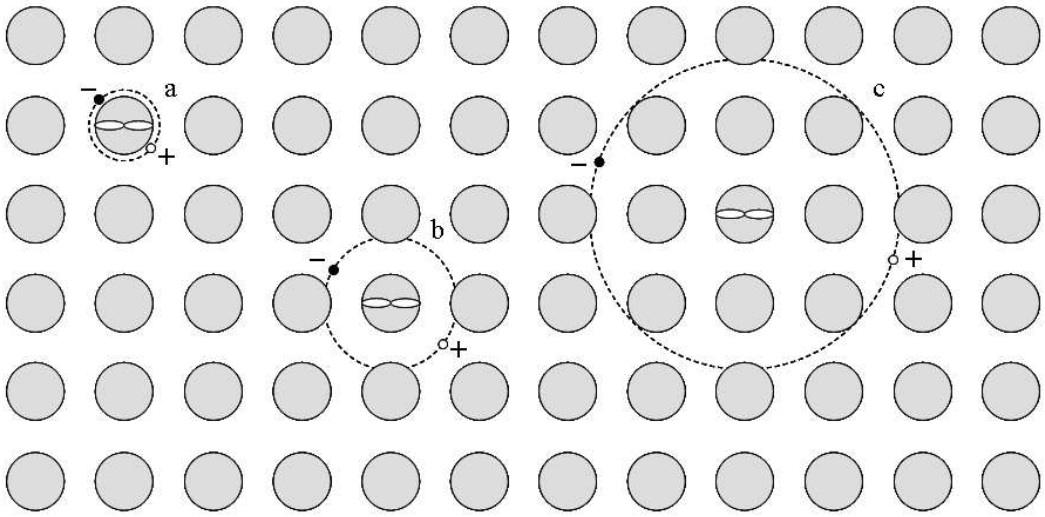

Figure 1.11: Schematic representation of (a) small-radius Frenkel exciton and (b) large-radius Wannier-Mott exciton. (c) intermediate or charge-transfer exciton.

1.4.1 Excitons

An important consequence of electron-electron interaction is the formation of bound particle-hole excitations, or excitons.

Excitons are bound states due to the Coulomb attraction between an electron excited to the conduction band and the hole left behind in the valence band (in the case of conjugated polymer this corresponds to a $\pi - \pi^*$ excitation).

Following the usual treatment of inorganic semiconductors, excitons in π-cojungated polymers can be classified as Frenkel or Wannier-Mott excitons (Figure 1.11).

When the electron and hole are tightly bound, the resulting exciton is strongly localized and is known as Frenkel exciton. The Frenkel exciton can be regarded as a correlated electron-hole pair that is located on the same molecular site and moves as a unit through the crystal lattice. Its radius, that is the average separation between the electron and the hole, is thus small (<5Å) compared to the intermolecular spacing (Figure 1.11a). The binding energy of such an exciton is of the order of 1 eV, and the associated energy states lie well within the band gap. Although a Frenkel exciton is essentially an excited states of a single molecule, the excitation can hop from one molecule to the other by virtue of the coupling between neighbors.

At the other extreme, the radius of the excition can be much larger than the intermolecular separation (40-100Å, Figure 1.11b). Such a weakly localized, loosely bound exciton is called Wannier-Mott exciton and has a binding energy of less than 50 meV. The energy levels associated with Wannier-Mott lie very close to the gap and resemble the Rydberg series of the hydrogen

atom. Wannier-Mott excitons are more common in inorganic systems where the interaction energy is great and the dielectric constant is high.

In organic systems, the nature of the lowest energy transition (whether it is due to free carrier absorption or to tightly bound excition absorption) is widely debated. For instance, experimental values currently reported for the binding energy of PPV range from 0.2-0.5 eV [41, 42] to around 1 eV [43, 44] and a value of less than 0.1 eV is also proposed [45]. These values correspond to spatial extension varying form a single monomer (Frenkel-like exciton) to many repeating units (Wannier-like exciton).

Theoretical studies for anthracene [46] showed that the lowest absorption transition can be generated either by strongly bound excitons (with a binding energy of 0.64 eV) or by a free electron-hole pair, depending whether the polarization direction is perpendicular or parallel to the chain axis.

In the intermediate situation, the electron and the hole could be located on nearest neighbor sites, while still forming a bound pair, leading to the formation of charge-transfer excitons (Figure 1.11c).

1.5 3D models: the role of inter-chain interactions

So far, we discussed the properties of π-conjugated polymers in the framework of 1D models, with or without el-ph coupling. The long polymer chains can indeed be thought as one-dimensional systems, and, as we have seen, the main properties of these materials can be ascribed to the mobile π-electrons moving along the polymer backbone. In this picture, the elementary photoexcitations are intra-chain species [47, 48].

Nonetheless, isolated chain models are not enough to describe the properties of solid state organic materials. Interactions between adjacent chain proved to influence absorption and emission (being detrimental for light emitting devices REF) as well as transport properties REF. It is thus clear that a complete description of the physics underlying optical and electronic phenomena in π-conjugated systems must include inter-chain coupling. In these scenario, new inter-chain photoexcited species are formed as an effect of chain proximity, such as excimers, polaron pairs and exciplexes.

Since conjugated polymers are inherently disordered systems, it is often complicated to distinguish between intra- and inter-molecular effects. An understanding of the role of inter-chain interactions is thus strongly influenced by chain conformation and film morphology. A review on how inter-molecular interaction are affected by the specific packing of the polymer chain is given in [24].

In the following we will first introduce some of inter-chain species formed upon photoexcitations. Then a few models explicitly taking into account the effect of side chains will be presented. As an extension of the theories pre-

viously described, a 3D tight binding approach will be discussed where the dipole moment is expressed as a function of the hopping integral for the direction perpendicular to the polymer chains. Recently, *ab intio* calculations were performed to derive the optical and electronic properties of crystalline organic semiconductors. We will discuss the predictions of these models concerning mainly the effect of inter-chain interactions on optical spectra.

1.5.1 Inter-chain photoexcitations

A variety of inter-chain species are generated when two adjacent chains interact with each other.

Excimers are dimers that exist only in the excited state. They are formed when two neighboring polymers share their π-electrons equally in the excited state but not in the ground state [10, 49]. These emissive excited state complexes have a dissociative ground state, that is, the ground state of the dimer spontaneously dissociates into two ground-state molecules. Furthermore, the excimer cannot be directly excited optically. Instead, an intramolecular singlet exciton is photoexcitation that later delocalizes over two molecules, forming the excimer. Excimer formation is accompanied by a strong geometric distortion along the intermolecular axis that, when combined with the dissociative nature of the ground state, leads to featureless, strongly Stokes-shifted emission of films in comparison to dilute solution. Excimer formation was observed in PPV-based films [11], leading to quenching of luminescence, due to their large non radiative decay in this polymer.

While excimers exist only in the excited state, interchain interaction may also lead to ground-state interactions, with formation of aggregate states [1]. Upon aggregation, both the ground- and excited-state wave functions are delocalized over several polymer chains. The aggregate is therefore directly accessible spectroscopically. The existence of this species was suggest in ladder type polymers [14] and poly-pyridine films [13]where it appears to be detrimental for PL efficiencies, as is evidenced by the reduced efficiencies of film samples as compared to solution.

Upon excitation of strongly interacting chains, charge transfer can occur, leaving a positive polaron on one chain and a negative polaron on the other. This charge-separated inter-chain species are known as polaron-pairs [15, 16].

Inter-chain excited states, labeled exciplex, can also be formed when an unequal sharing of π-electron density between chains or a partial degree of charge transfer occur [10, 50].

1.5.2 Extended tight-binding model

A relatively simple model that takes into account inter-chain interactions was developed in [51] to account for both the dispersion of the real and imaginary part of the dielectric constant and pump polarization anisotropy of trans-polyacetylene (*trans*-CH_x). This model is an extension of the tight-binding

model and provides an analytic expression for the dipole moment components as a function of a single parameter, namely the inter-chain hopping integral $t_\perp$.

Trans-CH_x has a herringbone crystal structure, with two staggered chains per unit cell. According to the Block's theorem the wave function of the π electron can be written as

$$\Phi_{s\mathbf{k}}(\mathbf{r}) = e^{ik\cdot\mathbf{r}} u_{s\mathbf{k}}(\mathbf{r}) \tag{1.34}$$

where u is the periodic part, $\boldsymbol{k}$ is the wave vector of the vertical optical transition and s is the site on the chain.

Due to dimerization, the polymer chains acquire a zig-zag structure. Assuming planar zig-zag chains, the electronic transition moment can be written as:

$$\mathcal{M}_{ss'}(\mathbf{k}) = \frac{i}{V}\int u^*_{s'\mathbf{k}}(\mathbf{r})\nabla_k u_{s\mathbf{k}}(\mathbf{r}) d^3\mathbf{r} \tag{1.35}$$

where V is the volume of the unit cell.

Considering N unit cells in the crystal and taking into account only interactions of the π electron on the site s with its nearest neighbors, we can express the wave function as a linear combination of atomic orbitals belonging to the two non equivalent chains in one unit cell:

$$\Phi_{s\mathbf{k}}(\mathbf{r}) = N^{1/2}\sum_{l=1}^{N_x}\sum_{m=1}^{N_y}\sum_{n=1}^{N_z} e^{A(l,m,n)} B(l,m,n) \tag{1.36}$$

where $N = N_x \times N_y \times N_z$ is the total number of unit cells, and

$$A(l,m,n) = i\mathbf{k}\cdot[(l-1)a\mathbf{e_x} + (m-1)b\mathbf{e_y} + (n-1)c\mathbf{e_z}] \tag{1.37}$$

being a,b, and c the dimensions of the unit cell along the axes x, y, and z.

$$\begin{aligned} B(l,m,n) = {} & C_1^{s\mathbf{k}}\phi_{4l-3,4m-3,4n-3} + C_2^{s\mathbf{k}}\phi_{4l-2,4m-2,4n-2} \\ & + C_3^{s\mathbf{k}}\phi_{4l-1,4m-1,4n-1} + C_4^{s\mathbf{k}}\phi_{4l,4m,4n} \end{aligned} \tag{1.38}$$

The x component of the dipole moment can be expressed as:

$$\mathcal{M}^x_{ss'}(\mathbf{k}) = \sum_{p=1}^{4}\left[C_p^{s'*}C_p^s x_p + C_p^{s'*}\frac{\partial}{\partial k_x}C_p^s x_p\right] \tag{1.39}$$

Similar expressions hold for y and z directions. Considering only inter-chain interactions between neighboring chains along the x direction.

If only the interaction with the closest chain along the x axis is considered, we are left with a 2x2 equation of the form:

$$\begin{vmatrix} \varepsilon & t_1 + t_2 e^{-ik_z c} + t_\perp e^{-ik_x a} \\ t_1 + t_2 e^{-ik_z c} + t_\perp e^{-ik_x a} & \varepsilon \end{vmatrix} = 0. \tag{1.40}$$

where t_1 and t_2 indicate the intra-chain transfer integral along the single and double bonds, respectively, and t_perp is the inter-chain transfer integral.

The inter-chain and intra-chain components of the transition moment can be eventually expressed as:

$$\begin{aligned} \mathcal{M}_{cv}^{\perp}(\mathbf{k})_{inter} &= \frac{a}{4\epsilon^2}[\epsilon^2 - \epsilon_0^2 - t_{\perp}] \\ \mathcal{M}_{cv}^{\perp}(\mathbf{k})_{intra} &= \frac{c}{4\sqrt{3}} \end{aligned} \tag{1.41}$$

From these expression the optical response function can be calculated using the results that will be derived in Section 2.6. In particular, the electronic susceptibility of the π electron in a conjugated polymer is:

$$\chi_{\pi}(\omega) = \frac{4e^2}{(2\pi)^3}\int_{BZ} d^3k \left[\frac{|\mathcal{M}_{cv}(k)|^2}{\epsilon_{cv}(k) - \hbar\omega - i\hbar\Gamma} + \frac{|\mathcal{M}_{cv}(k)|^2}{\epsilon_{cv}(k) + \hbar\omega + i\hbar\Gamma}\right] \tag{1.42}$$

1.5.3 Other 3D models

Focusing mainly on the influence of inter-chain interactions on the optical properties of π-conjugated systems, in the following we will summarize some of the theoretical findings obtained in recent years. Their predictions will also be compared, if possible, with the experimental results reported in Chapter 3 (and 4).

Ab initio calculations of the impact of inter-chain coupling on the optical properties of reference materials are typically performed through density functional theory in the local density approximation.

Calculations performed on both isolated chains and the crystalline phase PPV (characterized a herringbone structure) [52] predict a decrease of the exciton binging energy in the solid state with respect to the single chain picture (0.2-0.3 eV versus 0.6-0.7 eV). Strongly bound excitons were also found for trans-CH isolated chains, with binding energies of the order of 0.5 eV, while in the crystalline arrangement it is drastically reduced to 0.05 eV [53]. This is attributed to the screening of the electron-hole interaction, which is more efficient in crystals, and to the spread of the electron and hole pair over several neighboring chains in the crystalline phase. Both effects increase the average distance between the electron and the hole and thereby reduce the exciton binding energy. Due to inter-chain interactions and crystal symmetry the lowest electronic excitation in crystalline PPV is a dark exciton and as a result photoluminescence can be strongly quenched [52]. Though preserving a quasi 1D character, these states strongly depend on inter-chain coupling and crystal structure, as shown for polythiophene crystals [54]. The Davydov splitting between excitonic states arising form the specific crystal symmetry is strongly dependent on inter-chain interaction. For crystalline PPV it was calculated that an increase of 20% in the interchain distance in the π-stack direction

leads to an increase in the binding energy (to 0.4 eV) and a drastic decrease in the Davydov splitting by an order of magnitude, thus restoring radiative efficiency.

Transport parameters calculated with the same first principle method [55] for two typical morphologies shown by PPV (herringbone-PPV and displaced π stacks-MEH-PPV) allow to predict the effect of interchain interactions in specific packing environments. It is interestingly found that the transfer integral is 1 order of magnitude larger for π stacks in the stacking direction than for herringbone packing, showing that 3D arrangement can be indeed crucial in the design of materials with efficient transport properties.

The effect of an applied pressure, that is a reduction of intermolecular distances with a subsequent enhancement of inter-chain interactions, was simulated for crystalline anthracene [46]. The calculated imaginary part of the dielectric constant showed that the lowest absorption peak can be generated either by strongly bound excitons or by a free electron-hole pair, depending whether the polarization direction is parallel to the short or to the long molecular axis. An increase of band dispersion due to the overlap of teh wave functions between neighboring chains and band splitting has been obtained, resulting in a band gap reduction and consequently a redshift and broadening of the optical absorption peaks.

1.6 Optical processes

So far, we presented an overview of the main theories of electronic states in conjugated polymers. In the following, some of the important optical processes will be described with the aim of connecting the previous theoretical findings to the experimental results presented in the next Chapters. We will first recall useful a expression relating the dielectric constant to the refractive index, and we will introduce the Kramers-Kronig relations for the real and imaginary part of the dielectric function. Eventually, an expression for the reflection and transmission coefficients will be given. The processes of absorption and emission will be then discussed allowing to introduce the Franck-Condon principle

1.6.1 Interaction of light with the medium

Electromagnetic waves interacting with a non magnetic and neutral medium are described by Maxwell's equations (cgs units) [56]:

$$\nabla \times \mathbf{E} = -\frac{1}{c}\frac{\partial \mathbf{H}}{\partial t} \qquad \nabla \cdot \mathbf{E} = 0 \tag{1.43a}$$

$$\nabla \times \mathbf{H} = \frac{\epsilon}{c}\frac{\partial \mathbf{E}}{\partial t} + \frac{4\pi\sigma}{c}\mathbf{E} \qquad \nabla \cdot \mathbf{H} = 0 \tag{1.43b}$$

where $\mathbf{E}$ and $\mathbf{H}$ are the electric and magnetic field, respectively, and σ and ϵ are the conductivity and dielectric constant of the medium.

The electric field $\mathbf{E}$ induces a polarization $\mathbf{P}$ (dipole moment per unit volume), which is due to the redistribution of positive and negative charges. In general the i-th component of $\mathbf{P}$ can be expressed in terms of the electric field components by a power series of the form:

$$P_i = \sum_j \chi_{ij} E_j + \sum_{i,j} \gamma_{i,j,k} E_j E_k \tag{1.44}$$

For isotropic media, a linear approximation can be made, and we can assume that

$$\mathbf{P} = \chi \mathbf{E} \tag{1.45}$$

where χ is the electric susceptibility.

Equations (1.43) allow plane wave solutions for the electric and magnetic field, which can be written as:

$$\mathbf{E}(\mathbf{r}, t) = \mathbf{E}_0 e^{i(\hat{\mathbf{q}} \cdot \mathbf{r} - \omega t)} \tag{1.46a}$$

$$\mathbf{H}(\mathbf{r}, t) = \mathbf{H}_0 e^{i(\hat{\mathbf{q}} \cdot \mathbf{r} - \omega t)} \tag{1.46b}$$

where $\mathbf{r}$ is the position vector, ω is the frequency, $\mathbf{E}_0$ is the wave amplitude and $\hat{\mathbf{q}}$ is the wave vector. As we will show, in order to account for both energy dissipation and wave propagation, the wave vector has to be a complex quantity.

Manipulating Equation (1.43) and using the vector identity

$$\nabla \times (\nabla \times \mathbf{E}) = \nabla \cdot (\nabla \cdot \nabla) - \nabla^2 \mathbf{E} \tag{1.47}$$

it is possible to obtain the wave equation for plane waves propagating in an energy absorbing medium

$$\nabla^2 \mathbf{E} = \frac{\partial^2 \mathbf{E}}{\partial t^2} + \frac{4\pi\sigma}{c^2} \frac{\partial \mathbf{E}}{\partial t} \tag{1.48}$$

Then, inserting Equation (1.46) into (1.48), we can define a complex wave vector, hence a complex refractive index of the medium trough the relation

$$\hat{q} = \frac{\omega}{c} \hat{n} = \frac{\omega}{c} (n + ik) \tag{1.49}$$

Now Equation (1.46) for the electric field can be re-written as

$$\mathbf{E} = \mathbf{E}_0 e^{-\frac{\omega}{c} \mathbf{k} \cdot \mathbf{r}} e^{i(\frac{\omega}{c} \mathbf{n} \cdot \mathbf{r} - \omega t)} \tag{1.50}$$

The first exponential describes the the attenuation of the wave amplitude with distance. The second exponential in Equation (1.50)is related to the

imaginary part of the wave vector and describes a wave traveling with phase velocity c/n, hence the identification of n as the refractive index.

A complex wave vector implies a complex susceptibility:

$$\chi = \chi_1 + i\chi_2 \tag{1.51}$$

which means that the electric field $\mathbf{E}$ and the polarizability $\mathbf{P}$ are non in phase. Similarly we can define a complex dielectric function $\epsilon = \epsilon_1 + i\epsilon_2$ that relates the electric field to the displacement $\mathbf{D}$:

$$\mathbf{D} = \mathbf{E} + 4\pi\mathbf{P} = \epsilon\mathbf{E} = (\epsilon_1 + i\epsilon_2)\mathbf{E} \tag{1.52}$$

and a complex conductivity that relates the electric filed to the current

$$\mathbf{J} = \sigma\mathbf{E} = (\sigma_1 + i\sigma_2)\mathbf{E} \tag{1.53}$$

Inserting Equations (1.46) into (1.43) the Maxwell's equations become:

$$\mathbf{q} \times \mathbf{E} = \frac{\omega}{c} \qquad \mathbf{q} \cdot \mathbf{E} = 0 \tag{1.54a}$$

$$\mathbf{q} \times \mathbf{H} = -\frac{\omega}{c}\epsilon\mathbf{E} \qquad \mathbf{q} \cdot \mathbf{H} = 0 \tag{1.54b}$$

Form these equations it is clear that $\mathbf{q}$, $\mathbf{E}$, and $\mathbf{H}$ must be mutually perpendicular.

Using the equality:

$$\hat{\epsilon} = \epsilon_1 + i\epsilon_2 = \hat{n}^2 \tag{1.55}$$

useful relationships relating the components of the dielectric function to those of the refractive index can be obtained

$$\epsilon_1 = n^2 - k^2 \qquad \epsilon_2 = 2nk \tag{1.56a}$$

$$n = \sqrt{\frac{1}{2}\sqrt{\epsilon_1^2 + \epsilon_1^2} + \epsilon_1} \qquad k = \sqrt{\frac{1}{2}\sqrt{\epsilon_1^2 + \epsilon_1^2} - \epsilon_1} \tag{1.56b}$$

ϵ_1 and ϵ_2, as well as n and k, are not independent quantities, but they are related, as we shall see in the following Section, by dispersion relations.

Finally, the absorption coefficient α can be easily expressed in terms of the imaginary part of the refractive index k as follows.

The absorption coefficient which describes the fractional decrease in intensity with distance, is given by

$$\alpha = -\frac{1}{I}\frac{dI}{dr} \tag{1.57}$$

where I is the intensity. Since the intensity is proportional to the square of the wave amplitude, from Equations (1.46) and (1.56) we find that:

$$\alpha = 2\omega k/c = 4\pi k/\lambda \tag{1.58}$$

where λ is the wavelength of light in the vacuum.

1.6.2 Kramer-Kronig dispersion relations and sum rules

A dispersion relation is an integral formula relating a dispersive process to an absorption process. In general, dispersion relations follow rigourously form the requirement of causality. The dispersion relation that can be derived for a linear system are quite general and apply also for the real and imaginary part of the complex dielectric constant. Form Equations (1.45) and (1.52) we can derive the relation between polarization and electric field

$$\hat{\epsilon} - 1 = 4\pi \frac{\mathbf{P}}{\mathbf{E}} \tag{1.59}$$

which of course obeys to the causality principle (no polarization can be induced before an electric field is applied). The dispersion relations for ϵ_1 and ϵ_2 are known as Kramers-Kronig relations [56]:

$$\epsilon_1(\omega) = 1 + \frac{2}{\pi} \wp \int_0^\infty \frac{\omega' \epsilon_2(\omega')}{(\omega')^2 - \omega^2} d\omega' \tag{1.60a}$$

$$\epsilon_2(\omega) = -\frac{2\omega}{\pi} \wp \int_0^\infty \frac{[\epsilon_1(\omega') - 1]}{(\omega')^2 - \omega^2} d\omega' \tag{1.60b}$$

where $\wp$ is the principal part of the integral. Form the Kramers-Kronig relations (1.60) it is possible to derive a sum rule for solids. Equation (1.60b) can be written as:

$$\epsilon_1(\omega) - 1 = \frac{2}{\pi} \wp \int_0^{\omega_c} \frac{\omega' \epsilon_2(\omega')}{(\omega')^2 - \omega^2} d\omega' + \frac{2}{\pi} \wp \int_{\omega_c}^\infty \frac{\omega' \epsilon_2(\omega')}{(\omega')^2 - \omega^2} d\omega' \tag{1.61}$$

where ω_c is a cut-off frequency such that there is no absorption at higher frequencies ($\epsilon_2 = 0$ for $\omega > \omega_c$). If we want to determine ϵ_1 for $\omega \gg \omega_c$, then we can neglect ω' in the denominator of the first integral in Equation (1.61). The second integral is zero because we set $\epsilon_2 = 0$ for $\omega > \omega_c$. Under these conditions, Equation (1.61) becomes:

$$\epsilon_1(\omega) = 1 - \frac{2}{\pi\omega^2} \wp \int_0^{\omega_c} \omega' \epsilon_2(\omega') d\omega' \quad \text{for} \quad \omega \gg \omega_c \tag{1.62}$$

In the high frequency limit, the real dielectric function is given by:

$$\epsilon_1(\omega) = 1 - \frac{\omega_p^2}{\omega^2} = 1 - \frac{4\pi N e^2/m}{\omega^2} \tag{1.63}$$

where ω_p is the plasma frequency, N is the density of electrons, and m is the free mass of the electron. Comparisons of Equations (1.62) and (1.63) shows that:

$$\int_0^\infty \omega\epsilon_2(\omega)d\omega = \frac{1}{2}\pi\omega_p^2 \tag{1.64}$$

where the upper limit of integration has been extended to ∞ because $\epsilon_2 = 0$ for $\omega > \omega_c$[7]. The physical meaning of sum rule (1.64) originates from the rate of energy absorption per unit volume form an electric field is:

$$\frac{d\mathcal{E}}{dt} = \Re\left(\mathbf{E}\cdot\frac{\partial}{\partial t}\hat{\mathbf{D}}\right) = \Re\left[\mathbf{E}\cdot(\epsilon_1 + i\epsilon_2)\frac{\partial}{\partial t}\mathbf{E}\right] \tag{1.65}$$

If $\mathbf{E}$ has a time dependence of the form $e^{-i\omega t}$, this becomes

$$\frac{d\mathcal{E}}{dt} = \omega\epsilon_2|\mathbf{E}|^2 \tag{1.66}$$

Thus the integral

$$\int_0^\infty \omega\epsilon_2(\omega)d\omega \tag{1.67}$$

is a measure of the energy absorption for all frequencies.

Sum rules are frequently defined in terms of an effective number of electron per atom, n_{eff}, contributing to the optical properties over a finite frequency range. Thus,

$$\int_0^{\omega_c} \omega\epsilon_2(\omega)d\omega = \frac{1}{2}\pi\frac{4\pi N_a e^2}{m}n_{eff} \tag{1.68}$$

where N_a is the density of atoms.

1.6.3 Reflection and transmission at normal incidence

Consider a beam of light incident on a surface as shown in Figure 1.12. Let I_i, I_r, and I_t be the incident, reflected and transmitted flux densities, respectively, which is defined as

$$I = \frac{v\epsilon}{2}E_0^2 \tag{1.69}$$

where v is the velocity of light in the medium of dielectric constant ϵ.

The incident power, that is the energy per unit time, is then $\mathrm{I}_i A\cos\theta_i$, $\mathrm{I}_r A\cos\theta_r$, and $\mathrm{I}_t A\cos\theta_t$ for the incident, reflected and transmitted beams, respectively, where A is the beam area. *Reflectance* is defined as the ratio of the reflected power to the incident power:

[7]This sum rule holds for energy absorption by transverse fields -such as photons. A sum rule can also be obtained for longitudinal fields [56].

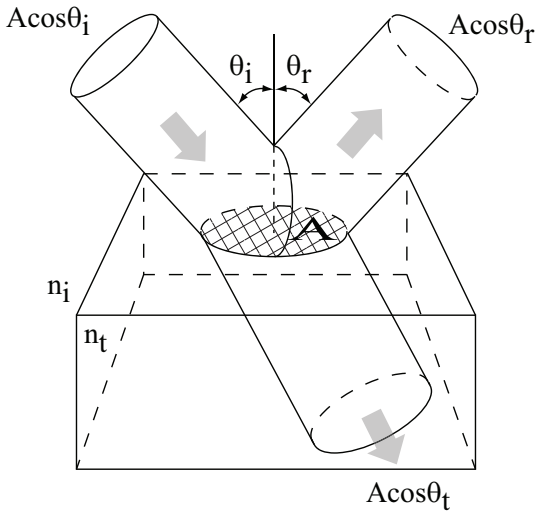

Figure 1.12: Incident, reflected and transmitted light beams at the interface between two media of refractive index n_i and n_t. A is the beam area.

$$R \equiv \frac{I_r A \cos\theta_r}{I_i A \cos\theta_i} = \frac{I_r}{I_i} \tag{1.70}$$

Similarly, *transmittance* is defined as:

$$T \equiv \frac{I_t A \cos\theta_t}{I_i A \cos\theta_i} = \frac{I_t}{I_i} \tag{1.71}$$

Using (1.69) one obtains:

$$R = \left(\frac{E_{0r}}{E_{0i}}\right)^2 = r^2 \tag{1.72a}$$

$$T = \frac{n_t \cos\theta_t}{n_i \cos\theta_i}\left(\frac{E_{0r}}{E_{0i}}\right)^2 = \left(\frac{n_t \cos\theta_t}{n_i \cos\theta_i}\right) t^2 \tag{1.72b}$$

being r and t the Fresnel coefficient for the amplitude of the reflected and transmitted light, respectively. For the conservation of energy, assuming there is no absorption, the following relation has to be verified:

$$R + T = 1 \tag{1.73}$$

It is convenient to separate the components of both R and T:

$$R_\perp = r_\perp^2 \qquad R_{//} = r_{//}^2 \tag{1.74a}$$

$$T_\perp = \left(\frac{n_t \cos\theta_t}{n_i \cos\theta_i}\right) t_\perp^2 \qquad T_{//} = \left(\frac{n_t \cos\theta_t}{n_i \cos\theta_i}\right) t_{//}^2 \tag{1.74b}$$

For normal incidence, $\theta_t = \theta_i = 0$ and any distinction between the parallel and perpendicular component vanishes. In this case, Equations (1.74b) become:

$$R = R_{\perp} = R_{//} = \left(\frac{n_t - n_i}{n_t + n_i}\right)^2 \tag{1.75a}$$

$$T = T_{\perp} = T_{//} = \frac{4n_t n_i}{(n_t + n_i)^2} \tag{1.75b}$$

Taking into account the complex form of the refractive index derived in the previous Section, and setting $n_i = 1$, we can rewrite R in Equation (1.75b) as:

$$R = \frac{(n-1)^2 + k^2}{(n+1)^2 + k^2} \tag{1.76}$$

1.6.4 Einstein coefficient for absorption and emission

The decay process of an electron form an excited state might involve emission of light (radiative decay), and, as we will see, a useful relationship exists the rate of radiative decay and the measured absorption coefficient.

The processes of light emission and absorption are governed by rate equations whose coefficients were calculated by Einstein. Let us consider the two level system depicted in Figure 1.13. Here the electronic states are labeled with i and j, and the vibrational levels are indicated with μ and ν. When a photon is absorbed, an electron is raised from (i,μ) to (j, ν). From the excited state, the electron can go back to the lowest energy levels via stimulated or spontaneous emission. Einstein calculated the relationships between the rate constants for absorption $B_{i\mu\rightarrow j\nu}$, stimulated emission $B_{j\nu\rightarrow i\mu}$, and spontaneous emission $A_{j\nu\rightarrow i\mu}$:

$$B_{i\mu\rightarrow j\nu} = B_{j\nu\rightarrow i\mu} \tag{1.77a}$$

$$\frac{A_{j\nu\rightarrow i\mu}}{B_{j\nu\rightarrow i\mu}} = \frac{8\pi^3\nu^3 n^3}{c^3} \tag{1.77b}$$

where n is the refractive index.

The transition probabilities for absorption and emission are proportional to the transition dipole moment:

$$B_{i\mu\rightarrow j\nu} = \frac{8\pi^3}{3h^3}|M_{i\mu\rightarrow j\nu}|^2 \tag{1.78a}$$

$$A_{j\nu\rightarrow i\mu} = \frac{64\pi^4\nu^3 n^3}{3h^3c^3}|M_{i\mu\rightarrow j\nu}|^2 \tag{1.78b}$$

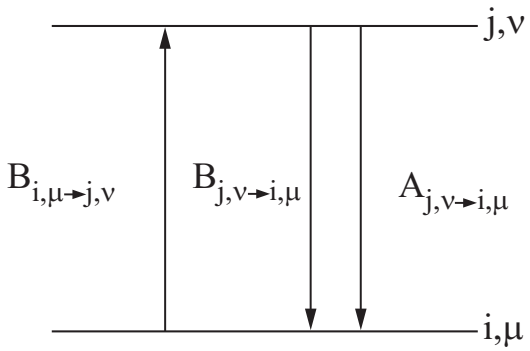

Figure 1.13: Illustration of Einstein coefficients for a 2 level system. $B_{i\mu\rightarrow j\nu}$ refers to absorption, $B_{j\nu\rightarrow i\mu}$ to stimulated emission, and $A_{j\nu\rightarrow i\mu}$ to spontaneous emission.

B is directly related to the experimental absorption parameter through the equation:

$$B_{i\rightarrow j} = \sum_{\nu} B_{i0\rightarrow j\nu} \propto \int \frac{\alpha(\nu)d\nu}{\nu} \tag{1.79}$$

being α the molar extinction coefficient.

The radiative lifetime of the excited state is the inverse of the transition probability of spontaneous emission:

$$\tau_{rad}^{-1} = \sum_{\mu} A_{j0\rightarrow i\mu} \tag{1.80}$$

Defining the quantity:

$$< \bar{\nu}^{-3} >^{-1} = \frac{\int I(\bar{\nu})d\bar{\nu}}{\int \bar{\nu}^{-3} I(\bar{\nu})d\bar{\nu}} \tag{1.81}$$

the lifetime of (j,ν) can be estimated using the relation:

$$\tau_{rad}^{-1} = \frac{8\pi hc}{n} < \bar{\nu}^{-3} >^{-1} B_{i\rightarrow i} \tag{1.82}$$

1.6.5 Franck-Condon principle

Following the absorption of light, an electron moves to an excited state and eventually relaxes back to the ground state. The wave functions of both these states, however, in the Born-Oppenheimer limit, can be separated into the product of a purely electronic and a vibrational component. As a result, any given electronic state is composed of many vibrational levels. In molecular crystals, the intra-molecular vibrational states (arising form the internal vibration of the molecule) are sometimes observed in their spectra. The different vibronic levels are numbers as in Figure 1.14.

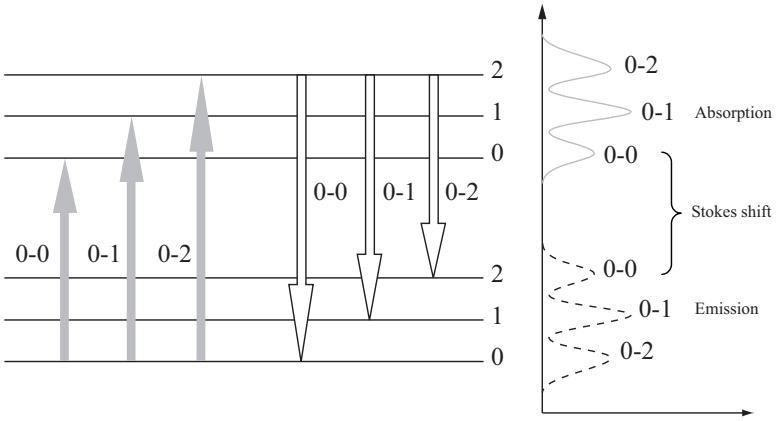

Figure 1.14: Schematic of vibronic absorption transitions. The vibrational levels in the ground and excited state are labeled 0,1,2... Transition between vibrational states are sometimes observed in conjugated polymer spectra.

It follows form Equations (1.78) that the evaluation of important parameters such as the absorption and emission coefficients requires the evaluation of the transition dipole moment. The calculation of transition dipole moments can be significantly simplified by the Franck-Condon principle. This is essentially a testament of the Born-Oppeneheimer approximation, as it assumes that electron transitions occur so quickly that nuclear coordinated remain stationary. This is generally valid being nuclear motion times roughly 10 times longer than electronic transition times.

After the electronic transition has taken place, the nuclei respond by moving along the adiabatic potential energy surface of the excited state to a new equilibrium position, resulting in a change of the molecule to the excited state configuration. This configurational change is known as relaxation and the energy involved is the relaxation energy, E_{rel}. Emission follows the same path. In the potential energy surface diagram the transition is vertical, as represented in Figure 1.15

Describing the nuclear motion in terms of normal coordinates Q, for small displacements from the equilibrium position, each normal mode can be considered as an harmonic oscillator. The relaxation of the nuclear coordinate Q to the bottom of the adiabatic energy curve leads to the Stokes shift between absorption and emission, illustrated in Figure 1.16.

Within the Franck-Condon approximation, the wave function describing the state i can be separated into its electronic, vibronic, and spin part:

$$\Psi_i = \psi_i \phi_i \chi_i \tag{1.83}$$

The transition probability between two states i and j can then be written as:

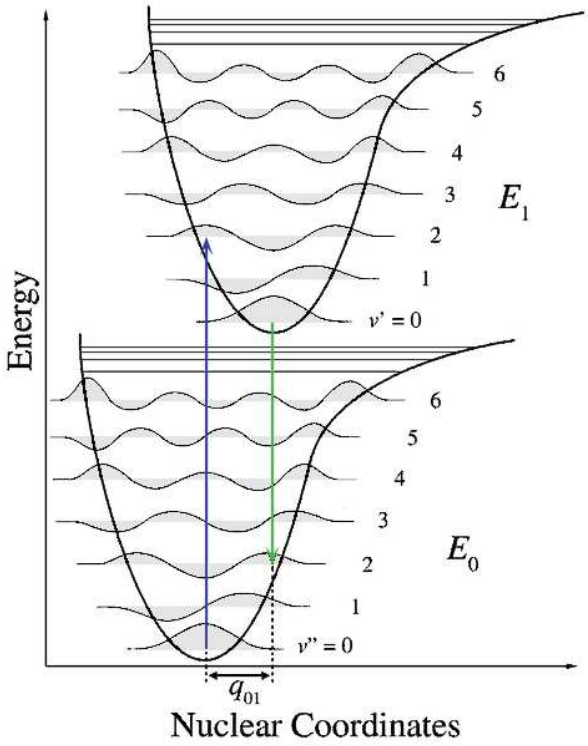

Figure 1.15: Representation of the Franck-Condon principle. The potential energy surfaces of the ground and excited states are plotted as a function of the normal coordinates describing the nuclear motion.

$$R_{i\to j} \propto |<\Psi_i|M|\Psi_j>|^2 = <\psi_i\phi_i\chi_i|M|\psi_j\phi_j\chi_j> \\ = <\psi_i|M|\psi_j><\phi_i|\phi_j><\chi_i|\chi_j> \tag{1.84}$$

where the dipole moment operator M appears only in the electronic term in virtu of the Franck-Condon approximation.

The Franck-Condon factors are defined as:

$$F_{\mu\nu} = |<\mu_i|\nu_j>|^2 \tag{1.85}$$

and they represent a weight for the intensity of each of the vibronic transitions. At T=0K, since only the lowest vibrational state is occupied, the Franck-Condon factor is:

$$F_{0\nu} = |<0|\nu>|^2 = \frac{e^{-A^2/2}(A^2/2)^\nu}{\nu!} \tag{1.86}$$

where A is:

$$A = \sqrt{\frac{M\omega}{\hbar}}\Delta Q \tag{1.87}$$

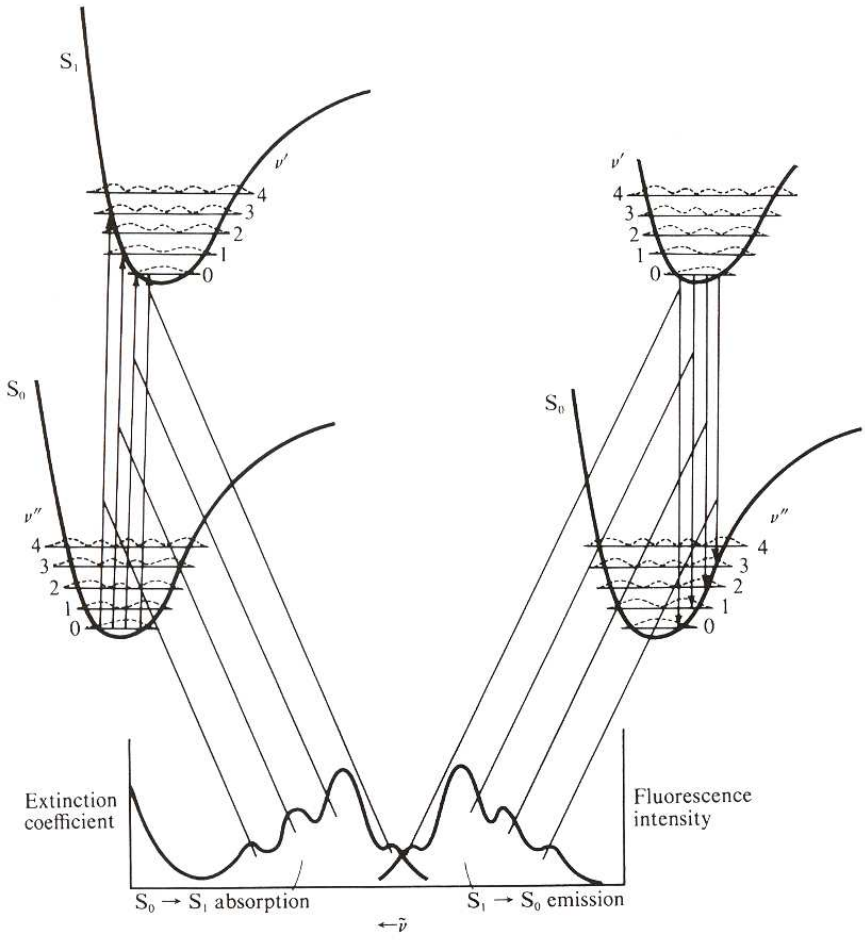

Figure 1.16: Potential energy curves with vibrational probability functions showing the mirror image relationship between absorption and emission.

Equation (1.86) is commonly written as:

$$F_{0\nu} = \frac{e^{-S}(S)^{\nu}}{\nu!} \tag{1.88}$$

where S is the Huang-Rhys parameter defined by:

$$S = \frac{A^2}{2} = \frac{M\omega}{2\hbar}\Delta Q^2 \tag{1.89}$$

where Δ Q=Q_i-Q_j, being Q_i and Q_j the normal coordinate of the ground and excited state, respectively.

The Huang-Rhys parameter is related to the relaxation energy through:

$$S\hbar\omega = E_{rel} = \left(\nu + \frac{1}{2}\hbar\omega\right) \tag{1.90}$$

A few remarks can be done:

- Only 0-0 transitions occur when S=0.
- $F_{0\nu}$ satisfies the sum rule $\sum_{\nu} F_{0\nu}$=1, so as S increases oscillator strength is transferred from the 0-0 transition to higher transitions .
- The dominant transition is to the ν vibrational state where ν=S-1/2. Therefore vertical classical transitions are dominant.
- In general, $F_{0\nu}$ follows a Poisson distribution. However, as S increases the profile becomes more Gaussian.
- S may be obtained empirically form the experimental vibronic progression since S=F_{01}/F_{00}.

Chapter 2

Experimental methods

The Chapter describes the materials studied in this work and the experimental techniques used to characterize them. A brief introduction to diamond anvil cells is given, before the specifications of the two different cells used in this work are discussed. Each of the measurements here described was performed for different applied pressure, so the DAC was combined with every set up described. The role of intermolecular interactions in highly oriented PPV was studied by means of Raman and polarized reflectance and transmittance spectroscopy. A soluble derivative of PPV was also studied, namely MEH-PPV. Transient photoinduced absorption spectra of MEH-PPV were recorded, with a set up that allows a temporal resolution less than 150 fs. Steady-state photoinduced absorption and photoluminescence of MEH-PPV were performed both at room and low temperature. Finally, the dependence of photoinduced absorption on the modulation of the pump beam is described.

2.1 Materials

This study was devoted to the characterization of poly-p-phenylene vinylene (PPV) and one of its soluble derivatives, namely poly (2-methoxy, 5-(2'-ethyl)-hexyloxy) paraphenylene vinylene (MEH-PPV).

The following Chapter discusses and analyzes the optical response of highly oriented PPV. Its anisotropic nature and the previous detailed assignment of its primary photo-excitation, turn this material in one of the best candidates to help understand the still unraveled role of intermolecular interactions.

The molecular structure of PPV is shown in (Figure 2.1).

The self-standing film of PPV studied in this work was oriented by tensile drawing, with an elongation ratio up to λ=5. The structure of the non-oriented film is heterogenous, including crystallites and amorphus regions. As a result of the stretching process, both the crystalline regions and macromolecular chains are simultaneously aligned along the draw direction. Furthermore, a symmetry is induced in the film, which originates from the alignment of the crystallites.

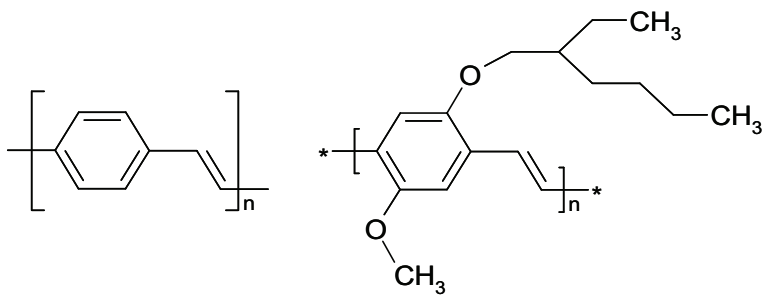

(a) (b)

Figure 2.1: Molecular structure of (a) poly-p-phenylenevinylene (PPV) and (b) poly(2-methoxy, 5-(2'-ethyl)- hexyloxy)paraphenylene vinylene (MEH-PPV).

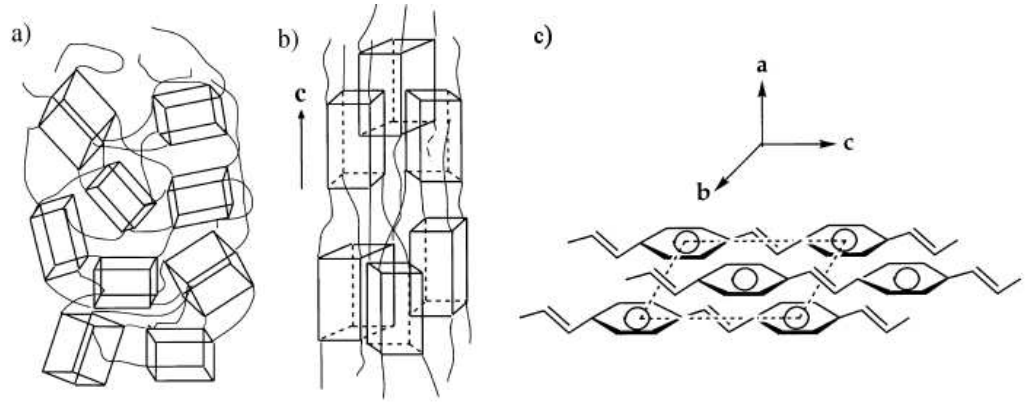

Figure 2.2: The effect of stretching on PPV structure: a) non-stretched PPV; b) oriented PPV, where boxes represent the crystallites and lines the polymer chains in amorphus regions; c) projection of the unit cell of the crystalline phase of PPV along a-axis (adapted from [57]).

This process is depicted in Figure 2.2.

The crystallinity degree and the symmetry of the film were found to be strongly dependent on the draw ratio [57]. In this film the crystallinity is ∼70% of the volume, with a typical crystallite size of 20 nm. In the crystalline phase, the chains are packed in an orthorhombic structure with the c-axis of the crystallites parallel to the draw direction as shown in Figure 2.2. Since the orientation of each crystallite in the a,b plane is random, the system has cylindrical symmetry. The translational periodicity along the b-axis (corresponding to the inter-chain distance) is 5 Å and the intermolecular spacing between benzene ring layers inside the unit cell is 3.9 Å [57].

As a result of the stretching procedure, PPV gained an extremely extended conjugation length. In general, it is possible to estimate the conjugation length through a combination of optical absorption, Raman scattering, and fluorescence spectroscopies. Unfortunately, a direct study has not been done for

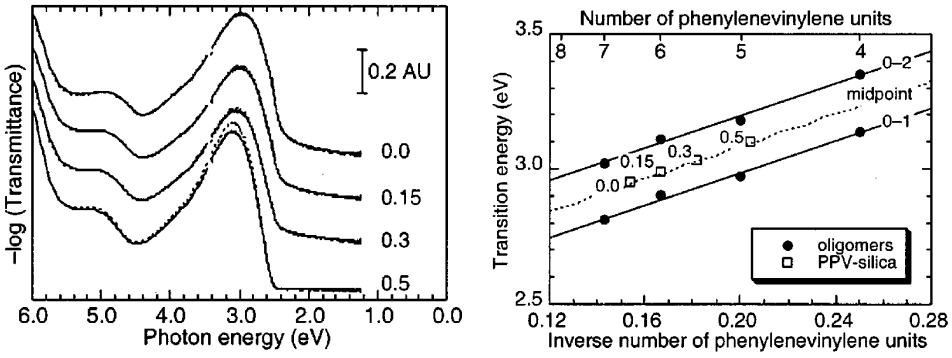

(a) (b)

Figure 2.3: Transmission spectra of PPV and PPV-SiO_2 films (SiO_2 volume fraction marked on the plot) (a) and calibration plot to evaluate the optical absorption conjugation length based on the mean energy of the 0-1 and 0-2 vibronic transitions of oligomers (b). Adapted form [58].

highly oriented PPV, but to an idea of its conjugation length, we can compare the optical results for this sample with those obtained for PPV-SiO_2 nanocomposites [58]. Based on the mean energy of the 0-1 and 0-2 vibronic transitions of PPV oligomers, reported in Figure 2.3, it can be concluded that being the transition energy of highly oriented PPV at 2.5 eV, its conjugation length is incredibly higher. A rough estimation of number of consecutive PPV units might be ~ 20.

For the high pressure study, a small piece of PPV of about 600x200 μm and 15-16 μm thick was cut from the self-standing film and positioned inside the pressure cell chamber. A fragment of PPV smaller than the sample chamber was necessary in order to collect transmission through the cell, which was used to normalize the data (Chapter 4). The stretching direction along which the chains are aligned (c-axis in Figure 2.2), will be named "parallel" while dealing with the polarized optical response of oriented PPV. This direction is also highlighted by a blue arrow in Figure 2.9.

Theoretical results on the electronic properties of PPV-based polymer crystals show that different morphologies (herringbone and π-stacking) dramatically influence inter-chain interactions [55]. The parameter of interest in this case is the transfer integral, which can be calculated for both the direction parallel and perpendicular to the polymer chains. It is found that the transfer integral orthogonal to the backbone is very sensitive to different inter-chain environments, being one order of magnitude greater for π-stacking in the π direction than for the herringbone structure. In this respect, MEH-PPV, a soluble derivative of PPV, possessing a displaced π-stacking structure, is particularly interesting for the study of inter-chain interactions.

In this work, thin films of pristine MEH-PPV were prepared from solutions in toluene (7 mg of MEH-PPV : 1 mL of toluene). The molecular structure

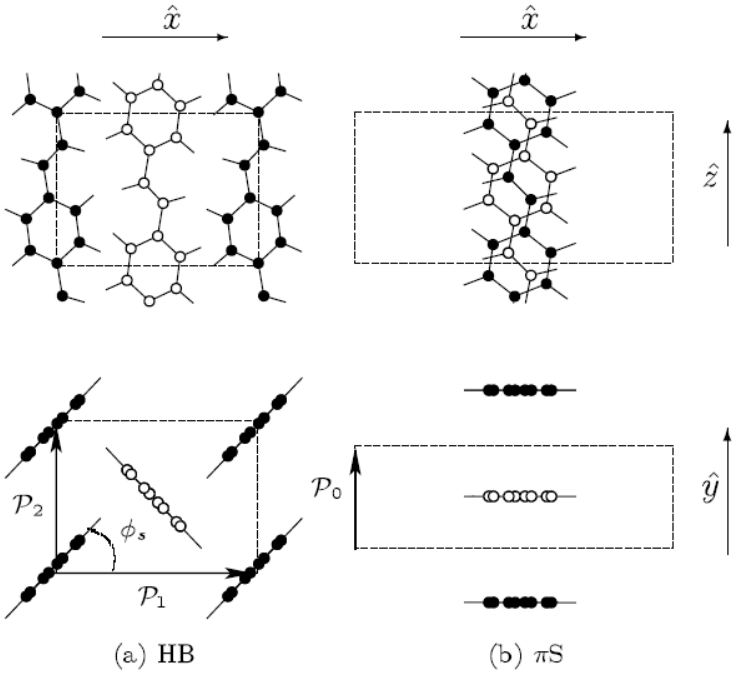

Figure 2.4: Chain arrangement in herringbone (HB) structure (monoclinic unit cell) and displaced π stack (base-centered orthorhombic Bravais lattice). (adapted from [55]).

of MEH-PPV is shown in Figure 2.1. MEH-PPV powder was purchased by American Dye Source (Canada). The films were drop cast onto a glass surface and let dry in air until evaporation of the solvent was completed. A tiny piece of film (250x250 μm) was peeled off the substrate and cut to fit the sample chamber of the diamond anvil cell. Since no background is required to normalize PA measurements the sample can almost fill the whole sample chamber. Based on simulations of PL spectra of oligomer having different size [59], we can estimate the conjugation length of MEH-PPV as roughly 5 repeating units. Such a short conjugation length is to be expected for disordered systems.

2.2 Applying pressure: the diamond anvil cell

The basic principle of a diamond anvil cell (DAC) is very simple. A sample placed between the flat parallel faces of two opposed diamond anvils is subject to a pressure exerted by pushing the anvils closer together. Since pressure is force divided by area, the modest force applied creates an extremely high pressures between the small faces of the diamonds. Figure 2.5 also shows the fundamental components of a diamond anvil cell: two opposed diamonds separated by a metal gasket, with a hole for sample containment.

DACs were introduced in the 40's to study the behavior of various materials subject to high pressures such as compressibility, optical and magnetic

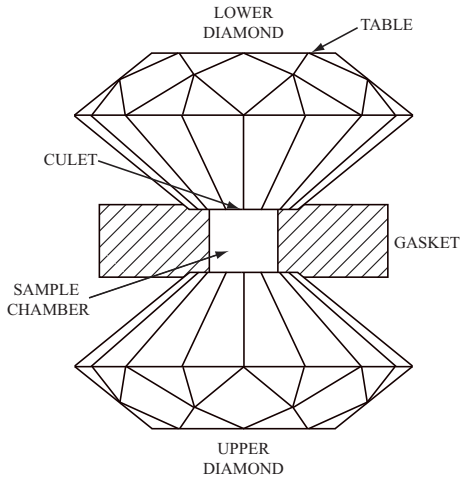

Figure 2.5: The basic parts of a DAC: two opposed diamond for sample confinement in a pressure transmitting medium.

properties. Since then, many different types of cells have been designed for different purposes. For spectroscopic studies the most common cell is the so-called Merrill-Bassett DAC (after Merrill and Bassett [60]). The basic construction of a Merrill-Bassett DAC is shown in Figure 2.6. The diamond anvils are embedded into two parallel plates, made of Be-Cu. Pressure is applied by tightening the set of 3 or 4 screws located at the apexes of the upper plate. The Be support is suitably shaped to provide wide-angle access to the incoming beam.

Each of the component of a DAC has been carefully designed over the years to guarantee the best performances. In the following the basic characteristics of each part of a DAC are described.

Due to its hardness and optical transparency in the visible and infrared, diamond is an ideal material for construction of high pressure cells. Diamonds for DACs are usually selected form brilliant-cut gem stones and they are classified as type I and type II according to their purity. For optical applications type II diamonds are preferred due to their smooth absorption spectrum that does not change dramatically under applied uni-axial stress. A further classification divides diamonds into type Ia (larger aggregates of nitrogen impurities), type Ib (single nitrogen dopants), type IIa (considered pure), and type IIb (including boron impurities). Among these, type IIa diamonds are preferred for optical investigations. Furthermore, a stone with lower internal stress will have a more narrow Raman line shape and lower birefringence, an important issue for polarized optical studies.

The size of the diamonds used for DACs may vary from $\frac{1}{8}$ to $\frac{1}{2}$ carat[1]. The anvil flat (called culet) is usually set parallel to the (100) or the (110) plane of the diamond and ranges from 0.3 to 0.7 mm. The octagonal surface opposite to the anvil flat is referred to as the table and its size varies form about 2 mm

[1] 1 carat is defined as 200 mg.

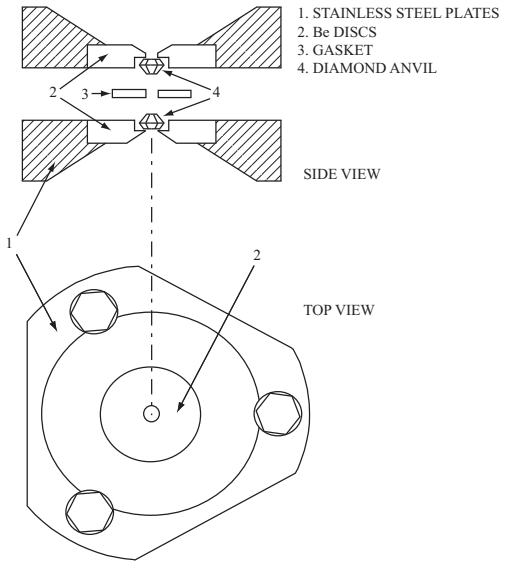

Figure 2.6: The basic parts of a DAC: two opposed diamond for sample confinement in a pressure transmitting medium [61].

in $\frac{1}{8}$ carat diamonds to 3.5-4.5 mm in larger diamonds.

The use of a gasket for containment of a hydrostatic medium was first demonstrated in 1965 by Van Valkenburg [62]. The gasket is prepared by drilling a hole in a piece of metal foil, that must have a diameter approximately half of that of the culet. Then, it has to be seated onto the lower diamond flat, with the center of the hole matching the center of the diamond. The centering of the gasket is followed by filling the hole with the sample and pressure transmitting medium and by sealing bringing the upper anvil on the gasket. Inconel[2] and tempered stainless steel are generally used as gasket materials. The gasket, besides providing containment for the pressure transmitting medium and creating the sample chamber, extrudes around the diamonds, deforming plastically when squeezed between the two anvils, as shown in Figure 2.7. Moreover, the gasket acts as a supporting ring, preventing failure of the anvils due to the concentration of stresses at the edge of the anvil faces.

For pressure distribution to be uniform all over the sample, the gasket is usually pre-indented. This is done compressing the gasket between the two anvils with a pressure approximately equal to the maximum reachable value. In practice, pre-indentation is necessary when extremely high pressure (>3 GPa) are achieved.

The thickness of the gasket will affect the maximum pressure the cell can experience without failure. A thinner gasket will raise the maximum pressure obtainable reducing the risk of deformation of the sample chamber, whereas a thicker gaskets is much easier to load and there is a greater volume within

[2]Inconel refers to a family of nickel-based alloys.

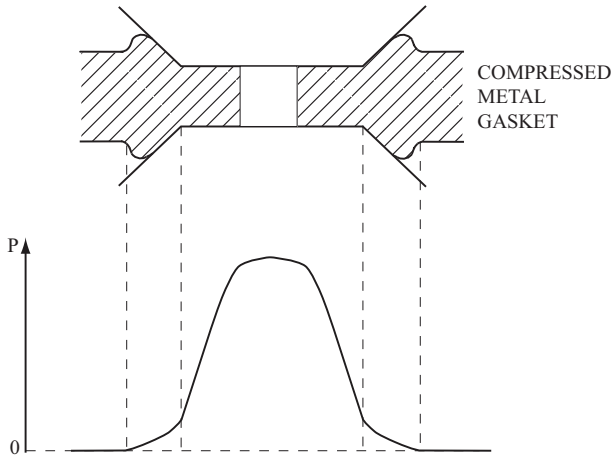

Figure 2.7: Shape of a gasket squeezed between the anvils, supporting the diamond edges [61] and pressure distribution on the gasket.

the sample chamber. At higher pressures thicker gaskets tend to deform more readily into an oval shape as one side of the pressure chamber translates relative to the other.

With the introduction of the ruby fluorescence method in 1972 [63] a major problem with the DAC, namely pressure calibration, was removed, clearing the way for the widespread use od DAC for high pressure studies.

Forman *et al.* [63] first showed that the R lines of Cr-doped Al_2O_3 shift linearly with hydrostatic pressure in the range of $1 \div 22$ kbar. Further work by Piermarini, Block, and Barnett [64] made the ruby fluorescence technique a rapid and convenient in situ method for measuring pressure. A tiny chip of ruby is placed in the pressure transmitting medium along with the sample, and fluorescence is usullay excited by a Ar^+ laser (488 nm). The R ruby lines are quite intense, the wavelengths of the doublet R_1 and R_2 being at 692.7 and 694.2 nm respectively. Under pressure these shift to higher wavelengths and the shift is linear with pressure, with an accuracy in pressure determination of 0.3 kbar. Piermarini [65] showed that the linearity holds up to 300 kbar and that the ruby R lines shift at the same time. Moreover, it was found that the R lines broaden if the ruby experiences non-hydrostatic stresses.

The role of the pressure medium inside of the sample chamber is to transform the uni-axial compression of the diamonds into a hydrostatic pressure environment for the samples. Sometimes a 4:1 methanol-ethanol mixture is preferred as pressure medium. The main advantage of a liquid pressure medium is the ease of loading the cell but one of the major disadvantages is sample solvent interaction. For organic polymers samples the inert nature and the useable pressure range of the argon medium is preferred. Argon, which condenses into a liquid at 87 K and freezes at 84 K at 1 atmosphere, freezes at 12 kbar but retains hydrostatic pressures inside the sample chamber up to about 90 kbar. In general the use of inert gases like helium, nitrogen, and argon makes the cell loading rather complicated, due to their high compressibility. Solid media

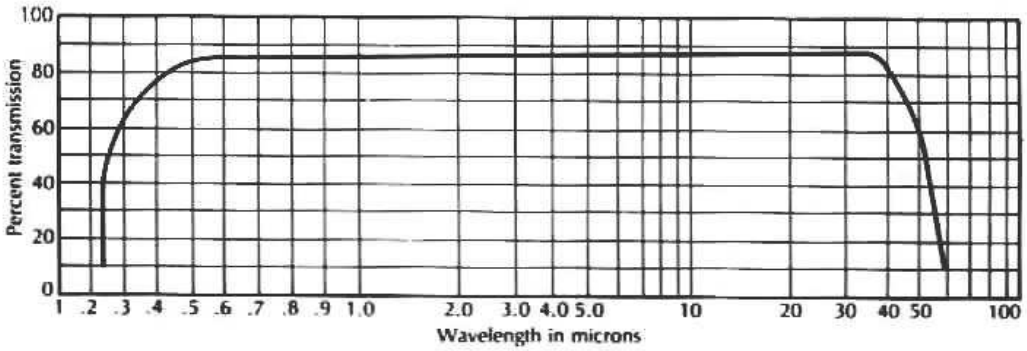

Figure 2.8: Transmittance spectrum of CsI, form www.harrricksci.com

such as CsI, KBr, and NaCl are good pressure transmitting media too, providing a hydrostatic environment up to 10-15 GPa. They are also particularly indicated for spectroscopic measurements, because of their transparency over a wide spectral range, with no absorption bands, as showed in Figure 2.8 for CsI. Moreover, the ease of the loading procedure makes their use in diamond cells extremely convenient.

In this work two diamond anvil cells were used. Due to the different spectroscopic techniques which the cell was combined with, the choice of the pressure transmitting medium and the method used for pressure determination were not the same for highly oriented PPV and MEH-PPV. In the following the main characteristics of the two DACs are presented and the methods to measure pressure are discussed.

Figure 2.9 shows the DAC used to study highly oriented PPV (a) and a magnified image of the sample inside the cell The blue arrow indicates the chain orientation (draw direction) along which the film can be readily broken. The type IIa diamonds of this cell have a culet diameter of 1.2 mm, allowing a gasket hole of 500 μm.

The gasket was hand made, drilling hole in a 300 μm thick foil of stainless steel via electro-erosion. A scheme of the electro-erosion apparatus is shown in Figure 2.10. In this set up, the drill bit (a copper wire) and the metal gasket, immersed in a mixture of petroleum and paraffin, are the electrodes. Whenever their distance falls below a certain critical value (determined by the dielectric rigidity of the dielectric liquid), electric sparks are produced and an electron bombardment mechanism is triggered. Microscopic pieces of metal are then removed from the gasket, starting to form the hole. For a perfectly round hole, the erosion process has to be maintained in a steady-state regime, keeping the bit-gasket separation as constant as possible, that is the bit has to approach the gasket with a speed the equals the erosion rate. The values of the capacitance C, applied voltage V, and load resistance R depend on the wire diameter and dielectric liquid. In the system showed in Figure 2.10, C=15 pF, V=150 V, and R=100 Ω. Due to the moderate pressures applied, non pre-indented gasket were used in this work.

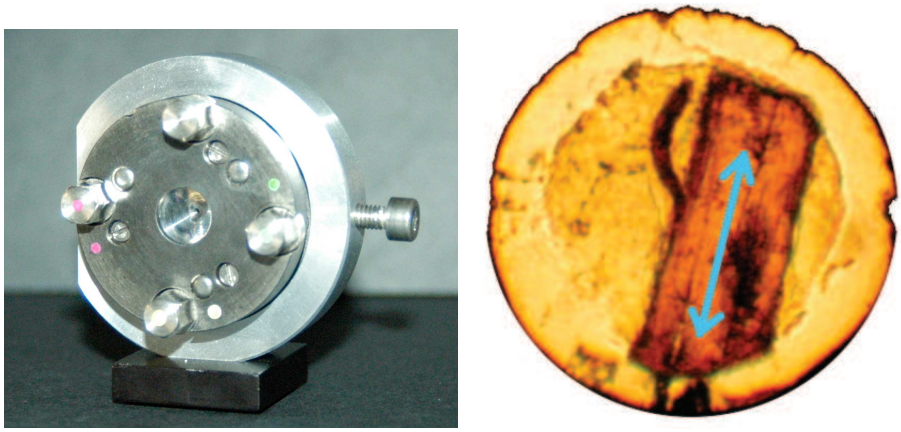

(a) (b)

Figure 2.9: Diamond anvil cell used for spectroscopic measurements of highly oriented PPV (a). A small piece of highly oriented PPV inside the DAC. The blue arrow indicates the direction of the polymer chains (b).

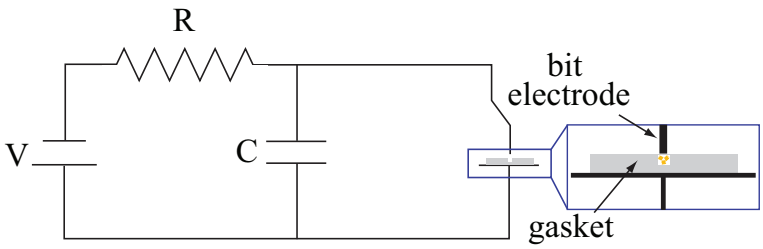

Figure 2.10: Electro-erosion apparatus used to prepare the gaskets. The drill bit is a copper wire with the same diameter of the needed hole. The gasket is immersed in a petroleum-paraffin mixture and in the values C=15 pF, V=150 V, and R=100 Ω were chosen according to the electrode wire diameter.

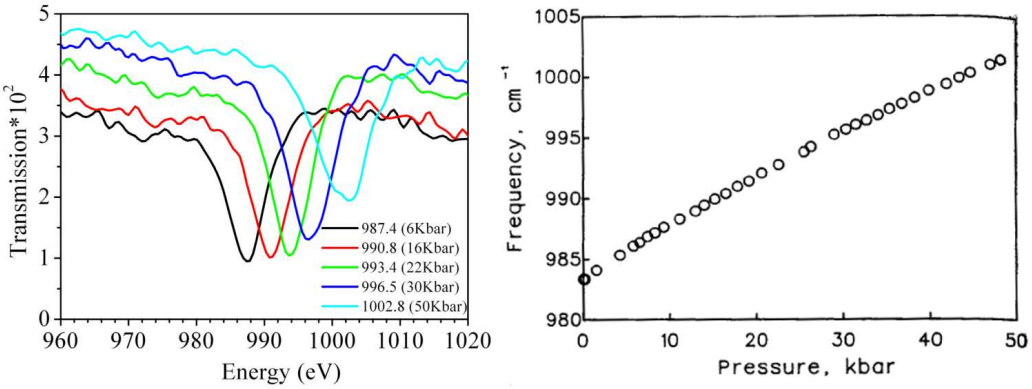

Figure 2.11: Spectral position of the SO_4 stretching mode, recorded with a FTIR spectrometer for each pressure applied to PPV. Spectral position of the SO_4 stretching mode versus applied pressure [66].

CsI was used a pressure transmitting medium, due to is wide transparency spectral range and absence of absorption bands. CsI guarantees a highly hydrostatic environment through the whole sample volume up to a few MPa.

For Raman, reflectance and transmittance spectroscopy of highly oriented PPV, the applied pressure was determined measuring the shift with pressure of the IR-active vibrational mode at 983.4 nm of $BaSO_4$. This corresponds to the stretching mode of SO_4 and its position as a a function of pressure is calibrated up to 50 kbar against Ruby fluorescence in [66] (Figure 2.11). A small amount of $BaSO_4$ was placed in the in the gasket hole, together with the sample and CsI. The spectral position of the SO_4 mode was recorded with a FTIR spectrometer for each pressure applied to PPV and the measurement is shown Figure 2.11. It can be noticed that the line width of this mode is almost constant for each pressure, thus providing a further check on the isotropy of pressure distribution.

A different cell was used for pump/probe spectroscopy of MEH-PPV under pressure.This is shown in Figure 2.12 together with a scheme of its basic construction parts. The 600 μm culet diameter of this DAC required a gasket hole of 300 μm. Non pre-indented stainless steel gaskets were used, purchased form the cell manufacturer (High Pressure Diamond Optics, Inc.)

Type IIa diamonds were used to build this cell, and the transmittance spectrum of the front diamond recorded with a FTIR spectrometer is shown in Figure 2.13. The presence of a strong absorption band at low energies prevented the detection of any signal below 0.28 eV.

Pressure determination for MEH-PPV required a different approach with respect to the ones previously described. As a matter of fact, ruby fluorescence occurs in the energy range probed by transient and steady-state photoinduced absorption experiments (Chapter 5), interfering with the measurements. A way to avoid inserting in the diamond cell anything but the sample and pressure transmitting medium, is to determine pressure through the sample itself.

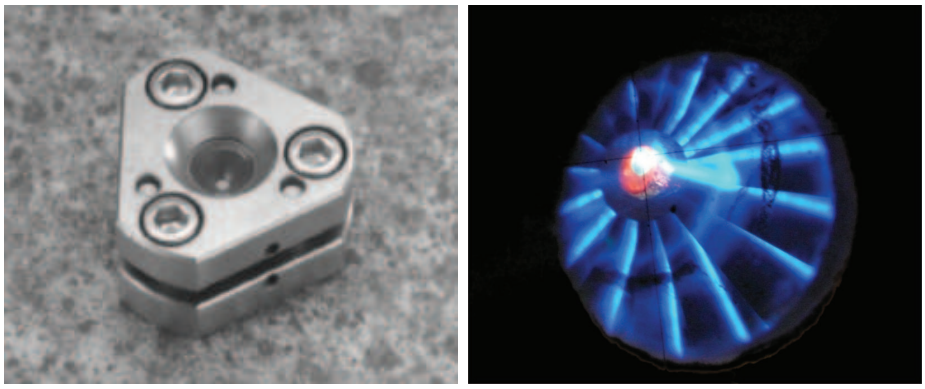

(a) (b)

Figure 2.12: DAC used for pump/probe spectroscopy of MEH-PPV (a) and a fragment of MEH-PPV inside the cell (b). The pump laser crosses a hole in the sample.

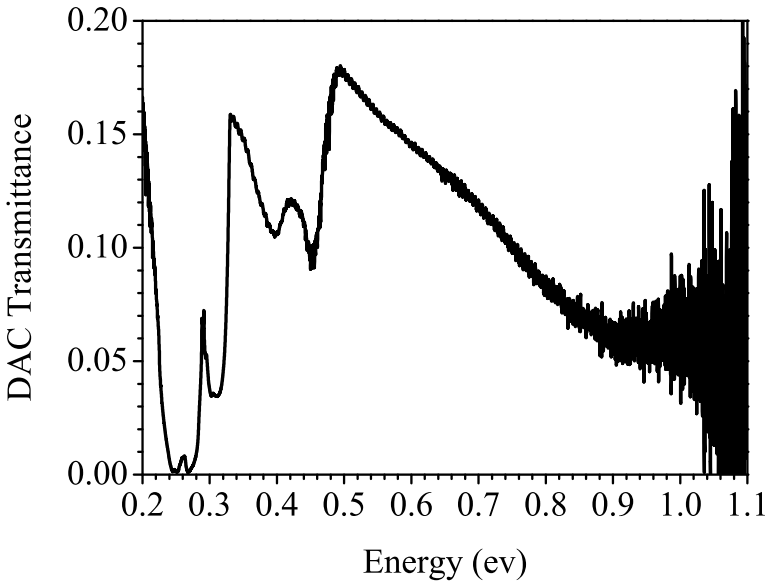

Figure 2.13: Transmission spectrum of the front diamond (type IIa) of the DAC used for pump/probe experiments. The spectrum was recorder with an FTIR spectrometer.)

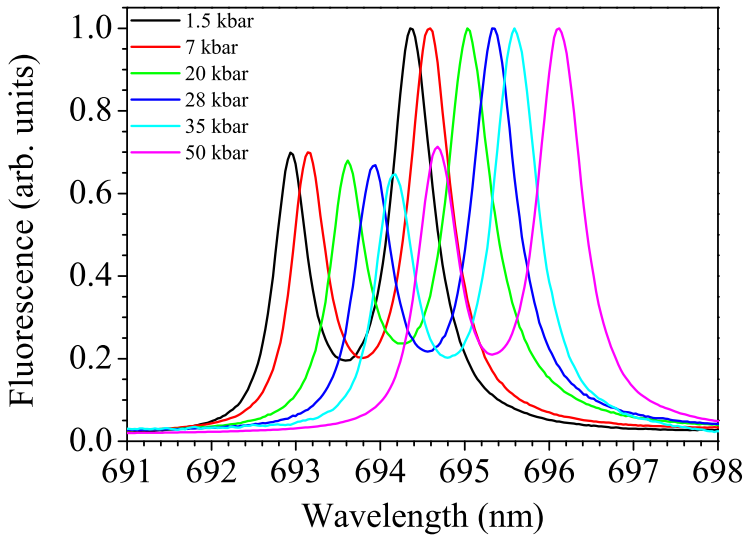

Figure 2.14: Ruby fluorescence for different applied pressures.

Prior to pump/probe experiments, we performed a calibration measurement loading the cell with both the sample and a tiny ruby chip. For a few applied pressures, we recorded both the ruby fluorescence and MEH-PPV IR absorption spectrum. We determined pressure form the spectral shift of the R_1 ruby line, according to the relation:

$$P = \frac{1094}{b}[(1 + \frac{\delta\lambda}{\lambda_0})^b - 1]$$

where λ and λ_0 are the R_1 wavelength shift (in nm) under pressure and the wavelength at ambient pressure, respectively, and b is a parameter, either be 5 or 7.665 corresponding to non-hydrostatic or quasi-hydrostatic pressure respectively. The ruby R lines are shown in Figure a, where the values of the applied pressures are also indicated. Figure b reports the IR absorption spectrum of MEH-PPV at the same pressures. The position of the peaks at 2860 and 2940 cm_{-1} as obtained with a Gaussian fit show a linear pressure dependence (inset of Figure b) and were used to determine pressure in subsequent experiments. Though this procedure allows to use the sample itself for pressure determination, it obviously carries a greater error. This is mainly due to the fact that as pressure increases the IR lines of MEH-PPV broadens and lose intensity.

Finally, liquid perfluorotributylamine (PFTBA) was used a pressure transmitting medium, which fulfilled two important requirements: first, it is not a solvent for MEH-PPV, and it is transparent in the spectral range investigated with pump/probe spectroscopy.

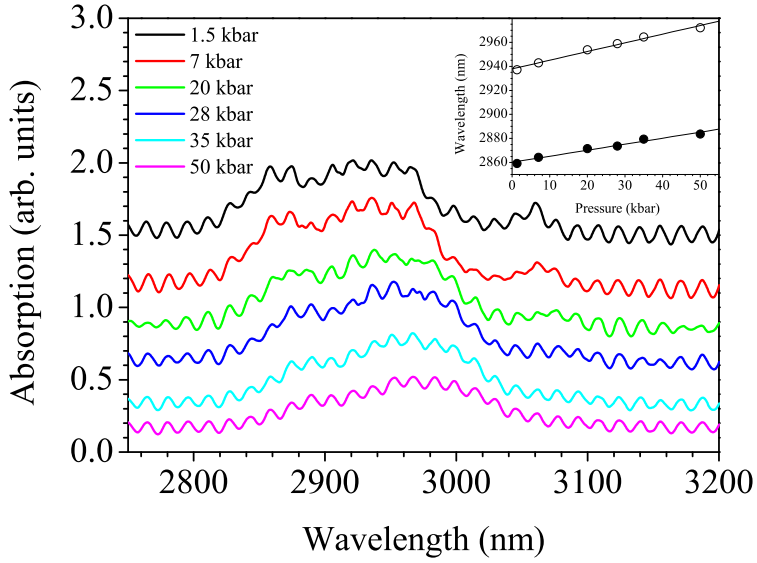

Figure 2.15: MEH-PPV absorption lines used for pressure calibration. and recorder at the same pressures as Ruby fluorescence in Figure 2.14. The peaks at 2860 and at 2940 cm^{-1} were fitted with Gaussian to determine the peak position. The inset show the linear dependence on pressure of those peaks.

2.3 Optical probes

2.3.1 Raman scattering

When quasi-monochromatic light impinges onto a surface, most of the scattered photons will have the same energy as the incident ones. This elastic scattering process is known as Rayleigh scattering. However, a small fraction of the photons ($\sim 10^{-6} \div 10^{-7}$) will be inelastically scattered, and thus will have an energy lower or higher than the incident ones. This phenomenon, called spontaneous Raman scattering, was predicted in 1923 by A. Smekal and experimentally observed in 1928 by C.V. Raman [67].

As we shall see, the difference in energy between the incident and the scattered photon is related to the vibrational levels in the ground state specific of the sample, and yields insight into its molecular structure.

A schematics of the all the processes occurring during a Raman experiment is shown in Figure 2.16.

Consider a molecule in its fundamental vibrational state, indicated as $|0>$[3]. An incident photon of energy $h\nu_i$ is absorbed raising the system to some intermediate or virtual state. Form this state a photon can be emitted (scattered) with energy $h\nu_i < h\nu_s$ (Stokes scattering). For energy to be conserved, the

[3]The following description actually holds even if the initial state is not the fundamental.

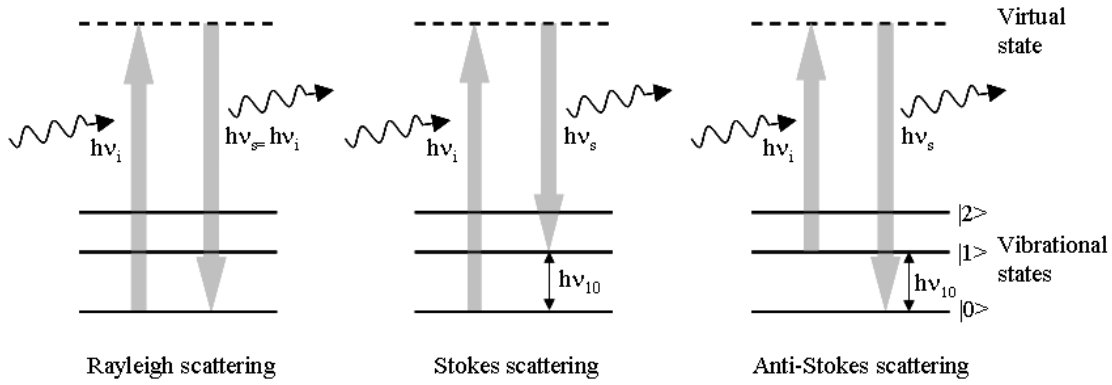

Figure 2.16: Raman scattering process.

difference $h\nu_s - h\nu_i = h\nu_{10}$ goes into exciting the molecule into a higher vibrational level.

If the initial state of the molecule is an excited ones, say |1> (this is always the case if the sample is at temperature >0 K), after absorbing and emitting a photon, the molecule may drop back to a lower state. In this instance $h\nu_s > h\nu_i$, meaning that some vibrational energy $h\nu_s - h\nu_i = h\nu_{21}$ of the molecule is converted into radiation energy. This process is called Anti-Stokes scattering (Figure 2.16)

The basic features of Raman spectroscopy can be explained using classic electrodynamics. When a photon interacts with a molecule, the electric field $\overrightarrow{E}$ induces a dipole moment $\overrightarrow{P}$ in the molecule:

$$\mathbf{P} = \alpha \cdot \mathbf{E} \tag{2.1}$$

The proportionality constant α is the polarizability tensor of the molecule. The induced dipole moment of the molecule can be easily calculated [] as:

$$\mathbf{P} = \underbrace{\alpha_0 \mathbf{E}_0 \cos(2\pi\nu t)}_{Raileigh} + \frac{1}{2}\mathbf{E}_0 \sum_n \alpha_n [\underbrace{\cos 2\pi(\nu - \nu_n)t}_{Stokes} + \underbrace{\cos 2\pi(\nu + \nu_n)t}_{Anti-Stokes}] \tag{2.2}$$

where ν_n represent the frequencies of all normal modes of coordinate Q_n.

This relation shows that, besides the elastically scattered Rayleigh line, a typical Raman spectrum is composed by additional lines shifted by $\pm\nu_n$ with respect to the excitation light. In π-conjugated systems with distributed electron clouds, the double bonds can be easily distorted by an electric field. Bond stretching and bending changes the distribution of electron density and causes a large variation in the induced dipole moment. Thus Raman scattering occurs because a molecular vibration can change the polarizability $d\alpha/dQ$.

As a consequence of Equation (2.2) the Stokes and Anti-Stokes band positions appear to be symmetric to the Rayleigh line. However, the intensity of the Anti-Stokes lines is smaller than that of the corresponding Stokes lines.

The intensity ratio between these lines can be easily calculated in the frame of quantum-mechanics[4]. If the sample is in thermal equilibrium, the relative number of molecules in different vibrational states is given by the Boltzmann distribution. In the above instance (Figure 2.16), the number of molecules N_1 in the first excited vibrational state |1> relative to the number of molecule N_0 in the fundamental state can be written as:

$$\frac{N_1}{N_0} = \frac{g_1}{g_0} e^{-h\nu_{10}/K_B T} \tag{2.3}$$

where $h\nu_{10}$ is the energy difference between the states |1> and |0> and g_0 (g_1) is the degeneracy of the lower (higher) vibrational state. According to this relation, the probability of finding a molecule in the ground state is much higher than that of finding it an excited state. The intensity of the Stokes and Anti-Stokes lines is proportional to the Boltzmann factor:

$$\frac{I_{Anti-Stokes}}{I_{Stokes}} \sim e^{-h\nu_{10}/K_B T}. \tag{2.4}$$

Therefore, at room temperature the Stokes bands will dominate. In most cases, Raman spectroscopy only deals with the Stokes part of the spectrum, which already carries all the information about the molecular structure of the sample and is more easily detected[5].

A quantum mechanical treatment of the Raman scattering can be made in the frame of the time-dependent perturbation theory. The dipole moment transition element between an initial state |i> and a final state |f> can be written as [34]:

$$\begin{aligned}\mathcal{M}_{if} =& < i|M|f > \cos(2\pi\nu_{if}t) \\ &+ \frac{E_0}{h\nu} \sum_j \left[\left(\frac{\nu_{ij}}{\nu_{ij}+\nu} - \frac{\nu_{jf}}{\nu_{jf}+\nu} \right) < i|M|j >< j|M|f > \right] \sin[2\pi(\nu+\nu_{if})t] \\ &+ \frac{E_0}{h\nu} \sum_j \left[\left(\frac{\nu_{jf}}{\nu_{jf}+\nu} - \frac{\nu_{ij}}{\nu_{ij}+\nu} \right) < i|M|j >< j|M|f > \right] \sin[2\pi(\nu-\nu_{if})t]\end{aligned} \tag{2.5}$$

In quantum mechanical terms, the Anti-Stokes process correspond to the annihilation of a phonon, while in the Stokes process a phonon is created.

In this thesis, Raman measurement of highly oriented PPV under pressure were performed with a Dilor-Labram spectrometer. A schematic top-view of the instrument in shown in Figure 2.17. The excitation was provided by a He-Ne laser with an intensity of 20 mW. The excitation wavelength (λ_{exc} = 632.8 nm, 1.96 eV) is close to the absorption edge of PPV (hence, this is

[4]The scattering intensity is $\propto (d\alpha/dQ)^2$.

[5]It is interesting to notice that the intensity ratio between Stokes and Anti-Stokes lines provides a powerful tool to determine the temperature of the sample.

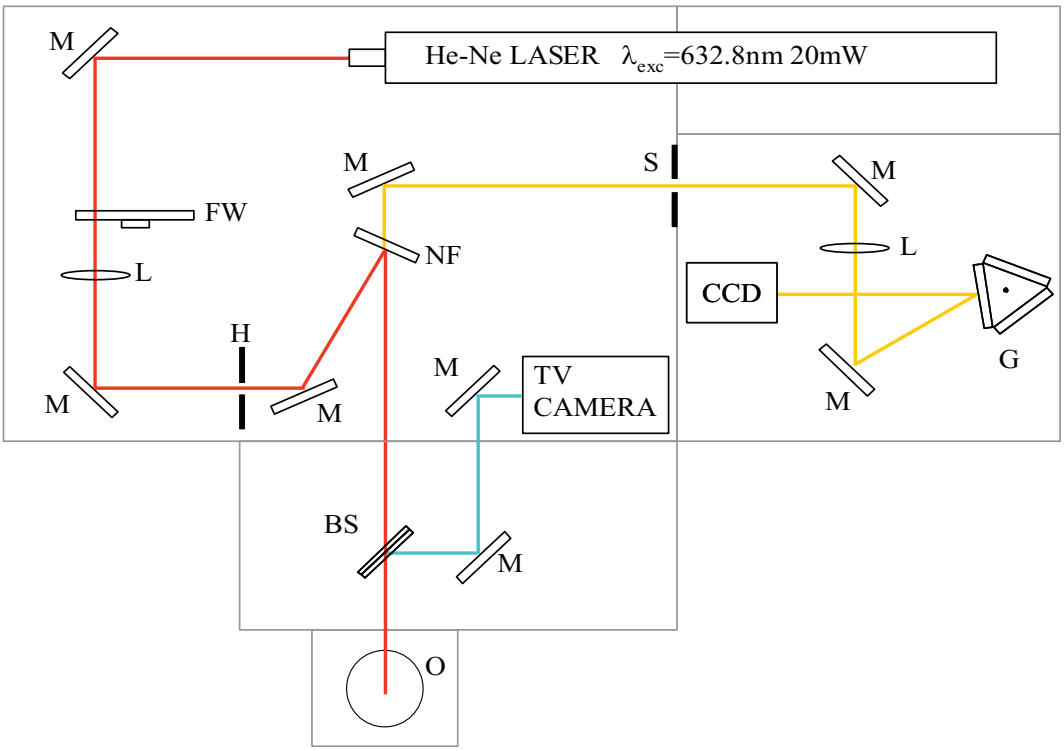

Figure 2.17: Schematic top view of Dilor-Labram spectrometer. The basic optical system is shown. M = mirrors; L = lenses; FW = filter wheel equipped with neutral density filters of OD 0.3, 0.6, 1, 2, 3; H = hole conjugated to the sample; NF = Super Notch Filter; S = entrance slit of the spectrometer; G = grating (1800 g/mm or 600 g/mm); BS = beam splitter redirecting the beam to the TV camera; O = objectives 10x NA 0.25, 50x NA 0.7, 100x NA 0.9

called pre-resonant Raman scattering), thus a photoluminescence background is detected along with the Raman signal. No filter was used to reduce the laser intensity, while a Super Notch Filter with a drop off Stokes edge <120 cm^{-1} was utilized to block the elastically scattered light. A 1800 g/mm grating was used for these measurements. The spectral resolution is about 2 cm^{-1}, as determined by the entrance slit width (70÷200 μm)[6]. The DAC was simply placed on the motorized table underneath the objective. Due to the size of the cell a 10x objective could only be used to focus the incident light onto the sample. Though the laser beam of the instruments is 500:1 polarized, the aperture provided by this objective prevented the detection of polarized Raman spectra. As a matter of fact, diamond birefringence [68] induced by defects is more effective with such a wide probe beam (100 μm^2) crossing a large area of the front diamond. Nonetheless, a rough alignment was made in order to collect the intense Raman spectra with polarization parallel to the polymer chains.

[6]The resolution of a grating spectrograph has a wavelength dispersion that goes as λ^{-2}.

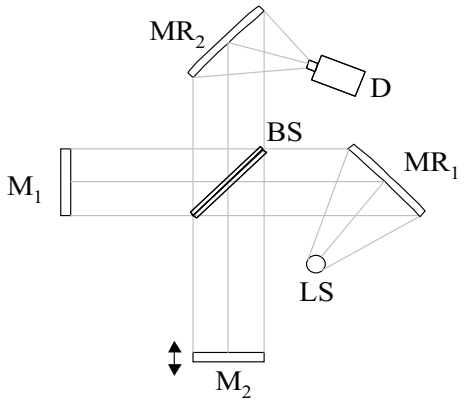

Figure 2.18: Michelson-Morley interferometer

2.3.2 Fourier transform spectroscopy

Reflectance and transmittance of highly oriented PPV were measured with a Fourier transform (FT) spectrometer (Bruker IF66S).

The principle of FT spectroscopy relies on a Michelson-Morley interferometer (1880), in Figure 2.18. The radiation emitted from a light source LS is collected by the mirror MR_1 and directed onto a 50% beam splitter BS, that splits the beam in two parts of equal intensity. These two beams are reflected by the flat mirrors M_1 and M_2 and recombine on the mirror MR_2 which focuses them onto a detector where they interfere due to their different optical paths.

Consider a monochromatic plane wave of wave number $\overline{\nu} = 1/\lambda$ emitted by LS along the z direction. The electromagnatic field can then be written as:

$$E(\overline{\nu}, z) = E_0(\overline{\nu}) e^{i(\omega t - 2\pi\overline{\nu}z)} \tag{2.6}$$

If z_1 and z_2 are the optical paths of the two beams separeted by the beam splitter BS, the electric field detected by D is:

$$E(\overline{\nu}, z_1, z_2) = rtE_0(\overline{\nu})[e^{i(\omega t - 2\pi\overline{\nu}z_1)} + e^{i(\omega t - 2\pi\overline{\nu}z_2)}] \tag{2.7}$$

where r and t are the Fresnel reflection and transmission coefficients of the BS. The average radiation intensity measured by the detector for unit time and surface is given by:

$$S_r(\overline{\nu}, z_1, z_2) = \frac{c}{8\pi} E_r(\overline{\nu}, z_1, z_2) E_r^*(\overline{\nu}, z_1, z_2) \tag{2.8}$$

Using Equation (2.8) and introducing the path difference $\delta = z_2 - z_1$ between the two beams, one obtains:

$$S_r(\overline{\nu}, \delta) = \frac{c}{4\pi} |rt|^2 E_0^2(\overline{\nu})[1 + cos(2\pi\overline{\nu}\delta)] \tag{2.9}$$

In the general case of a non monochromatic light source, the intensity measure by the detector D is obtained summing over all $\overline{\nu}$:

$$I = \int_0^\infty S_r(\overline{\nu}, \delta)\delta\overline{\nu} = \frac{c}{4\pi}|rt|^2 \int_0^\infty E_0^2(\overline{\nu})[1 + cos(2\pi\overline{\nu}\delta)]d\overline{\nu} \tag{2.10}$$

which is composed by a constant part plus a function of δ. Taking into account only the variable part of the light intensity, the interferogram is thus defined as:

$$F = \frac{c}{4\pi}|rt|^2 \int_0^\infty E_0^2(\overline{\nu})cos(2\pi\overline{\nu}\delta)d\overline{\nu} \tag{2.11}$$

Since the intensity of the light source is $S(\overline{\nu}) = cE_0^2(\overline{\nu})/8\pi$, the interferogram can be finally written as:

$$F(\delta) = 2|rt|^2 \int_0^\infty S(\overline{\nu})cos(2\pi\overline{\nu}\delta)d\overline{\nu} \tag{2.12}$$

Being $E(\overline{\nu})$ hermitian, it follows that $S(\overline{\nu}) = S(-\overline{\nu})$, so Equation(2.12) can be re-written in complex notation:

$$F(\delta) = K \int_{-\infty}^{+\infty} S(\overline{\nu})e^{i(2\pi\overline{\nu}\delta)}d\overline{\nu} \tag{2.13}$$

where K is a constant. This relation states that the interferogram is the Fourier transform of the spectrum $S(\overline{\nu})$ emitted by the light source. The source spectrum is simply the anti- FT of the interferogram:

$$S(\overline{\nu}) = K \int_{-\infty}^{+\infty} F(\delta)e^{-i(2\pi\overline{\nu}\delta)}d\delta \tag{2.14}$$

Through Equation (2.14), the measurement of the interferogram can provide information on the spectral response of the sample. Experimentally, the interferogram can be obtained by scanning the position of the mirror M_2 and recording the light intensity as a function of δ. Ideally, the spectrum $S(\overline{\nu})$ is obtained integrating $F(\delta)$ over all δ (Equation(2.14)). Practically the integration is performed over a finite δ domain corresponding to a limited scanning range of M_2, form δ_{min} to δ_{max}.

FT spectroscopy offers two major advantages over dispersive spectroscopy, namely (Fellget and Jacquinot advantages [69]):

- the spectral resolution is inversely proportional to the maximum difference of the optical paths (δ_{min}-δ_{max}). It is thus improved just by increasing the scanning range of the moving mirror, since it does not depend on the spectrometer slit dimension;

- the whole spectrum is acquired within a single scan of the moving mirror. In a given time it is possible to average multiple scans, thus improving considerably the signal to noise ratio.

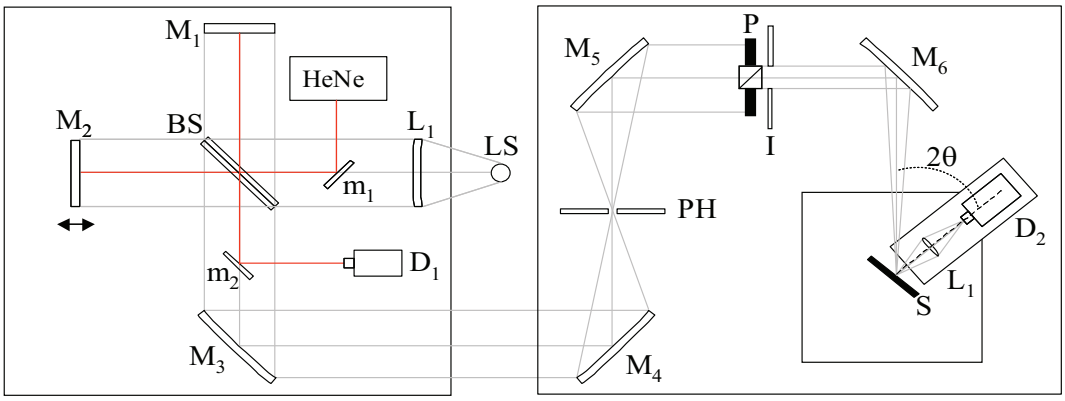

Figure 2.19: Scheme of the set up used to collect polarized R and T spectra of PPV under applied pressure. A commercial FT spectrometer (Bruker IFS 66/S) is coupled to a home-made microreflectometer that provides a probing spot of about 50 μm with an angular divergence of the incident light cone of 1°.

The experimental set up used to measure polarized reflectance and transmittance spectra under pressure is shown in Figure 2.19. A commercial Fourier Transform spectrometer (Bruker IFS 66/S) was used to record the spectral response of the sample in the range form 1.5 to 4.5 eV (276 ÷ 827 nm) with a spectral resolution of 8 cm^{-1}. A discharge lamp used as light source was placed in front of the entrance of the spectrometer. The interferogram of a He-Ne laser following the same path as the white beam is used to determine the relative position of the mirror M_2, that is δ.

The FT spectrometer was equipped with the home-made optical system sketched in Figure 2.19 (micro-reflectometer). The incident light coming out from the FT spectrometer is focused by the parabolic off-axis mirror M_4 onto a pinhole PH which now plays the role of new light source (owing to the Huygens principle). The mirror M_5 collects the light from the pinhole and directs it onto the sample S inside the DAC. A Si detector D_2 was used to collect the signal. This set up provides a probing spot of about 50 μm with an angular divergence of the incident light cone of 1°. These features are fundamental, since a probing spot smaller than the sample allows to collect a reference T measurement which is used to normalize transmission spectra. Furthermore, such a tiny incident beam allows to probe the sample through a small volume of the front diamond. As explained in Chapter 4 diamond has a strong strain-induced birefringence, which affects the possibility of collecting polarized spectra. Thus, a little incident spot improves the control on polarization of the outcoming beam.

The incident light was linearly polarized with a standard Glan-Taylor polarizer operating in the range 200 ÷ 2800 nm. The polarizer P, placed before a diaphragm I, was mounted on a rotation stage. The parallel/ perpendic-

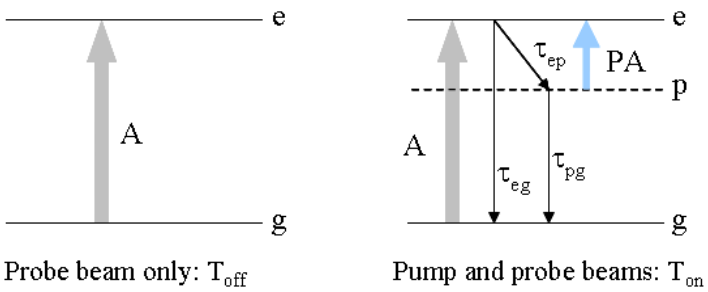

Figure 2.20: Schematic of the photoinduced absorption process in a three level system.

ular components of polarized R and T spectra refer to light polarized parallel/perpendicularly to the polymer chains, which are aligned to the stretching direction (see also Figure 2.9).

2.3.3 Pump/probe techniques

Pump and probe spectroscopy employs two light beams to measure the changes in the material properties due to a modulated photoexcitation. The quantity of interest is the differential transmittance spectrum

$$-\frac{\Delta T}{T} = -\frac{T_{off} - T_{on}}{T_{off}}, \tag{2.15}$$

which is obtained as schematically illustrated in Figure 2.20.

The probe beam, a tunable light source, allows to measure the transmittance spectrum, named T_{off}, corresponding to the linear absorption A. The pump beam, with energy in the absorption region of the material under study, generates new photoexcitation, i.e. new electronic states within the gap, that can be studied by measuring photoinduced (PA) absorption. Therefore, following photoexcitation, a new feature emerges in the transmittance T_{on} spectrum, corresponding to the transition p→g in Figure 2.20.

In a typical $-\Delta T/T$ spectrum, the population depletion of the ground state g, corresponding to the g→e transition, will reualt in a negative peak, known as photobleaching (PB). A a positive peak at the energy will instead correspond to the photoinduced p→e transition (PA).

Time-resolved photoinduced absorption measurements provide information on the dynamics of the non-linear photoexcitations, which is fundamental for understanding the basic events occurring in the excited state. In particular, the decay times τ_{ep} and τ_{pg} can be probed via photoinduced absorption, while photobleaching is related to the relaxation processes to the ground state (τ_{eg}, τ_{pg} and τ_{pg} in Figure 2.20). Since in conjugated polymers linear absorption typically occur in the visible spectral range, intra-gap non-linear excitations will have their signatures at lower energies, typically in the near-infrared (NIR)

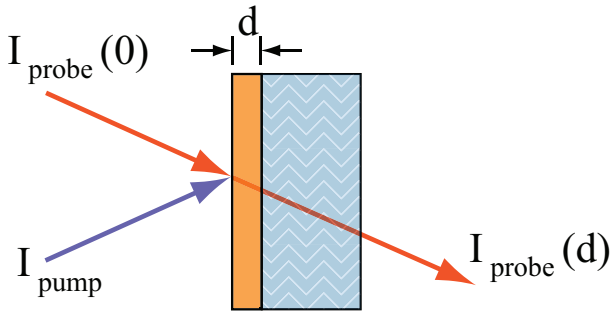

Figure 2.21: Schematics illustrating pump-probe techniques.

spectral region.

The photoinduced changes in absorption and reflection are in general due to two factors: thermo-modulalation (that is, a change in temperature accompaniing the change in absorption) and photoexcited states (appearance of new optical transitions). The latter, which we are interested in, can be probed either by continuous wave photomodulation or by transient spectroscopy.

Steady-state pump/probe spectroscopy

In continuous wave (cw) experiments, the probe beam constantly illuminates the sample and the steady state changes in transmission are detected. The pump beam is usually an Ar^+ laser, while for the probe beam a broad spectrum light such as an incandescent lamp (tungsten or other) is used. Both the pump and the probe beams are focused onto the same spot on the sample surface. The probe light is collected, filtered through a monochromator and detected by a photodetector. Since the change in transmission ΔT is very small ($\Delta T/T<10^{-4}$) a lock-in technique has to be used for detection. This requires the pump light to be modulated at a reference frequency and therefore ΔT is modulated too. An analysis of the frequency dependence of ΔT will be given later in this section. By measuring T and ΔT as a function of the probe wavelength, the spectrum of the $\Delta T/T$ signal is obtained.

A scheme of the pump/probe technique is shown in Figure 2.21. Here, I_{pump} is the intensity of the pump beam, $I_{probe}(0)$ is the intensity of the probe beam at the sample surface and $I_{probe}(d)$ is the intensity of the light transmitted through the sample of thickness d. Since T is given by:

$$T = \frac{I_{probe}(d)}{I_{probe}(0)}, \tag{2.16}$$

$\Delta T/T$ is can be written as:

$$\frac{\Delta T}{T} = \frac{\Delta I_{probe}(d)}{I_{probe}(d)} \tag{2.17}$$

It can be shown that this quantity is proportional to the change of the absorption coefficient $\Delta\alpha$.

After passing through the sample, the probe beam is given by the Lambert-Beer law:

$$I_{probe}(d) = I_{probe}(0)e^{-\alpha d}(1-R) \tag{2.18}$$

where (1-R) takes into account the reflection form the sample surface, and higher order of reflection are neglected. We can also write:

$$\Delta I_{probe}(d) = [I_{probe}(d)]_{pump-on} - [I_{probe}(d)]_{pump-off} \tag{2.19}$$

Equation (2.19) can be manipulated setting:

$$[I_{probe}(d)]_{pump-off} = [I_{probe}(0)]e^{-\alpha_{off}d}(1-R_{off}) \tag{2.20}$$

$$[I_{probe}(d)]_{pump-on} = [I_{probe}(0)]e^{-\alpha_{on}d}(1-R_{on}) \tag{2.21}$$

and

$$\Delta\alpha = \alpha_{on} - \alpha_{off} = \alpha_{on} - \alpha \longrightarrow \alpha_{on} = \Delta\alpha + \alpha \tag{2.22}$$

$$\Delta R = R_{on} - R_{off} = R_{on} - R \longrightarrow R_{on} = \Delta R + R \tag{2.23}$$

Then, the changes induced by the pump beam can be expressed as:

$$\Delta I_{probe}(d) = I_{probe}(d)(1-R)(e^{-\Delta\alpha d} - 1) - \Delta R I_{probe}(0)e^{-(\alpha+\Delta\alpha)d} \tag{2.24}$$

Normalizing Equation (2.24) by $I_{probe}(d)$ and assuming $\Delta\alpha d \ll 1$ we get an expression for $\Delta T/T$:

$$\frac{\Delta T}{T} = \Delta\alpha d - \frac{\Delta R}{(1-R)} \tag{2.25}$$

Being $\Delta T/T$ typically in the range of $10^{-3} \div 10^{-4}$, the second term in Equation (2.25) can be neglected compared to $\Delta\alpha d$ [7]. With this assumption, the fractional change in transmission is [70]:

$$\frac{\Delta T}{T} \simeq -\Delta\alpha d \tag{2.26}$$

It's worth noting that this relation holds in the small signal limit for thin films ($\Delta\alpha d \ll 1$): the pump beam has to be uniformly absorbed, creating an equal distribution of $\Delta\alpha$ across the film. In addition, we assume a perfect overlap between the pump and the probe beams and neglect the 3D spatial distribution of the optical fields.

Equation (2.26) states that, within the assumptions made, the quantity $\Delta T/T$ is directly proportional to the change of the linear absorption coefficient and thus can be used to detect directly new photoinduced optical transitions.

[7] This is not the case when ΔT and ΔR are of the same order of magnitude and they have both to be measured to calculate $\Delta\alpha$

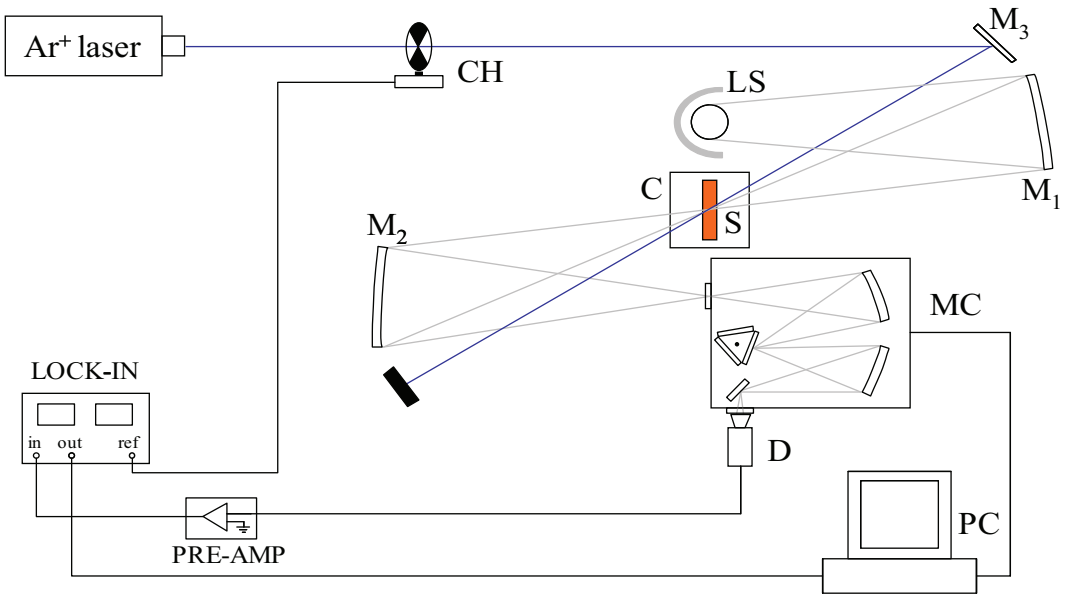

Figure 2.22: Set up used to measure cw pa. The basic parts are: an Ar^+ laser at 488 nm (pump beam), chopped by a mechanical chopper running at 300 Hz; a tungsten lamp LS (probe beam), the mirrors M_1 and M_2 focus the probe beam onto the sample and the monochromator respectively; the detector D connected to the lock-in amplifier.

For example, if N photons are absorbed in a unit volume of the film, and each of them excites one electron-hole (e-h) pair, we can write:

$$\Delta\alpha(\lambda) = N_{ex}\sigma_{e-h}(\lambda) \tag{2.27}$$

where λ is the probing wavelength, N_{ex} is the density of photoexcited species and σ_{e-h} is the effective absorption cross section for an e-h pair at the probe wavelength [71].

The set up used to measure cw PA of MEH-PPV is shown in Figure 2.22. A tungsten lamp was the probe beam, while the pump excitation was provided by an Ar^+ laser (488 nm) shining a power of 100 mW onto the sample. The chopper C, running at 300 Hz, was placed in front of the monochromator MC to measure T, and was used to modulate the pump beam while measuring PA. Two differen detectors and a set of filters for the Ar^+ laser were necessary to cover the spectral range from 0.31 to 2.25 eV. These are summarized in Table 3.1.

Cw PA spectra for different applied pressure were collected both at room and low temperature. In the latter case, the DAC was placed inside a the cryostat C.

The same set up allows to measure photoluminescence (PL) as well: this is done blocking the probe beam and recording the emission from the sample with the proper filter in front of the entrance slit of the monochormator. If a PL signal is present, it has to be recorded and subtracted form the PA signal, as

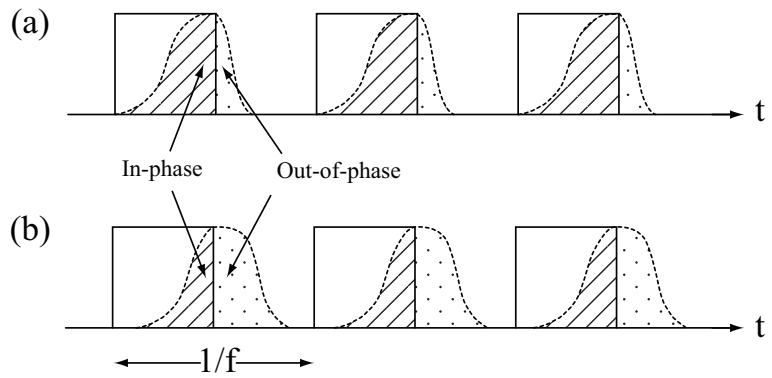

Figure 2.23: Modulation of the system response. The solid line represent the modulated excitation; the dashed line is the system response to the chopped pump beam. The dashed/dotted area corresponds to the in-phase/out-of-phase component of the signal.

it represents the background on top of which the photomodulated signal rides (practically, to obtain $\Delta T/T$ form the sample one has to calculate PA-PL/T).

In the set up shown in Figure 2.22 the pump beam is modulated at a frequency ω=300Hz using a mechanical chopper. This modulation causes ΔT to vary in time with a magnitude and phase that depend on ω.

The system response to the chopped pump beam is illustrated in Figure 2.23. Fast photoexcitation can respond readily and the signal in-phase with ω will have a greater magnitude (the blue area in Figure 2.23) than the out of phase (gray area). The opposite will be true for slow photoexcitations. It is thus clear that this technique provides information about excited states whose lifetimes range from a few ms to $\sim$ 1 s. This is done by simultaneously recording of the in phase and out of phase signals.

An expression for $\Delta T(\omega)$ can be obtained assuming a monomolecular recombination dynamics with a single lifetime. In this case the rate equation for the photoexcited species is:

Table 2.1: Filters and detectors used for each spectral range in cw PA experiment.

Spectral Range	Filter	Detector
550-1100 nm	long pass 550 nm	Si
1100-1400 nm	long pass 800 nm	InSb N-cooled
1300-1900 nm	long pass 1300 nm	InSb N-cooled
1800-2500 nm	long pass 1800 nm	InSb N-cooled
2500-4000 nm	long pass 2500 nm	InSb N-cooled

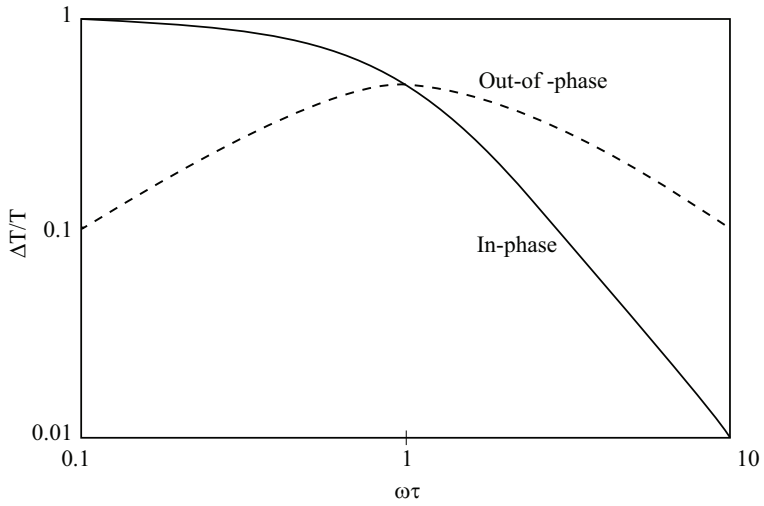

Figure 2.24: Modulation of the system response. The solid line represent the modulated excitation; the dashed line is the system response to the chopped pump beam.

$$\frac{N(t)}{dt} = G(t) - \frac{N(t)}{\tau} \tag{2.28}$$

where G(t) is the generation rate and N(t)/τ describes the relaxation rate. G(t) is defined as γP(t)/hν, where P(t) is the pump power, hν is the energy of a single photon at the pumping wavelength and γ is the quantum efficiency in creating a particular photoexcitation. Neglecting higher orders, G(t) can be expressed taking into account only the fundamental Fourier component:

$$G(t) = G(\omega)e^{-i\omega\tau} \tag{2.29}$$

Thus, the solution of Equation (2.28) has the same form:

$$N(t) = N(\omega)e^{-i\omega\tau} \tag{2.30}$$

Inserting Equation (2.30) in Equation (2.28) and solving for N, we get:

$$N(\omega) = \frac{G(\omega)\tau}{1+(\omega\tau)^2} - i\frac{G(\omega)\omega\tau^2}{1+(\omega\tau)^2} \tag{2.31}$$

Using Equation (2.26), (2.27), and (2.31), we can express $\Delta T/T$ as:

$$\Delta T/T = \frac{G(\omega)\tau\sigma d}{1+(\omega\tau)^2} - i\frac{G(\omega)\omega\tau^2}{1+(\omega\tau)^2}\sigma d \tag{2.32}$$

The first term on the right side of this Equation is in phase with pump signal. The second term represents the out-of-phase signal (also called quadrature), and has a 90° phase with respect to the pump signal. The frequency dependencies of the in-phase and quadrature signals is shown in Figure 2.24

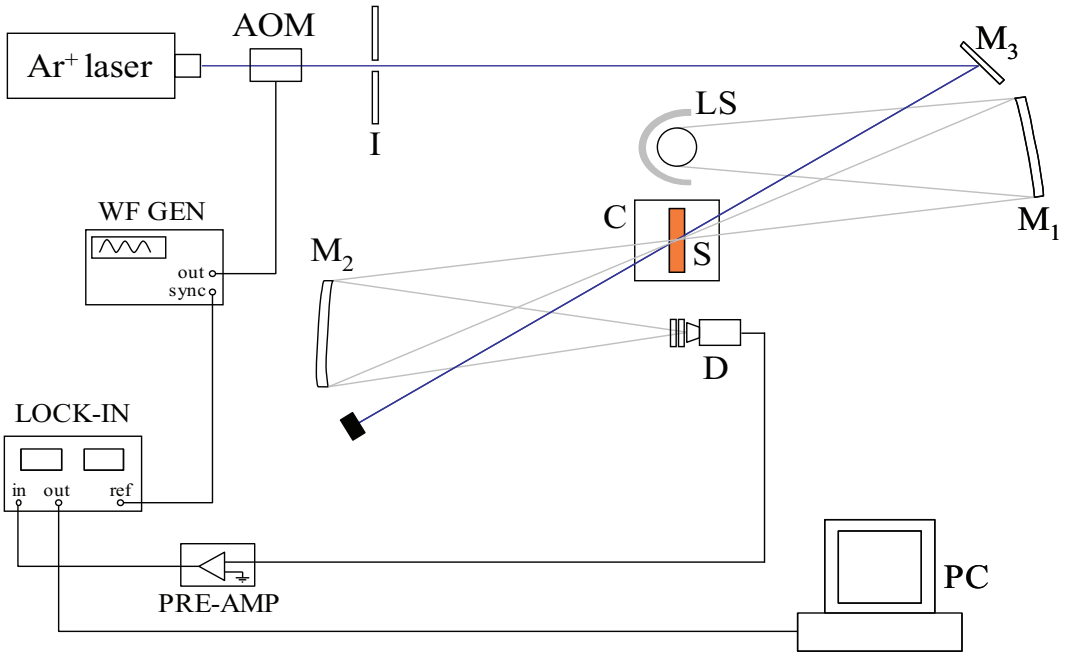

Figure 2.25: Modualtion of the system response. The solid line represent the modulated excitation; the dashed line is the system response to the chopped pump beam.

It can be seen that for low modulation frequencies, the amplitude of the in phase signal is greater than that of the out of phase, as observed also in Figure 2.23. The opposite occurs when the modulation frequency is high. The crossing point between the in phase and the out of phase gives the lifetime of the photoexcited state.

The set-up used to record ΔT as a function of ω is similar to that used for cw PA, and is schematized in Figure 2.25.A wave function generator (WFG) drives the AOM with a sine wave allowing a frequency swipe form 1 to 10^5 Hz. A set of long and short pass filters is needed to collect all the light in the desired energy range.

Transient pump/probe spectroscopy

Transient photomodulation spectroscopy was done with a two-color pump-probe correlation technique with two pulsed and linearly polarized lasers.

The primary ultrafast laser system was a series of commercial lasers to pump an optical parametric oscillator (OPO) for frequency conversion. Figure 2.29 shows the configuration set up. A 10 Watt, 532 nm cw solid-state laser (Millennia Xs, Spectra-Physics) pumps a 100 fs titanium-sapphire pulsed laser with a repetition rate of about 80 MHz (Tsunami, Spectra-Physics), which in turn pumps the OPO (Opal, Spectra-Physics).

Frequency conversion allows a tunable probe beam and is achieved by the OPO parametric down conversion in a nonlinear optical crystal (a Brewster-

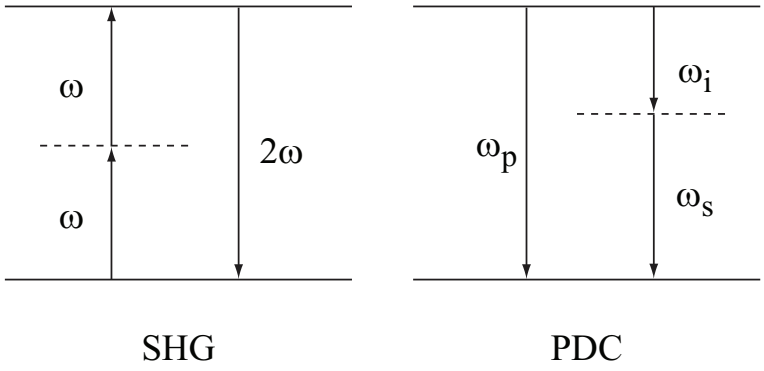

Figure 2.26: Second harmonic generation (SHG) and parametric down conversion (PDC). The OPO exploits parametric down conversion in a nonlinear optical crystal to achieve tunability.

cut lithium triborate (LiB_3O_5 crystal or LBO). Parametric down conversion is a second-order three photon interaction, requiring crystals with a high second-order nonlinear susceptibility, and can be viewed as the inverse of second harmonic generation or sum frequency mixing, as schematically illustrated in Figure 2.26.

An input pump photon (ω_p) transfers its energy to lower energy photons such that energy is conserved, i.e.,

$$\omega_p = \omega_s + \omega_i \quad \text{for} \quad \omega_s > \omega_i \tag{2.33}$$

The beam with higher frequency (ω_s) is called the signal and the lower (ω_i), the idler. Momentum conservation,

$$k_p = k_s + k_i \tag{2.34}$$

is achieved by satisfying the phase-matching conditions:

$$n_p\omega_p = n_s\omega_s + n_i\omega_i \tag{2.35}$$

where n is the refractive index.

The output of the OPO was used as the probe beam in our photomodulation experiments, requiring an ultrafast laser source tunable in the infrared region of the spectrum.

In an OPO, the nonlinear crystal is placed in an optical resonator cavity (Figure 2.27). By carefully tuning the OPO alignment and/or crystal temperature, we can measure photoinduced absorption with probe energies ranging in from 0.45 eV to 1.1 eV with 150 fs resolution. To achieve full output spectral range, the OPO needs to be pumped with two different wavelengths, namely 775 and 810 nm, and consequently two different optics sets in the OPO optical cavity (1.3 μm and 1.5 μm) must be interchanged. Lower energies from 0.25-0.43 eV can be reached by inserting a difference frequency generation (DFG)

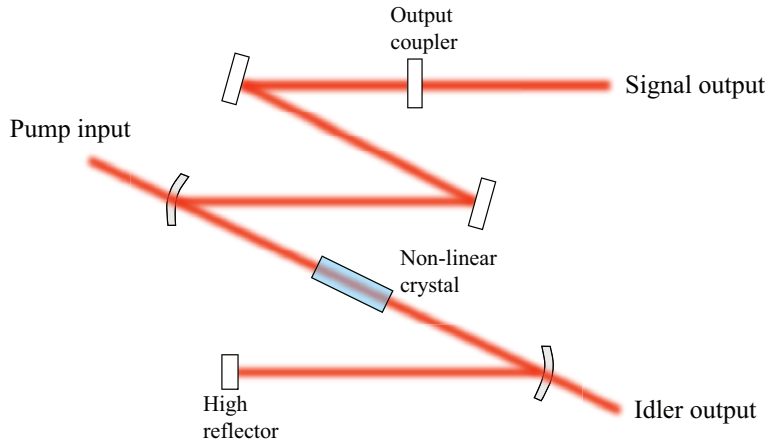

Figure 2.27: Optical parametric oscillator configuration.

crystal ($AgGaS_2$), as shown in Figure 2.21. This is also a second-order non linear process and it uses both the signal and idler as pump beams for the non linear crystal. Carefully adjusting both the spatial and temporal overlap between the signal and idler pulses, and their phase matching[8], the DFG process generate a probe beam in the new frequency range

$$\omega_{DGF} = \omega_s - \omega_i \quad \text{for} \quad \omega_s > \omega_i \tag{2.36}$$

The power output of the OPO is reported in Figure 2.28, showing the full energy range covered.

Typical pump energy/pulse is about 0.1 nJ and kept below 5 μ J/cm^2 per pulse, which corresponds to $\sim$ 1000 initial photoexcitation density per pulse in the illuminated sample. This low-intensity system, generating low exciton density, avoids complications from exciton-exciton annihilation, polymer degradation, and non-linear effects such as two-photon absorption.

Some of the OPO input beam reflects off the LBO crystal surface and exits the Opal. This residual beam is fed through an acousto-optic modulator (AOM) to pump the sample with the fundamental energy of 1.55 eV (below the optical gap of MEH-PPV).

The relative delay between pump and probe beams is achieved by changing the probe time of flight by translating a motorized stage.

Two modulations are used separately in the set up as shown in Figure 2.21. One is the mechanical chopper, operateing at 300 Hz: this is used to modulates the probe beam when measuring sample transmission T. The second modulation is provided by the AOM, running at 30 kHz, that synchronizes the lock-in amplifier to the pump pulse when measuring changes in transmission ΔT. An AOM is used instead of an optical chopper to improve the signal to

[8]This is done by rotating the crystal.

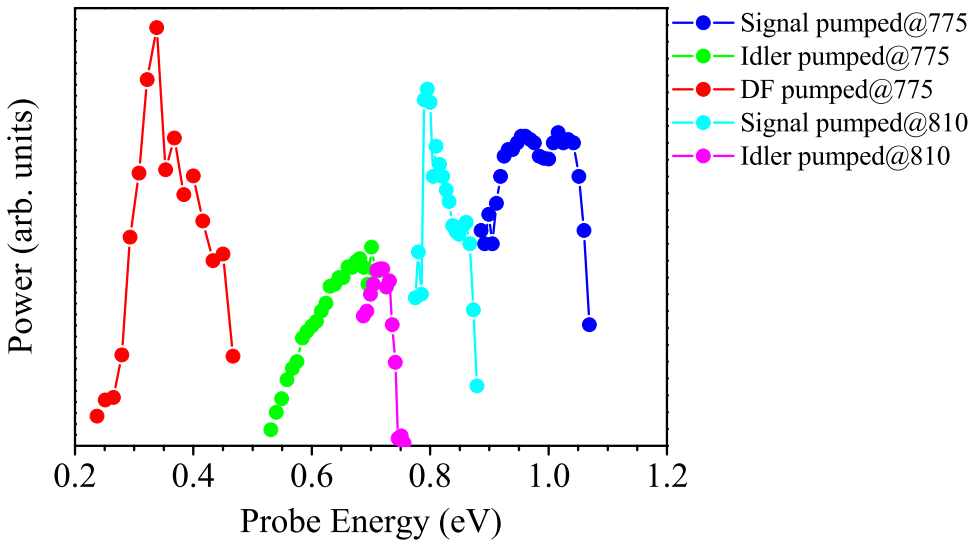

Figure 2.28: Energy range covered by the tunable laser system used for transient pump/probe spectroscopy. The power output of the OPO is in arbitrary units.

noise ratio for the low-signal ΔT measurements. Typical signal sensitivity of $\Delta T/T$ is on the order of 10^{-7}.

Two filters are used in the set up: one is placed before the sample to filter all but the desired probe beam, the other is before the detector to eliminate any scattered pump light. A liquid nitrogen cooled indium antimonide (InSb) detector was used. Both detectors were used in the photovoltaic unbiased mode, that provides optimum signal to noise ratio for our modulation frequency.

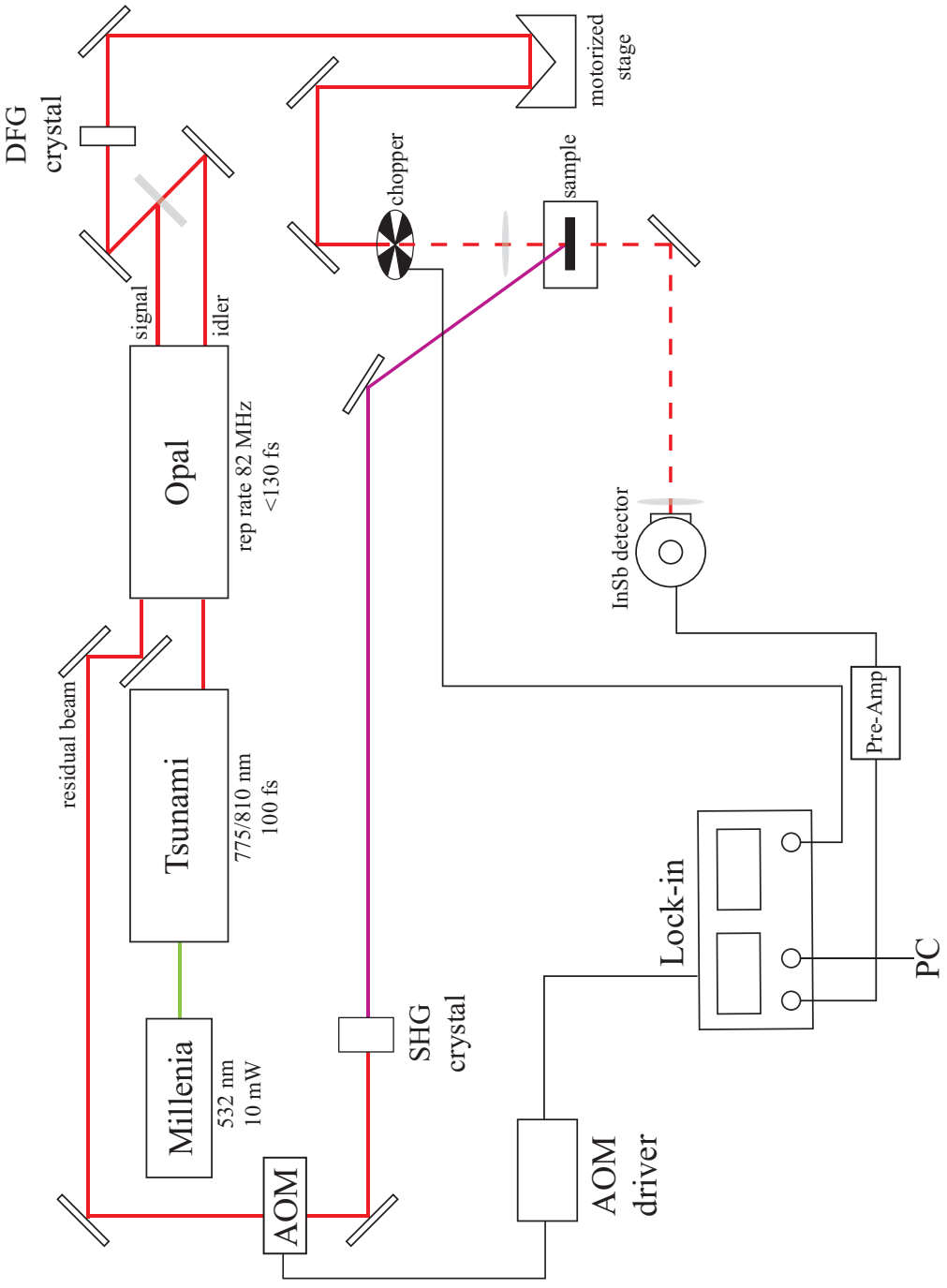

Figure 2.29: Schematic illustrating the main component on the set up used for femtosecond pump/probe spectroscopy. The red lines represent the probe beam path, while the purple line represents the pump beam.

-

Chapter 3

Inter- vs intra-chain interactions in highly oriented PPV

In this Chapter, the role of intermolecular interactions in thick, highly oriented poly(p-phenylene-vinylene) (PPV) is investigated. Raman, reflectance and transmittance spectroscopy under applied hydrostatic pressure are presented and discussed. Raman spectra allow to infer important information on the geometrical changes of the polymer induced by pressure. These results, together with reflectance spectra, allow to clarify the role of inter-chain effects, though electron-phonon coupling cannot be discarded. Furthermore, R spectra are analyzed in the frame of an optical model developed to take into account diamond birefringence. The parallel and perpendicular components of the dielectric constant are also derived with a parametric procedure and their behavior as a function of pressure is studied. These findings are compared to the pressure dependence of the parameters used to obtain the anisotropic dielectric function. Finally, an analysis of the oscillator strengths for both polarizations is presented.

3.1 Introduction

When a polymer is subject to an external applied pressure, several effects originating from different mechanisms are induced simultaneously.

From a geometrical or structural point of view, the most obvious change caused by pressure is a planarization of the backbone chains. Conformational changes due to pressure have been studied by various authors mainly through diffraction and Raman spectroscopy [72–74]. For instance, in crystalline poly(3-octylthiophene)(POT) [75] pressure decreases the lattice parameter perpendicular to the chains while in the parallel direction the polymer proved to be rather incompressible. This different compressibility was related to an improved planarity along the chain axis, while alkyl groups act as rigid spacers between the chains. Flattening of the polymer backbone was also ob-

served in para-quaterphneyl [76]. While at room pressure, the phenyl rings undergo torsional oscillation about the single C-C bonds (primarily due to the repulsion between neighboring ortho-hydrogen artoms), pressure tends to make the ring lie in a plane. At a critical pressure, a phase transition was observed with the abrupt disappearance of IR active modes. In general, as a consequence of planarization, an increase in the conjugation length occurs, causing a pressure-induced red shift of absorption and emission spectra [73, 77–79].

Applied pressure does not only induce intra-chain effects, such as planarization, but also increases the inter-chain wave function overlap due to intermolecular forces between the π-orbitals of neighboring chains. The increment of steric interaction between adjacent chains brought closer together is a fundamental issue: despite interactions along the polymer chain are dominant and determine the main optical and electronic properties of organic semiconductors, 3D effect can dramatically alter this 1D picture [25].

When pressure is applied to decrease intermolecular spacing, two main effects are observed in the optical spectra: a red shift of all the transitions, joined to a clear broadening [79–82]. In polymeric systems, however, it is generally not possible to unambiguously attribute these spectral features to inter-chain coupling. Indeed, polymers are usually weakly ordered materials, and the clear observation of intermolecular interactions is strongly hampered (although in some cases not fully inhibited) by the random distribution of both polymeric chains and their conformations. In disordered systems, flattening of the backbone chains is mainly responsible for the observed red shift and the effects of intra- and inter-molecular interactions are usually not easy to unravel. In a recent paper [83], the pressure-induced red-shift of the PL spectrum of poly(9,9-di-n-octylfluorene-altbenzothiadiazole) (F8BT) was compared to that of a solid state solution of the same polymer. The red-shift observed in the latter was attributed to intra-chain coupling only, being the chains well separated. Instead, the greater red-shift recorded for the thin film PL spectrum was interpreted as the consequence of both intra- and inter-molecular interactions, the additional contribution being du to inter-chain coupling.

Furthermore, it is important to notice that, el-ph coupling is not negligible in weakly ordered systems [25], and also leads to an overall broadening of the electronic and vibronic transitions. The order of the system is a crucial parameter to disentangle between intra- and inter-molecular contribution. Single crystal represent the optimal system to investigate the role of inter-chain interactions but only a few molecular semiconductors are available in this form [26]. In general, disorder intrinsic to π-conjugated systems masks their fundamental properties, affecting the distribution of conjugation lengths and molecular weights, as well as the presence of unreacted monomers and catalyst residual. It is thus clear that a detailed study of inter-chain interactions requires a careful choice of the investigated system.

Highly stretch-oriented PPV has a double advantage with respect to other systems: first, it possesses both a very good optical quality and a high anisotropy

[84,85], that diminish any contributions from disorder. Second, it is a reference system for physics, chemistry and devices: this makes all information extracted from it particularly interesting for the scientific and technological community working in the field. Previous studies on highly oriented PPV [86, 87] correlated the existence of two emitting states observed in PL to the amorphous and crystalline phases co-existing in the oriented PPV [57]. In amorphous regions, the electronic transitions mainly stem from isolated macromolecules (emitting at higher energies), while in the crystalline phase intermolecular interactions would affect the electronic structure, reducing the energy gap and thus lowering the emission energy.

In the following we illustrate the results of Raman and polarized reflectance and transmittance spectroscopy of highly oriented PPV under applied pressure. These findings allow to interpret the role of inter-chain interactions, distinguishing it intra-chain pressure induced changes and comparing it with el-ph coupling.

3.2 Pre-resonant Raman scattering

In this work, Raman spectroscopy was used to probe the geometrical changes induced by pressure in highly oriented PPV. The results are compared to similar studies on other PPV samples and help understand the effect of the increased chain proximity on both the supramolecular structure and conjugation length of this extremely anisotropic polymer.

Pre-resonant Raman spectra (λ_{exc} = 632.8 nm), recorded up to 30 kbar, are shown in Figure 3.1. At room pressure five modes are clearly detectable (at 1170 cm^{-1}, 1329 cm^{-1}, 1548 cm^{-1}, 1583 cm^{-1}, and 1627 cm^{-1}), whose assignment is reported in Table 3.1, according to [81, 88]. Additional very weak modes are also identified but they promptly disappear under pressure and they are not meaningful for the present discussion. These vibrational details are studied in [88].

Table 3.1: Assignment of Raman modes of PPV according to [88]. The last three columns report the shifts as a function of pressure of the Raman modes of non oriented PPV as reported in [88] and in [79] and of highly oriented PPV.

Raman shift	Main assignment [88]	dν/dP (cm^{-1}/kbar) non oriented PPV [79]	dν/dP (cm^{-1}/kbar) non oriented PPV [79]	dν/dP (cm^{-1}/kbar) oriented PPV
1170 cm^{-1}	C-C stretching + C-H bending of the phenyl ring	0.358	0.264	0.34
1330 cm^{-1}	C=C stretching + C-H bending of the vinyl group	0.18	0.168	0.16
1548 cm^{-1}	C=C stretching of the phenyl ring	0.39	0.403	0.33
1583 cm^{-1}	C-C stretching of the phenyl ring	0.352	0.369	0.28
1627 cm^{-1}	C=C stretching of the vinyl group	0.35	0.392	0.36

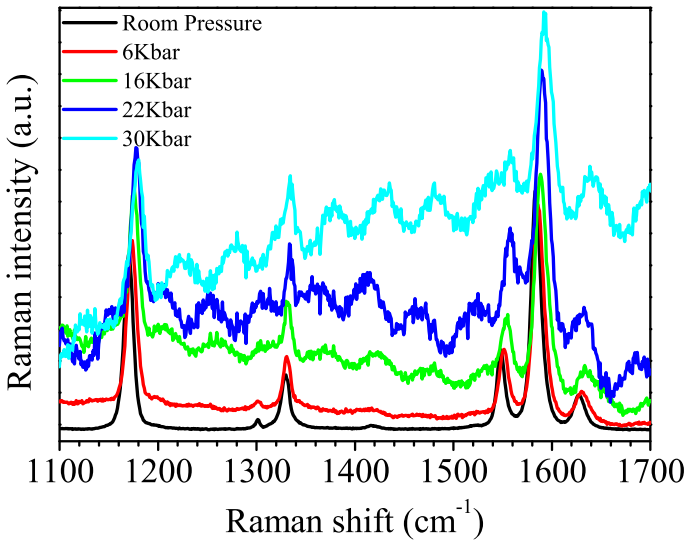

Figure 3.1: Raman spectra ($\lambda_{exc} = 632.8$ nm) of highly oriented PPV for different applied pressure. A photoluminescence background progressively appears as pressure increases, which causes an upward shift of the spectra.

All vibrational modes increase their frequency upon applying pressure (Figure 3.2) with a rate (dν/dP) ranging from 0.16 to 0.36 meV/kbar (Figure 3.3). The hardening of Raman modes with applied pressure was previously observed by other author and Table 3.1 compares the shift rates for oriented PPV with analogous literature data recorded for non oriented PPV films [79, 82]. The different synthetic procedures used to obtain these samples does not allow to easily rationalize the pressure rates of the vibrational modes for oriented and non oriented PPV. In general, the supramolecular structure of π-conjugated polymers is strongly dependent on the synthetic route used to process them. Therefore, despite the same chemical structure, crystalline or amorphous materials can be grown, showing different behavior as a function of pressure.

However, for oriented PPV it can be noticed that the Raman modes assigned to the CC phenyl stretching (1548 cm^{-1} and 1583 cm^{-1}) have a softer dependence on pressure with respect to those of non oriented samples. The lower dν/dP values observed for oriented PPV can be related to its high crystallinity degree (about 70% [57,89]) and to its intrinsic long conjugation length. In the crystalline regions, phenyl rings are better packed and then weakly perturbed by the applied pressure. This interpretation is in full agreement with data for polydiacetilenes where dν/dP for crystalline polymers is less than that of amorphus ones [90]. Also, high pressure studies on different polymorph of poly(3-octylthiophene) (POT) showed that the disordered phase is more compressible than the crystalline phase [91].

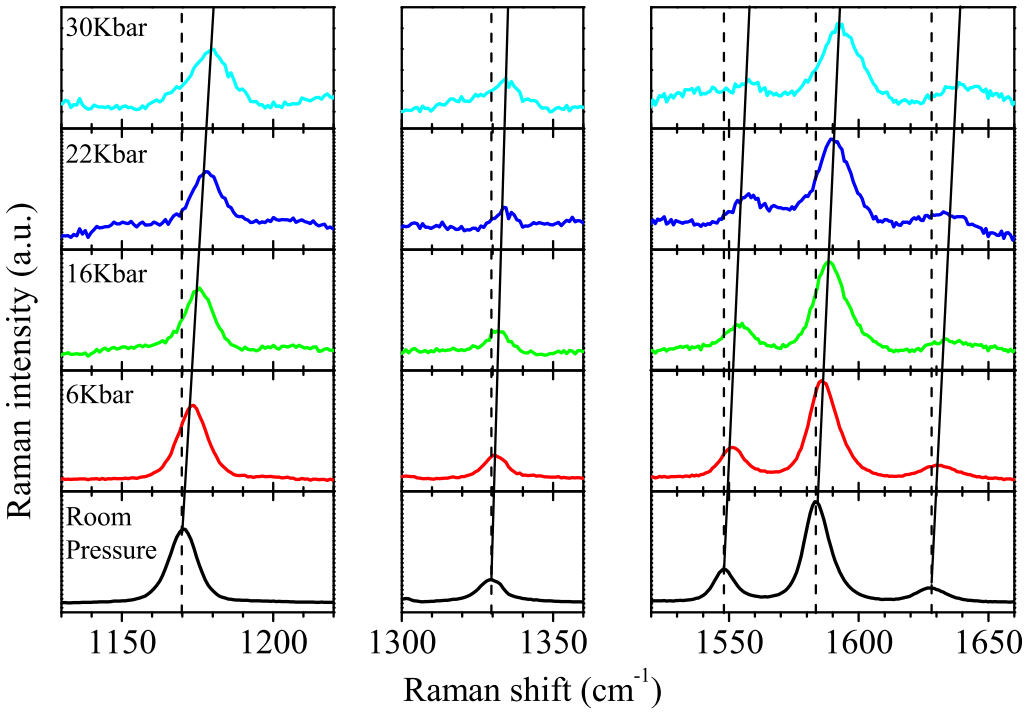

Figure 3.2: Shifts of Raman modes of highly oriented PPV upon applying pressure. Raman spectra are shown for each applied pressure after the background has been subtracted. Vertical dashed and solid lines are guides for the eyes to help follow the shifts induced by pressure of the different modes.

Upon increasing the applied pressure, a background progressively appears in Raman spectra (Figure 3.1). This background shows a well resolved interference fringes pattern that resembles the one previously observed [92] and attributed to photoluminescence (PL). Increasing pressure, the excitation at 632.8 nm becomes closer and closer to the absorption onset (which moves toward lower energies), thus providing a more efficient PL excitation[1]. Due to the high optical quality of the sample, this emitted light is reflected back and forth from the sample surfaces, resulting in Fabry-Perot cavity-like interference fringes [92]. The presence of photoluminescence emission reveals the extremely extended conjugation length of the polymer chains. Figure 3.2 also shows Raman spectra after a smooth PL background has been subtracted. This correction does not alter significantly the spectral position of Raman modes.

[1]Despite this effect, the resonance condition for Raman scattering is not achieved even at the highest pressure applied. Indeed, the weakness of the Raman signal and the presence of a PL background prevent the observation of any "resonant" enhancement of the Raman peaks.

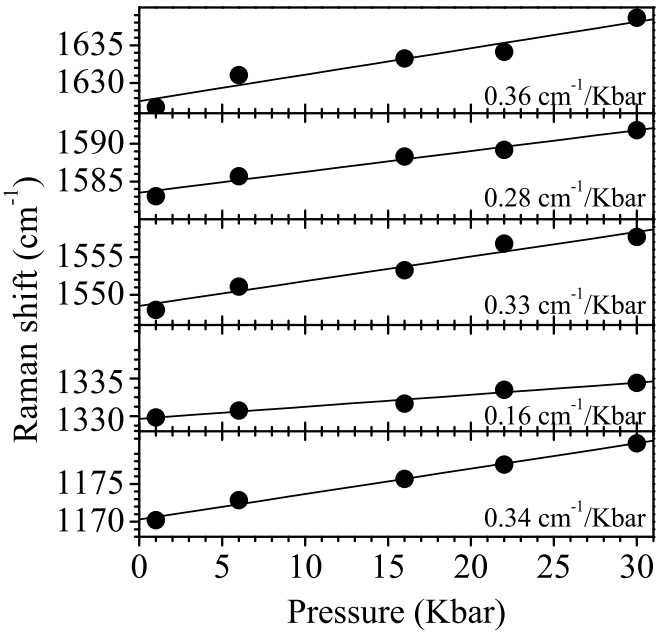

Figure 3.3: Pressure dependence of the position of Raman modes in highly oriented PPV.

No new band appears in Raman spectra due to applied pressure.

Additional insight on the photophysical properties of this material can be obtained analyzing the relative intensities of the Raman bands. In particular, the modes at 1170 cm^{-1}, assigned to the C-H bending of the phenyl ring, at 1548 cm^{-1}, of the C=C phenyl stretching, and at 1627 cm^{-1}, of the vinyl stretching are relevant for the present discussion (see Table 3.1 [81, 88]). It has been observed [81, 93] that the ratio between the bands associated with CC stretching modes of the phenyl ring and those attributed to the vinylene group are fundamental to asses the planarity of the chains and consequently the conjugation length of PPV macromolecules. Thus, Raman scattering provides a powerful tool for monitoring the geometrical changes induced by pressure in the polymer structure, yielding a qualitative criterion for evaluating the conjugation extension. In particular, the ratio between the bands at 1548 cm^{-1} and at 1627 cm^{-1} (I_{1548}/I_{1627}) is greater (less) than one for long (short) conjugated segments, while the ratio I_{1170}/I_{1627} is related to the torsion of the phenyl rings, being greater (less) than one for planar (twisted) polymer chains [81, 88, 93, 94].

Data for highly oriented PPV show that the ratios I_{1548}/I_{1627} and I_{1583}/I_{1627} are almost independent on pressure (being $\sim$2.5 and $\sim$10) up to 16 kbar (Figure 3.4). For higher applied pressure both the interference fringes and structured background prevent the determination of band intensities. Similarly, the ratio

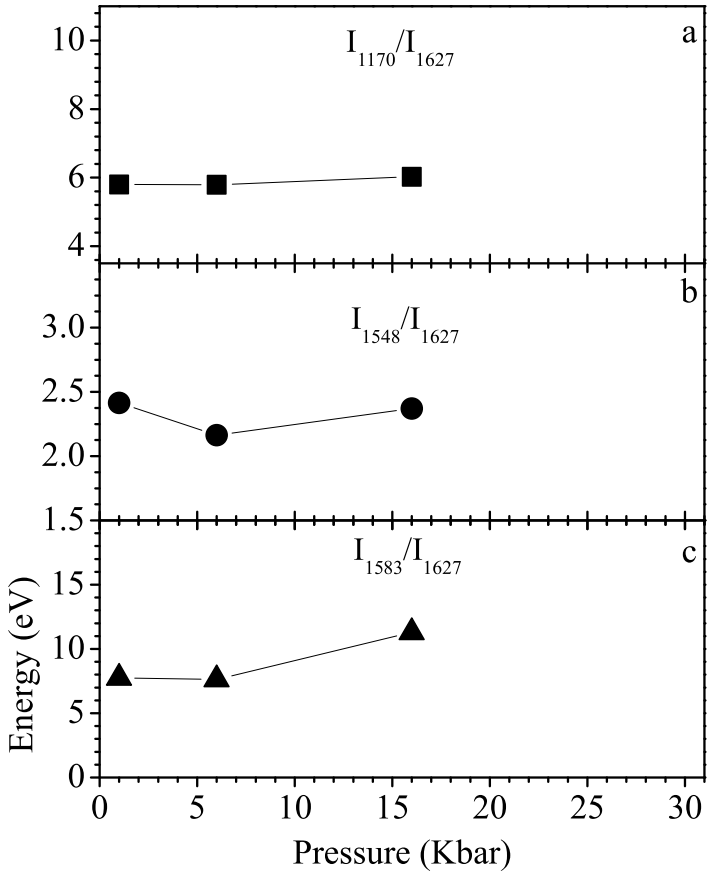

Figure 3.4: Intensity ratio I_{1170}/I_{1627} (a), I_{1548}/I_{1627} (b), and I_{1583}/I_{1627} (c) for highly oriented PPV.

I_{1170}/I_{1627}, also plotted in Figure 3.4, is practically independent on pressure up to 16 kbar and equal to ~ 6.

It is interesting to compare the data for oriented PPV with those for both non oriented PPV [79, 82] and oligophenyl para-hexaphenyl (PHP) [74], a polycrystalline material with a non planar conformation. In non oriented PPV I_{1543}/I_{1622} grows from 1 to 2.4 upon changing applied pressure up to 80 kbar [82]. In the case of oriented PPV the value of 2.4 is already achieved at room pressure and does not change by applying pressure (Figure 3.4). This indicates that the conjugation extension of stretched PPV is not substantially increased by pressure, such a high value of I_{1543}/I_{1622} being achieved by standard PPV at high pressures only. Furthermore, it is worth noting that, for highly oriented PPV, the ratio I_{1170}/I_{1627} is also independent on pressure (Figure 3.4a), i.e. phenyl rings have a very low twisting angle. This behavior is dramatically different with respect to that observed both in spin cast PPV [95]

and PHP [74], where the remarkable increase of this ratio is detected up to 50 kbar indicates a progressive planarization of the macromolecules with increasing pressure.

These observations point out that, even at room pressure, stretch oriented PPV possesses a high degree of planarity and consequently an exceedingly extended conjugation length, which is not significantly improved by applying pressure. As a consequence, minor effects due to planarization and to an increase of the conjugation length are expected to affect the optical properties of oriented PPV under pressure.

Finally, a broadening of Raman bands with increasing pressure seem to be apparent in Figure 3.2. However, a detailed analysis indicates that the full width half maximum of Raman peaks is almost constant. The apparent broadening is in fact due to the reduction of the signal intensity upon increasing pressure. The independence of broadening on applied pressure in oriented PPV indicates that anharmonicity plays a minor role on the vibrational properties of the system. In other conjugated polymers, like polydiacetylene [90], a highly crystalline system, the broadening of Raman peaks was instead assigned to phonon distribution correlated to intramolecular ordering (flattening) upon increasing pressure. Therefore, we deduce that in oriented PPV, order is almost independent on applied pressure, further indicating that main effects of pressure observed in the optical spectra are due to different reasons. Moreover, the modest change of the Raman scattering intensities, along with the absence of new Raman bands, further supports the negligible modifications of the intra-chain conformation geometry.

3.3 Reflectance and transmittance

In the following we will discuss the effect of pressure on reflectance (R) and transmittance (T) spectra. To make the analysis of the pressure dependencies easier, we will first summarize the assignment of the features observed in R and T spectra outside the DAC. These measurements are literature data obtained for the same PPV sample [84, 86, 87, 92].

3.3.1 Main features

Figure 3.5 shows room pressure reflectance (R) and transmittance (T) of highly oriented PPV films for both polarizations.

The main spectroscopic features of the parallel component of reflectance ($R_{//}$) are in the high energy region of the spectrum (>2 eV). The purely electronic transition (0-0, or peak I) between delocalized molecular levels d-d*, is located at a significantly low energy (2.48 eV-500 nm), indicating a long conjugation length of the polymeric chains in these samples. This transition is known to be strongly polarized along the chain axis, as discussed in [96–107]. A well resolved vibronic progression appears with peaks at 2.70 and 2.95 eV

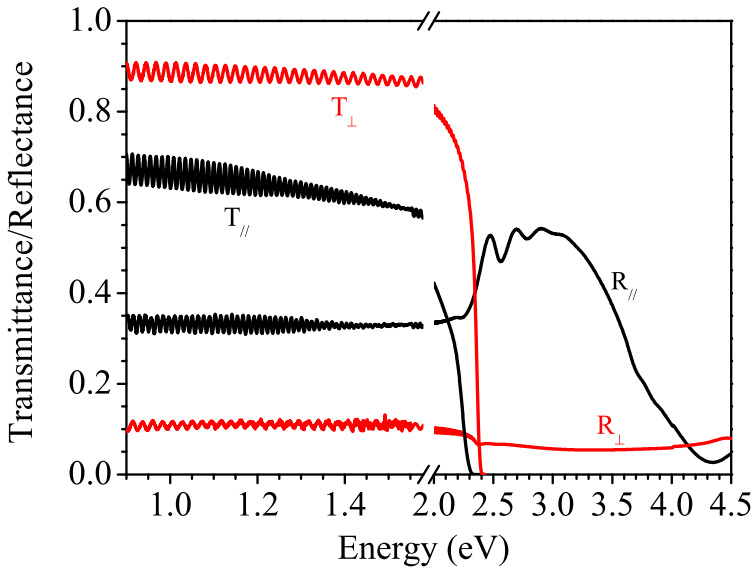

Figure 3.5: Polarized reflectance and transmittance spectra of highly stretch-oriented PPV [92]. The black (red) lines refer to the parallel (perpendicular) component. The energy scale is expanded below 1.7eV to highlight interference fringes.

(460 and 420 nm), respectively, reflecting a narrow distribution of conjugation lengths.

At higher energies, a shoulder is observed in the parallel reflectance spectrum at about 3.7 eV (340 nm), usually referred as peak II . This feature is polarised along the chain axis [97, 108–111] and originate from a mixing of transitions between delocalized levels (d-d*) induced by finite-size effects. On the basis of quantum chemical calculations peak II has been assigned to conjugation chain ends [84, 92] and its intensity is expected to decrease in long conjugated polymers [112].

For energies lower than 2 eV, an interference pattern is manifested, due to the sum of contributions of light reflected from the front and from the back surface of the film. The presence of interference fringes testify the high optical quality of the sample under study.

In the perpendicular reflectance, the onset of absorption results in an abrupt reduction of the reflectivity intensity around 2.48 eV (500 nm). The lowest optical transition and its vibronic satellites are practically not detectable along this polarization component. This confirms that the polymer chains are very well oriented and the misalignment angle is very small. Below 2.4 eV, a reflectance signal arising from the contribution of the back surface and a series of interference fringes are clearly detected. Changes in the path of these fringes with respect to that observed for the parallel component point out the

anisotropy of the refractive index.

Figure 3.5 also shows the room pressure polarized transmittance (T) of highly oriented PPV. As in reflectance spectra, the appearance of interference fringes testifies the good optical quality of the films. The optically thick sample used in this work does not allow a direct determination of the transmission spectra above 2.48 eV (500 nm), the sample being no longer transparent at this wavelength. The remarkable difference between the two polarization in the transmittance onset is the result of the different optical strength of the parallel and perpendicular component of the lowest optical transition ($\pi - \pi^*$), arising from chain misalignment.

For a complete discussion of the spectroscopic features of highly oriented PPV, see [84, 86, 87, 92].

3.3.2 Reflectance under pressure: raw data

Measured reflectance spectra for different applied pressures, with light polarization parallel to the polymer chains, are shown in Figure 3.6. At room pressure, the lowest energy peak, due to the $\pi - \pi^*$ transition, is located at 2.46 eV (504 nm). As already pointed out (Section 3.2), the considerably low energy of this purely electronic (0-0) transition testifies an exceedingly long conjugation length of the polymer chains in this sample, even at room pressure. Well resolved vibronic replicas are also observed at 2.70-2.90-3.09 eV (460-427-401 nm). The clear spectral resolution of these features reflects the high degree of structural order possessed by this sample, a fundamental issue in order to deeply investigate its optical and electronic properties.

Furthermore, another transition -peak II- can be detected as a shoulder around 3.77 eV (329 nm). This is indicated by the arrow in Figure 3.6. The intensity of this structure is expected to decrease as chain length increases [92, 112, 113]. Its weakness thus further confirms the extremely long average conjugation length of the macromolecules in this sample.

The overall effect of pressure on the parallel component of R is twofold: a rigid red shift of the whole spectrum and a broadening of the vibronic transitions. In particular, the $\pi - \pi^*$ transition shifts of -3.7 meV/kbar, as summarized in Figure 3.9a, while the dependence on pressure of peak II (Figure 3.9b), whose spectral position was identified by the zeros in the third derivative[2] of R, is weaker, -2.7 meV/kbar.

A pressure-induced red shift of the optical transitions was observed for a number of different polymers [73,74,79]. This effect can in principle result from the interplay of two different phenomena: an increase in the average conjugation length of the polymer, due to planarization of the backbone chains, and an enhancement of inter-chain interaction, due to an increase of wavefunction delocalization on neighboring chains favored by the reduction of the inter-chain

[2]In order to determine the spectral position of peak II as a function of pressure, R was fitted with a smooth function around peak II and this function was subsequently derived.

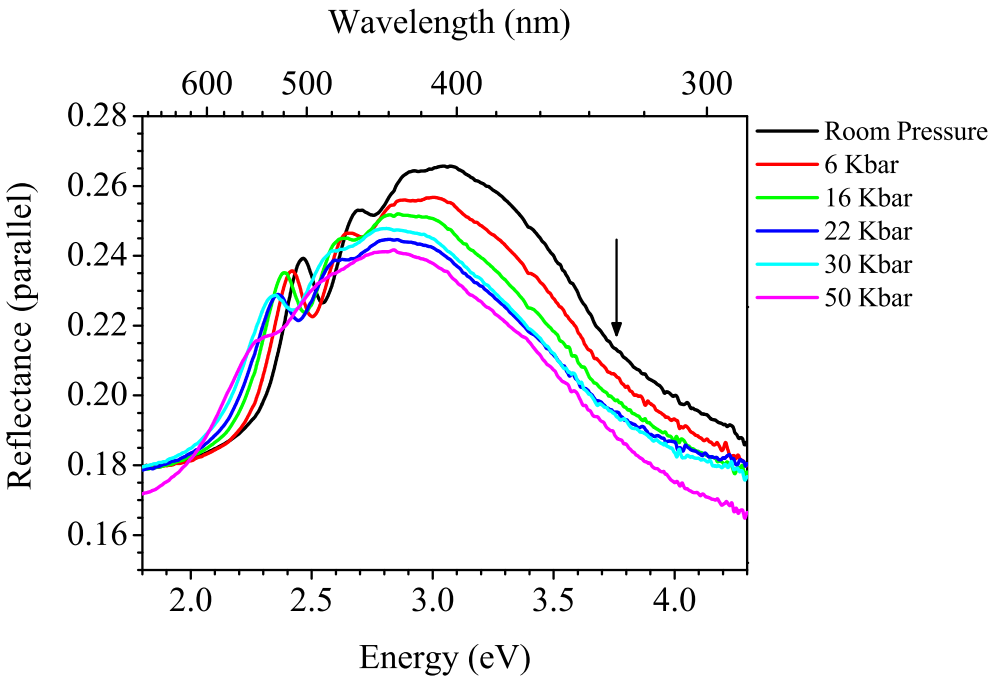

Figure 3.6: Parallel component of reflectance spectra of highly oriented PPV for different applied pressure. The arrow indicates a shoulder corresponding to peak II.

distances.

As outlined in Section 3.2, the analysis of the Raman modes of stretch oriented PPV showed that neither geometrical changes nor an increase of conjugation length are induced by pressure. Furthermore, the pressure dependence of peak II (which -we recall- is an intra-chain species assigned to conjugation chain ends) points out that intra-chain effects are indeed weak. As a consequence, the deep modification of the $\pi - \pi^*$ transition revealed by its stronger pressure dependence has to be ascribed to different mechanisms.

Furthermore, the spectra in Figure 3.6 also exhibit a broadening of all electronic transitions and vibronic replicas upon increasing pressure. As a matter of fact, inter-chain interactions induce a splitting of the HOMO and LUMO levels of the isolated chains with the overall effect of broadening the electronic and vibronic transitions. Another contribution to spectral broadening is in general due to el-ph coupling. The enhanced delocalization caused by interacting chains might also reduce the el-ph coupling, bringing to a redistribution of the intensity of the vibronic progression in absorption spectra.

To better understand the nature of the effects observed in the optical spectra so far described, it is then necessary to compare the inter-chain interaction bandwidth (W_{inter}) and the strength of the el-ph coupling (W_{el-ph}). Indeed,

the value of the ratio W_{inter}/W_{el-ph} determines the weak ($\ll 1$), intermediate (~ 1) or strong ($\gg 1$) coupling regime in the investigated system and then the correspondent spectral shape.

As an example, let us consider the spectral effect of el-ph coupling on molecular aggregates [114].

In the limit of strong coupling (Figure 3.7(a)), the Born-Oppenheimer separability of intra-molecular electronic and vibrational wave functions is applicable. Thus, the allowed excited electronic states of identical molecules in an aggregate will interact, and the vibrational envelope will follow along. In a dimer (Figure 3.7(a), middle panel) a splitting will occur (although some of the components might be forbidden) and the excitation will be distributed over both molecules, so the vibrational frequencies of the excited state will change. In the ideal case of an infinite polymer (Figure 3.7(a), lower panel) a much larger exciton splitting will be observed, but the bandwidth of the allowed component will now become extremely narrow, due to the fact that only the 0-0 vibrationless electronic transition is now allowed by the Franck-Condon principle.

Weak coupling correspond to the failure of Born-Oppenheimer separability. In this regime (Figure 3.7(b), right panel), no spectral band shape change is observed, but second order effects, such as hypochromism or hyperchromism might occur. In the intermediate coupling the electronic and vibrational wave functions are also not separable, and a general broadening of the band contour may result, as schematically depicted in Figure 3.7(b), left panel.

It is thus clear that an unambiguous interpretation of the data presented up to now requires the evaluation of both W_{inter} and W_{el-ph}. In order to obtain these values further manipulations on the data are necessary. In the following sections we will present a method for the derivation of the dielectric constant, based on a parametric fitting procedure, that will allow us to derive W_{el-ph} directly form the parallel dielectric constant, and to evaluate W_{inter} form the fitting parameters.

Figure 3.8 shows the perpendicular component of reflectance spectra for different applied pressures. For this polarization the shape of R spectra exhibits some difference when compared to the ones previously reported for instance in [84, 87] at room pressure outside the diamond anvil cell.

Although the lowest energy transition and its vibronic replica between 2.46 and 3.09 eV are hardly detectable (as expected for a highly oriented and thus optically anisotropic sample), some features can be identified.

In the low energy region of the R perpendicular spectrum, up to about 2.3 eV, by increasing the photon energy the signal decreases due to the increasing absorption. This might be attributed to polymer chain misalignment (inevitable also in highly oriented polymers), which provides a projection of parallel component into the perpendicular one [84]. The effect of absorption on the perpendicular reflectance can also be observed in the spectra measured outside the cell reported in Figure 3.5. Moreover, in the perpendicular com-

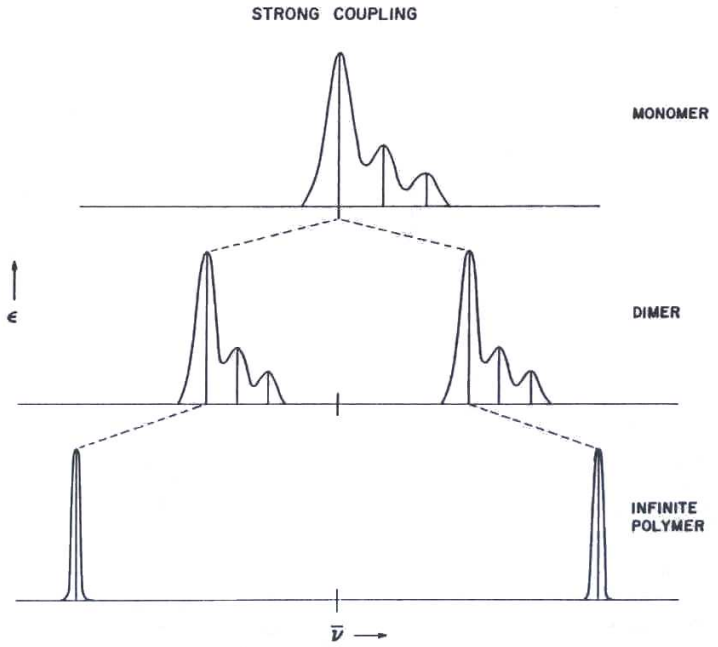

(a) Strong el-ph coupling.

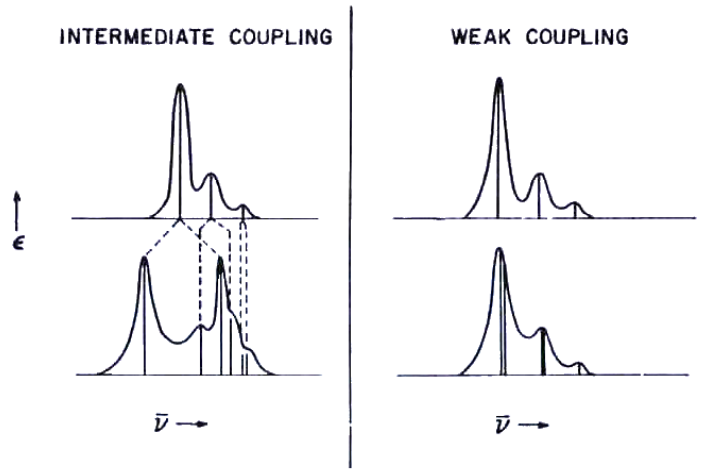

(b) Weak and intermediate el-ph coupling.

Figure 3.7: Spectral effects of strong (a), weak, and intermediate (b) el-ph coupling on electronic transitions and vibrational states of a molecular aggregate [114].

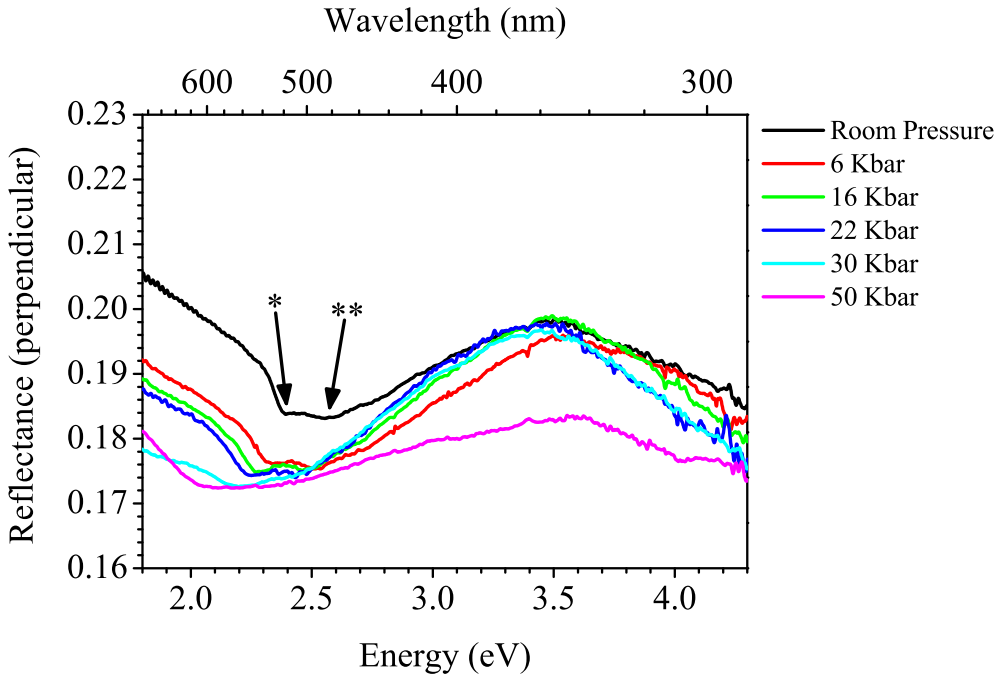

Figure 3.8: Perpendicular component of reflectance spectra of highly oriented PPV for different applied pressure.

ponent of R, a weak structure appears around 2.5 eV denoted with asterisks in Figure 3.8 and for higher energies a maximum is also observed at about 3.5 eV. However, the optical analysis of the data previously described (Section 3.4) shows that this high energy structure is an artifact due to polarization mixing caused by diamonds birefringence, which mainly affect the perpendicular polarization owing its very weak intensity.

Upon applying pressure, the onset of R perpendicular (marked with * in Figure 3.8) shifts towards lower energies at a rate of dE/dP= −5.8 meV/kbar. This value is close to the absorption edge of the $\pi - \pi^*$ transition observed in the parallel transmittance spectrum (Figure 3.10a), being due to the sum of peak energy and broadening rates (Figure 3.9) [86].

The feature at about 2.5 eV, indicated with two asterisks in Figure 3.8, shows a pressure rate of dE/dP= −4.4 meV/kbar similar to that observed for the 0-0 peak of parallel reflectance spectrum, thus suggesting its origin as due to chain misalignment.

The shift rates with pressure of the features observed in R spectra for both polarization are summarized in Figure 3.9.

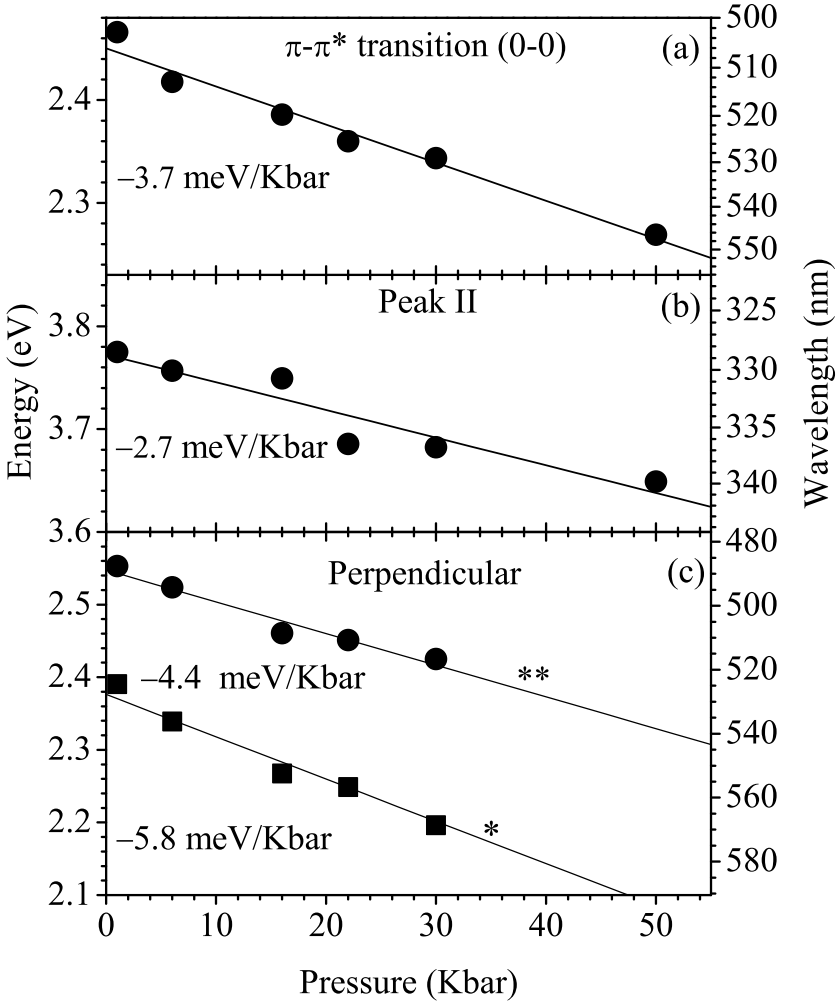

Figure 3.9: Shift with applied pressure of $\pi - \pi^*$ (a) transition and peak II (b) as determined from the analysis of the parallel component of reflectance in Figure 3.6. The linear fits are also shown, and the values of respective slopes are reported. (c) shows the pressure dependence for the double structure denoted with asterisks in perpendicular component of reflectance spectra (Figure 3.8). The values of dE/dP resulting form a linear fit are also reported.

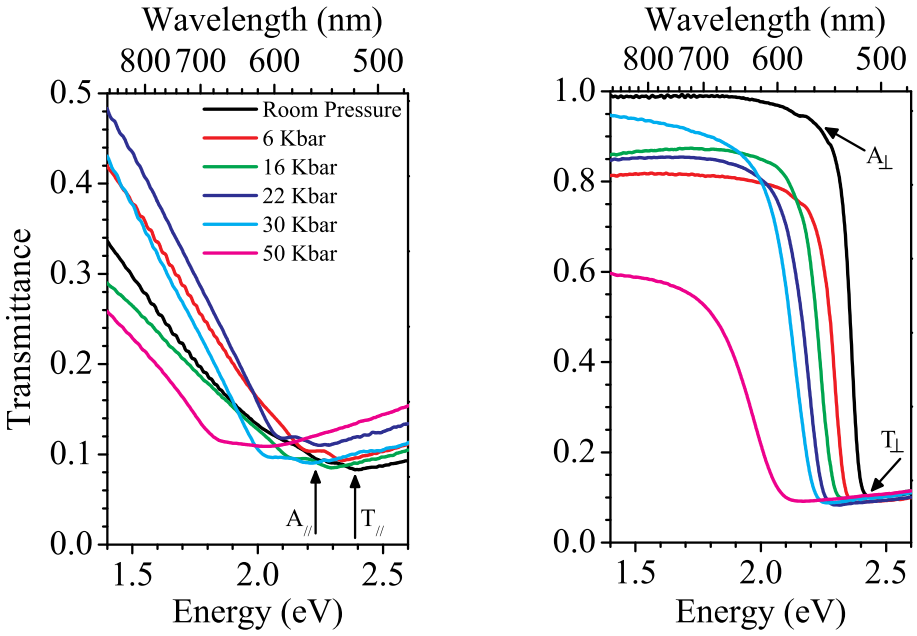

(a) Parallel.

(b) Perpendicular.

Figure 3.10: Parallel and perpendicular component of transmittance of highly oriented PPV for different applied pressures. In (a), the two features corresponding to the double step-like structure are labeled $A_{//}$ and $T_{//}$. In (b) the absorption and transmission onsets are indicated as $A_{\perp}$ and $T_{\perp}$.

3.3.3 Transmittance under pressure

Figure 3.10 shows the parallel and perpendicular components of measured transmittance (T) for different applied pressures. It can be noticed that both these spectra do not approach zero in the energy region above the optical gap. This behavior, different with respect to previous findings, can be (partially) related to light diffusion arising from PPV/diamond interface and due to surface roughness.

Both parallel and perpendicular T spectra display a bathochromic shift of their spectral features upon applying pressure.

For the parallel component (Figure 3.10a) the spectral signature of the absorption onset (identified as the energy where T rapidly drops off) is not evident. Nonetheless, a feature with a double step-like character is recognizable. In Figure 3.10a these structures, highlighted by arrows, are located at 2.25 and 2.40 eV (551 and 517 nm) in the room pressure spectrum and labeled $A_{//}$ and $T_{//}$, respectively.

In the perpendicular T spectrum two clear features can be identified: the absorption (at 2.29 eV -541 nm, at room pressure) and transmission onset (at 2.43 eV - 510 nm, at room pressure). These are marked $A_{\perp}$ and $T_{\perp}$ in Figure

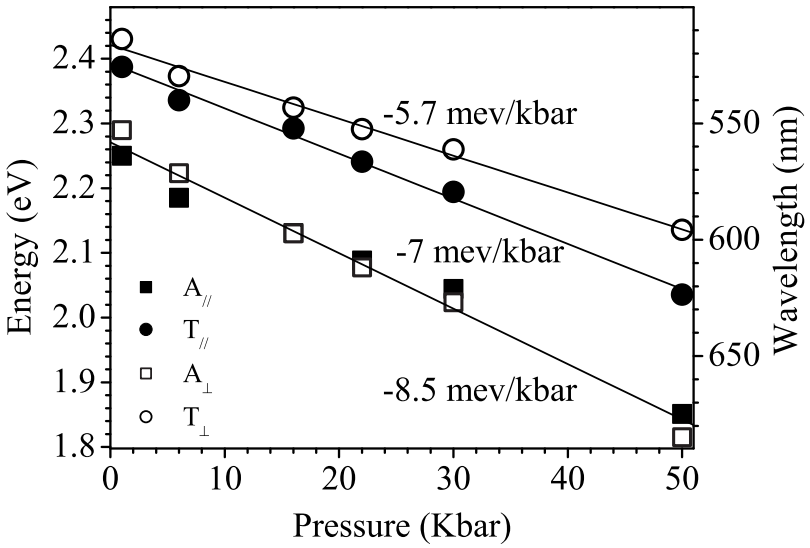

Figure 3.11: Pressure dependence of the different spectral features detected in the perpendicular component of transmittance.

3.10b.

Figure 3.11 compares the pressure dependencies of $A_{//}$, $A_{\perp}$, $T_{//}$, and $T_{\perp}$. It can be noticed that $A_{//}$ and $A_{\perp}$ exhibit a similar pressure dependence (-8.5 meV/kbar). Both $A_{//}$ and $A_{\perp}$ can be ascribed to the absorption onset corresponding to the $\pi - \pi^*$ transition, having mainly a parallel character but with a perpendicular component due to both chain misalignment and polarization mixing, as already observed in Section 3.3.2.

$A_{//}$ and $T_{//}$, highlighted in Figure 3.10a, evolve as a function of pressure in a similar manner, as shown in Figure 3.11. These shift rates (-8.5 and -7 meV/kbar for $A_{//}$ $T_{//}$ and respectively) are twice as big as that of the $\pi - \pi^*$ transition as obtained from parallel R spectra (-3.7 meV/kbar), indicating that a broadening occurred upon applying pressure. Indeed, the shift rate of the $\pi - \pi^*$ transition derived from R spectra comprises both its peak position as a function of pressure and its broadening, which strongly affects the value of dE/dP.

For the perpendicular polarization (Figure 3.10b) the whole T spectrum clearly shifts towards lower energies with increasing pressure but different dependencies can be detected. The onset of absorption, marked as $A_{\perp}$, has a pressure dependence of -8.5 meV/kbar, while the onset of transmission $T_{\perp}$ varies with pressure by -5.7 meV/kbar. These dissimilar values also clearly show that a broadening of the transition giving rise to absorption occurs.

3.4 A model for data analysis: corrections to R spectra

In the following we will describe the optical model developed to correct the spectra reported in the previous Sections. Data reduction was necessary since in addition to the optical response of the sample, several other contributions affect the measured spectra, and must be properly considered for a correct data analysis. These can be summarized as follows:

- reflection contribution from the front surface of the diamond anvil cell;
- dielectric contrast between diamond and sample instead of the usual air/sample interface;
- diamond birefringence [68] induced by defects and/or by strain, which inhomogeneously rotate the plane of polarization of light, introducing a polarization mixing in the sample optical response;
- light scattering from the sample itself, as inferred from previous spectroscopic measurements [92].

In general, all mentioned contributions exhibit a smooth spectral dependence, so the main spectral features characterizing PPV, particularly for the parallel polarization, can be interpreted analyzing the raw data, as in Sections 3.3.

Nevertheless, a more detailed discussion and a quantitative evaluation of the relative strengths of the observed spectral features require a more careful inspection of the data, due to the problems cited above. A simple model, considering the diamond anvil as a thick transparent layer, allows the calculation of the contributions to reflectance and transmittance of the air/diamond and diamond/sample interfaces and can easily account for the first two issues. As concerns strain-induced birefringence of diamond, the small angular divergence (1°) provided by the set up used for the measurements (Chapter 2) minimizes the volume of diamond crossed by the probing beam. This improves the control on polarization of the outcoming beam, reducing the effect of polarization mixing due to diamond birefringence. In addition, a series of calibration measurements were performed on the front diamond of the DAC (half cell). These fully characterize its polarized spectral response and depolarization effects, and allowed to renormalize our data.

All reflectance and transmittance spectra were normalized, i.e. their values are absolute. Nevertheless, R and T data have to be analyzed with different approaches. The reference measurement used to normalize T spectra could be recorded through a spot within the gasket hole that was not occupied by the sample. Thus the effect due to both the front and back diamond of the DAC was easily removed from T spectra, which need no further corrections. Instead, such a reference spectrum could not be used to normalize reflectance.

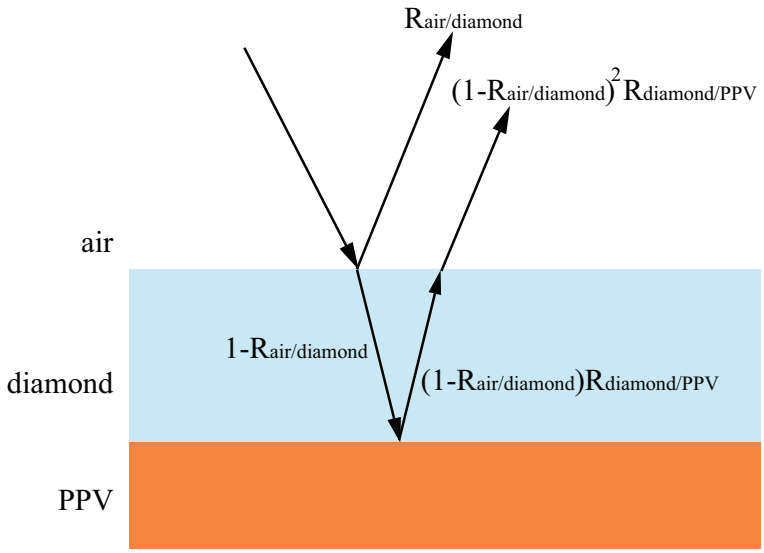

Figure 3.12: Schematics of the model used for analysis of reflectance spectra.

As a matter of fact, the presence of diamond, that serves as optical window, strongly affects reflectance spectra, modifying both their intensity and shape.

The DAC containing the sample was represented as a three-layer system composed by PPV, diamond and air, with two interfaces (air/diamond and diamond/PPV). Each of the interfaces separately contributes to the total reflectivity. A schematic is depicted in Figure 3.12.

Within this model, the experimental reflectivity R_{exp} is the sum of two contributions, and can be written as:

$$\begin{aligned} R_{exp} &= R_{air/diamond} + (1 - R_{air/diamond})^2 R_{diamond/PPV} \\ &= R_{air/diamond} + T_{air/diamond/air} R_{diamond/PPV} \end{aligned} \tag{3.1}$$

In this expression, the first term accounts for the reflectivity of air/diamond interface, while the second is due to the diamond/PPV interface. In the second expression of Equation (3.1), use has been made of the equality between the transmittance of a double air/diamond interface and the term enclosed by parenthesis [67]. Furthermore, higher order terms, arising from multiple reflections between the interfaces, are neglected in this model.

Equation (3.1) represents the absolute values measured for reflectance (Figure 3.6 and Figure 3.8). Actually, these values are higher than expected for a bare PPV/air interface, since they include the contribution due to the air/diamond reflectance, namely:

$$R_{air/diamond} = \frac{(1 - n_{diamond})^2}{(1 + n_{diamond})^2} \tag{3.2}$$

which is independent on polarization and roughly 17% if $n_{diamond}$ is simply set equal to 2.4. Diamond refractive index dispersion (Palik WVase Library)

is also taken into account in evaluating $R_{air/diamond}$. The effect of the corrections embedded in Equations (3.1) and (3.2) to measured reflectance spectra are shown in Figure 3.14(a) and 3.14(b) for the parallel and perpendicular component.

The effect of diamond on reflectance spectra is not thoroughly comprised in this simple model and further corrections to the data are need. Even when the air/diamond reflectance is taken into account as previously discussed, room pressure R spectra measured through the DAC present for both polarization an anomalous shape if compared to the spectra recorded outside the cell reported in Figure 3.5 [92]. In particular, the intensity of the parallel component of R (Figure 3.14(a)) is lower than expected in the whole spectral range, with a greater decrease in the high energy region. The perpendicular component (Figure 3.14(b)), rather than being quite flat with an absolute value between 3 and 4%, has a swinging behavior, assuming negative values for energies higher than 4 eV. This effect is caused by the refraction through a planar interface, which introduces spherical aberration that alters the detected light intensity. A theoretical analysis for the simple case of one planar interface is proposed in [115]. Here, however, two interfaces should be considered (air/diamond and diamond/sample, see Figure 3.12), and a detailed model accounting for this effect is beyond the scope of the present study.

In order to compensate for the intensity loss of the spectra, reflectance and transmittance of half, empty cell (basically, the front diamond of the DAC) has been recorded and used to renormalize all the reflectance data as follows. The loss factor α has been evaluated experimentally from the total reflectivity of the empty diamond anvil cell using the relation:

$$\begin{aligned} R_{exp}^{emptyDAC} &= \alpha R_{air/diamond} + \alpha^2 (1 - R_{air/diamond})^2 R_{diamond/PPV} \\ &= \alpha R_{air/diamond} + \alpha^2 T_{air/diamond/air} R_{diamond/PPV} \end{aligned} \tag{3.3}$$

where $T_{air/diamond/air}$ is the transmittance through the double air/diamond interface, measured independently and for both polarizations, and $R_{air/diamond}$ is the ideal reflectance of the air/diamond interface given by Equation (3.2) and including $n_{diamond}$ dispersion. Once α is known over the entire spectral range, the reflectivity of the sample can be obtained inserting Equation (3.1) in the following:

$$R_{diamond/PPV} = \frac{R_{exp} - \alpha R_{air/diamond}}{\alpha^2 T_{air/diamond/air}} \tag{3.4}$$

where R_{exp} is the experimental reflectivity of PPV measured inside the DAC (Figure 3.6 and 3.8), α is obtained via Equation (3.3), and $R_{air/diamond}$ is given by Equation (3.2). $R_{diamond/PPV}$ is derived through Equation (3.4) for both polarizations.

The phenomenological loss factor α increases the absolute values for both polarizations and removes the pathological behavior of the perpendicular component at high energies, as shown in Figures 3.14(a) and 3.14(b). Nonetheless,

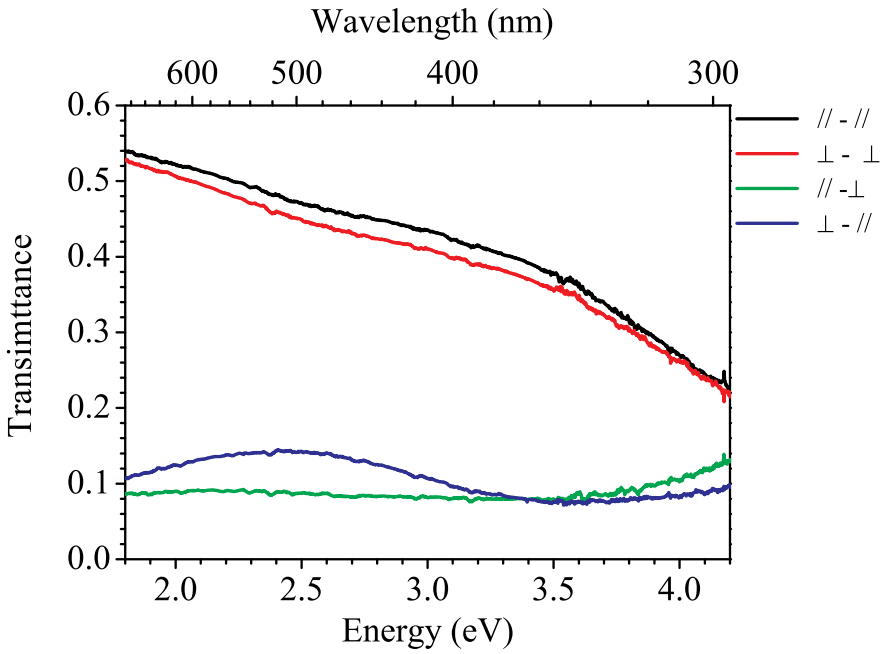

Figure 3.13: Transmittance through the half, empty DAC in a double polarizer experiment. The symbols refer to polarizer and analyzer polarization, respectively.

another correction is necessary. Indeed, the absolute value of $R_{//}$ is still lower compared to the reference spectra recorded outside the DAC, while the intensity of $R_{\perp}$ is higher over the whole spectral range and further increases in the high energy region.

The well-known strain-induced birefringence possessed by diamond [68], and caused by defects such as dislocations, lattice parameter variations, inclusions, fractures, and plastic deformation that possesses a strong, needs to be taken into account when dealing with polarized measurements inside the DAC. A mixing of the parallel and perpendicular polarizations is to be expected, that prevents a direct interpretation of the experimental data.

In order to clarify this effect, a double polarizer transmittance measurement of the empty cell was performed. The incident light was polarized before impinging on the sample and an analyzer was placed in front of the detector. Transmitted light was found to be non zero even with crossed polarizers, showing a strong energy dependence. These spectra are reported in Figure 3.13.

Assuming the same polarization mixing occurs for all applied pressures, the amount of mixing can be easily determined by the coefficients:

$$a = \frac{T^{//\perp}}{T^{////} - T^{//\perp}} \tag{3.5}$$

$$b = \frac{T^{\perp\perp}}{T^{\perp\perp} - T^{\perp//}} \tag{3.6}$$

being T the transmittance of the empty cell shown in Figure 3.13, where the symbols refer to the polarizer and analyzer, respectively. The coefficients a and b calculated via Equation (3.5) and Equation (3.6) were fitted with second order polynomials, that were instead used for corrections to avoid introducing further artificial noise in the spectra. Then, the recorded parallel/perpendicular component including also a contribution form the other polarization, can be expressed in terms of the correctly polarized spectra:

$$R^{//}_{diamond/PPV}(mixed) = aR^{//}_{PPV} + (1-a)R^{\perp}_{PPV} \tag{3.7}$$

$$R^{\perp}_{diamond/PPV}(mixed) = bR^{\perp}_{PPV} + (1-b)R^{//}_{PPV} \tag{3.8}$$

Once the mixing coefficient a and b are known over the whole spectral range, the correctly polarized spectra can be obtained inverting Equation (3.7) and (3.8):

$$R^{//}_{PPV} = \frac{(1-a)R^{\perp}_{diamond/PPV}(mixed) - bR^{//}_{diamond/PPV}(mixed)}{1-a-b} \tag{3.9}$$

$$R^{\perp}_{PPV} = \frac{(1-a)R^{//}_{diamond/PPV}(mixed) - bR^{\perp}_{diamond/PPV}(mixed)}{1-a-b} \tag{3.10}$$

Figures 3.14(a) and 3.14(b) show a comparison between the room pressure spectra obtained for both polarizations after each step of the correction procedure (Equations (3.1),(3.2),(3.4)),(3.9), and (3.10)). The corresponding spectrum recorded outside the DAC [87, 116] is also reported.

The correction procedure described so far adjusts both intensity and shape of room pressure spectra, giving a satisfactory agreement with the ones recorded outside the DAC for both polarizations and used as references. In particular it can be noticed that the high energy bump in $R_{\perp}$ disappears in the corrected spectrum (Equation (3.10) and Figure 3.14(b)).

Nonetheless, the present mathematical modeling affects the energy range useful for data analysis, resulting in an increased noise level in the high energy region. This forbids any reliable interpretation for energies higher than 3.5 eV. Since the complex dielectric constants will be derived by fitting these corrected R spectra, as described in the following Section, the subsequent analysis of transition energies and broadening upon applying pressure must be limited the spectral range where the adjustment procedure does not fail.

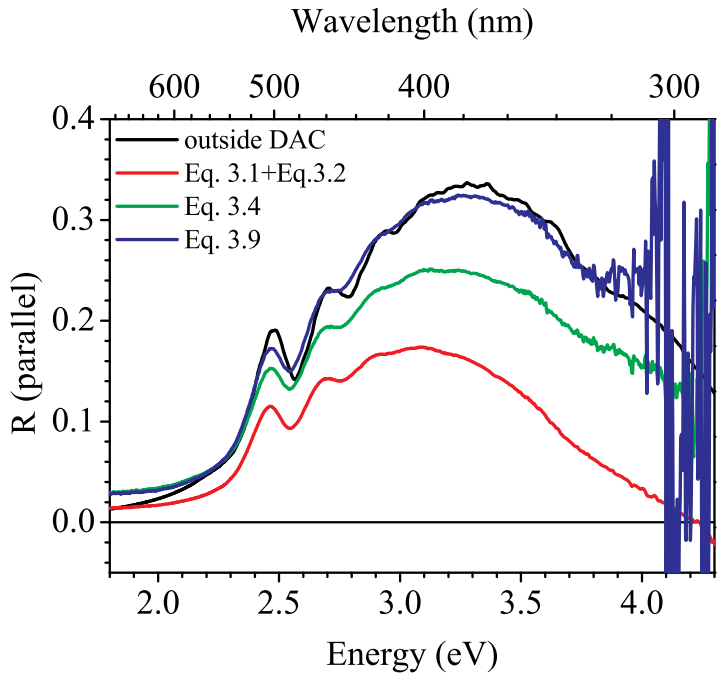

(a) Parallel.

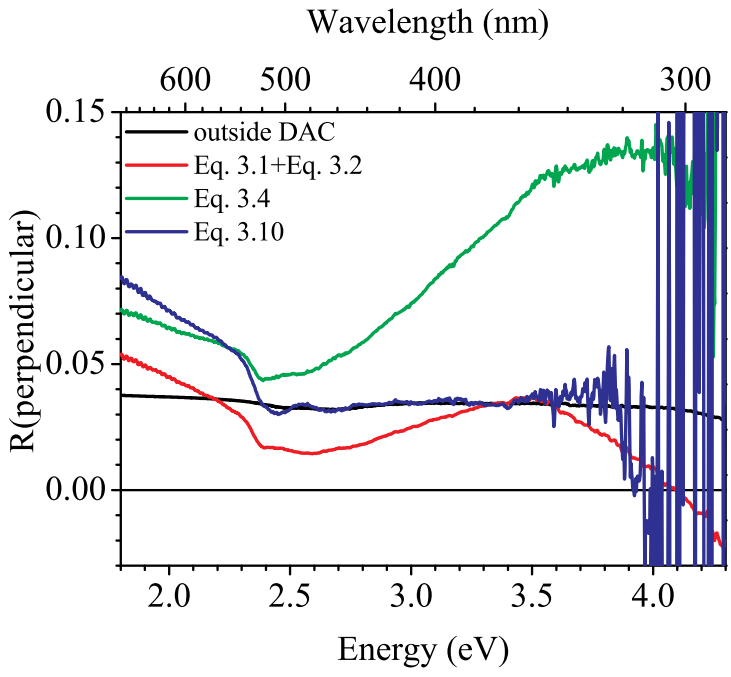

(b) Perpendicular.

Figure 3.14: Comparison between the room pressure spectra obtained for the parallel (a) perpendicular (b) polarizations after each step of the correction procedure and the corresponding spectrum recorded outside the DAC (Figure 3.5). The labels refer to the equation used to obtain the spectrum.

Some minor discrepancies, probably ascribed to light scattering from the sample still remain and cannot be accounted for without arbitrary assumptions. Moreover, since the normalization procedure is based on data measured at ambient pressure, some caution has to be used to interpret the spectra at higher pressures.

Nevertheless, the features we want to discuss do not depend on the adopted procedure, showing a regular evolution with pressure, which is not affected by the renormalization. Some care has to be anyway used in the interpretation of the data related to the perpendicular polarization since these spectra are much less intense than the parallel ones and thus more sensitive to uncertainties.

3.5 Corrected reflectance spectra

As discussed in the previous Section, the presence of diamond strongly affects the intensity and polarization of PPV spectra. The correction procedure there described allowed to extract the parallel and perpendicular components of reflectance that provide the input to determine the polarized components of the complex dielectric constant.

Corrected spectra for each applied pressure are shown in Figure 3.15(a) and Figure 3.15(b) for parallel and perpendicular component, respectively. It can be noticed that the spectral range (1.8-3.5 eV) is reduced with respect to the direct measurement reported in Figure 3.6 and Figure 3.8. As previously observed, the experimentally determined corrections applied to the spectra result in an increase of noise level, particularly in the high energy region. This limits the range of reliability of the present study, preventing any analysis beyond 3.5 eV.

After correction, a higher intensity and a different shape of the spectra can be observed for both polarization. For the parallel component (Figure 3.15(a)), the effect of pressure, besides a red shift, is a clear broadening of all transitions, with a progressive disappearance of the vibronic structure.

The structure at 3.5 eV observed in measured perpendicular reflectance (Figure 3.8) disappears after correction, in the room pressure spectra but an increase of intensity occurs upon applying pressure in the high energy region. This behavior might be attributed to residual chain misalignment and/or to a non perfect data reduction. Any of these effect is particularly evident for this polarization of R due to its intrinsic low intensity. As a consequence, the following discussion will be restricted to the region where perpendicular R spectra exhibit the least spectral dependence.

Finally, attention should be paid in evaluating any spectral features lying below the optical gap of PPV, in the transparency region. As a matter of fact, the model used to obtain the dielectric constants does not take into account multiple reflections arising from the back surface of PPV. Thus, any contribution to reflectance below 2.2 eV and 2.4 eV for parallel and perpendicular component, respectively, must be neglected. In this low energy range, T spec-

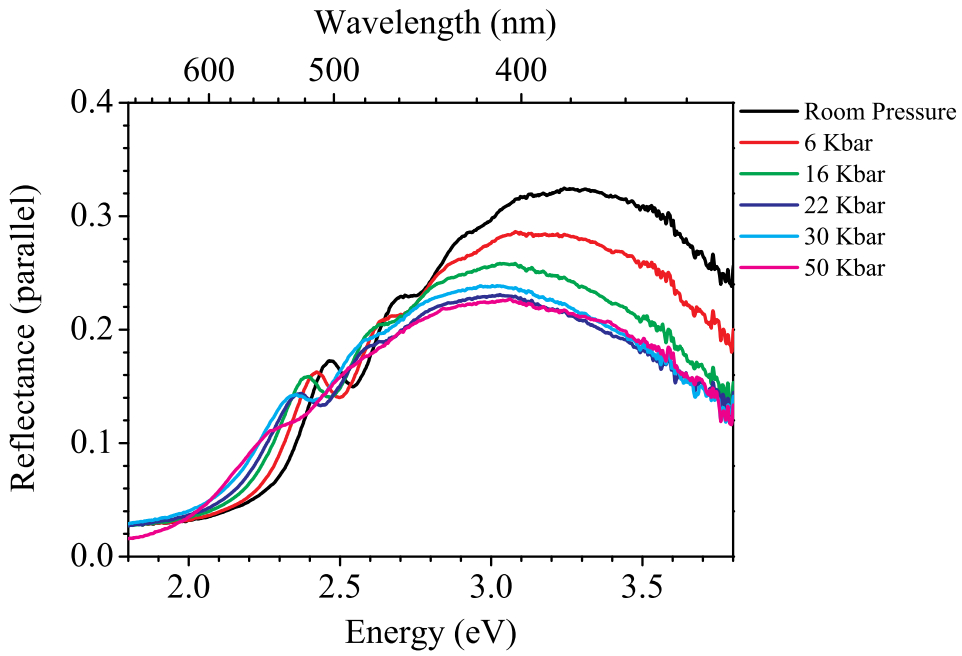

(a) Parallel.

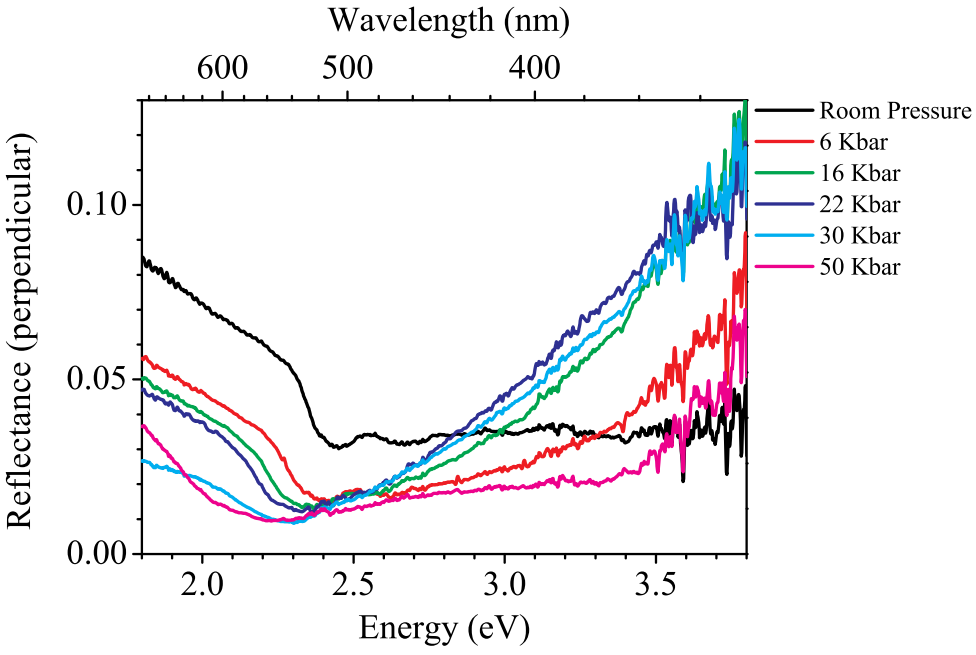

(b) Perpendicular.

Figure 3.15: Parallel (a) and perpendicular (b) reflectance spectra obtained after the manipulations illustrated in Section 3.4.

tra provide all information about the dependence of the absorption onset on applied pressure.

Bearing in mind these observations, a thorough analysis of the behavior of all spectral features of the parallel and perpendicular component of R, will be carried out examining the corresponding dielectric constant and comparing this findings with the parameters used in the fitting procedure.

3.6 A method to determine the dielectric constants

A detailed analysis of the effect of pressure on the photophysical properties of PPV concerning transition energies and broadening cannot arise directly form measured spectra, though corrected to remove diamond-induced distortions. The reason is that reflectivity includes contributions from both the real and imaginary part of the refractive index, which describe a traveling wave and its attenuation with distance, respectively. The physical process occurring when light impinges on PPV is thus fully comprised in the dielectric constants of the material, whose complex components represent the grounds of a meaningful interpretation.

In order to determine the anisotropic optical constants of highly oriented PPV, many methods can be employed. In [92] the complex dielectric constant of highly oriented PPV was determined via a Kramers-Kronig (K-K) transformation of reflectivity spectra joined with ellipsometry, while in [87] a combination of K-K analysis and an interferometric method was used.

In the present work, due to the limited spectral range that could be detected, a direct K-K analysis of the spectra is forbidden and a parametrization procedure has been developed to determine the complex dielectric constants ($\epsilon = \epsilon_1 + i\epsilon_2$) of PPV under applied pressure. The dielectric constants at room pressure and outside the DAC of highly oriented PPV derived in [92] were used as a starting point of the procedure. The imaginary part of the dielectric constant (ϵ_2) measure outside the DAC was expressed as a sum of Gaussians:

$$\epsilon_2 = \sum_{i}^{11} a_i e^{[-(\frac{p_i - x}{\gamma_i})^2]} \tag{3.11}$$

where p_i is the position of the i-th peak, a_i is its height, and γ_i is related to its half width at half maximum (HWHM) by:

$$HWHM_i = \gamma_i \sqrt{ln2} \tag{3.12}$$

Form Equation (3.11), it is in principle possible to determine the real part of the dielectric constant (ϵ_1) using the Kramers-Kronig relations in Equation (1.60). This gives:

$$\epsilon_1 - \epsilon_{inf} = \frac{2}{\pi}\wp \int_0^\infty \frac{x'}{x'^2 - x^2} e^{[-(\frac{p-x}{\gamma})]} dx' \tag{3.13}$$

Such an integral function, however, does not have an analytic form. Therefore, we developed a parametric form of ϵ_1, able to reproduce it over the desired spectral range, without handling its exact integral form. This Kramers-Kronig compatible function contains numeric coefficients set to values that mimicked the real part of the dielectric constant calculated in [92], and takes the form:

$$\epsilon_1 = \epsilon_{inf} + 0.63662 \sum_i^{11} z_i \tag{3.14}$$

where ϵ_{inf} is the high frequency value of the dielectric constant and

$$z_i = \frac{1.876(q_i^2 - x^2)a_i q_i \gamma_i}{(q_i^2 - x^2)^2 + (1.876\gamma_i)^2 x^2} + 6.77 a_i e^{[-(\frac{q_i - 0.05\gamma_i - x}{1.3\gamma_i})^2]} - 6.77 a_i e^{[-(\frac{q_i + 0.05\gamma_i - x}{1.3\gamma_i})^2]} \tag{3.15}$$

being

$$q_i = p_i(1 + 0.225(\frac{\gamma_i}{p_i})^2) \tag{3.16}$$

The parameters p_i, a_i, and γ_i were fitted to determine the best values according to a nonlinear least squares fitting routine for ϵ_2. Consequently, ϵ_1 was simulated using the same set of parameters.

Once ϵ_2 and the parametric form of ϵ_1 were known, the analytic expression of the reflectivity spectrum at room pressure could be obtained through the relation:

$$R = \frac{\sqrt{\epsilon_1^2 + \epsilon_2^2} - n_{dia}\sqrt{2(\epsilon_1 + \sqrt{\epsilon_1^2 + \epsilon_2^2})} + n_{dia}^2}{\sqrt{\epsilon_1^2 + \epsilon_2^2} + n_{dia}\sqrt{2(\epsilon_1 + \sqrt{\epsilon_1^2 + \epsilon_2^2})} + n_{dia}^2} \tag{3.17}$$

Here n_{dia} is the refractive index of diamond as reported in Wase Library. In the spectral range of interest the dispersion of n_{dia} can be expressed as:

$$n_{dia} = 2.41396 - 0.0291x + 0.01461x^2 \tag{3.18}$$

As a test for the procedure, Figure 3.16 shows the result for the parallel component of R recorded outside the DAC, the whole method being applied for both polarizations. The analytic form of R allows now the determination of the dielectric constants for different applied pressures. Each reflectivity spectrum, measured at a different applied pressure, can be fitted with Equation (3.17), that includes both ϵ_1 and ϵ_2. The variables p_i, a_i, and γ_i contained in this expression are the free parameters of the best-fitting procedure. Once the suitable set of parameters has been determined for each applied pressure, it is used to get the optical constant of PPV.

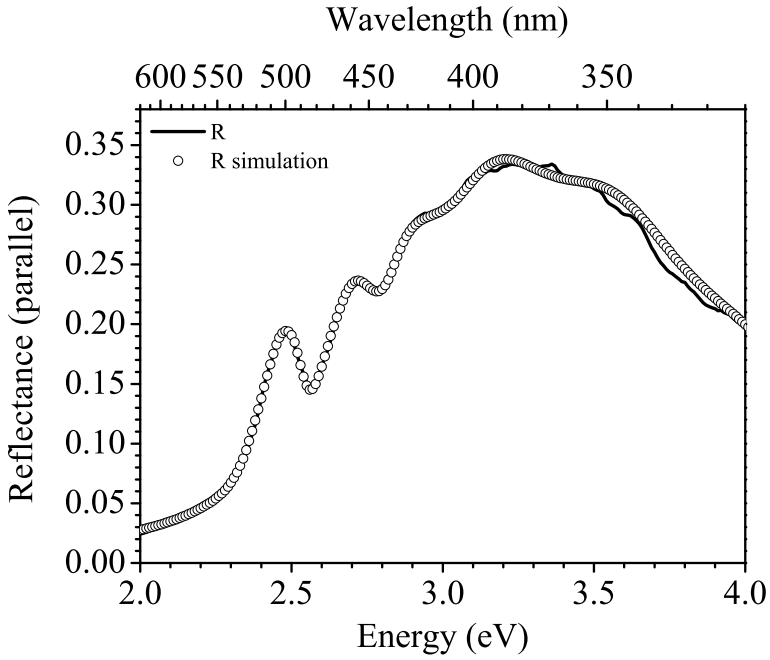

Figure 3.16: Parallel component of R at room pressure reproduced by a Kramers-Kronig compatible analysis.

3.7 Data analysis

3.7.1 Anisotropic dielectric constants

Figure 3.17 shows the real and imaginary part of the dielectric constant (ϵ_1 and ϵ_2 in Figure 3.17 a and b, respectively) with polarization parallel to the chain axis.

Applied pressure induces a red shift of both ϵ_1 and ϵ_2 and a broadening of the vibronic progression, as previously observed for R spectra. In ϵ_1 the lowest energy peak occurs at 2.42 eV (512 nm) while the following peaks are at 2.58 eV (481 nm) and 2.77 eV (448 nm). The $\pi - \pi^*$ transition is detected in ϵ_2 at 2.48 eV (500 nm) at room pressure, and it is followed by its vibronic replica at 2.65 eV (468 nm) and 2.81 eV (441 nm).

In order to determine the rates of shift as a function of pressure of the spectral features observed in the complex dielectric constants components, the second derivatives of ϵ_1 and ϵ_2 were calculated (shown in Figure 3.18 a and b). Here, the peaks in ϵ_1 and ϵ_2 correspond to minima. As pressure increases, the $\pi-\pi^*$ (0-0) peak bathochromcally shifts of -4.4 meV/kbar as determined[3] from the corresponding minimum of $d^2\epsilon_2/dE^2$. This value is comparable, within

[3]The linear fit was performed up to 30 kbar, being the determination of the 0-0 peak less reliable at the highest applied pressure.

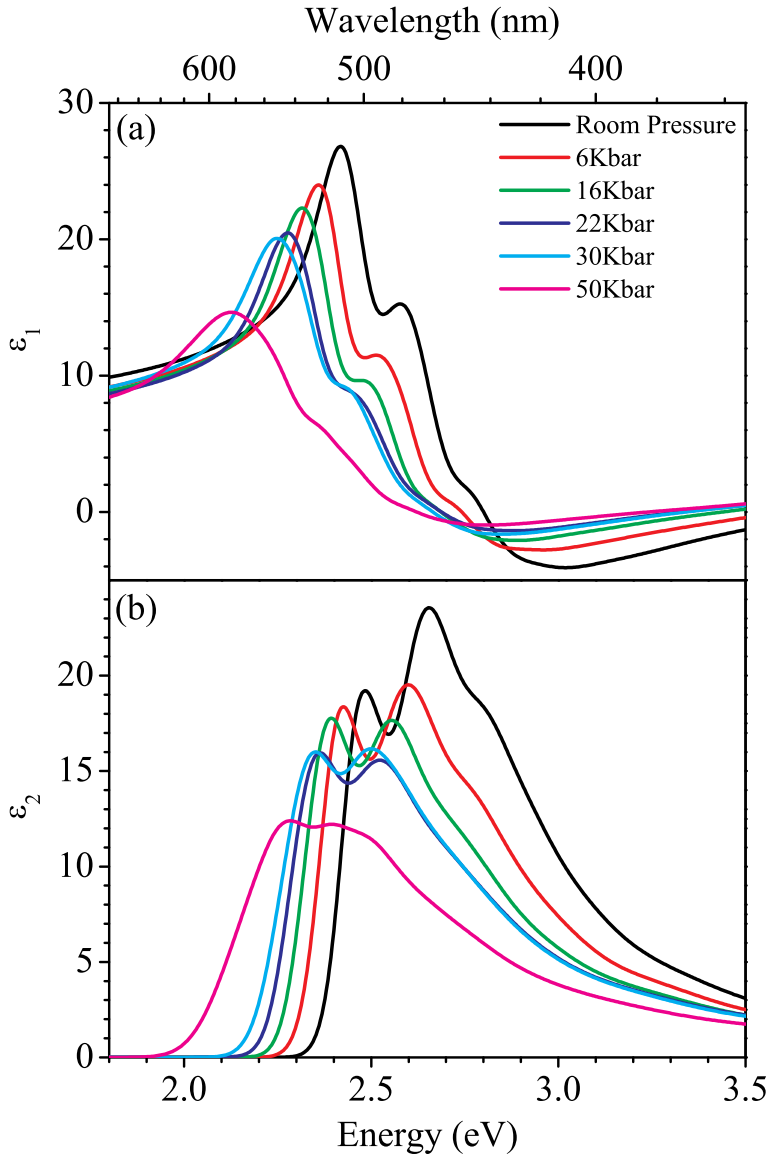

Figure 3.17: Parallel component of the real (a) and imaginary (b) part of the dielectric constant.

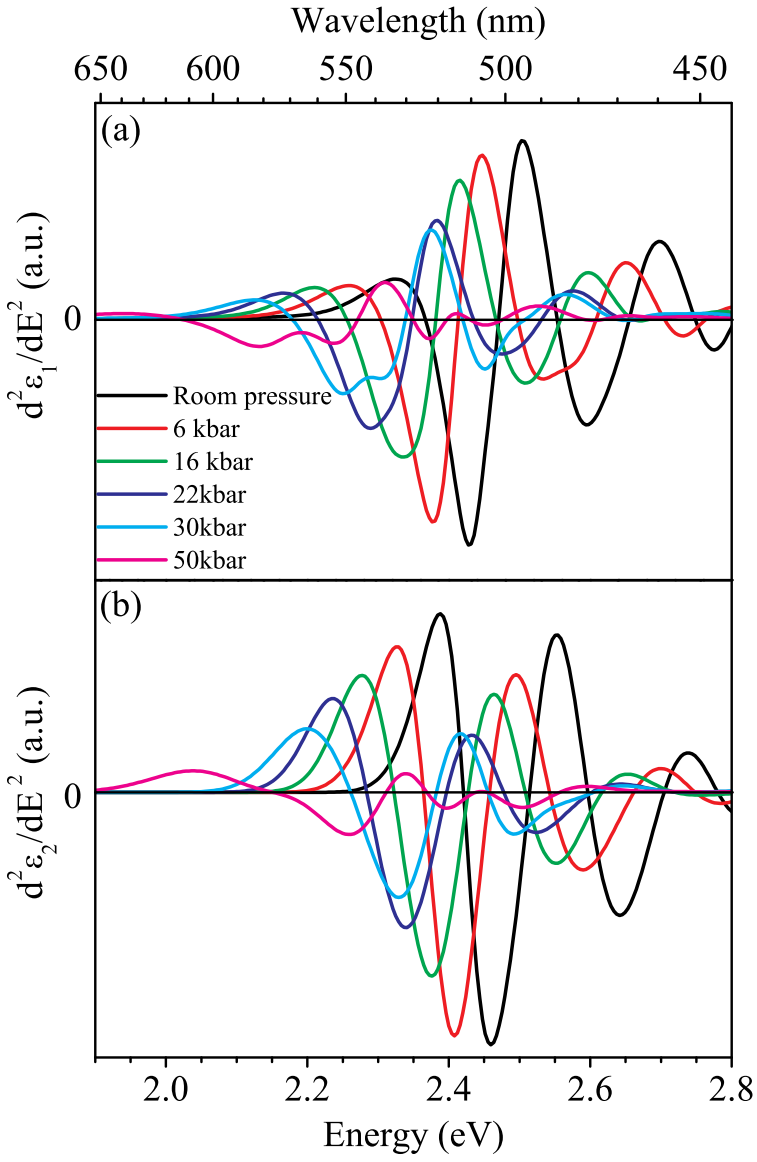

Figure 3.18: Second derivatives of the real (a) and imaginary (b) part of the parallel dielectric constant.

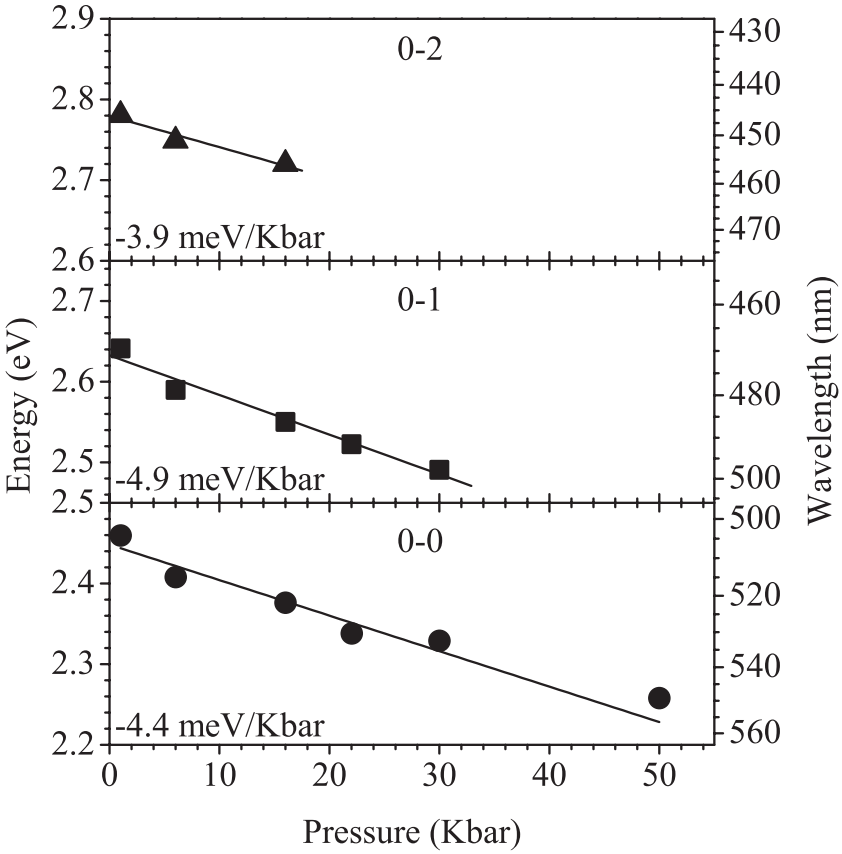

Figure 3.19: Shift of the parallel component of the 0-0 transition and its vibronic replicas as a function of pressure. Peak positions are determined as minima in $d^2\epsilon_2/dE^2$ (Figure 3.18). Linear fits are also shown, with the corresponding slope values.

experimental error, to the previous findings from the analysis of R spectra (Figure 3.6). Similarly, the shifts of the 0-1 and 0-2 vibronic replicas, shown in Figure 3.19, can be obtained.

It can be noticed that the shift of the purely electronic transition is close, but not identical, to those of its vibronic replicas. Discrepancies in the values obtained are mainly due to the prompt disappearance upon applied pressure of the vibronic replicas peaks and to the splitting of all the transitions into a double structure (Figure 3.18) already at 22 kbar, which prevents a clear determination of their spectral position.

An additional effect of pressure clearly detectable form Figures 3.17 is a broadening of both the electronic transition and vibronic replicas. This effect, also observed in R spectra (Figure 3.6), can be attributed to an enhancement of inter-chain interactions as well as to el-ph coupling, as discussed in Section 3.3.2. A quantitative evaluation of the el-ph and inter-molecular interaction will be provided when analyzing the fit parameters in Section 3.7.2.

The analysis of second derivative of ϵ_2 allows a quantitave determination

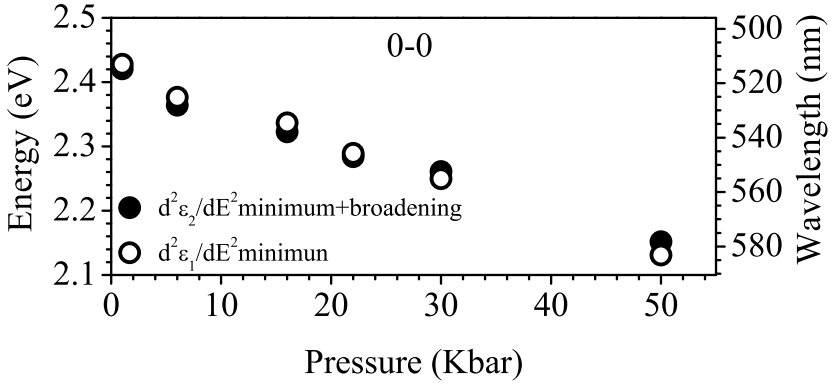

Figure 3.20: Comparison between the shifts the minimum of $d^2\epsilon_2/dE^2$ (-4.4 meV/kbar) plus its broadening (1.33 meV/kbar) and the shifts the minimum of $d^2\epsilon_1/dE^2$ (-5.87 meV/kbar).

of the broadening of the 0-0 transition. The half width of this peak can be approximately evaluated subtracting the energy position of the zero intersection of $d^2\epsilon_2/dE^2$ (corresponding to the change in the slope of ϵ_2) from that of the following minimum (that is, the peak position in ϵ_2). It is found that the half width of the $\pi - \pi^*$ transition varies with pressure with a rate of +1.33 meV/kbar.

Within the Lorentz model, the energy of a transition, corresponding to a peak in ϵ_2, is related to the position of the peak of ϵ_1 by its width. With a similar analysis on the second derivative, the pressure dependence of he minimum of $d^2\epsilon_1/dE^2$ is found to be -5.87 meV/kbar. This rate positively compares with the shift of the minimum of $d^2\epsilon_2/dE^2$ (-4.4 meV/kbar) plus its broadening (1.33 meV/kbar) for all applied pressures as shown in Figure 3.20.

An important effect of pressure can be noticed in the second derivatives of both ϵ_1 and ϵ_2. As pressure increases, the minima corresponding to the electronic transitions highlight a double structure. This phenomenon, particularly evident in $d^2\epsilon_1/dE^2$, can related to the modulation of inter-chain interactions due to the reduction of the separation between neighboring chains. Indeed, this solid state effect is a consequence of a Davydov splitting [1] due to the peculiar crystal symmetry of PPV, with two chains per unit cell. The splitting of the excitonic states is to be expected also at room pressure, and strongly depends on inter-molecular interactions, as accounted for by theoretical *ab initio* calculation of the optical properties of PPV [81]. Though in this case a double structure in the dielectric constants is not evident at room pressure, the splitting becomes clearer and more pronounced when inter-molecular distances are decreased as a result of the applied pressure. This aspect will be further discussed when analyzing the fitting parameters used to obtain the dielectric

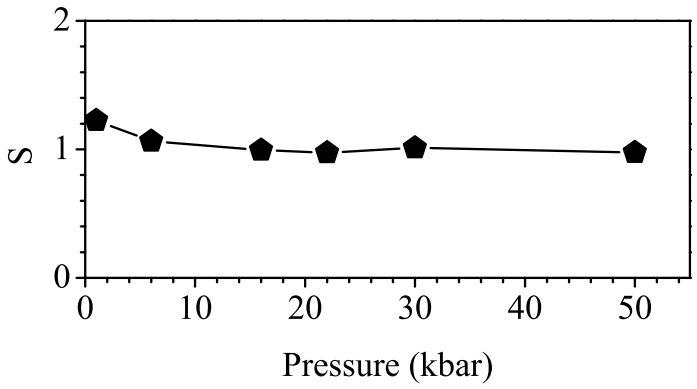

Figure 3.21: Pressure dependence of the energies of the excited state molecular vibrations estimated through the fitting parameters.

constants.

Finally, form ϵ_2 in Figure 3.17, it is also possible to derive the values of the Huang-Rhys factor S defined in Equation (1.89). S is a measure of the coupling between electronic transitions and a phonon modes and it's related to the phonon frequency through the displacement of ground and excited states minima of the potential energy. Figure 3.21 shows the ratios of the 0-1 to 0-0 area for each applied pressure. Upon changing the applied pressure, the Huang-Rhys factor remains constant, with a value close to unity. This observation, together with the previous findings on Raman spectra, where no new band was detected upon applying pressure, further indicates that minor effects due to el-ph interaction occur in the optical properties of highly oriented PPV.

It is interesting to compare this result with recent findings on P3HT [117]. A value close to one was found for dilute solutions of P3HT where the PL spectrum was fit with a Franck-Condon model. For P3HT films, the 0-0 and 0-1 intensities could not be fit with a Franck-Condon progression and a model of weakly interacting H-aggregate proposed. It was assumed S=1 for the film as well, as obtained for non interacting planar polythiophene chains [118].

It is important to observe that the Huang-Rhys factor cannot be reliably obtained form neither the absorption (α) nor the extinction (κ) coefficients. This is particularly evident in highly oriented PPV, where the intensity ratio of the 0-0 to 0-1 transition in these spectra changes dramatically compared to ϵ_2.

A similar analysis can be done also for the perpendicular polarization. The complex dielectric constant derived for this polarization with the procedure described in Section 3.6 is shown in Figure 3.23, while the corresponding second derivative is in Figure 3.24. It is worth recalling that, due to the low intensity of R spectra for this polarization, the perpendicular component of ϵ

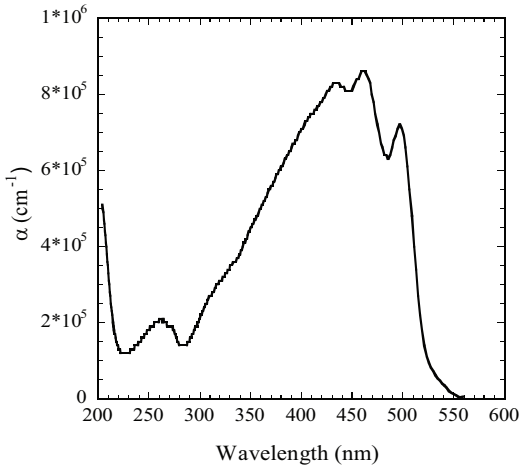

(a) Absorption coefficient α.

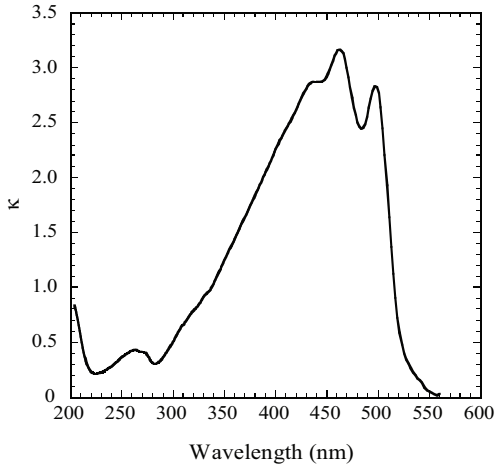

(b) Extinction coefficient κ.

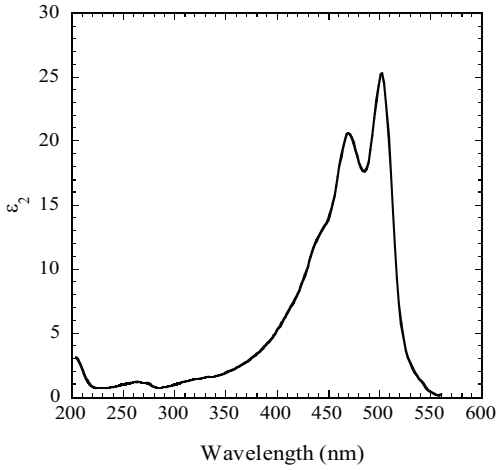

(c) Imaginary part of the dielectric constant.

Figure 3.22: Absorption coefficient α (a), extinction coefficient κ (b), and imaginary part of the dielectric constant (c).

are intrinsically affected by a grater uncertainty than the parallel counterparts. In particular, in both ϵ_1 and ϵ_2 two structures can be detected around 2.5 eV. that reflect the behavior of R perpendicular and are thus likely to be due to chain misalignment. This attribution is confirmed by their shift rated with applied pressure (Figure 3.25), very close to that of the parallel component of the $\pi - \pi^*$ transition (Figure 3.9).

It can be notice that the behavior of ϵ_2 as a function of pressure is very different with respect to the other polarization (Fig. 3.11b). In particular, while the parallel component of ϵ_2 (Figure 3.17) at high energies decreases with increasing pressure, the perpendicular component of ϵ_2 shows a strong enhancement. This means that, at high energies, transitions polarized along the chain axis are hindered, those with perpendicular polarization gain inten-

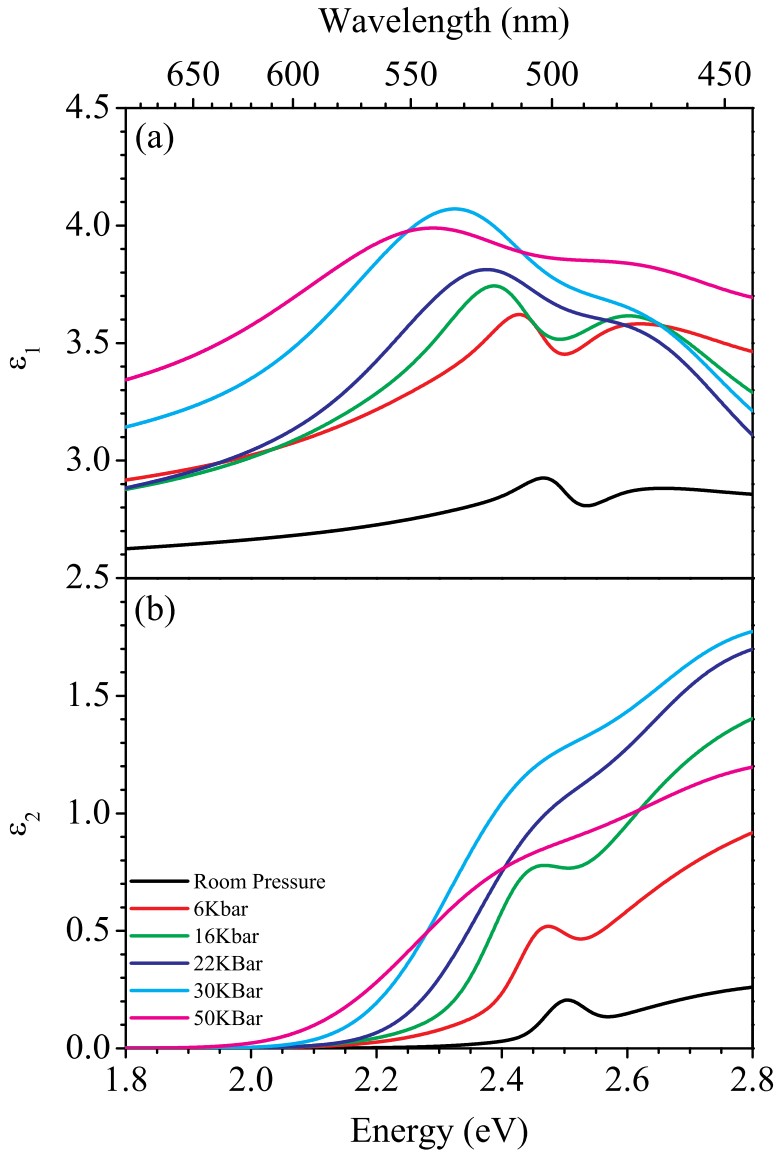

Figure 3.23: Perpendicular component of the real (a) and imaginary (b) part of the dielectric constant.

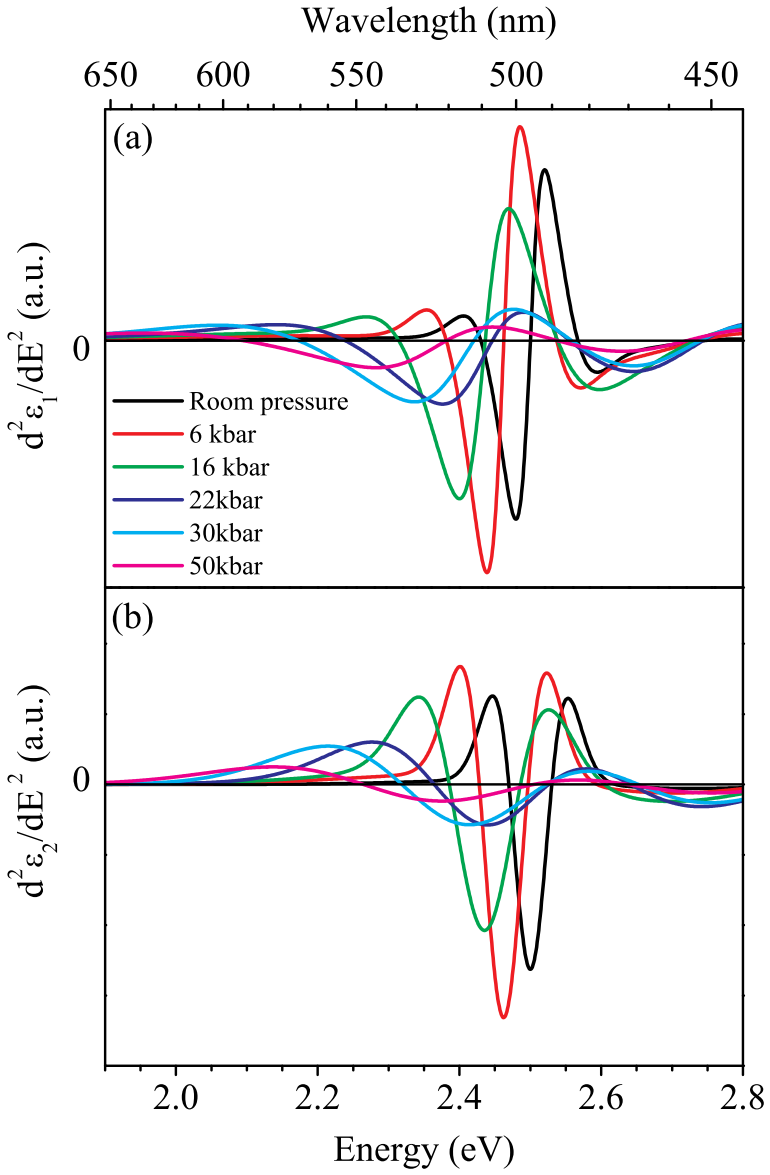

Figure 3.24: Second derivatives of the real (a) and imaginary (b) part of the perpendicular dielectric constant.

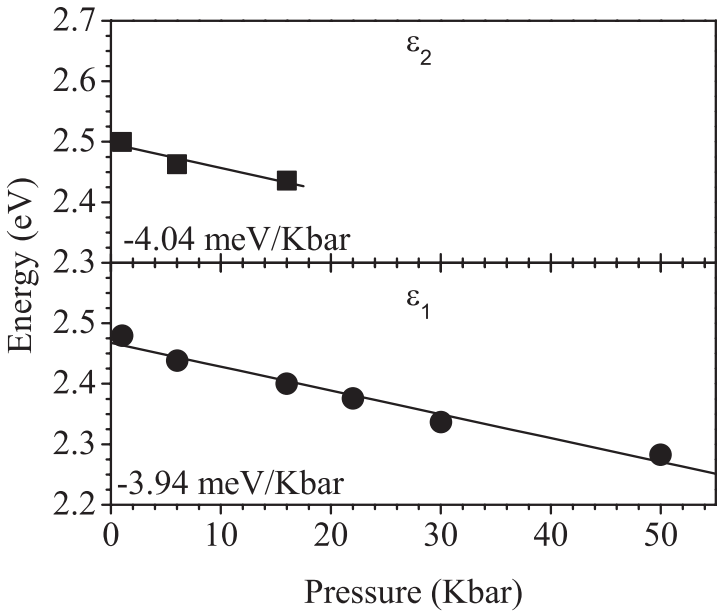

Figure 3.25: Shift of the perpendicular component of the 0-0 transition as a function of pressure detected in ϵ_1 and ϵ_2. Peak positions are determined as minima in $d^2\epsilon_2/dE^2$ (figure 3.18). Linear fits are also shown, with the corresponding values of the slopes.

sity. A particularly interesting physical interpretation of this will be discussed in terms of oscillator strength in Section 3.7.3.

3.7.2 Analysis of the fit parameters

The previous analysis of the second derivatives of the dielectric constant provided information on the pressure dependence of the main spectral features such as the lowest energy electronic transition and its vibronic replicas. However, though overall correct pressure dependencies were achieved, the details of the individual states were lost. Further insight on the role of intermolecular interactions can be gained considering the behavior of the fitting parameters characterizing each curve describing the electronic and vibronic transitions upon applied pressure. As a matter of fact, 11 Gaussians were used to simulate ϵ_2 with the parametrization procedure described in Section 3.6. The number of Gaussians (hence the number of fitting parameters) was chosen to be the minimum allowing to mimic R for each applied pressure. In the following, we will analyze the pressure dependencies of the best-fit parameters for the parallel component only, whose reliability allows a deeper and meaningful interpretation of the detailed spectral features here discussed.

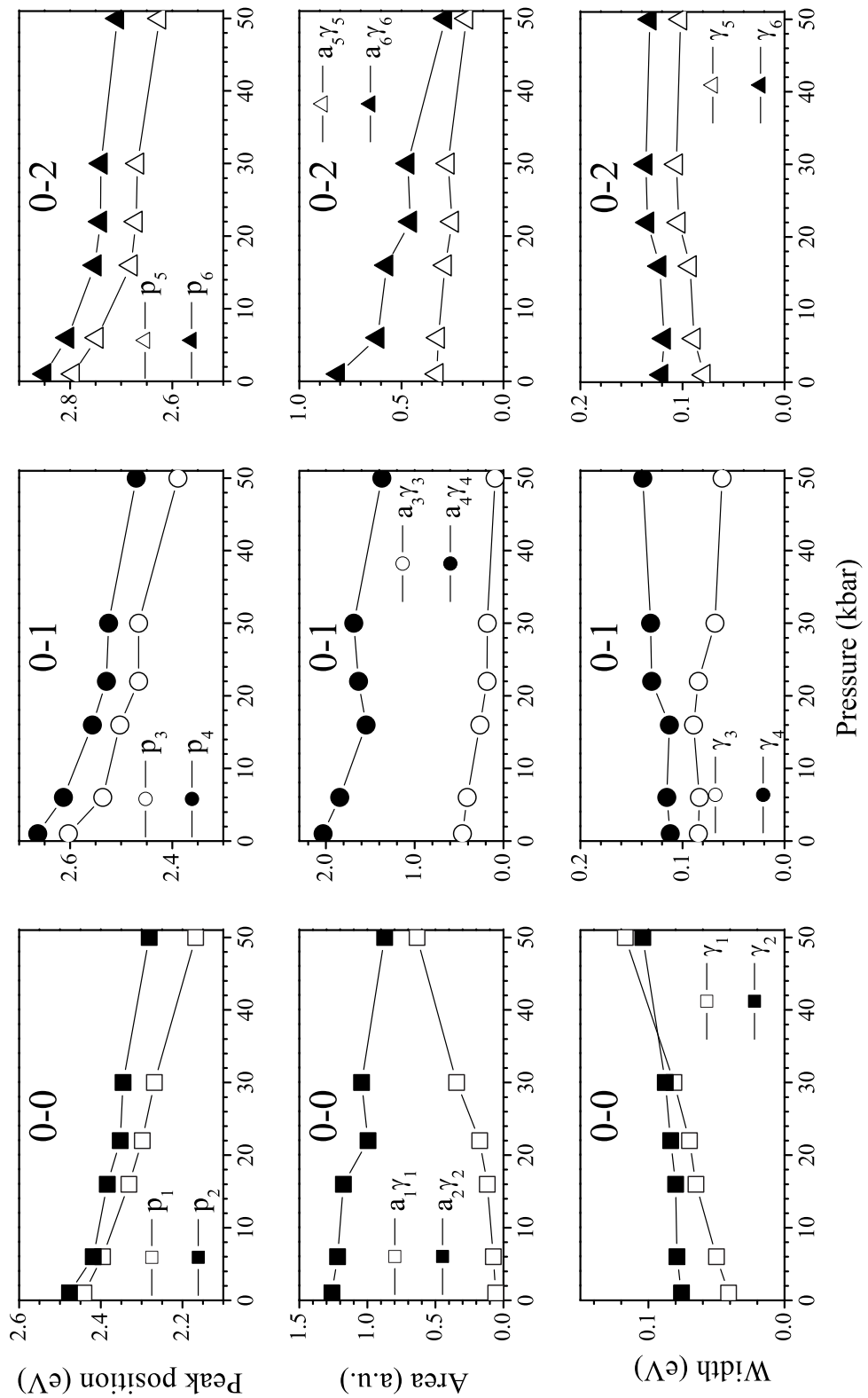

Figure 3.26: The fitting parameters corresponding to 0-0, 0-1, and 0-2 transitions as a function of pressure. The white (black) symbols refer to the lowest (highest) energy component of each doublet.

As described in Section 3.6, each R spectrum recorded at a specific pressure was fitted using a parametric form. The sets of parameters reproducing R allowed to obtain the dielectric constants for each applied pressure. Since ϵ_2 was expressed as a sum of 11 Gaussians (Section 3.6), these parameters will be referred to as belonging to the *i-th* curve, where i goes form 1 to 11 in order of increasing energy.

Recalling the remarks concerning the reliability of the spectral range (Section 3.4), we limit the present study to those parameters describing the energy, area, and width of the Gaussians corresponding to the 0-0, 0-1, and 0-2 transitions. Six out of the eleven Gaussians will be taken into account, that can be separated into three pairs.

Figure 3.26 shows the pressure dependence of the parameters p_i ($i = 1 \div 6$) corresponding to the energy positions of the *i-th* peak of the Gaussian in ϵ_2, of γ_i, which refers its width, and of $a_i\gamma_i$ evaluating the area underneath each curve. It's worth noticing that *two* curves, not just one, were necessary to reproduce the $\pi - \pi^*$ transition and its vibronic replicas, even at room pressure. This requirement becomes more and more pressing upon increasing hydrostatic pressure. We interpret this fact as a proof of the existence of intermolecular interactions, in agreement with the previous findings on the second derivative analysis of ϵ_2 (Section 3.7.1), where a Davydov splitting of the electronic transition was suggested.

As pressure increases, the values of p_i with $i = 1$, 2 move towards lower energies with dissimilar shift rates, being the shift of p_2 greater than that of p_1. Moreover, the subtended areas tend to balance for higher pressures and both curves became broader. In Figure 3.26 it is clear that at room pressure, the purely electronic transition 0-0 is mostly entirely due to the high-energy Davydov transition (p_2). When applied pressure increases, the oscillator strength of the lower-energy transition (i = 1) increases at the expense of the higher one (Figure 3.26). As a result of pressure, the splitting occurring between the two Davydov components describing the 0-0 peak becomes more pronounced when inter-chain spacing is reduced, confirming the major role of inter-chain interactions in highly oriented PPV. The role of inter-chain coupling in PPV (in both isolated chain and crystalline packing) investigated with *ab initio* calculations of the optical properties for [52], showed that the lowest correlated states of the PPV crystal involve more than one chain and are very dependent on crystal structure. In particular, due to inter-chain interactions and symmetry effects, the lowest electronic excitation is a dark exciton, which is optically inactive but provides a nonradiative decay path. These results are consistent with the findings on oriented PPV presented here.

The strength of the inter-chain coupling, as estimated from the Davydov splitting, amounts to about 100 meV at 50 kbar. In this respect, it is interesting discussing a recent study on regioregular poly(3-hexylthiophene) P3HT [117], a highly ordered material characterized by a lamellar structure. Here, a weakly interacting H-aggregate model was proposed to explain the variation of the

relative absorbance of the 0-0 and 0-1 vibronic peaks and to extract a magnitude of the intermolecular coupling energy of approximately 5 and 30 meV, depending on the solvent.

The results described so far for oriented PPV might suggest that an increase of inter-chain coupling causes a transition from an H-type (where the 0-0 transition is allowed) towards a J-type aggregate (where the 0-0 transition is forbidden). As a speculation, this change could be ascribed to a geometrical re-arrangement of adjacent chains, which modifies the interaction between them. However, drawing such a similarity is not straightforward: the nanomorphologies of the two material are rather different, and do not allow any simple comparison. Furthermore, any other evidence corroborating the idea a "phase" transition occurred due to applied pressure (for instance, x-ray diffraction), is still lacking.

Observations similar to those for the purely electronic transition hold true for the second vibronic replica (0-2), which corresponds to peaks i=5, 6. Instead, the parameters p_i (i = 3, 6) relative to the first replica, red shift upon applying pressure in a similar fashion. The splitting observed for the purely electronic transition is not clear for this vibronic replica, which is strongly affected both from lower and higher energy Gaussians reproducing neighboring transitions.

A comparison with the previous findings can be made considering the behavior of each pair as a whole. This can be done computing the total subtended area as the sum of the single curve area. The total area can then be used to weight the energy peak positions of 0-0, 0-1, and 0-2 and to calculate the HWHM as follows:

$$p(0-n) = \frac{p_i a_i \gamma_i}{a_i\gamma_i + a_j\gamma_j} + \frac{p_j a_j \gamma_j}{a_i\gamma_i + a_j\gamma_j} \tag{3.19}$$

$$A(0-n) = a_i\gamma_i + a_j\gamma_j \tag{3.20}$$

$$HWHM(0-n) = HWHM_i \frac{a_i\gamma_i}{a_i\gamma_i + a_j\gamma_j} + HWHM_j \frac{a_j\gamma_j}{a_i\gamma_i + a_j\gamma_j} \tag{3.21}$$

where n is either 0, 1, or 2, $HWHM_i$ is given by Equation (3.12), and i and j refer to either of the two Gaussians reproducing each transition. The results are reported in Figure 3.27. The weighted peak positions and HWHM of both the electronic transition and its vibronic replicas confirm that a red shift and broadening occur when pressure increases.

We can now exploit the pressure dependence of the fitting parameters to evaluated both W_{el-ph} and W_{inter}. According to Kasha [114] we evaluate the electron-phonon coupling with the phonon energy, namely subtracting the energy of the peak p_1 from that of p_3. The el-ph bandwidth as a function of pressure is reported in Figure 3.28. It is more difficult instead to find W_{inter}, which is hidden underneath the full width half maximum of the 0-0

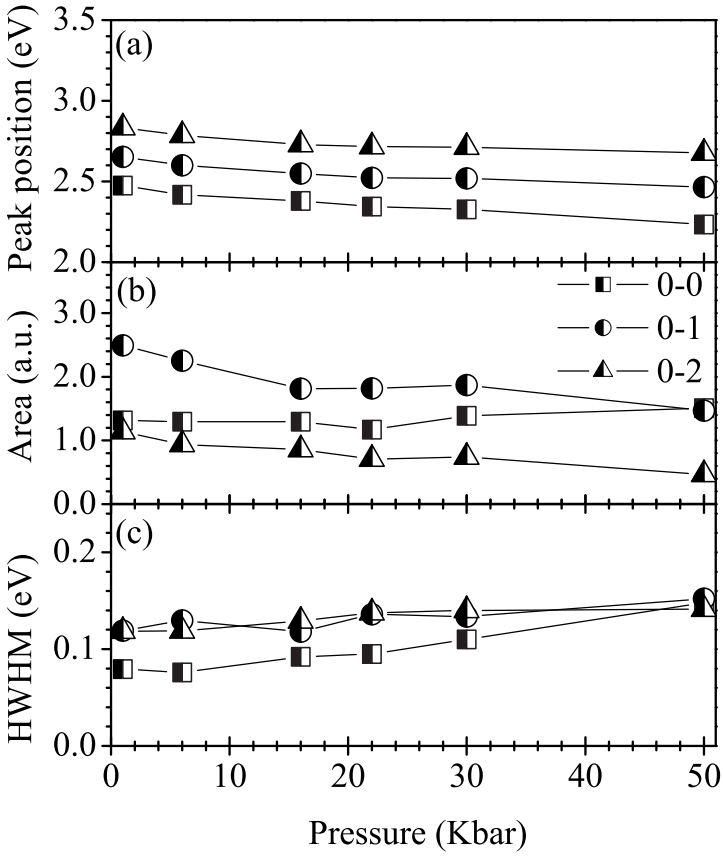

Figure 3.27: Weighted positions (lower panel), total area (middle) and weighted HWHM (upper panel) of the parameters corresponding to 0-0, 0-1, and 0-2 transitions.

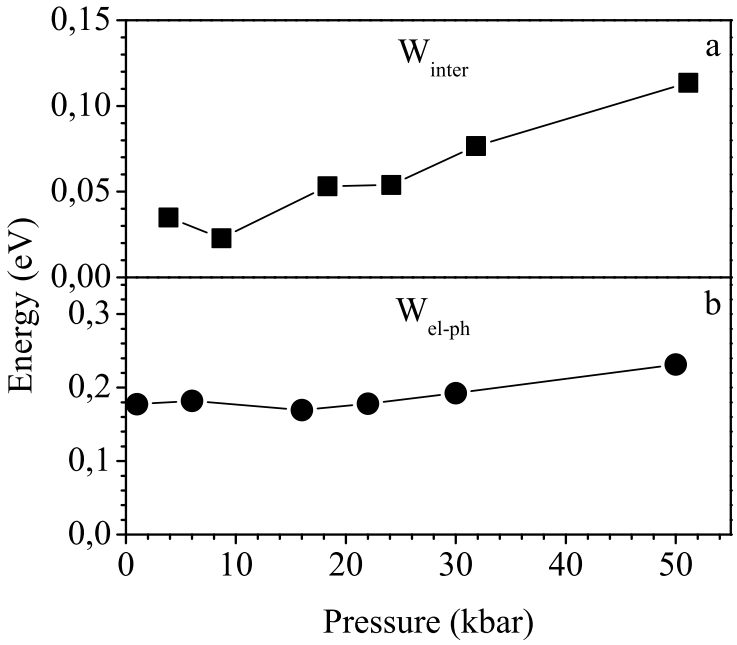

Figure 3.28: Pressure dependence of the el-ph and inter-chain interactions bandwidth.

line and its inhomogeneous broadening. A hint to solve such a problem comes from the analysis of the fitting parameters so far described, noticing that the R parallel spectrum is best fitted when the dielectric function is composed by two oscillators for each peak of the vibronic progression. We assume the separation of these two oscillators for the 0-0 peak of ϵ_2 as the value of Winter. The result is also shown in Figure 3.28.

At room pressure we get $W_{el-ph} = 0.18$ eV and $W_{inter} = 0.035$ eV. Then, at room pressure, W_{inter}/W_{el-ph}=0.19, implying a weak coupling regime. Upon increasing pressure, from the hardening of phonons, we can derive $W_{el-ph} \sim$ 0.23 while Winter is strongly enhanced up to a value of 0.113 eV, which results in W_{inter}/W_{el-ph}= 0.5 i.e. a weak/intermediate coupling regime. The evolution with applied pressure of such a ratio is reported in Figure 3.29. As a consequence, we deduce that upon applying pressure, intermolecular interactions play an incresingly important role being responsible for broadening in the optical spectra of the parallel polarization, even though a contribution from el-ph coupling cannot be completely ruled out. In particular, evidence of inter-chain interaction is found in the existence of a double structure underneath each transition in the parallel component of ϵ_2

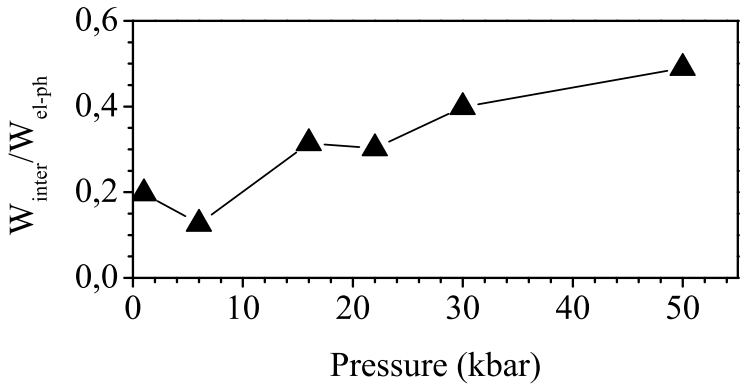

Figure 3.29: Pressure dependence of the ratio between the el-ph and inter-chain interactions bandwidth.

3.7.3 Oscillator strength

Additional information on the electronic structure of oriented PPV can be obtained by discussing the oscillator strength for parallel and perpendicular polarized transitions. Within the quantum theory of absorption and dispersion, the sum rule for the oscillator strength of optical transitions in a solid is provided by Equation (1.64):

$$\frac{m}{2\pi^2 N_c e^2}\int_0^{\omega_x} \omega\epsilon_2(\omega)d\omega = f(\omega_x) \tag{3.22}$$

where C is the carbon atom density (sixteen in an orthorhombic crystallographic cell 8.07x5.08x6.54 Å^3) [119], e the electronic charge, m its mass. Equation (1.64) relates the optical constants with the oscillator strength f of the optical response within the frequency x. The plots of the oscillator strength as a function of x are reported in Figures 3.30(a) and 3.30(b) for the parallel and perpendicular polarization, respectively.

Even though a complicate mathematical treatment has been done on the rough data in order to obtain ϵ_2 and then some approximations are implicit in our spectra, Figure 3.30(a) clearly indicates that for the parallel component an isosbestic point occurs around 2.75 eV (451 nm). The oscillator strength for electronic transitions having energy up to the isosbestic points is conserved for all pressures with a different spectral spread. At room pressure, when the system is closer to a single chain behavior, the oscillator strength is achieved with a sharp structure. Upon increasing pressure the same oscillator strength is distributed in a wider spectral range due to red-shift and broadening of transitions. For photon energies above the isosbestic point, the oscillator strength decreases upon applying pressure. Very different is the case of the perpendicular polarization (Figure 3.30(b)). Even though for this component of the

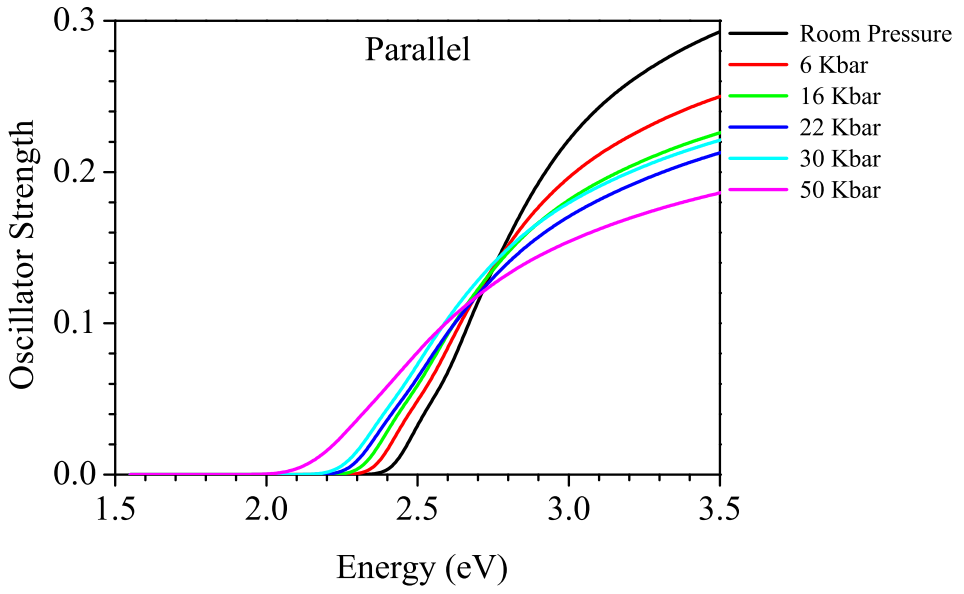

(a) Parallel component.

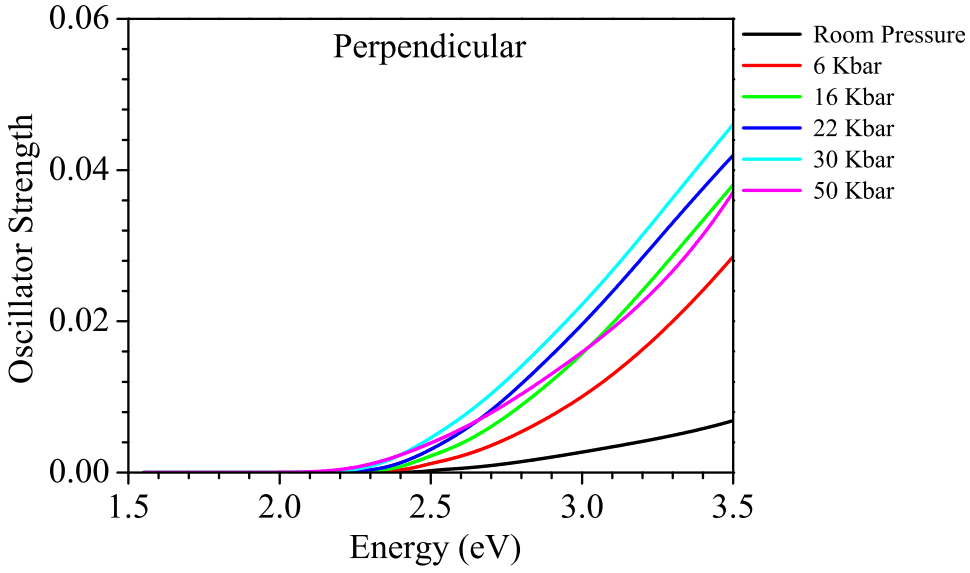

(b) Perpendicular component.

Figure 3.30: Oscillator strength derived by numerical integration of parallel (a) and perpendicular (b) components of ϵ_2.

optical constant, the role of approximation used in the data reduction is more relevant, an unambiguous trend is observed. The oscillator strength increases upon increasing applied pressure. Since the overall oscillator strength should be preserved, we deduce that an oscillator strength transfer from parallel to perpendicular polarization occurs, in particular for the highest energy spectral range. We interpret this transfer as an evidence of the effect of intermolecular interactions, which increase the system dimensionality. These data clearly show that applied pressure modifies the electronic structure of PPV giving rise to new dipole allowed transitions having a different polarization, namely parallel below the isosbestic point and perpendicular above it. We notice the internal consistency of our data, for which the overall oscillator strength (calculated as parallel plus two times perpendicular) is lower than one. The oscillator strength lacking to reach the value 1, which indicates the contribution of all the carbon π-electrons, can be due in part to the approximations used but in particular to the limited spectral range analyzed with quantitatively reliable anisotropy. As a matter of fact, π-electrons in PPV derivatives give rise to optical transitions up to 6-7 eV [84, 92, 120–122]. Comparison with theoretical calculations are at present very difficult since ϵ_2 spectra are reported only for molecular crystals like fluorene [123] or para-terphenyl [124] in their different phases. No anisotropic imaginary part of dielectric constant spectra or oscillator strength data have been so far reported. It is also difficult to extrapolate from molecular crystal calculations any information for corresponding polymers due to both different crystallographic structures and role of conjugation length, which was qualitatively elucidate by quantum chemical calculations [125, 126].

3.8 Conclusions

In this Chapter, we described and discussed the effect of a hydrostatic pressure on the optical properties of oriented PPV. Different spectroscopic techniques were employed to study the variation induced by tuning inter-chain interactions. Raman scattering allowed to prove that minor effects due to the pressure-induced extension of conjugation length occur and that order in oriented PPV is not significantly improved by pressure. Thus, we conclude that, while usually the main effect of pressure in amorphous polymeric systems have an intra-molecular origin, in our case main effects seems to be due to intermolecular interactions, which bathochromically shift the $\pi - \pi^*$ transition.

The development of a suitable optical model allowed to obtain form reflectance spectra the complex dielectric function of oriented PPV for all applied pressures. A careful analysis of the dielectric constants shows that for parallel polarization electronic transitions below 2.75 eV gain intensity while those at higher energies show a reduced oscillator strength. For perpendicular polarization, a generalized increase of oscillator strength in observed in all the spectrum indicating that this component is not only due to chain misalignment

but also to intermolecular interactions. The broadening of vibronic progression has been qualitatively assigned to a splitting of electronic states due to intermolecular interactions even though a not negligible contribution form el-ph interaction in the intermediate coupling regime have to be considered.

Chapter 4

Pump/probe spectroscopy on MEH-PPV under pressure

In this Chapter, a study of the effects of high pressure on the photophysical properties of a soluble substituted of PPV, namely MEH-PPV, is presented. Continuous-wave photoinduced absorption spectra allow to probe the pressure dependence of long-lives species such as triplet exciton and trapped polarons. The influence of pressure on the emission properties of MEH-PPV and on the triplet lifetime was also monitored. The primary photoexcitation in MEH-PPV and their behavior as a function of pressure were recorded using an ultrafast two color laser system. Polaron generation and singlet exciton transition were measured with a time resolution of 150 femtosecond in the IR spectral region with a probe energy ranging from 0.28 to 1.10 eV.

4.1 Introduction

Photoexcitations in conjugated polymers in general and PPV-based systems in particular have been extensively studied by both experiment and theory. Despite the general consensus that the primary photoexcitations in dilute solutions are intra-chain singlet excitons [17–20], the nature of the elementary species in films is still widely debated [21]. The controversy concerning the origin of the primary photoexcitations reflects the lack of understanding of interaction between adjacent polymer chains. A wide variety of possible species (labeled as excimers [10–12], aggregates [13, 14], polaron pairs [15, 16], and exciplexes [10]) has been proposed to explain the differences between the optical spectra of dilute solutions (where excitations are expected to have an intra-chain character) and thin films.

One controversy in particular, concerns the underlying mechanism of charge carrier (polaron) photogeneration (PG) in MEH-PPV. Sheng *et al.* have shown that in films [127] a relatively weak transient photoinduced absorption (PA) band in the mid-IR spectral range ($\sim$ 0.4 eV) is instantaneously generated

along with the PA band of the singlet excitons (at $\sim$ 0.9 eV). The 0.4 eV band was assigned to photogenerated polaron-pairs on neighboring chains based on the peak position and associated with charge excitations on the chain due to some correlation with photoinduced infrared active vibrational (IRAV) modes [128]. The reduction PL quantum efficiency, as well as various nanoprobe images [24], allowed to deduce that the degree of inter-chain interaction in MEH-PPV films sensitively depends on the solvent used in casting the film. It was subsequently found that film nanomorphology deeply influences the PG efficiency of the polaron species in MEH-PPV films [127]. It can thus be concluded that carrier PG mechanism in PPV polymers depends on the chain packing in the solid state [127]. Figure 4.1 recalls the primary photoexcitations occurring in MEH-PPV within their respective manifolds. Their spectral signatures, also shown, will be discussed throughout the Chapter.

Although all mentioned observation point out the crucial role played by inter-chain interactions in the formation of photoexcited species, a direct demonstration that charge PG in polymer films mainly depends on intermolecular coupling is still missing. Variations of the optical properties depending on the processing history (choice of the solvent or thermal annealing) of both the film and the solution from which it is cast do not allow a straightforward rationalization. Indeed, the strong dependence of the photo-generated species on the peculiar film morphology is the origin of many contradictions between literature data. For instance, estimations of the fraction of photoexcitation that result in inter-chain species range from practically zero [22] to 90 % [23]. Furthermore, a clear description of the role of inter-chain interaction on the polymer photophysics in the solid state, such as aggregates formation, charge transport and exciton migration, is still lacking.

The formation and nature of inter-chain species are critical issues for device design and optimization. Although charge transport might benefit form inter-chain coupling, the presence of weakly emissive inter-chain states may lead to significant PL quenching in films. In particular, device efficiency may depend on the ratio η of charged (polarons) to neutral (excitons) photoexcitations following photon absorption. Specifically, solar cell and solid-state photodetectors are improved if η is large. In contrast, for OLEDs it is preferable to use polymers with small.

It is thus obvious that the role intermolecular coupling is fundamental in order to establish the nature of the primary photoexcitations in conjugated systems, and to determine their influence on emission properties. Although a variety of optical probes have been applied to the class of π-conjugated polymers for over two decades, in the majority of previous studies, tuning of the intermolecular interaction in the material has often relied upon chemical modifications (variation of side groups length), or modified film processing conditions (solvent or thermal treatment) [24]. Applying hydrostatic pressure is instead a clean, simple method to probe intermolecular interactions of a material for a range of intermolecular distances without such alterations. Previous

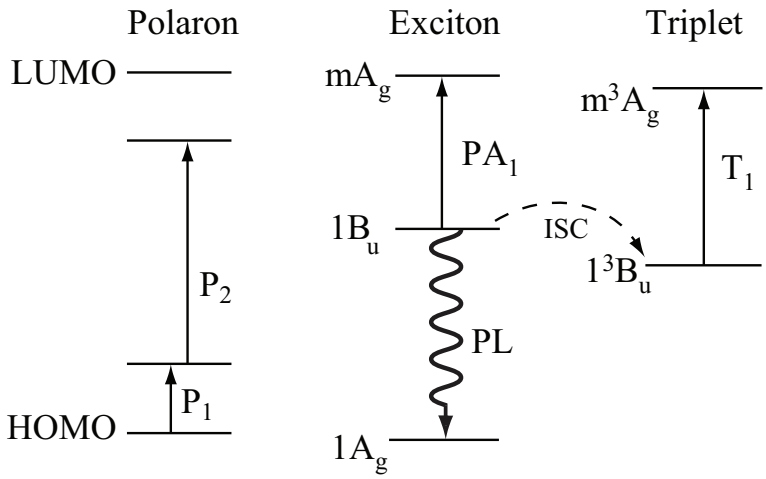

Figure 4.1: Primary photoexcitations occurring in MEH-PPV within their respective manifolds.

high pressure optical studies of π-conjugated polymers used optical absorption and reflection, photoluminescence, Raman scattering and transient and continuous wave (cw) photomodulation [79, 129–137]. Since pressure enhances intermolecular interactions and also changes intramolecular conformation (such as planarization, for example [131–133]), it has been difficult to separate these two effects [136]. This is especially true since cw spectroscopies mainly probe the lowest lying available states in the polymer chains, thus missing the direct pressure effect on the primary photoexcitations, which might be more sensitive to high pressure.

4.2 Steady state spectroscopy

4.2.1 Photoluminescence

When a polymer is photoexcited with an energy within the absorption band, the excition that forms may decay either radiatively, via symmetry allowed transitions, or non radiatively. In the former case, typical emission spectra exhibit a clearly resolved vibronic progression. Vibronic structures are instead usually absent in absorption spectra of disordered polymers, where inhomogeneous broadening due to a distribution of conjugation lengths leads to a broad and featureless optical absorption. On the other hand, emission originats solely form the lower energy chain segments, with longer conjugation length. It is Stokes shifted with respect to absorption and has a reduced inhomogeneous broadening, showing a well resolved vibronic progression. This is the case for MEH-PPV, whose photoluminescence spectrum at 300 K and 30 K is shown in Figure 4.2.

In the room temperature PL spectrum, the 0-0 electronic transition and its 0-1 and 0-2 vibronic replicas are detectable, and located at 2.05, 1.96, and

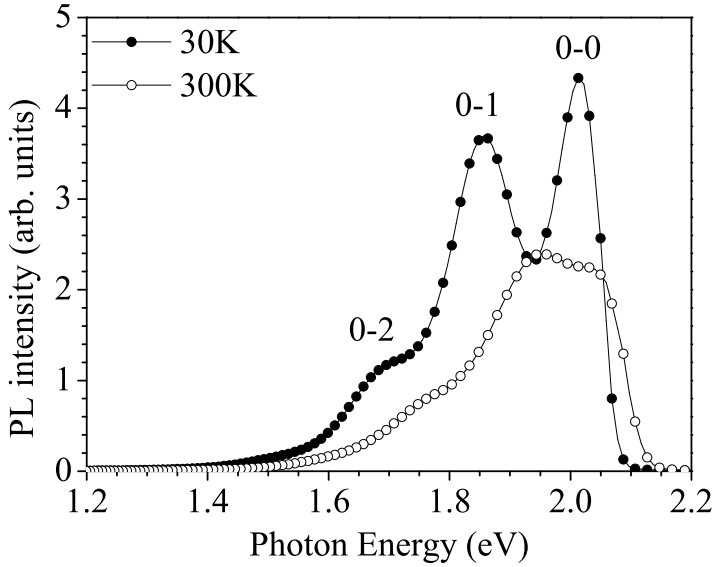

Figure 4.2: Room (open symbols) and low (solid symbols) temperature PL of a film MEH-PPV at room pressure.

1.80 eV, respectively, as determined with a Gaussian fitting. PL is dominated by the 0-1 vibronic transition.

Low temperature PL is red shifted with respect to the room temperature spectrum by 40 meV, owing to the suppression of thermal disorder at low temperatures. Moreover, the spectrum shows clearly resolved spectral features corresponding to the 0-0, 0-1, and 0-2 vibronic transitions, positioned at 2.01, 1.87, and 1.70 eV, respectively.

Figure 4.3 shows the PL spectrum of MEH-PPV for different applied pressures. A strong reduction of PL can be observed both at room and low temperature (Figure 4.3(a)). In particular, at 30 K PL intensity deceases by 60% form 4 to 51 kbar[1]. PL quenching is indeed a dramatic effect of pressure observed in polymers, both in the amorphus and crystalline phase [79, 130, 138, 139]. Various possible mechanisms are evoked to account for the decrease of PL intensity. An increase of the exciton mobility to quenching sites due to the improved degree of conjugation that facilitates the motion of the exciton along the polymer chain was suggested to contribute to both the red shift and decrease of PL in polythiophene [130] and m-LPPP [140]. In sexithiophene single crystals PL quenching was attributed to the decay of the primary photoexcitations into non emissive inter-chain species [139]. Variations in PL quantum yield were already observed in MEH-PPV and related to different chain confor-

[1]PL intensity fluctuations in the room temperature spectra are likely to be due to laser instability.

mations depending on the specific solvent used [141]. Photoluminescence and wavelength-dependent excitation indicated formation of aggregates in MEH-PPV. The overall PL quantum yield was found to depend both on polymer conformation and on aggregation due to polymer concentration.

It is important to notice that in the spectra of Figure 4.3, not only PL is quenched, but in addition it also gradually loses the 0-0 phonon satellite at high pressures. This indicates that the 0-0 transition changes its symmetry with pressures. Such a symmetry change indicates that the PL at high pressures originates from aggregates that are formed in the film, where the 0-0 transition is strictly forbidden in case of H-aggregates [142]. Aggregates formation in solution was already observed in MEH-PPV [141] and recently it has been suggested [143] that aggregates act as shallow traps for both electrons and hole, serving as non-radiative recombination centers in MEH-PPV light emitting diodes. Since the cw photophysics is sensitive to the lowest state available, we believe that the PL at high pressures are from excitons trapped in aggregates that are formed due to the increased inter-chain interaction.

A clear red shift of PL is observed both at room and low temperature and can be estimated determining the center at half maximum of each PL spectrum as a function of pressure. A non linear dependence of the center of PL was previously found for MEH-PPV in [138], where the PL energy decrease with pressure was fit with a quadratic function ($E_{PL} = -11P + 0.11P^2$, being E_{PL} expressed in meV and P in kbar). The pressure dependence of the center of PL is shown in the insets of Figure 4.3(a) and 4.3(b), along with a quadratic function ($E_{PL} = -10P + 0.11P^2$), close to the one previously found in [138]. A linear fit (~ -2 meV/kbar) of the data is also reported, which helps comparing the red shift of PL for MEH-PPV to that of other polymers.

A linear pressure dependence of PL was indeed found for different polymers such as polyacetylene [89], polythiophene [130], m-LPPP [132], PHP [73], with values ranging form 2 to 6 ∼meV/kbar. Higher pressure dependencies are usually observed for polymers with non planar configurations. The observed pressure induced red shift of PL is explained as a superposition of several effects. Conformational changes deriving from planarization of the backbone chains increase the overlap between π-electron orbitals, thus decreasing the HOMO-LUMO gap. The decrease of the absorption band gap as a consequence of enhanced inter-chain interactions and its relation with PL red shift have been investigated both theoretically [126] and experimentally [83, 130, 132]. Though in disordered polymer, this intra-chain contribution to the red shift is dominant, a reduction of the band gap is also related to a greater overlap between adjacent chains, which is enhanced by pressure. In this respect, Raman spectroscopy proves to be a valuable tool to monitor both the hardening of vibrational modes and geometrical modifications of the polymer under pressure. However, the weakness of the Raman signal compared to the strong luminescence possessed by a huge class of conjugated systems prevents the measurement of Raman scattering. This is the case for MEH-PPV, whose

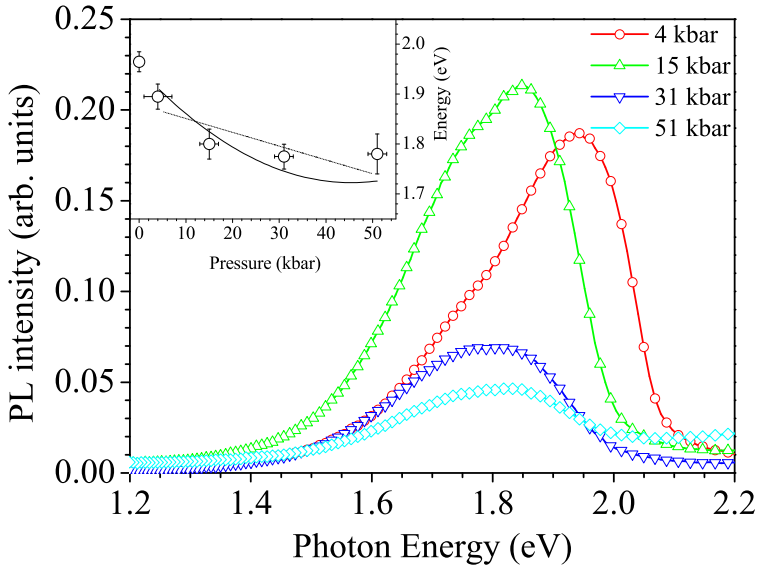

(a) 300 K. Quadratic function: E_{PL}=-10P+0.11P^2. Linear functions: E_{PL}= -2.76 P, where E_{PL} is in meV and P is in kbar.

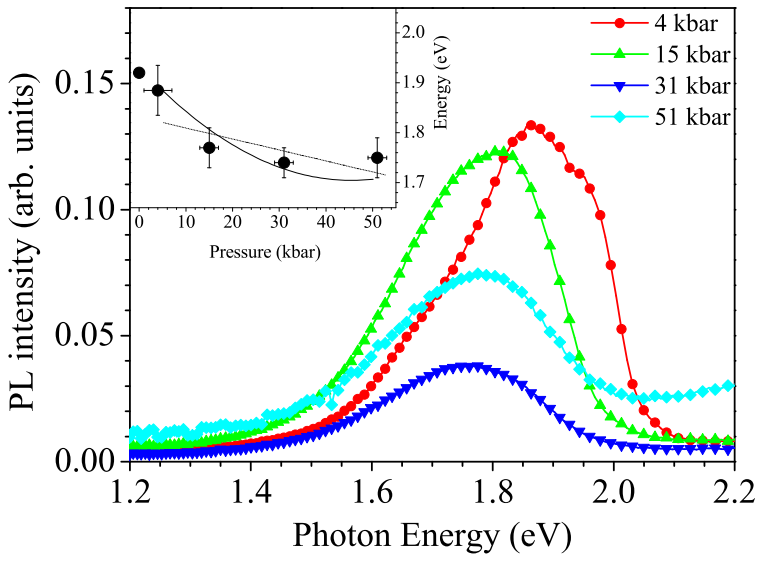

(b) 30 K. Quadratic function: E_{PL}=-10P+0.11P^2. Linear functions: E_{PL}= -2.22 P, where E_{PL} is in meV and P is in kbar.

Figure 4.3: PL of MEH-PPV at 300 K and at 30 K for different applied pressures. The inset shows the pressure dependence of the PL center along with a linear fit.

strong emission over a wide spectral range (1.6 - 2.1 eV) reported in Figure 4.2, masks the Raman signal.

4.2.2 Cw photoinduced absorption under pressure

As described in Chapter 2, in a cw PA experiment the pump beam which photoexcites the sample is a cw laser modulated by a mechanical chopper. These measurements allow to probe the long-lived photoexcited species, their time scale being of the order of ms for the in-phase component[2]. The photoinduced fractional change in transmission, $\Delta T/T$ is a modulated signal detected with a lock-in amplifier. For thin films, and when reflectivity can be neglected, $\Delta T/T \approx -d\Delta\alpha$ (d is the sample thickness, and α is absorption), thus the modulated signal provides information about the density of photoexcited states.

In this Section the effect of pressure on the long-lived species photogenerated in MEH-PPV by the pump laser is presented and discussed.

Figure 4.4 shows both the in and out-of phase components of the cw PA signal for MEH-PPV film drop cast onto a sapphire substrate. Measurements were performed both at room and low temperature. The in-phase component is dominated by a strong PA band peaked at 1.46 and 1.38 eV at 300 K and 30 K respectively. This band arises from the lowest triplet exciton transition T_1 [144, 145]. Moreover, it can be notice that a transition is barely detectable around 0.4 eV in the room temperature spectrum in Figure 4.4(a). The presence of such a band (P_1) can be related to a thermally-induced generation of polarons, trapped by defects along the chains. Formation of trapped polarons can also be obtained via photo-oxidation, with prolonged UV illumination of the sample [132, 146]. No band corresponding to polaron transition is instead observed in the low temperature measurement Figure 4.4(b).

Cw PA spectra of MEH-PPV for different applied pressures are shown in Figure 4.5 at both room and low temperature.

The triplet exciton transition T_1 characterizes both room and low temperature spectra for different applied pressures. The initial and final states involved in this transition and its spectral signature are schematically depicted in Figure 4.1. Figure 4.5 shows that the triplet PA band (T_1) at ~ 1.38 eV at both 30 K and 300 K *red-shifts* and *intensifies* with increasing pressure. A red shift of ~ -2.4 meV/kbar can be estimated for T_1, in agreement with that measured for other polymers [139]. For instance, a red-shift of the lowest triplet exciton due to applied pressure was observed in m-LPPP [132] and it was suggested to be related to the higher degree of conjugation due to the stronger overlap of π-electrons along the backbone chains, i.e. a higher degree of planarity or shorter inter-ring bonds. However, it has been shown that lowest triplet exciton T_0 (not shown in the diagram in Figure 4.1) is localized on a single monomer [147], and therefore the energy level 1^3B_u is not expected to undergo significant changes with pressure. The observed red-shift of T_1 can be thus

[2]Much longer lived species can be probed through the out-of-phase PA signal.

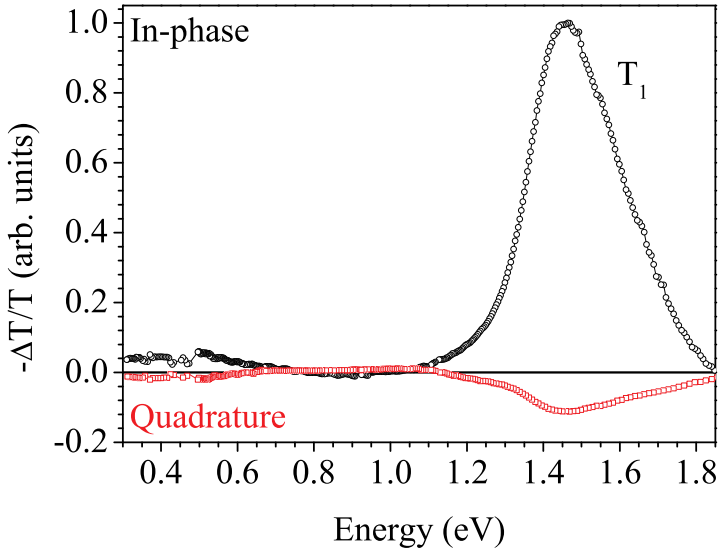

(a) 300 K.

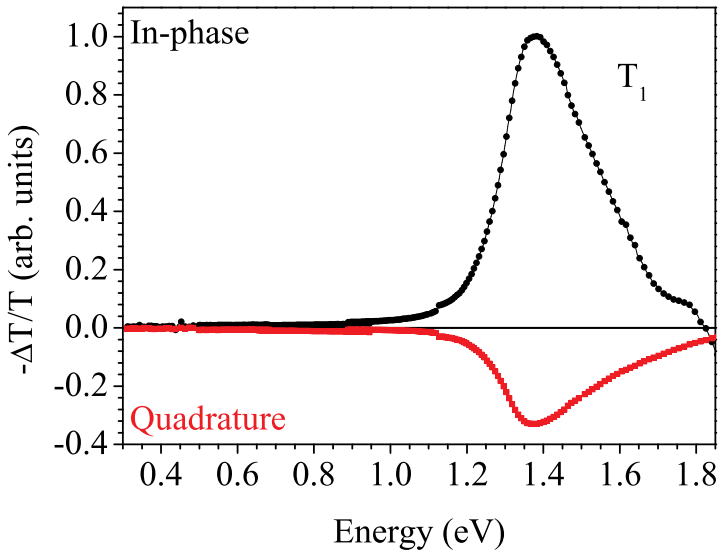

(b) 30 K.

Figure 4.4: Room pressure cw PA spectra at different applied pressures, measured at 300 K (a) and 30 K (b).

interpreted as a result of aggregate formation. Since the energy of the level 1^3B_u does not change much with pressure, the shift of the T_1 transition reflects the pressure induced changes of the final state, labeled m^3A_g in Figure 4.1.

While T_1 is the only band detectable in cw PA spectra at 30 K, another transition is observed at room temperature around 0.4 eV, where the triplet PA is significantly reduced (Figure 4.5(a)). This feature arises form defect-induced polarons. No polaron band is instead detectable for any of the applied pressures at 30K (Figure 4.5(b)), suggesting temperature plays a role in their formation. A reversible mechanism for polaron generation in pristine MEH-PPV films was proposed in [146] in which prolonged UV illumination transforms *cis* native defects in the polymer chains into metastable deep traps that substantially increase the photogenerated polaron lifetime in the film.

The spectral position and intensity of the polaron band P_1 (Figure 4.5(a) 4.6) seems to be rather independent on pressure. In fact, P_1 is a broad transition, extending up to 0.2 eV [148]. Due to the spectral range in Figure 4.5(a) limited by transmission intensity, a clear pressure dependence of P_1 can't be derived form cw PA spectra. We note however that the cw PA spectrum of pristine MEH-PPV films does not show polaron excitations [149]. Nevertheless P_1 band is still formed and dominates the IR range at high pressures. We therefore conclude that the polaron PG quantum efficiency increases due to the increased interchain interaction at high pressure. This is directly verified below using transient spectroscopy (Section 4.3).

Close inspection of the P_1 band (Figure 4.6) reveals a sharp dip, or anti-resonance (AR) that develops at ~ 0.36 eV (~ 2800 cm^{-1}), close to the frequency of the IRAV C-H stretching on the alkoxy group in MEH-PPV [150] [3]. This indicates that the AR feature originates from Fano-type quantum interference between the broad P_1 band and the narrow IRAV absorption line [128]. The appearance of this IRAV as a bleaching, due to a Fano-type anti-resonance, was already observed in other polymers. For instance, an ordered form of polydiacetylenes (polyDCHC) [151] shows photoinduced IRAV modes affected by Fano coupling between electronic and vibrational states. More recently, Fano-type AR was observed in regio-regular polythiophene (rr-P3HT) [152], which is known for its lamellae structure (and thus has increased inter-chain interactions). This similarity, supports the existence of aggregates in MEH-PPV at high pressure suggested to explain the behavior of PL as a function of pressure (Section 4.2.1). Indeed, a Fano-type AR, which also develops in the transient PA spectra (Section 4.3), is indicative that applied pressures increases el-ph coupling.

[3] These modes were used for pressure calibration as described in Chapter 2. A complete characterization of the IR vibrational modes of MEH-PPV is given in [148].

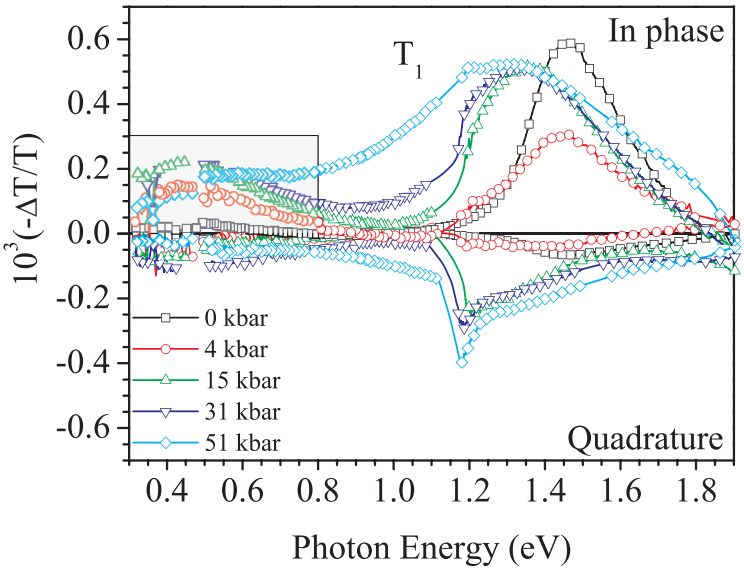

(a) 300 K.

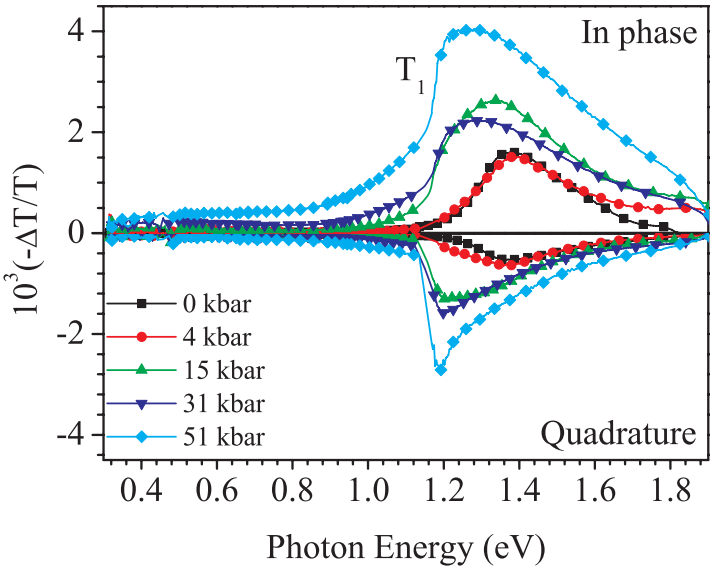

(b) 30 K.

Figure 4.5: Transient photomodulated spectrum of MEH-PPV at room and low temperature. Positive (-ΔT/T) represents the signal component in phase with the chopped pump beam, while negative (-ΔT/T) is the quadrature, or out-of-phase component.)

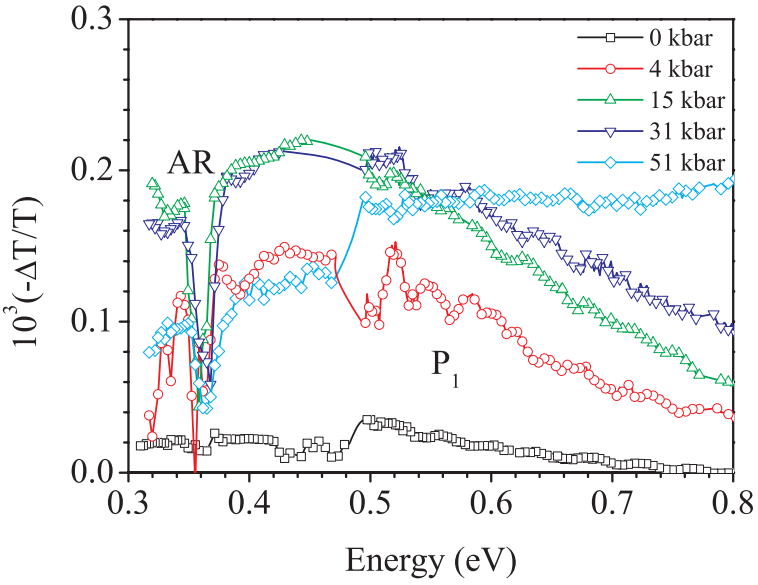

Figure 4.6: Mid-IR photoinduced absorption spectra of MEH-PPV at 300 K emphasizing the polaron band P_1 where the AR feature is assigned.

4.2.3 Frequency dependence response

The study of the PA dependence on the modulation frequency ω and on the pump intensity I provides information on the lifetimes τ of the metastable states and on their recombination mechanisms. It is known [70] that in steady state conditions, the PA signal scales linearly with the laser intensity for photoexcitations which recombine monomolecularly, while for species with bi-molecular recombination, a square-root dependence is expected. In this Section, the recombination kinetics of the triplet exciton of MEH-PPV are studied, through the frequency dependence response of the polymer in the spectral range from 1.3 to 1.5 eV. The laser intensity was kept constant during the measurements.

Due to greater signal intensity, reliable results were obtained at low temperature only. The frequency response of T_1 at 30 K is shown in Figure 4.7 and the lifetime for each applied pressure was determined from least-squares fit to the function:

$$\Delta T(\omega) = G\tau[1 + (i\omega\tau)^{\alpha}] \tag{4.1}$$

where G is the generation rate amplitude, $\alpha < 1$ is the dispersion parameter, τ is the average lifetime, and $\omega = 2\pi f$ [149]. For monomolecular processes, τ is independent on G, while for bi-molecular processes, its dependence on G can be assumed of the form $\tau = (Gb_0)^{1/2}$, being b_0 a mean recombination rate.

Triplet lifetime τ versus pressure can be fit by a linear function with a slope of -1.97 ns/kbar (Figure 4.8). From the fits we conclude that there is a significant decrease in τ at high pressure, indicating that a higher exciton diffusion is accompanying the increased interchain coupling. In general, the

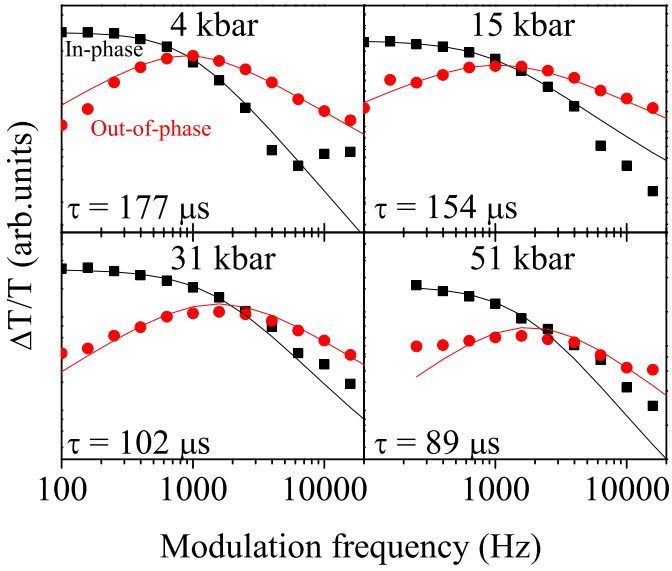

Figure 4.7: Modulation frequency dependence data and least-squares fit of the triplet exciton T_1 (1.3 - 1.55 eV) of MEH-PPV for different applied pressures at 30 K.

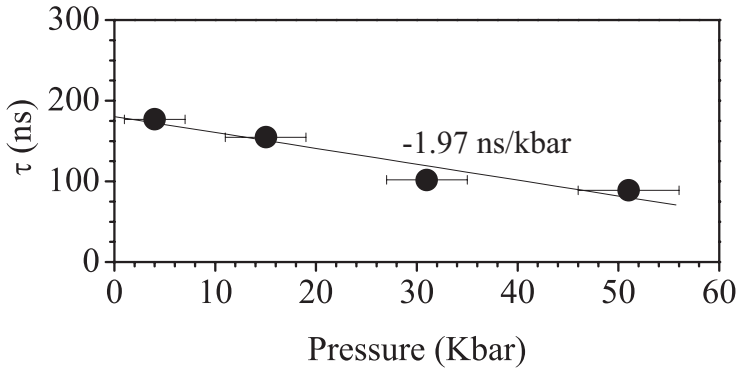

Figure 4.8: Pressure dependence of the triplet exciton lifetime τ .

steady-state PA intensity is given by the relation PA $\sim I_L \eta \tau$, where I_L is the absorbed laser intensity in the film, and η is the PG quantum efficiency [136].

As illustrated in the previous Section, T_1 doubles its intensity at high applied pressures. At the same time, its lifetime τ decreases with pressure. Based on the above relation, we conclude that η for triplet excitons increases at high pressure. We do not expect that the intersystem crossing (ISC, Figure 4.1) rate would change at high pressure, thus we attribute the increase in η simply to longer lived singlet excitons at high pressure that are available when the intersystem crossing time sets in.

4.3 Ultrafast pump/probe spectroscopy

The majority of the previous studies of intermolecular coupling in π-conjugated polymers exploits steady-state techniques which provide only limited information on the dynamics of long-lived photoexcited states. Combining the use of a DAC to apply pressure with ultra-fast transient spectroscopy is in fact rather challenging form the experimental point of view. It offers nonetheless a unique opportunity to clarify the photophysics of these materials, giving direct access to the pressure dependence of the photoexcitations generated instantaneously, i.e. within a hundred of femtoseconds form the pump pulse. To our knowledge, ultrafast spectroscopy was used to investigate the influence of intermolecular interaction through only in sexithiopene single crystals [133]. In particular, time-resolved PL under pressure showed that the pressure-induced quenching of the photoluminescence is caused by an ultrafast formation of intermolecular species, but negligible changes of the exciton lifetime were observed. It was suggested that reducing interchain distance enhanced generation of polarons due to the stronger intermolecular character of the primary excitations which facilitates electron-hole separation, and, on the other hand, reduced the probability for the excitons to relax towards the lower Davydov levels, from which light emission occurs.

The two-color laser system described in Chapter 2, Section 2.3.3 allows to measure transient photoinduced absorption spectra of MEH-PPV films under pressure within a temporal resolution of ∼120 fs. In the following, The transient photomodulated (PM) spectra of MEH-PPV for different applied pressure are discussed. The dynamics of the primary photoexcitations in the IR energy range help distinguish between different species and provide information on their temporal evolution as a function of pressure. Finally, it is shown how to gain information on longer lived states though the background that accumulates for each in-phase spectrum detected.

4.3.1 Transient photoinduced absorption

Figure 4.9 shows the transient photomodulated (PM) spectrum of a MEH-PPV film cast from toluene solution at t=0. It contains two bands at 0.35 and ∼1

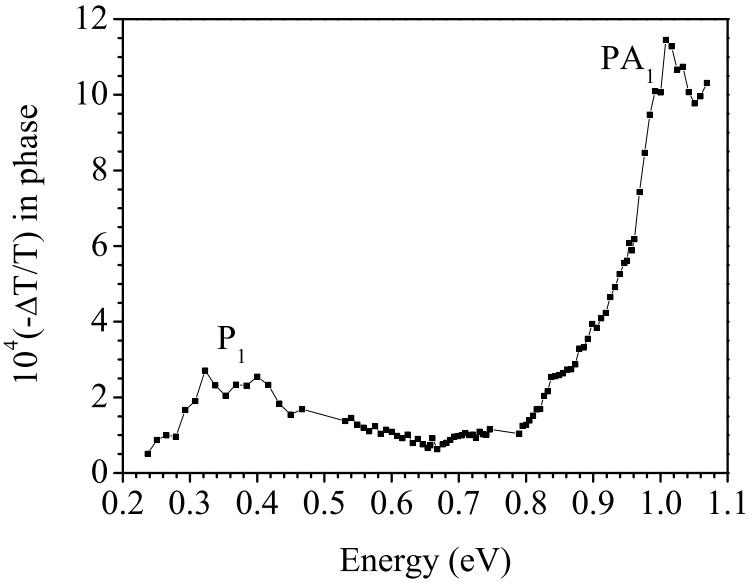

Figure 4.9: Transient photoinduced absorption of a MEH-PPV film cast form toluene solution and deposited onto a sapphire substrate. P_1 and PA_1 refer to polaron and exciton, respectively.

eV, corresponding to the primary photoexcitations in MEH-PPV films. The photoinduced band at 0.35 eV, named P_1, has been ascribed to free polaron absorption [127] (Figure 4.1). It is interesting to notice that such a band is not apparent in PA spectra of MEH-PPV in solution as well as in films with weak inter-chain interactions, such as DOO-PPV [127]. Also, P_1 was proved to be strongly affected by the peculiar nanomorphology of the film, which in turn depends on the specific process (solvent, thermal treatment...) used to obtain the film [127].

The photoinduced absorption band PA_1 at 1 eV in Figure 4.9 has a controversial interpretation. While it is well established that in systems with poor inter-chain interactions, this band PA_1 originates form the $1B_u$ optical excition, in films the nature of this PA band is still widely debated. In [23] PA_1 has been assigned to polaron pairs (Chapter 1), while in a recent paper [153] it is attributed to excimers. According to the latter assignment, the P_1 absorption is form the lowest excimer to the lowest polaron pair. The influence of inter-chain interactions on the PA spectra was calculated [153] from an Hamiltonian including both intra and inter-chain transfer integral. It was concluded that the lowest excited state of a system composed by two coupled chains is an excimer or inter-chain charge transfer exciton. Indeed, while, in the single chain, PA_1 corresponds to the transition from the $1B_u$ to the mA_g, the initial and final states of PA_1 absorptions in the two-chain systems are both excimers.

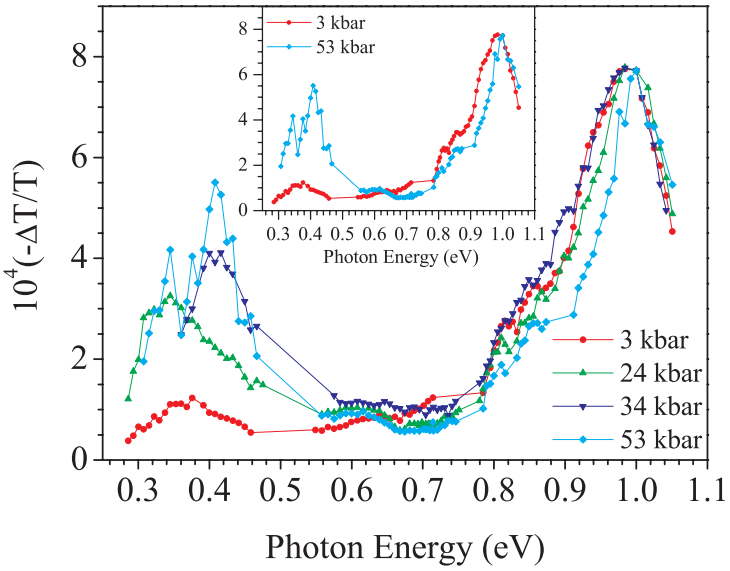

Figure 4.10: Transient photoinduced absorption spectra at t=0 for MEH-PPV film at the respective pressures: 3 kbar (circles); 24 kbar (up triangle); 34 kbar (left triangle); 53 kbar (diamond). The inset shows the spectra corresponding to the lowest and highest applied pressures.

Furthermore, the strength of the P_1 absorption is a measure of inter-chain interactions. Calculations showed that increasing the inter-chain hopping matrix parameter causes a lowering of the energy of the lowest excimer, that should blue shifts both P_1 and PA_1.

Figure 4.10 shows the transient PA at t = 0 (that is, within 150 fs) at four different pressures, normalized to the PA band at 1 eV[4]. The P_1 and PA_1 bands, due to intrachain polarons and excitons, respectively [127] are clearly visible, peaked at about 0.4 eV and 1.0 eV, respectively.

Upon increasing pressure a few changes can be detected. First, at high pressure PA_1 slightly blue-shifts, as shown in the inset of Figure 4.10, while it a clear blue-shift of P_1 cannot be detected. It is thus not possible to establish any relation between these two photoexcited species due to enhanced interchain interactions. The slight pressure dependence of PA_1 can be interpreted in the light of the previous findings on steady state spectroscopy, being explained as due to the evolution of the exciton states when forming aggregates. This is schematically shown in Figure 4.17.

A significant variation with pressure of the relative strength of the initial P_1 band can be observed in Figure 4.10. The intensity of the polaron band dramatically increases reaching $\sim 40\%$ of PA_1 at 53 kbar. Thus, an increase by a factor of four is observed as a consequence of applied pressure in the ratio of charged (polarons) to neutral (excitons) photoexcitation following photon

[4]A fair comparison should be made for measurements done on the same sample. However, to avoid photodegradation, different samples were prepared, being the collection of each spectrum $\sim$1 week long.

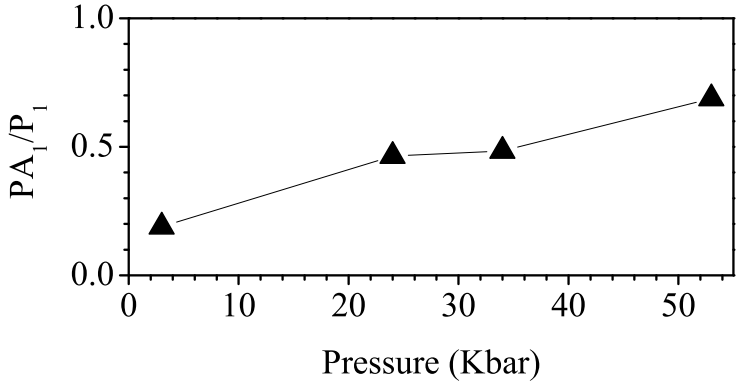

Figure 4.11: Ratio between the integrated area under each PM band (PA_1 to P_1) for different applied pressures.

absorption, that is the branching ratio η. This is summarized in Figure 4.11, where ratio between the integrated area under each PM band (PA_1 to P_1) was calculated is shown. The branching ratio is an important parameter in device design, since a large η is needed in efficient solar cells, while a small η is preferable for LEDs [154]. η varies depending on the polymer structure and film nanomorphology [127], being related to the morphology of the film. It is thus a measure of the strength of inter-chain interactions. Different values of η have been so far obtained for both films and solution of PPV derivatives (heeger-valy), topically ranging from 0.1% to 10%. Values as large as 30% of polaron PG quantum efficiency were recently obtained in another polymer, namely rr-P3HT films [127], where the interchain interaction is large due to the lamellae nanomorphology [147]. The similarity between the value of η of MEH-PPV and that of rr-P3HT further supports the formation of aggregates at high pressure in MEH-PPV.

Finally, the Fano-type AR feature intensifies (Figures 4.10 and 4.12). The presence in the transient spectra of the AR feature, already encountered in cw PA spectra under pressure, confirms that it is not merely an experimental artifact, but is rather a genuine spectral feature characteristic of the polaron PA band upon increased interchain coupling [128].

4.3.2 Dynamics

Transient photoinduced absorption gives simultaneous monitoring of charged (polaron) and neutral (exciton) species . With the set-up described in Chapter 2, the instantaneous (that is, within 120 fs) generation and decay with time of this photoexcitations can be probed and information about lifetimes, photogeneration quantum efficiency and diffusion processes can be obtained.

Figure 4.12 shows the time evolution of the PA spectrum in the mid-IR

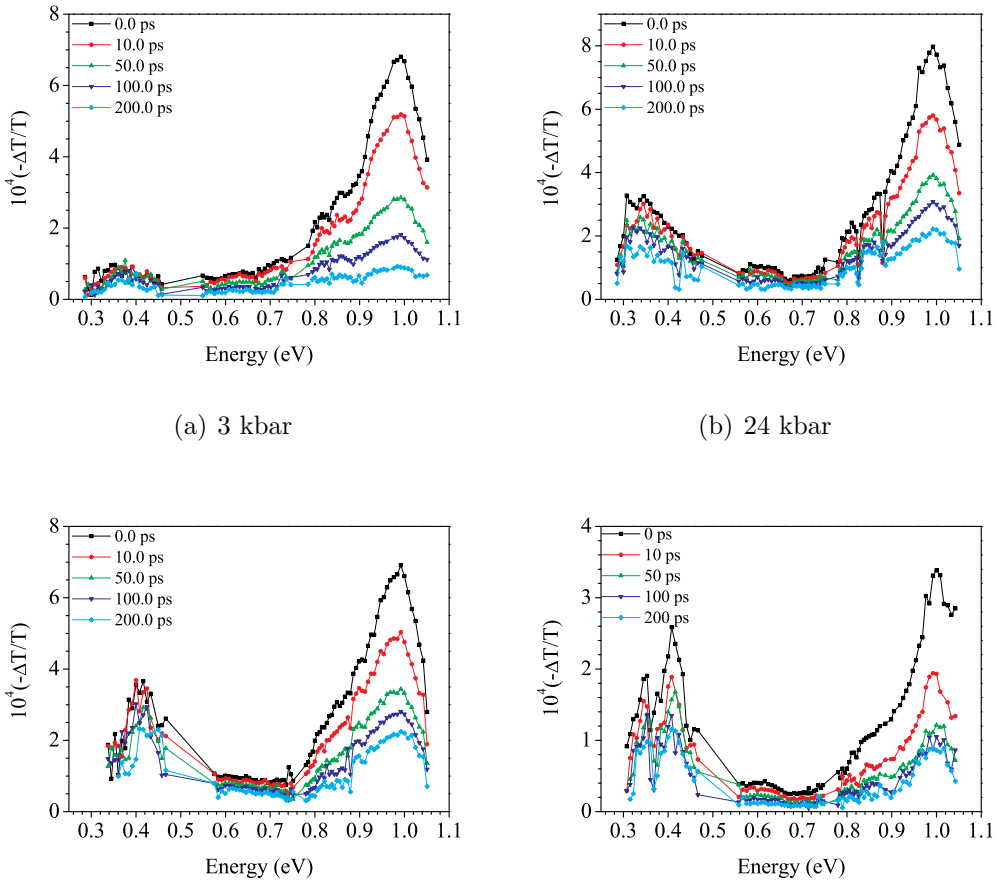

(a) 3 kbar

(b) 24 kbar

(c) 34 kbar

(d) 53 kbar

Figure 4.12: Spectral decay of the photoinduced absorption signal of MEH-PPV for each applied pressure. Figure 4.10 shows the spectra at t = 0.

spectral range at each applied pressures. The PA_1 band decays with time for all pressures. It is clear though that its decay is not the same for all pressures, being faster at 53 kbar. The decay of P_1 is, instead, slower. In particular, at 3 kbar the PA signal has roughly the same intensity for all time delays. The different time evolution of these photoexcitations was already observed in [127] and excludes the possibility that these two PA bands belong to a single photogenerated species. In addition, the AR feature superimposed on P_1 is still prominent at longer time, in support for its genuine characteristics.

The P_1 and PA_1 decay dynamics are shown for all pressures in Figure 4.13. The slower decay of P_1 (Figure 4.13(b)) with respect to PA_1 is more obvious here. It can be noticed that its decay dynamics does not change much with pressure. On the contrary, the PA_1 decay dynamics substantially changes with pressure: while it is best fit by a single exponential at low pressure, the PA_1 decay at high pressure can be fit using double exponential of the form:

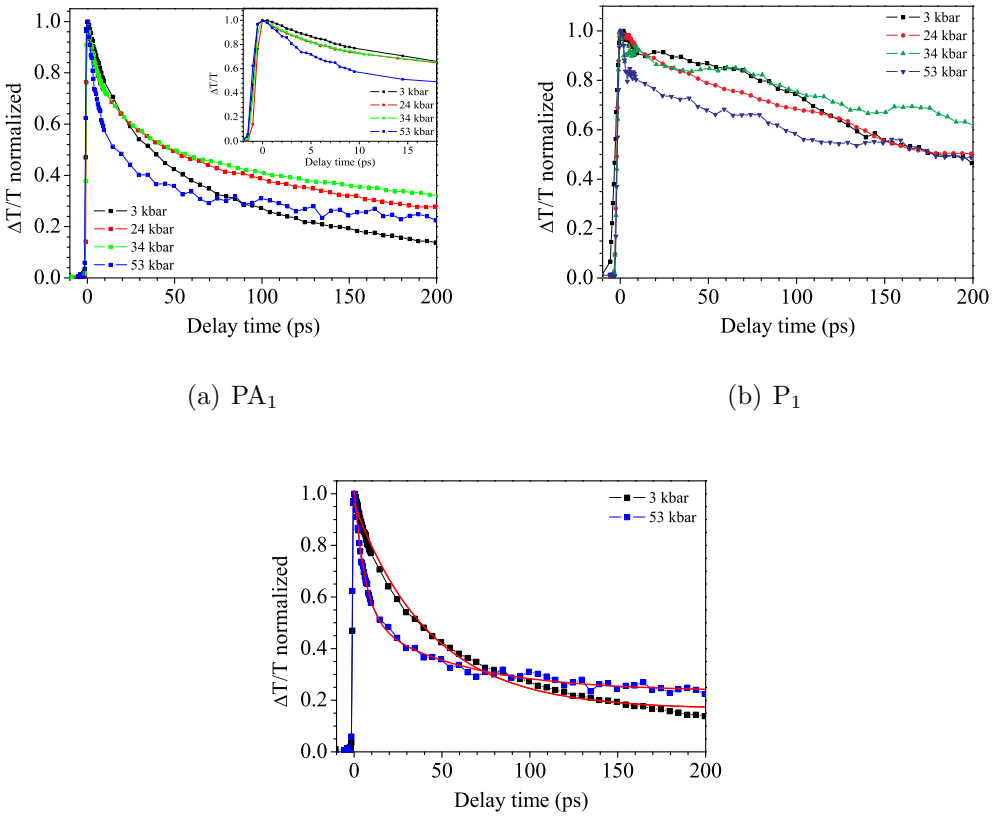

(a) PA_1

(b) P_1

(c) PA_1 fit

Figure 4.13: Transient decay dynamics of the exciton PA_1 and polaron P_1 at each applied pressure.

$$\Delta T = R_1 e^{(-t/\tau_1)} + R_2 e^{(-t/\tau_2)} \tag{4.2}$$

where τ_1 and τ_2 are the component lifetimes and R_1 and R_2 are their respective weights. At 53 kbar the time constants are $t_1 = 6$ ps and $t_2 = 56$ ps, with $R_1 = 0.48$ and $R_2 = 0.29$. The fit results are shown in Figure 4.13(c) for the lowest and highest applied pressures[5]. We interpret the double exponential decay at high pressure as due to exciton trapping and recombination, respectively, and we suggest that the excitonic traps can be identified as aggregates [143] that form more abundantly at high pressure. This shows that the photogenerated excitons live longer in the aggregates and consequently are more available for intersystem crossing into the triplet manifold. As previously discussed in Section 4.2.2, this causes an increase of η for triplet excitons at high pressure (Figure 4.5). The longer exciton lifetime at high pressure does

[5]Due to the lower signal to noise ratio of the time evolution of P_1, a reliable fit could not be obtained. For this reason, P_1 dynamics will be discussed only qualitatively.

not increase the PL efficiency, however, since the radiative rate of aggregates are much lower than that of free excitons [128, 155]; and this explains the weaker PL emission at high pressure even that excitons lifetime increases.

4.3.3 Background

A typical transient signal is shown in Figure 4.14(b). At a time t less than zero (that is before the pump pulse impinges onto the sample), ΔT is expected to be equal to zero and after a certain time it is should decay back to this value. However, due to the high repetition rate (82 MHz) of the pump laser, the transient signal rides on top of a background, as schematically represented in Figure 4.14(a). This is due to the fact that the next pulse arrives when the system is not relaxed yet, and the ΔT induced by this pulse sums up to the first one. So, the transient signal does not decay completely to zero before another pulse arrives and a steady-state background accumulates[6]. This background is far from being meaningless, since it embeds information about the long lived component of the photoexcited species that appear in the corresponding in-phase signal $\Delta T/T$ (Figure 4.10) or in the in-phase signal of cw PA measurements.

The amplitude of the background, on which the transient PM signal rides, is shown in Figure 4.15 for a film of MEH-PPV onto a sapphire substrate. Only one out of the two bands observed in the in phase PA signal (Figure 4.10) is obvious in the background, namely the polaron band P_1 peaked at 0.35 eV. The absence of the PA_1 band indicates a different dynamics, hence a different origin, of the two photogenerated species.

Figure 4.16 shows the pressure dependence of the background spectra corresponding to the in-phase signals of Figure 4.10 normalized at 1 eV. A band is detected at 0.35 eV, corresponding to the long lived component of P_1. The presence of this band occurs since the polaron band does not decay in between the pump excitation pulses, which are ∼12 ns apart. Therefore from the background amplitude we can derive the PA spectrum at t = 30μsec, which corresponds to t = 1/f, being f = 30 KHz the modulation frequency to which the lock-in amplifier is synchronized. As a consequence of applied pressure, the intensity of the polaron band increases up to 40% at 53 kbar. Besides the substantial increase of the polarons photogeneration, an increase of a second PA band at higher energy (∼1 eV) can be observed. This 'high energy' band is not due to PA_1 (which decays in between pulses, as demonstrated in Figures 4.12 and 4.13), but rather it is caused by the tail of the T_1 PA band that red-shifts and intensifies with pressure, as observed in cw-PA spectra (Figure 4.5).

[6]It is easy to calculate that for each modulation, at a frequency of 30 KHz, 2750 pulses of the pump laser occur.

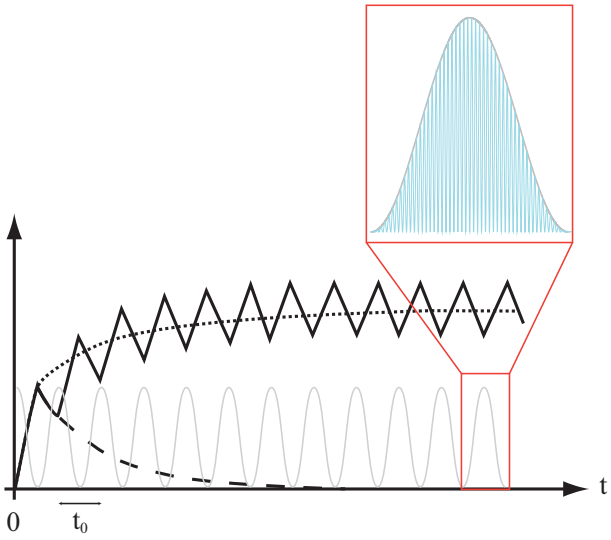

(a) The pump laser is modulated at f = 30 kHz. Within each modulation, 2750 pulses occur.

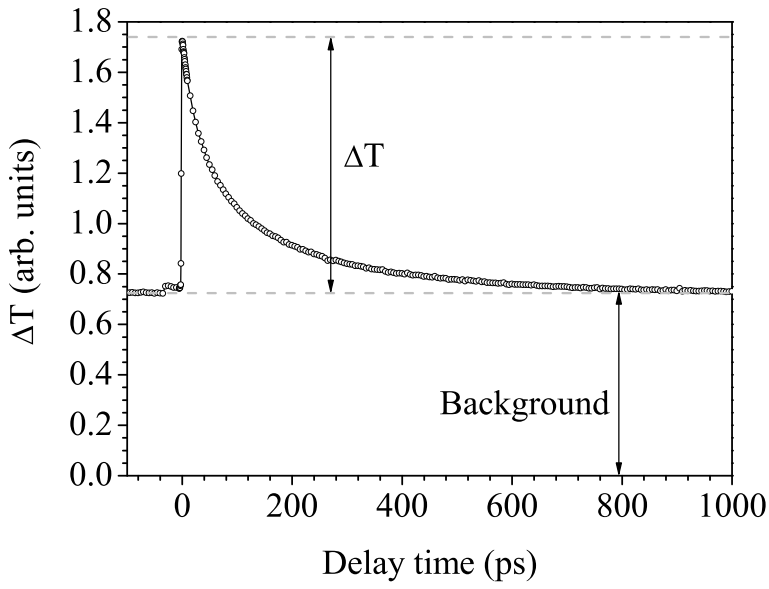

(b) Definition of the in-phase (ΔT) and background signals.

Figure 4.14: Due to the high repetition rate of the pump laser, a steady-state background accumulates in transient pump/probe measurements (a) and a typical transient signal recorded is shown in (b).

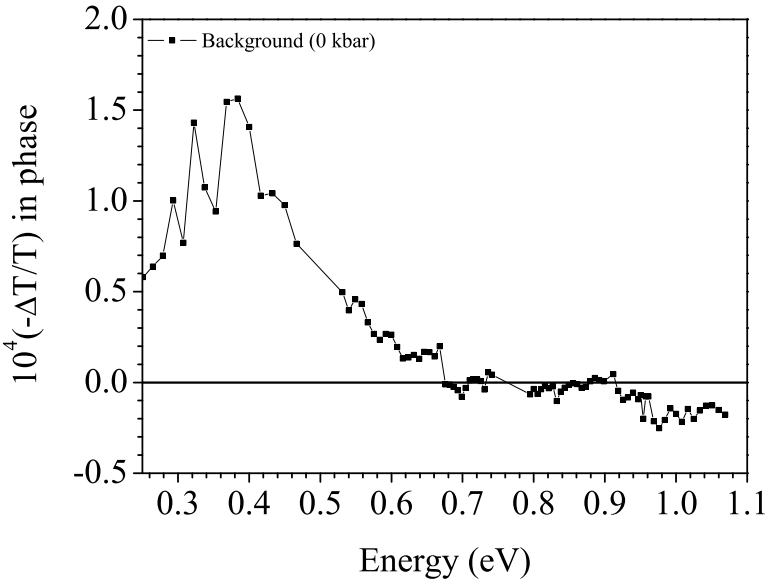

Figure 4.15: Background spectrum of the transient PM signal. The background corresponds either to the in-phase signal $\Delta T/T$ (Figure 4.10) or to the in-phase signal of cw PA measurements.

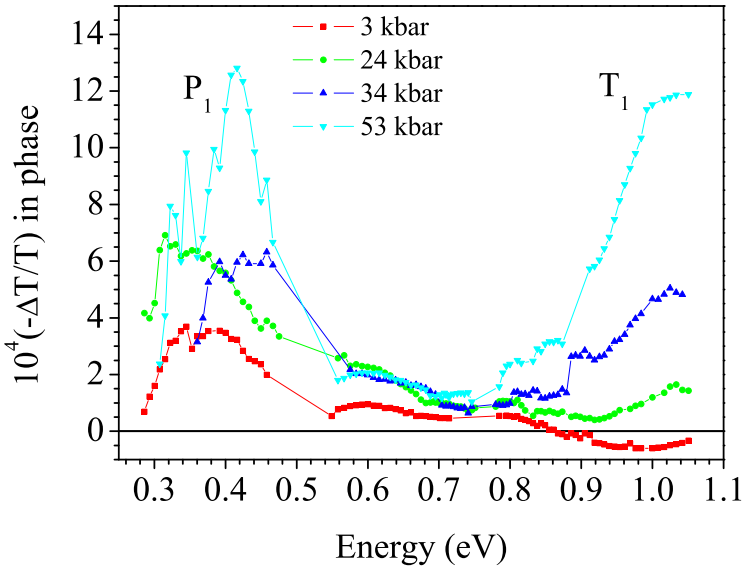

Figure 4.16: The background amplitude spectra, as defined in Figure 4.14, for different applied pressures. P_1 and T_1 PA bands are indicated.

4.4 Conclusions

Using a variety of transient and steady-state spectroscopy, we studied the effect of hydrostatic pressure up to 53 kbar on a substituted poly(phenylene-vinylene), namely MEH-PPV. The effect of pressure as derived from the whole set of measurements is summarized in Figure 4.17.

We found that the cw photoluminescence band weakens, loses its zero-phonon satellite, and red-shifts by $-\sim$2 meV/kbar. We interpret this behavior as indicative of aggregate formation in the film. At the same time, the triplet PA intensifies, in spite of showing a faster dynamics, and red shifts with pressure dependence close to that of PL. The significant decrease of the triplet lifetime as a function of pressure indicates that higher exciton diffusion that accompanies the increased inter-chain coupling. Since the intensity of T_1 increases and simultaneous its lifetime shortens, we conclude that for triplet excitons the photogeneration quantum efficiency, η, increases at high pressure. We do not expect that the intersystem crossing rate would change at high pressure, and thus we attribute the increase in η to longer lived singlet excitons that are available at high pressure, when the intersystem crossing time sets in.

The ps singlet exciton PA band slightly blue shifts with pressure, and changes its dynamics, having a faster decay at high pressure. On the other hand, the ps polaron PA band increases fourfold up to 40% of the exciton PA, and shows a superimposed vibrational Fano-type anti-resonance. These pressure-induced effects indicate enhanced aggregates formation caused by the increased interchain interaction.

Figure 4.17 summarizes the effect of pressure on the relevant exciton states in the singlet and triplet manifolds. The corresponding optical transitions for isolated chain (room pressure) and for interacting chains (high pressure) when aggregates ar formed are also shown.

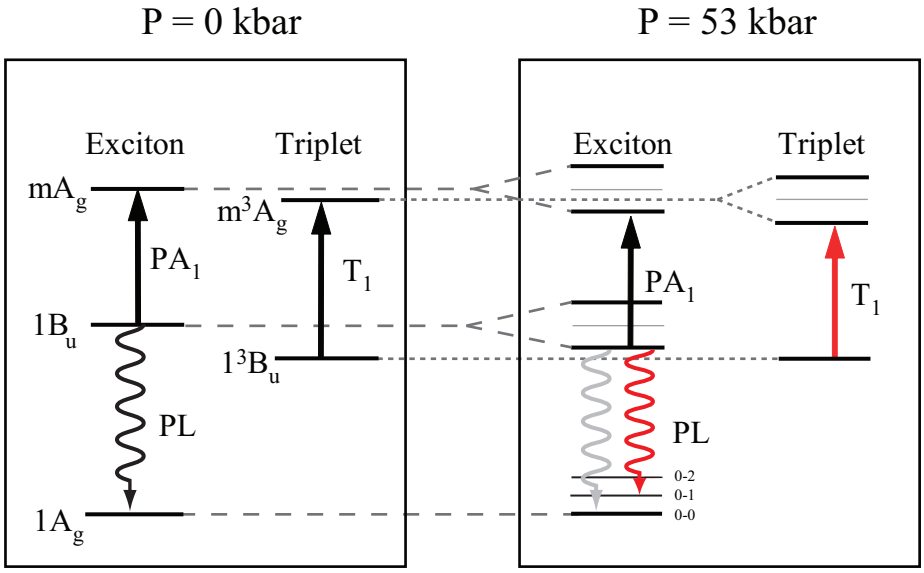

Figure 4.17: Schematic of the prominent exciton states in the singlet and triplet manifolds and associated optical transitions for isolated chain at room pressure and when forming aggregates at high pressure.

Chapter 5

Conclusions and future perspectives

This thesis presented a study of the influence of inter-chain interactions in two π-conjugated polymers belonging to the same family, namely PPV and MEH-PPV. Tuning of inter-chain interactions was achieved by means of a diamond anvil cell, which -coupled to a variety of optical techniques- allowed to obtain a wide spectroscopic characterization of both samples under applied pressure.

In this work, a peculiar form of PPV was studied: the sample was oriented by tensile stretching with an elongation ratio of 5. Highly oriented PPV, besides being a reference model, proved to be an ideal system to investigate the role played by intermolecular interactions.

In general, in amorphous polymeric systems, the main effect of pressure is an increase of intramolecular order due to planarization of the backbone chains. Through Raman spectroscopy it was possible to rule out any significant pressure-induced geometrical change. Thus, having proved that minor effects due to an extension of the conjugation length occur, we conclude that the bathochromic shift of the $\pi - \pi^*$ transition observed in reflectance and transmittance spectra has to be ascribed mainly to intermolecular interactions.

In order to take into account both the diamond birefringence and its contribution to reflectivity, the development of a suitable optical model was necessary. From the re-normalized reflectance spectra it was then possible to obtain the complex dielectric function of oriented PPV for all applied pressures. Indeed, the physical the photophysical properties of PPV concerning transition energies and broadening are fully comprised in the dielectric constants of the material, whose complex components represent the grounds of a meaningful interpretation.

A careful analysis of the complex dielectric constant shows that for parallel polarization electronic transitions below 2.75 eV gain intensity while those at higher energies show a reduced oscillator strength. For perpendicular polarization, a generalized increase of oscillator strength in observed in all the

spectrum indicating that this component is not only due to chain misalignment but also to intermolecular interactions. The broadening of vibronic progression has been qualitatively assigned to a splitting of electronic states due to intermolecular interactions even though a not negligible contribution form el-ph interaction in the intermediate coupling regime have to be considered.

The second part of this thesis was devoted to study the effect of high hydrostatic pressure, on the photophysics of a substituted poly(phenylene-vinylene) derivative, namely MEH-PPV. Form the structural point of view, this material is a disordered system, exhibiting strong inter-chain coupling.

Using a variety of transient and steady-state spectroscopy, we could probe the effect of hydrostatic pressure up to 53 kbar. We found that the cw photoluminescence band weakens, loses its zero-phonon satellite, and red-shifts by $\sim$2 meV/kbar. We interpret this behavior as indicative of aggregate formation in the film. At the same time, the triplet PA intensifies, in spite of showing a faster dynamics, and red shifts with pressure dependence close to that of PL. The significant decrease of the triplet lifetime as a function of pressure indicates that higher exciton diffusion that accompanies the increased inter-chain coupling. Since the intensity of T_1 increases and simultaneous its lifetime shortens, we conclude that for triplet excitons the photogeneration quantum efficiency, η, increases at high pressure. We do not expect that the intersystem crossing rate would change at high pressure, and thus we attribute the increase in η to longer lived singlet excitons that are available at high pressure, when the intersystem crossing time sets in.

The ps singlet exciton PA band slightly blue shifts with pressure, and changes its dynamics, having a faster decay at high pressure. On the other hand, the ps polaron PA band increases fourfold up to 40% of the exciton PA, and shows a superimposed vibrational Fano-type anti-resonance. These pressure-induced effects indicate enhanced aggregates formation caused by the increased interchain interaction.

During the past 20 years, a huge variety of studies (both theoretical and experimental) appeared in the literature concerning inter-chain interactions and their effect on the optical and electronic properties of π-conjugated systems. Nonetheless, a clear understanding of the role played by intermolecular coupling in these materials has not been achieved yet. Due to their strong dependence on the geometrical arrangement of the polymer chains and on the degree of disorder, a unified picture is far from being achieved.

Among the issues to be clarified on inter-chain interaction, an appealing one is whether and how they could be responsible for photoluminescence quenching. In this respect, highly oriented PPV provides an ideal playground. Under pressure emission measurements might help to unravel the origin of PL reduction of films as compared to solutions.

Recently, the study of P3HT attracted much attention, due its applications mainly for photovoltaic devices. Depending on the chemical synthesis, P3HT assumes two different structures: either it is disordered, with a random coil

arrangement of the chains (regio-random), or it self organizes in a π-stacked lamellar structure (regio-regular). This highly ordered supramolecular packing of the chains is maintained in thin films and gives rise to an outstanding field-effect mobility approaching that of amorphous silicon. It is thus obvious that such a material represents an optimal candidate to investigate inter-chain interactions and establish a relationship between coupling among adjacent chains and supramolecular order. A hint for future work would be the simultaneous study of the photophysics of both regio-regular and regio-random P3HT under pressure.

Appendix A

Raman spectra of fluorinated Poly(p-phenylenevinylenes)

A.1 Introduction

Chemical engineering of side groups in conjugated polymers is an important tool for tailoring properties of π-conjugated materials based on specific needs. Indeed, a proper choice of substituents not only improves material processability from solution, but also enables to tune the electronic properties, and the supramolecular solid state organization. This in turn deeply affects intermolecular interactions, and offers a further opportunity to better understand the role of inter-chain coupling.

In recent years, functionalization of conjugated polymers with fluorine atoms has attracted considerable interest, since this structural modification is able to improve the stability of materials against photo-oxidation (a major issue in device design), as well as to modify their optical and electrical properties. These effects are related to the strong electronegativity of the fluorine atom and to the strength of the F-C bond. Solid state supramolecular organization is also affected by fluorination.

In order to investigate the influence of side groups on the spectroscopic properties of different materilas, Raman spectroscopy is indeed a valuable tool. As discussed in Chapter 3, not only the Raman shift provides information on the conjugation length, but additional insight can be gained analyzing the dependence of relative band intensity on electron delocalization. As a matter of fact, the intensity of bands assigned to C-C, C=C, C-H stretching modes of phenyl ring and vinylene group depends on ring torsion, which in turn modifies the extension of the conjugation length.

In this Section, the vibrational spectra of different PPV derivatives, with and without fluorinated vinylene side groups, are presented and discussed. The samples were prepared by Prof. G.M. Farinola, Dipartimento di Chimica, Università di Bari. Moreover, thanks to a collaboration with the National

Nanotechnology Laboratory (NNL) of CNR-INFM, Università del Salento, a theoretical assignment of the Raman modes was possible by means of density functional theory (DFT) calculations. Without entering the details of the simulations, experimental spectra will be compared to theoretical findings, and an overall picture of the vibrational properties of all the samples will be outlined.

A.2 Experimental

Commercial MEH-PPV was purchased by Sigma Aldrich. In addition, MEH-PPV as well as its fluorinated counterpart, MEH-PPVDF, were prepared in Bari using the same synthetic procedure [156]. The availability of such polymers offers a twofold opportunity to compare the photophysical properties of a well known reference system (MEH-PPV) with those of newly synthesized material (MEH-PPDFV). Commercial MEH-PPV is first compared with its analogous prepared in Bari. Moreover, the properties of MEH-PPDFV can be compared with those of MEH-PPV synthesized by the same method, reducing possible differences related to the synthetic procedure.

The chemical structure of both MEH-PPV and MEH-PPDFV is shown in Figure A.1. In the following, for sake of clarity, MEH-PPV synthesized in Bari will be named sMEH-PPV.

Raman measurements were performed with a Dilor-Labram spectrometer (Chapter 2), using a 10x objective and He-Ne laser excitation (λ_{exc} = 632.8 nm). All measurements were recorded at room temperature on both powders and drop cast films from chloroform solutions.

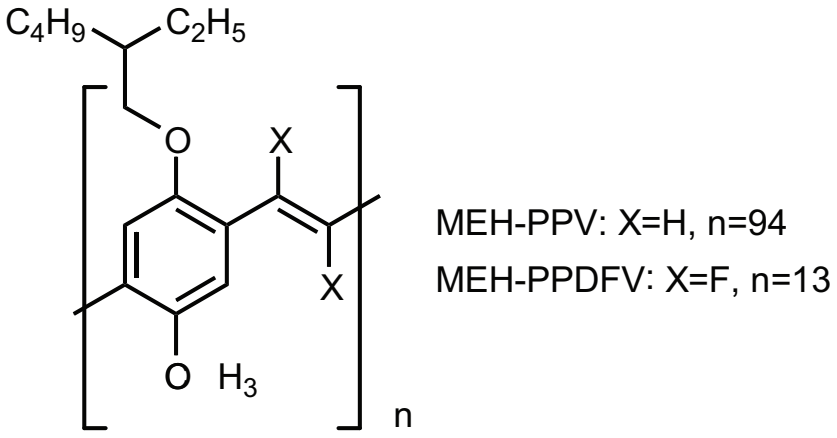

Figure A.1: Chemical structure of MEH-PPV and MEH-PPDFV.

A.3 Results and discussion

Figure A.2 shows the experimental Raman spectra of MEH-PPV and sMEH-PPV in the 800-1800 cm^{-1} Raman shift range for both powders and films. A smooth photoluminescence background has been subtracted from the spectra here reported.

The Raman spectra of MEH-PPV and sMEH-PPV, both powder and film (Figure A.2), closely resemble each other, the major difference being the higher intensity of the newly synthesized polymer with respect to the commercial one. All the spectra present two weak bands at about 966 and 1110 cm^{-1} and two bands of medium intensity at 1282 and 1309 cm^{-1} can also be recognized. A strong peak is then detected at about 1585 cm^{-1}, accompanied by two weak side bands at 1555 cm^{-1} and 1621 cm^{-1}. Notice that the side band at 1555 cm^{-1} is just barely detectable in commercial MEH-PPV. The Raman shifts of all sample are summarized in Table A.1. Moreover, ti can be noticed that the Raman spectrum of sMEH-PPV film is superimposed to an interference fringes pattern, suggesting its better optical quality with respect to MEH-PPV film. No significant difference is observed in the Raman shift of the vibrational modes of all the samples, the slight discrepancies between the values reported in Table A.1 being within the spectrometer experimental resolution.

The Raman spectrum of MEH-PPDFV reported in Figure A.3 contains fewer bands compared to that of MEH-PPV (Figure A.2). Three very weak bands are observed at 934, 1000, 1038 cm^{-1}. At 1320 cm^{-1} a strong band is detected, which is anticipated by a broad shoulder, setting off around 1250 cm^{-1}. A band at 1564 cm^{-1} of weak/medium intensity is observed and it is followed by a very strong band at 1611 cm^{-1}. Finally, a strong and broad band at 1689 cm^{-1} is detected. The Raman shifts of the vibrational modes of MEH-PPDFV are listed in Table A.2 together with their intensities.

Comparing between the spectra of MEH-PPV and MEH-PPDFV a few difference are obvious. First, the mode attribute to vinylene stretching [157] in MEH-PPV is located at 1621 cm^{-1}, whereas in MEH-PPDFV the same vibration gives rise to a strongly broadened and intense band at 1688 cm^{-1}. Its broad shape, strong intensity and relative shift to higher wavenumbers are the major fingerprint of the fluorinated systems.

In the region between 1250 and 1350 cm^{-1}, experimental data show two bands of medium intensity for MEH-PPV while for MEH-PPDFV a strong band accompanied by a broad shoulder at smaller Raman shifts appears.

An additional difference between the two polymers concerns the relative intensities of the bands belonging to the group of modes between 1500 and 1800 cm^{-1} [1]. In the experimental spectrum of MEH-PPV, the band at 1555 cm^{-1} is very weak with respect to the strong band at 1585 cm^{-1}. Instead, for MEH-PPDFV the intensity of the mode at 1564 cm^{-1} relative to that of the strongest mode at 1611 cm^{-1} is much higher.

[1] These modes arise from phenylene stretching vibrations [157].

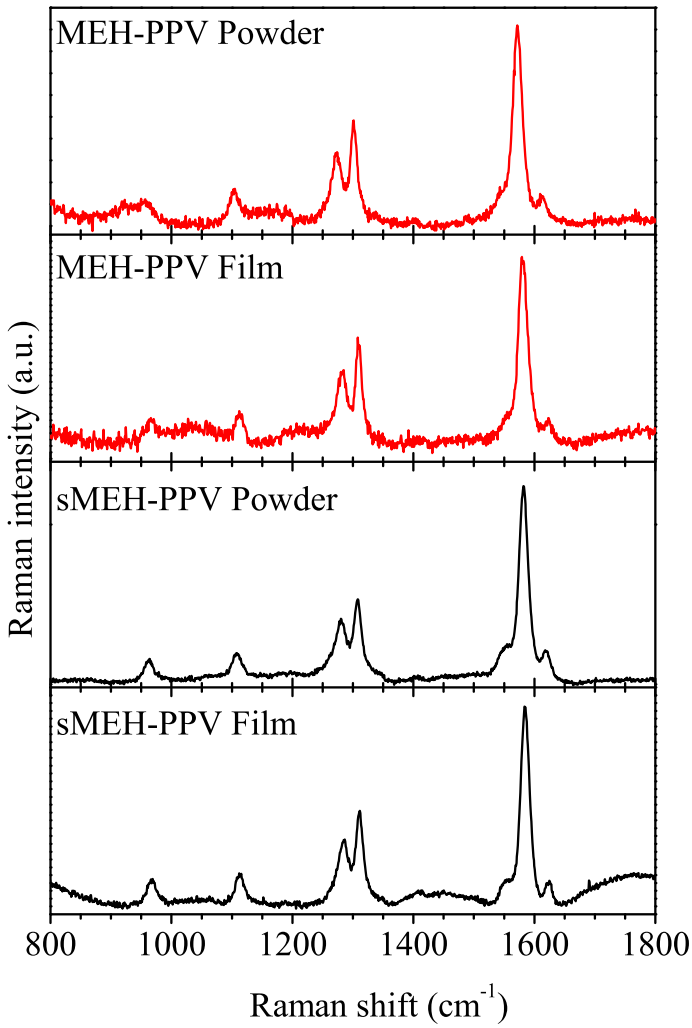

Figure A.2: Raman spectra of commercial MEH-PPV (upper panels, red) and sMEH-PPV (lower panels, black), both powder and film.

Table A.1: Raman shift (cm^{-1}) of the vibrational modes of MEH-PPV and sMEH-PPV, both powders and films. Intensities are indicated as vw=very weak, w=weak, m=medium, s=strong.

MEH-PPV powder	957 w	1104 w	1272 m	1301 m		1572 s	1611 w
MEH-PPV film	968 w	1110 w	1282 m	1309 m		1581 s	1624 w
sMEH-PPV powder	962 w	1108 w	1280 m	1308 m	1552 vw	1582 s	1620 w
sMEH-PPV film	967 w	1112 w	1286 m	1311 m	1553 vw	1584 s	1620 w

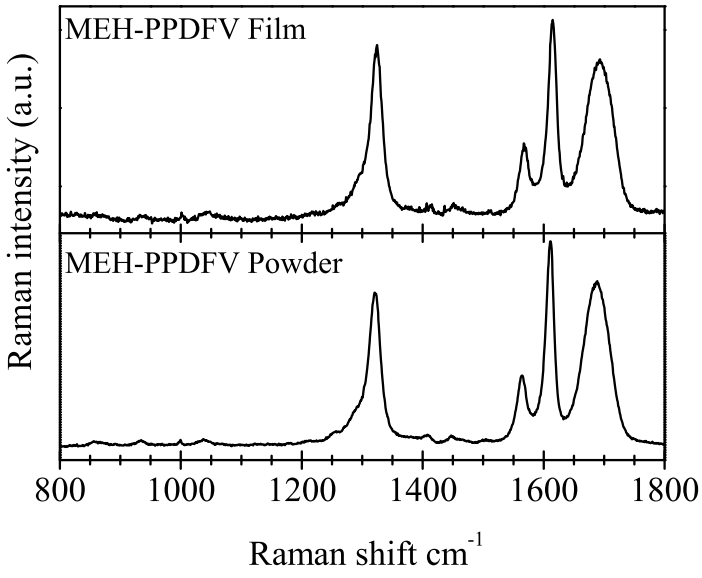

Figure A.3: Raman spectra of MEH-PPDFV, both powder and film.

Table A.2: Raman shift (cm^{-1}) of the vibrational modes of MEH-PPDFV, both powder and film. Intensities are indicated as vw=very weak, w=weak, m=medium, s=strong, vs=very strong.

MEH-PPDFV powder	934 vw	1000 vw	1038 vw	1320 s	1564 w/m	1611 vs	1689 s
MEH-PPDFV film	937 vw	1003 vw	1040 vw	1324 s	1567 w/m	1615 vs	1692 s

The differences observed between MEH-PPV and MEH-PPDFV spectra can be in principle due to different interdependent effects such as conjugation length, mass of the vinylene substituents (larger for the fluorinated polymer) or changes in the molecular structure/conformation due to fluorination.

In order to better understand the vibrational properties of both MEH-PPV and MEH-PPDFV, quantum chemical calculations were performed by Dr. M. Piacenza, National Nanotechnology Laboratory (NNL) of CNR-INFM, Università del Salento.

Fluorinated and non fluorinated trimer oligomers were used as main computational models, the main difference between these two molecular geometries being the torsional angles. The fluorinated trimer is indeed much more twisted then the non fluorinated compound due to the steric repulsion between the alkoxy groups and the fluorine atoms [158].

An overall good agreement between experimental spectra of MEH-PPV and theoretical calculations for the trimers and their fluorinated counterparts is found, thus allowing to assign the experimental bands to specific normal modes [157]. Nonetheless, a few minor discrepancies between measured and

calculated relative intensities are observed. In particular:

- in the calculated spectrum for MEH-PPV the band at 1555 cm^{-1} and appears like a very weak shoulder;
- theoretical calculations for MEH-PPDFV could not reproduce neither the intensity ratio between the bands at 1611 cm^{-1} and at 1689 cm^{-1}, nor the broad shape of the mode[2] at 1689 cm^{-1}. While in experimental spectra the 1611 cm^{-1} mode is the most intense, in simulated spectra a reversed situation occurs.

Discrepancies between experimental and calculated spectra might be attributed to different aggregation state for experiments (solid state samples) and theory (gas phase), and to the considerably different conjugation lengths of samples and model systems.

To clarify the role played by each of these issues, additional calculations were performed for fluorinated and non fluorinated dimer models. The comparison between the results obtained for dimer and trimer can be useful to address the effect of conjugation length on the vibrational properties of our samples. Moreover, the Raman spectra of distyrylbenzene and tetra-fluorinated distyrylbenzene (named DSB and DSBF, respectively) were also simulated. These almost planar structures correspond to bare phenylenevinylene trimers where all alkoxy substituents are replaced by hydrogen atoms, in order to simulate unsubstituted oligophenylene vinylenes. The details of the model systems used for simulations are described in [157].

Focusing only on the spectral region between 1500 and 1800 cm^{-1}, we will refer to the three bands there observed as LB, MB and HB, in order of increasing Raman shift.

Comparison between theoretical Raman spectra of the *non fluorinated* dimer, trimer and DSB shows minor differences in the frequency of MB. Instead, significant variations are observed both in the position and intensity of the side bands, LB and HB). This suggests that a complicate interplay between conjugation length and substituent characteristics affects bands intensities. In particular, the increase of oligomer length mainly affects the intensities of MB and HB for the dimer and trimer model. The relative intensity of HB decreases with increasing conjugation length, in good agreement both with experimental observations, where the band at 1621 cm^{-1} is much weaker than the one at 1585 cm^{-1}, and with previous theoretical findings in PPV [81, 88, 93], its oligomers [159] as well as in polyfluorene [83]. This trend of intensities vs conjugation length is similar for the fluorinated species.

The relative intensity of MB is very weak in the *fluorinated* dimer and increases in the trimer. This matches the experimental findings for the polymer (Figure A.3). Thus the intensity ratio of MB and HB is a sensitive indicator of the conjugation length for the investigated structures and can be used to

[2]The Raman mode at 1689 cm^{-1} is attributed to a vinylene stretching mode.

further characterize MEH-PPDFV in addition to the usual study of Raman shifts.

In spite of these good results, we notice that conjugation length effects alone cannot explain the experimental broadening of mode located at 1689 cm^{-1}. We are thus lead to consider the role of fluorine substituents and their effect on the relative intensity of MB and LB. Difference in these values are obtained in theoretical spectra. In particular, the non fluorinate trimer, DSB and DSBF have very similar Raman shifts, shapes and relative intensities of the bands, very close to the experimental Raman spectrum of MEH-PPV (Figure A.2). On the other hand, the spectrum of the fluorinated trimer is totally different, showing the highest intensity for the band HB. This behavior is likely to be related to the different molecular geometries of these systems: indeed, non fluorinate trimer, DSB and DSBF are approximately planar, while the fluorinated trimer is instead strongly distorted. As a consequence of the repulsive interaction between the fluorine and the neighbouring bulky alkoxy substituents, a strong shift of the bands and a remarkable change in their relative intensities occur, which should be reflected in the experimental results. As a matter of fact, when MEH-PPDFV macromolecules are aggregated, they show a distribution of torsional angles, which in turn gives rise to a distribution of frequencies (40-60 cm^{-1} according to model systems here considered) for HB, assigned to the vinylene CC stretching. This causes the inhomogeneous broadening of this mode observed in the experimental spectrum in Figure A.3. Notice also that the distribution of CC vinylene stretching rearranges the oscillator strength of each mode, reducing the peak intensity of HB. This explains the remarkable difference between the theoretical intensity ratio between MB and HB in the fluorinated trimer and its experimental value. According to this interpretation, we point out that our MEH-PPDFV samples possess a very short conjugation length, in agreement with previous findings based on electronic spectroscopy [158, 160].

A.4 Conclusions

The vibrational properties of two soluble derivatives of PPV are reported and discussed. The experimental results show that differences are observed between MEH-PPV and MEH-PPDFV spectra, mainly due to different interdependent effects such as conjugation length, mass of the vinylene substituents (larger for the fluorinated polymer) or changes in the molecular structure/conformation due to fluorination.

Raman spectra of both polymers have been assigned on the basis of quantum chemical calculations of corresponding dimer and trimer as well as of DSB and DSBF.

Major characteristic differences between non fluorinated and fluorinated structures deal with the intensity, frequency shift and broadening of CC vinylene stretching. Additional differences concern the relative intensity of CC

phenylene and vinylene CC stretchings as well as to deformation modes between 1250 and 1350 cm^{-1}. We demonstrated that significant differences in the spectra of MEH-PPV and MEH-PPDFV stem from changes of the molecular geometry and can be attributed to the larger distortion from planarity of the fluorinated species due to repulsive interactions between fluorine atoms on the vinylene units and oxygen atoms of the alkoxy groups bonded to the aromatic rings.

A.5 Acknowledgments

Thanks to Prof. Dr. G.M. Farinola for the synthesis of MEH-PPV and MEH-PPDFV, and to Dr. M. Piacenza, Prof. Dr. G. Gigli, and Dr. F. Della Sala for theoretical calculations.

Financial support for this work is from the Ministry of Instruction University and Research thorough the project *Fondo Investimenti per la Ricerca di Base*, FIRB 2003 n. RBNE03S7XZ, "Synergy".

Acknowledgements

This work would not have been possible without the help of many people.

I gratefully acknowledge both my Italian supervisors. Thanks to Davide Comoretto for his enlightening and enlightened guidance, and for being always willing to share his knowledge with me. Thanks to Franco Marabelli for helping me getting out the dark tunnel of fitting, and for stimulating discussions.

I am grateful to the people that over these 3 years worked in my lab: they all contributed to make me enjoy this period. I am particularly indebt with Matteo, who gave me the know-how about DACs and helped me getting out of troubles many times. Thanks to Pietro for getting me started with μ-Raman. Thanks to Michele, among other things, for solving my LateX problems and supporting my epiphanies (see cover page), and to Ale, for finding the time, while writing her own thesis, to unify the controversial issue of theses layout.

I spent 7 months out of the country during my PhD. In Salt Lake City, I found a great advisor in Valy Vardeny, who enormously supported me and whose scientific guidance allowed me to learn more than I could have ever imagined. Though when I was there, I thought Wednesday would have been a better day, now I definitely miss our *Monday-morning-group-meeting*!

I'm deeply indebt with Josh, who had the patience of teaching me how to use his complicated set-up and a lot more (including English). I wish I could return the favor one day. I'm also grateful to Tomer and Golda for being so nice to help me with cw-PA any time I needed it, and for chatting and laughing together. Thanks to Randy, whom I bothered more than anyone else, and to Leonard for helping overcoming an impasse with the pressure transmitting medium. Thanks to Maria, for the time shared outside the lab, and to Alex, Fujian, and Sanjeev.

Finally, I acknowledge Prof.Bongiovanni, for finding the time to read my thesis and for his interesting and helpful comments.

Bibliography

[1] M. Pope and C. Swenberg. *Electronic processes in organic crystals*. Clarendon Press Oxford University Press, Oxford, New York, 1982.

[2] C. K. Chiang, C. R. Fincher, Y. W. Park, A. J. Heeger, H. Shirakawa, E. J. Louis, S. C. Gau, and A. G. MacDiarmid. Electrical Conductivity in Doped Polyacetylene. *Phys. Rev. Lett.*, **39** (17): 1098–1101, Oct 1977.

[3] J. Burroughes, D. Bradley, A. Brown, R. Marks, K. Mackay, R. Friend, P. Burns, and A. Holmes. Light-emitting diodes based on conjugated polymers. *Nature*, **347** (6293): 539–541, 1990.

[4] R. Friend, R. Gymer, A. Holmes, J. Burroughes, R. Marks, C. Taliani, D. Bradley, D. Dos Santos, J. Bredas, and M. Loegdlun. Electroluminescence in conjugated polymers. *Nature*, **397** (6715): 121–128, 1999.

[5] H. Sirringhaus, P. Brown, R. Friend, M. Nielsen, K. Bechgaard, B. Langeveld-Voss, A. Spiering, and R. Janssen. Two-dimensional charge transport in self-organized, high-mobility conjugated polymers. *Nature*, **401** (6754): 685–688, 1999.

[6] H. Sirringhaus, N. Tessler, and R. Friend. Integrated Optoelectronic Devices Based on Conjugated Polymers. *Science*, **280** (5370): 1741, 1998.

[7] Y. Kim, S. Cook, S. Tuladhar, S. Choulis, J. Nelson, J. Durrant, D. Bradley, M. Giles, I. McCulloch, C. Ha, et al. A strong regioregularity effect in self-organizing conjugated polymer films and high-efficiency polythiophene: fullerene solar cells. *Nature Materials*, **5** (3): 197, 2006.

[8] C. Brabec, N. Sariciftci, and J. Hummelen. Plastic Solar Cells. *Advanced Functional Materials*, **11** (1): 15–26, 2001.

[9] G. Dennler and N. Sariciftci. Flexible conjugated polymer-based plastic solar cells: from basics to applications. *Proceedings of the IEEE*, **93** (8): 1429–1439, 2005.

[10] S. Jenekhe and J. Osaheni. Excimers and Exciplexes of Conjugated Polymers. *Science*, **265** (5173): 765–768, 1994.

[11] I. D. W. Samuel, G. Rumbles, and C. J. Collison. Efficient interchain photoluminescence in a high-electron-affinity conjugated polymer. *Phys. Rev. B*, **52** (16): R11573–R11576, Oct 1995.

[12] R. Jakubiak, C. Collison, L. Rothberg, and B. Hsieh. Aggregation Quenching of Luminescence in Electroluminescent Conjugated Polymers. *Journal of Physical Chemistry A*, **103**: 2394–2398, 1999.

[13] U. Lemmer, S. Heun, R. Mahrt, U. Scherf, M. Hopmeier, U. Siegner, E. Gö bel, K. Mü llen, and H. Bä ssler. Aggregate fluorescence in conjugated polymers. *Chemical Physics Letters*, **240** (4): 373–378, 1995.

[14] J. W. Blatchford, S. W. Jessen, L.-B. Lin, T. L. Gustafson, D.-K. Fu, H.-L. Wang, T. M. Swager, A. G. MacDiarmid, and A. J. Epstein. Photoluminescence in pyridine-based polymers: Role of aggregates. *Phys. Rev. B*, **54** (13): 9180–9189, Oct 1996.

[15] C. Collison, L. Rothberg, V. Treemaneekarn, and Y. Li. Conformational Effects on the Photophysics of Conjugated Polymers: A Two Species Model for MEH-PPV Spectroscopy and Dynamics. *Macromolecules*, **34** (7): 2346–2352, 2001.

[16] G. Gelinck, J. Warman, and E. Staring. Polaron Pair Formation, Migration, and Decay on Photoexcited Poly (phenylenevinylene) Chains. *Journal of Physical Chemistry*, **100**: 5485–5491, 1996.

[17] W. Graupner, G. Leising, G. Lanzani, M. Nisoli, S. De Silvestri, and U. Scherf. Femtosecond relaxation of photoexcitations in a solution of a poly (para-phenylene)-type ladder polymer. *Chemical Physics Letters*, **246** (1-2): 95–100, 1995.

[18] J. W. Blatchford, S. W. Jessen, L. B. Lin, J. J. Lih, T. L. Gustafson, A. J. Epstein, D. K. Fu, M. J. Marsella, T. M. Swager, A. G. MacDiarmid, S. Yamaguchi, and H. Hamaguchi. Exciton Dynamics in Poly(p-Pyridyl Vinylene). *Phys. Rev. Lett.*, **76** (9): 1513–1516, Feb 1996.

[19] M. Yan, L. J. Rothberg, E. W. Kwock, and T. M. Miller. Interchain Excitations in Conjugated Polymers. *Phys. Rev. Lett.*, **75** (10): 1992–1995, Sep 1995.

[20] B. Schwartz, F. Hide, M. Andersson, and A. Heeger. Ultrafast studies of stimulated emission and gain in solid films of conjugated polymers. *Chemical Physics Letters*, **265** (3-5): 327–333, 1997.

[21] T. Skotheim and J. Reynolds. *Handbook of Conducting Polymers*. CRC, 2007.

[22] N. Greenham, I. Samuel, G. Hayes, R. Phillips, Y. Kessener, S. Moratti, A. Holmes, and R. Friend. Measurement of absolute photoluminescence quantum efficiencies in conjugated polymers. *Chemical Physics Letters*, **241** (1-2): 89–96, 1995.

[23] M. Yan, L. J. Rothberg, F. Papadimitrakopoulos, M. E. Galvin, and T. M. Miller. Spatially indirect excitons as primary photoexcitations in conjugated polymers. *Phys. Rev. Lett.*, **72** (7): 1104–1107, Feb 1994.

[24] B. Schwartz. Conjugated polymers as molecular materials: How Chain Conformation and Film Morphology Influence Energy Transfer and Interchain Interactions. *Annual Reviews in Physical Chemistry*, **54** (1): 141–172, 2003.

[25] W. Barford. *Electronic and Optical Properties of Conjugated Polymers*. Oxford University Press, USA, 2005.

[26] D. Bloor, R. Chance, and P. of the NATO Advanced Research Workshop on Polydiacetylenes. *Polydiacetylenes*. Nijhoff, 1985.

[27] H. Shirakawa, E. Louis, A. MacDiarmid, C. Chiang, and A. Heeger. Synthesis of electrically conducting organic polymers: halogen derivatives of polyacetylene,(CH) x. *Journal of the Chemical Society, Chemical Communications*, **1977** (16): 578–580, 1977.

[28] F. Hide, M. Diaz-Garcia, B. Schwartz, and A. Heeger. New Developments in the Photonic Applications of Conjugated Polymers. *Accounts of Chemical Research*, **30**: 430–436, 1997.

[29] J. Halls, C. Walsh, N. Greenham, E. Marseglia, R. Friend, S. Moratti, and A. Holmes. Efficient photodiodes from interpenetrating polymer networks. *Nature*, **376** (6540): 498–500, 1995.

[30] G. Yu, J. Gao, J. Hummelen, F. Wudl, and A. Heeger. Polymer Photovoltaic Cells: Enhanced Efficiencies via a Network of Internal Donor-Acceptor Heterojunctions. *Science*, **270** (5243): 1789, 1995.

[31] H. Sirringhaus, T. Kawase, R. Friend, T. Shimoda, M. Inbasekaran, W. Wu, and E. Woo. High-Resolution Inkjet Printing of All-Polymer Transistor Circuits, 2000.

[32] P. Bruice. *Organic Chemistry*. Prentice Hall Upper Saddle River, NJ, 2001.

[33] N. Ashcroft and N. Mermin. *Solid state physics*. New York, 1976.

[34] F. Bassani and U. Grassano. *Fisica dello stato solido*. 2000.

[35] F. Meinardi, M. Cerminara, A. Sassella, A. Borghesi, P. Spearman, G. Bongiovanni, A. Mura, and R. Tubino. Intrinsic Excitonic Luminescence in Odd and Even Numbered Oligothiophenes. *Phys. Rev. Lett.*, **89** (15): 157403, Sep 2002.

[36] J. Mort and G. Pfister. *Electronic properties of polymers*. Wiley, 1982.

[37] R. Peierls. Quantum Theory ofSolids, 1955.

[38] W. P. Su, J. R. Schrieffer, and A. J. Heeger. Soliton excitations in polyacetylene. *Phys. Rev. B*, **22** (4): 2099–2111, Aug 1980.

[39] W. P. Su, J. R. Schrieffer, and A. J. Heeger. Solitons in Polyacetylene. *Phys. Rev. Lett.*, **42** (25): 1698–1701, Jun 1979.

[40] A. Heeger, S. Kivelson, J. Schrieffer, and W. Su. Solitons in conducting polymers. *Reviews of Modern Physics*, **60** (3): 781–850, 1988.

[41] L. Rossi, S. Alvarado, W. Rieß, S. Schrader, D. Lidzey, and D. Bradley. Influence of alkoxy substituents on the exciton binding energy of conjugated polymers. *Synthetic Metals*, **111**: 527–530, 2000.

[42] S. Barth and H. Bässler. Intrinsic Photoconduction in PPV-Type Conjugated Polymers. *Phys. Rev. Lett.*, **79** (22): 4445–4448, Dec 1997.

[43] J. M. Leng, S. Jeglinski, X. Wei, R. E. Benner, Z. V. Vardeny, F. Guo, and S. Mazumdar. Optical probes of excited states in poly(p-phenylenevinylene). *Phys. Rev. Lett.*, **72** (1): 156–159, Jan 1994.

[44] M. Chandross, S. Mazumdar, M. Liess, P. A. Lane, Z. V. Vardeny, M. Hamaguchi, and K. Yoshino. Optical absorption in the substituted phenylene-based conjugated polymers: Theory and experiment. *Phys. Rev. B*, **55** (3): 1486–1496, Jan 1997.

[45] D. Moses, J. Wang, A. Heeger, N. Kirova, and S. Brazovski. Exciton binding energy in poly (phenylene vinylene). *Synthetic Metals*, **125** (1): 93–98, 2001.

[46] K. Hummer, P. Puschnig, and C. Ambrosch-Draxl. Lowest Optical Excitations in Molecular Crystals: Bound Excitons versus Free Electron-Hole Pairs in Anthracene. *Phys. Rev. Lett.*, **92** (14): 147402, Apr 2004.

[47] N. T. Harrison, G. R. Hayes, R. T. Phillips, and R. H. Friend. Singlet Intrachain Exciton Generation and Decay in Poly(*p*-phenylenevinylene). *Phys. Rev. Lett.*, **77** (9): 1881–1884, Aug 1996.

[48] J. Bredas, J. Cornil, and A. Heeger. The exciton binding energy in luminescent conjugated polymers. *Advanced materials(Weinheim)*, **8** (5): 447–452, 1996.

[49] J. Birks and L. Christophorou. Excimer Fluorescence of Aromatic Hydrocarbons in Solution. *Nature*, **194** (4827): 442–444, 1962.

[50] D. D. Gebler, Y. Z. Wang, D.-K. Fu, T. M. Swager, and A. J. Epstein. Exciplex emission from bilayers of poly(vinyl carbazole) and pyridine based conjugated copolymers. *The Journal of Chemical Physics*, **108** (18): 7842–7848, 1998.

[51] D. Comoretto, G. Dellepiane, G. F. Musso, R. Tubino, R. Dorsinville, A. Walser, and R. R. Alfano. Interchain interactions in polyacetylene: Optical properties and photoconductive response. *Phys. Rev. B*, **46** (16): 10041–10047, Oct 1992.

[52] A. Ruini, M. J. Caldas, G. Bussi, and E. Molinari. Solid State Effects on Exciton States and Optical Properties of PPV. *Phys. Rev. Lett.*, **88** (20): 206403, May 2002.

[53] P. Puschnig and C. Ambrosch-Draxl. Suppression of Electron-Hole Correlations in 3D Polymer Materials. *Phys. Rev. Lett.*, **89** (5): 056405, Jul 2002.

[54] G. Bussi, A. Ruini, E. Molinari, M. Caldas, P. Puschnig, and C. Ambrosch-Draxl. Interchain interaction and Davydov splitting in polythiophene crystals: An ab initio approach. *Applied Physics Letters*, **80**: 4118, 2002.

[55] A. Ferretti, A. Ruini, E. Molinari, and M. Caldas. Electronic Properties of Polymer Crystals: The Effect of Interchain Interactions. *Physical Review Letters*, **90** (8): 86401, 2003.

[56] F. Wooten and S. Davis. *Optical Properties of Solids*, volume 41. AAPT, 1973.

[57] C. Yang, K. Lee, and A. Heeger. Tensile drawing induced symmetry in poly (p-phenylene vinylene) films. *Journal of Molecular Structure*, **521** (1-3): 315–323, 2000.

[58] K. Ho Peter and R. Friend. p-Electronic and Electrical Transport Properties of Conjugated Polymer Nanocomposites: Poly p-Phenylenevinylene with Homogeneously Dispersed Silica Nanoparticles. *J. Chem. Phys*, **116**: 6782, 2002.

[59] R. Chang, J. Hsu, W. Fann, J. Yu, S. Lin, Y. Lee, and S. Chen. Aggregated states of luminescent conjugated polymers in solutions. *Chemical Physics Letters*, **317** (1-2): 153–158, 2000.

[60] L. Merrill and W. Bassett. Miniature diamond anvil pressure cell for single crystal X-ray diffraction studies. Reu. *Sci. Instrum*, pages 45–290, 1974.

[61] A. Jayaraman. Diamond anvil cell and high-pressure physical investigations. *Reviews of Modern Physics*, **55** (1): 65–108, 1983.

[62] A. Van Valkenburg. Conference Internationale Sur-les-Hautes Pressions. *LeCreusot, Saone-et-Loire, France*, 1965.

[63] R. Forman, G. Piermarini, J. Barnett, and S. Block. Pressure Measurement Made by the Utilization of Ruby Sharp-Line Luminescence, 1972.

[64] G. J. Piermarini, S. Block, J. D. Barnett, and R. A. Forman. Calibration of the pressure dependence of the R_1] ruby fluorescence line to 195 kbar. *Journal of Applied Physics*, **46** (6): 2774–2780, 1975.

[65] G. Piermarini and S. Block. Ultrahigh pressure diamond-anvil cell and several semiconductor phase transition pressures in relation to the fixed point pressure scale. *Review of Scientific Instruments*, **46**: 973, 1975.

[66] P. Wong and D. Moffat. A New Internal Pressure Calibrant for High-Pressure Infrared Spectroscopy of Aqueous Systems. *Applied Spectroscopy*, **43** (7): 1279–1281, 1989.

[67] E. Hecht. *Optics*. Addison-Wesley, 1998.

[68] A. Lang. Causes of Birefringence in Diamond. *Nature*, **213** (5073): 248–251, 1967.

[69] P. Griffiths. Fourier transform infrared spectrometry. *Science*, **222** (4621): 297–302, 1983.

[70] C. Botta, S. Luzzati, R. Tubino, D. D. C. Bradley, and R. H. Friend. Photoinduced absorption of polymer solutions. *Phys. Rev. B*, **48** (20): 14809–14817, Nov 1993.

[71] J. Roncali, P. Marque, R. Garreau, F. Garnier, and M. Lemaire. Structural control of conjugation in functionalized polythiophenes. *Macromolecules*, **23** (5): 1347–1352, 1990.

[72] G. Heimel, P. Puschnig, M. Oehzelt, K. Hummer, B. Koppelhuber-Bitschnau, F. Porsch, C. Ambrosch-Draxl, and R. Resel. Chain-length-dependent intermolecular packing in polyphenylenes: a high pressure study. *Journal of Physics, Condensed Matter*, **15** (20): 3375–3389, 2003.

[73] S. Guha, W. Graupner, S. Yang, M. Chandrasekhar, H. Chandrasekhar, and G. Leising. Optical Properties of Poly (Para-Phenylenes) under High Pressure. *physica status solidi(b)*, **211** (1): 177–188, 1999.

[74] M. Chandrasekhar, S. Guha, and W. Graupner. Squeezing Organic Conjugated Molecules-What Does One Learn? *Adv. Mater*, **13** (8): 18, 2001.

[75] J. Mardalen, Y. Cerenius, and P. Haggkvist. The crystalline structure of poly (3-octylthiophene) at high pressure. *Journal of Physics: Condensed Matter*, **7**: 3501–3506, 1995.

[76] K. Zhuravlev and M. McCluskey. Flattening of organic molecules under pressure. *The Journal of Chemical Physics*, **114**: 5465, 2001.

[77] J. Maardalen, E. Samuelsen, O. Konestaho, M. Hanfland, and M. Lorenzen. Conducting polymers under pressure: syuchrotron x-ray determined structure and structure related properties of two forms of poly (octylthiophene). *Journal of Physics Condensed Matter*, **10**: 7145–7154, 1998.

[78] T. Kaniowski, S. Nizioł, J. Sanetra, M. Trznadel, and A. Proń. Optical studies of regioregular poly (3-octylthiophene) s under pressure. *Synthetic Metals*, **94** (1): 111–114, 1998.

[79] S. Webster and D. Batchelder. Absorption, luminescence and Raman spectroscopy of poly (p-phenylene vinylene) at high pressure. *Polymer(Guildford)*, **37** (22): 4961–4968, 1996.

[80] E. Mulazzi, A. Ripamonti, J. Very, B. Dulieu, E. Faulques, and S. Lefrant. Optical Properties of PPV and PPP Polymers. *Synthetic Metals*, **101** (1-3): 196–197, 1999.

[81] E. Mulazzi, A. Ripamonti, J. Wery, B. Dulieu, and S. Lefrant. Theoretical and experimental investigation of absorption and Raman spectra of poly(paraphenylene vinylene). *Phys. Rev. B*, **60** (24): 16519–16525, Dec 1999.

[82] Q. Zeng, Z. Ding, X. Tang, and Z. Zhang. Pressure effect on photoluminescence and Raman spectra of PPV. *Journal of Luminescence*, **115** (1-2): 32–38, 2005.

[83] J. Schmidtke, J. Kim, J. Gierschner, C. Silva, and R. Friend. Optical Spectroscopy of a Polyfluorene Copolymer at High Pressure: Intra-and Intermolecular Interactions. *Physical Review Letters*, **99** (16): 167401, 2007.

[84] D. Comoretto, G. Dellepiane, D. Moses, J. Cornil, D. dos Santos, and J. Brédas. Polarized reflectivity spectra of stretch-oriented poly (p-phenylene-vinylene). *Chemical Physics Letters*, **289** (1-2): 1–7, 1998.

[85] M. Galli, F. Marabelli, and D. Comoretto. Interferometric determination of the anisotropic refractive index dispersion of poly-(p-phenylene-vinylene). *Applied Physics Letters*, **86**: 201119, 2005.

[86] V. Morandi, C. Soci, M. Galli, F. Marabelli, and D. Comoretto. Optical probes of electronic states in highly anisotropic polymeric semiconductors. *Conference Proceedings-Italian Physical Society*, **94**: 75, 2007.

[87] C. Soci, D. Comoretto, F. Marabelli, and D. Moses. Anisotropic photoluminescence properties of oriented poly (p-phenylene-vinylene) films: Effects of dispersion of optical constants. *Physical Review B*, **75** (7): 75204, 2007.

[88] I. Orion, J. Buisson, and S. Lefrant. Spectroscopic studies of polaronic and bipolaronic species in n-doped poly (paraphenylenevinylene). *Physical Review B*, **57** (12): 7050–7065, 1998.

[89] D. Moses, A. Feldblum, E. Ehrenfreund, A. J. Heeger, T. C. Chung, and A. G. MacDiarmid. Pressure dependence of the photoabsorption of polyacetylene. *Phys. Rev. B*, **26** (6): 3361–3369, Sep 1982.

[90] L. X. Zheng, B. C. Hess, R. E. Benner, Z. V. Vardeny, and G. L. Baker. Resonant Raman-scattering spectroscopy of polydiacetylene films at high pressure. *Phys. Rev. B*, **47** (6): 3070–3077, Feb 1993.

[91] E. Samuelsen, J. MÍrdalen, O. Konestabo, M. Hanfland, and M. Lorenzen. Poly (octyl-thiophene) polymorphs under high pressure: Synchrotron X-Rays studies and the relation with spectral behaviour. *Synthetic Metals*, **101** (1-3): 98–99, 1999.

[92] D. Comoretto, G. Dellepiane, F. Marabelli, J. Cornil, D. A. dos Santos, J. L. Brédas, and D. Moses. Optical constants of highly stretch-oriented poly(p-phenylene-vinylene): A joint experimental and theoretical study. *Phys. Rev. B*, **62** (15): 10173–10184, Oct 2000.

[93] E. Mulazzi, C. Botta, D. Facchinetti, and A. Bolognesi. Evidence of conjugation length distributions in electroluminescent segmented PPV: absorption, photoluminescence and Raman scattering. *Synthetic Metals*, **142** (1-3): 85–92, 2004.

[94] G. Yi, V. Manoharan, S. Klein, K. Brzezinska, D. Pine, F. Lange, and S. Yang. Monodisperse Micrometer-Scale Spherical Assemblies of Polymer Particles. *Advanced Materials*, **14** (16): 1137, 2002.

[95] R. Mezzenga, J. Ruokolainen, G. Fredrickson, E. Kramer, D. Moses, A. Heeger, and O. Ikkala. Templating Organic Semiconductors via Self-Assembly of Polymer Colloids, 2003.

[96] N. Kirova, S. Brazovskii, and A. Bishop. A systematic theory for optical properties of phenylene-based polymers. *Synthetic Metals*, **100** (1): 29–53, 1999.

[97] S. Brazovskii, N. Kirova, A. Bishop, V. Klimov, D. McBranch, N. Barashkov, and J. Ferraris. Excitations and optical properties of phenylene-based conjugated polymers and oligomers. *Optical Materials*, **9** (1-4): 472–479, 1998.

[98] M. Chandross, S. Mazumdar, M. Liess, P. Lane, Z. Vardeny, M. Hamaguchi, and K. Yoshino. Optical absorption in the substituted phenylene-based conjugated polymers: Theory and experiment. *Physical Review B*, **55** (3): 1486–1496, 1997.

[99] M. Chandross and S. Mazumdar. Coulomb interactions and linear, nonlinear, and triplet absorption in poly (para-phenylenevinylene). *Physical Review B*, **55** (3): 1497–1504, 1997.

[100] Y. Shimoi and S. Abe. Electronic and optical properties of neutral and charged poly (p-phenylene vinylene). *Synthetic metals*, **78** (3): 219–226, 1996.

[101] J. Cornil, D. Dos Santos, D. Beljonne, and J. Bredas. Electronic Structure of Phenylene Vinylene Oligomers: Influence of Donor/Acceptor Substitutions. *The Journal of Physical Chemistry*, **99** (15): 5604–5611, 1995.

[102] M. Fahlman, M. Loegdlund, S. Stafstroem, W. Salaneck, R. Friend, P. Burn, A. Holmes, K. Kaeriyama, Y. Sonoda, F. Meyers, et al. Experimental and Theoretical Studies of the Electronic Structure of Poly (p-phenylenevinylene) and Some Ring-Substituted Derivatives. *Macromolecules*, **28** (6): 1959–1965, 1995.

[103] Y. Gartstein, M. Rice, and E. Conwell. Charge-conjugation symmetry breaking and the absorption spectra of polyphenylenes. *Physical Review B*, **51** (8): 5546–5549, 1995.

[104] Y. Gartstein, M. Rice, and E. Conwell. Electron-hole interaction effects in the absorption spectra of phenylene-based conjugated polymers. *Physical Review B*, **52** (3): 1683–1691, 1995.

[105] J. Cornil, D. Beljonne, R. Friend, and J. Brédas. Optical absorptions in poly (paraphenylene vinylene) and poly (2, 5-dimethoxy-1, 4-paraphenylene vinylene) oligomers. *Chemical Physics Letters, 223*, 1994.

[106] J. Cornil, D. Beljonne, Z. Shuia, T. Hagler, I. Campbell, D. Bradley, J. Brédas, C. Spangler, and K. Müllen. Vibronic structure in the optical absorption spectra of phenylene vinylene oligomers: a joint experimental and theoretical study. *Chemical Physics Letters*, **247** (4-6): 425–432, 1995.

[107] C. Ambrosch-Draxl and R. Abt. Optical properties of poly (p-phenylene vinylene) from first-principles calculations. *Synthetic Metals*, **85** (1-3): 1099–1100, 1997.

[108] E. Miller, D. Yoshida, C. Yang, and A. Heeger. Polarized ultraviolet absorption of highly oriented poly (2-methoxy, 5-(2ˆ{'}-ethyl)-hexyloxy) paraphenylene vinylene. *Physical Review B*, **59** (7): 4661–4664, 1999.

[109] E. Miller, C. Yang, and A. Heeger. Polarized ultraviolet absorption by a highly oriented dialkyl derivative of poly (paraphenylene vinylene). *Physical Review B*, **62** (11): 6889–6891, 2000.

[110] E. Miller, G. Maskel, C. Yang, and A. Heeger. Polarized ultraviolet absorption by an oriented derivative of poly (para-phenylene). *Physical Review B*, **60** (11): 8028–8033, 1999.

[111] J. Cornil, D. Beljonne, R. Friend, and J. Brédas. Optical absorptions in poly (paraphenylene vinylene) and poly (2, 5-dimethoxy-1, 4-paraphenylene vinylene) oligomers. *Chemical Physics Letters, 223*, **223** (1): 82–88, 1994.

[112] M. Chandross, S. Mazumdar, M. Liess, P. A. Lane, Z. V. Vardeny, M. Hamaguchi, and K. Yoshino. Optical absorption in the substituted phenylene-based conjugated polymers: Theory and experiment. *Phys. Rev. B*, **55** (3): 1486–1496, Jan 1997.

[113] M. Chandross and S. Mazumdar. Coulomb interactions and linear, nonlinear, and triplet absorption in poly(para-phenylenevinylene). *Phys. Rev. B*, **55** (3): 1497–1504, Jan 1997.

[114] M. Kasha. Energy transfer mechanisms and the molecular exciton model for molecular aggregates. *Radiat. Res*, **20** (1): 55, 1963.

[115] K. Baldwin and D. Batchelder. Confocal Raman Microspectroscopy through a Planar Interface.

[116] C. Soci, D. Comoretto, F. Marabelli, and D. Moses. Polarized photoluminescence of highly oriented poly(p-phenylene-vinylene). volume 5517, pages 98–105. SPIE, 2004.

[117] J. Clark, C. Silva, R. H. Friend, and F. C. Spano. Role of Intermolecular Coupling in the Photophysics of Disordered Organic Semiconductors: Aggregate Emission in Regioregular Polythiophene. *Physical Review Letters*, **98** (20): 206406, 2007.

[118] M. Theander, M. Svensson, A. Ruseckas, D. Zigmantas, V. Sundström, M. Andersson, and O. Inganäs. High luminescence from a substituted polythiophene in a solvent with low solubility. *Chemical Physics Letters*, **337** (4-6): 277–283, 2001.

[119] D. Chen, M. Winokur, M. Masse, and F. Karasz. A structural study of poly (p-phenylene vinylene). *Polymer(Guildford)*, **33** (15): 3116–3122, 1992.

[120] E. K. Miller, C. Y. Yang, and A. J. Heeger. Polarized ultraviolet absorption by a highly oriented dialkyl derivative of poly(paraphenylene vinylene). *Phys. Rev. B*, **62** (11): 6889–6891, Sep 2000.

[121] E. K. Miller, G. S. Maskel, C. Y. Yang, and A. J. Heeger. Polarized ultraviolet absorption by an oriented derivative of poly(para-phenylene). *Phys. Rev. B*, **60** (11): 8028–8033, Sep 1999.

[122] E. K. Miller, D. Yoshida, C. Y. Yang, and A. J. Heeger. Polarized ultraviolet absorption of highly oriented poly(2-methoxy, 5-(2′-ethyl)-hexyloxy) paraphenylene vinylene. *Phys. Rev. B*, **59** (7): 4661–4664, Feb 1999.

[123] G. Heimel, K. Hummer, C. Ambrosch-Draxl, W. Chunwachirasiri, M. J. Winokur, M. Hanfland, M. Oehzelt, A. Aichholzer, and R. Resel. Phase transition and electronic properties of fluorene: A joint experimental and theoretical high-pressure study. *Physical Review B (Condensed Matter and Materials Physics)*, **73** (2): 024109, 2006.

[124] P. Puschnig, K. Hummer, C. Ambrosch-Draxl, G. Heimel, M. Oehzelt, and R. Resel. Electronic, optical, and structural properties of oligophenylene molecular crystals under high pressure: An ab initio investigation. *Phys. Rev. B*, **67** (23): 235321, Jun 2003.

[125] D. Beljonne, J. Cornil, R. Silbey, P. Millié, and J. Brédas. Interchain interactions in conjugated materials: The exciton model versus the supermolecular approach. *The Journal of Chemical Physics*, **112**: 4749, 2000.

[126] J. Cornil, D. A. dos Santos, X. Crispin, R. Silbey, and J. L. Bredas. Influence of Interchain Interactions on the Absorption and Luminescence of Conjugated Oligomers and Polymers: A Quantum-Chemical Characterization. *Journal of the American Chemical Society*, **120** (6): 1289–1299, 1998.

[127] C. Sheng, M. Tong, S. Singh, and Z. Vardeny. Experimental determination of the charge/neutral branching ratio η in the photoexcitation of π-conjugated polymers by broadband ultrafast spectroscopy. *Physical Review B*, **75** (8): 85206, 2007.

[128] R. Österbacka, X. M. Jiang, C. P. An, B. Horovitz, and Z. V. Vardeny. Photoinduced Quantum Interference Antiresonances in π-Conjugated Polymers. *Phys. Rev. Lett.*, **88** (22): 226401, May 2002.

[129] B. C. Hess, G. S. Kanner, Z. V. Vardeny, and G. L. Baker. High-pressure effects on ultrafast-relaxation kinetics of excitons in polydiacetylene 4BCMU. *Phys. Rev. Lett.*, **66** (18): 2364–2367, May 1991.

[130] B. C. Hess, G. S. Kanner, and Z. Vardeny. Photoexcitations in polythiophene at high pressure. *Phys. Rev. B*, **47** (3): 1407–1411, Jan 1993.

[131] S. Guha, W. Graupner, R. Resel, M. Chandrasekhar, H. R. Chandrasekhar, R. Glaser, and G. Leising. Planarity of para Hexaphenyl. *Phys. Rev. Lett.*, **82** (18): 3625–3628, May 1999.

[132] S.-C. Yang, W. Graupner, S. Guha, P. Puschnig, C. Martin, H. R. Chandrasekhar, M. Chandrasekhar, G. Leising, C. Ambrosch-Draxl, and U. Scherf. Geometry-Dependent Electronic Properties of Highly Fluorescent Conjugated Molecules. *Phys. Rev. Lett.*, **85** (11): 2388–2391, Sep 2000.

[133] M. A. Loi, A. Mura, G. Bongiovanni, Q. Cai, C. Martin, H. R. Chandrasekhar, M. Chandrasekhar, W. Graupner, and F. Garnier. Ultrafast Formation of Nonemissive Species via Intermolecular Interaction in Single Crystals of Conjugated Molecules. *Phys. Rev. Lett.*, **86** (4): 732–735, Jan 2001.

[134] C. Martin, S. Guha, M. Chandrasekhar, H. Chandrasekhar, R. Guentner, P. de Freitas, and U. Scherf. Hydrostatic pressure dependence of the luminescence and Raman frequencies in polyfluorene. *Physical Review B*, **68**: 115203, 2003.

[135] V. Morandi, M. Galli, F. Marabelli, and D. Comoretto. Highly Oriented Poly (Paraphenylene Vinylene): Polarized Optical Spectroscopy Under Pressure. *Phys. Rev. B*, (In press).

[136] J. P. Schmidtke, J.-S. Kim, J. Gierschner, C. Silva, and R. H. Friend. Optical Spectroscopy of a Polyfluorene Copolymer at High Pressure: Intra- and Intermolecular Interactions. *Physical Review Letters*, **99** (16): 167401, 2007.

[137] J. P. Schmidtke, R. H. Friend, and C. Silva. Tuning Interfacial Charge-Transfer Excitons at Polymer-Polymer Heterojunctions under Hydrostatic Pressure. *Physical Review Letters*, **100** (15): 157401, 2008.

[138] R. Tikhoplav and B. Hess. Effect of pressure on photoluminescence and optical absorption in meh-ppv. *Synthetic Metals*, **101** (1-3): 236–237, 1999.

[139] M. Loi, A. Mura, G. Bongiovanni, Q. Cai, C. Martin, H. Chandrasekhar, M. Chandrasekhar, W. Graupner, and F. Garnier. Ultrafast Formation of Nonemissive Species via Intermolecular Interaction in Single Crystals of Conjugated Molecules. *Physical Review Letters*, **86** (4): 732–735, 2001.

[140] S. Guha, J. Rice, C. Martin, W. Graupner, M. Chandrasekhar, H. Chandrasekhar, and U. Scherf. Optical Spectroscopic Studies of a Soluble Fluorene-Based Conjugated Polymer: A Hydrostatic Pressure and Temperature Study. In *Materials Research Society Symposium Proceedings*,

volume 708, pages 299–304. Warrendale, Pa.; Materials Research Society; 1999, 2002.

[141] T. Nguyen, V. Doan, and B. Schwartz. Conjugated polymer aggregates in solution: Control of interchain interactions. *The Journal of Chemical Physics*, **110**: 4068, 1999.

[142] J. Clark, C. Silva, R. Friend, and F. Spano. Role of Intermolecular Coupling in the Photophysics of Disordered Organic Semiconductors: Aggregate Emission in Regioregular Polythiophene. *Physical Review Letters*, **98** (20): 206406, 2007.

[143] H.-E. Tseng, C.-Y. Liu, and S.-A. Chen. Determination of aggregates as charge trapping and recombination centers in poly[2-methoxy-5-(2[sup [prime]]-ethylhexyloxy)-1,4-phenylene vinylene] by time-resolved electroluminescence spectroscopy. *Applied Physics Letters*, **89** (23): 233510, 2006.

[144] X. Wei, B. C. Hess, Z. V. Vardeny, and F. Wudl. Studies of photoexcited states in polyacetylene and poly(paraphenylenevinylene) by absorption detected magnetic resonance: The case of neutral photoexcitations. *Phys. Rev. Lett.*, **68** (5): 666–669, Feb 1992.

[145] X. Wei, Z. V. Vardeny, N. S. Sariciftci, and A. J. Heeger. Absorption-detected magnetic-resonance studies of photoexcitations in conjugated-polymer/$C60$ composites. *Phys. Rev. B*, **53** (5): 2187–2190, Feb 1996.

[146] T. Drori, E. Gershman, C. Sheng, Y. Eichen, Z. Vardeny, and E. Ehrenfreund. Illumination-induced metastable polaron-supporting state in poly (p-phenylene vinylene) films. *Physical Review B*, **76** (3): 33203, 2007.

[147] A. P. Monkman, H. D. Burrows, L. J. Hartwell, L. E. Horsburgh, I. Hamblett, and S. Navaratnam. Triplet Energies of π-Conjugated Polymers. *Phys. Rev. Lett.*, **86** (7): 1358–1361, Feb 2001.

[148] K. Voss, C. Foster, L. Smilowitz, D. Mihailović, S. Askari, G. Srdanov, Z. Ni, S. Shi, A. Heeger, and F. Wudl. Substitution effects on bipolarons in alkoxy derivatives of poly (1, 4-phenylene-vinylene). *Physical Review B*, **43** (6): 5109–5118, 1991.

[149] T. Drori, E. Gershman, C. X. Sheng, Y. Eichen, Z. V. Vardeny, and E. Ehrenfreund. Illumination-induced metastable polaron-supporting state in poly(p-phenylene vinylene) films. *Physical Review B*, **76** (3): 033203, 2007.

[150] K. F. Voss, C. M. Foster, L. Smilowitz, D. Mihailović, S. Askari, G. Srdanov, Z. Ni, S. Shi, A. J. Heeger, and F. Wudl. Substitution effects on

bipolarons in alkoxy derivatives of poly(1,4-phenylene-vinylene). *Phys. Rev. B*, **43** (6): 5109–5118, Feb 1991.

[151] D. Comoretto, C. Cuniberti, G. Musso, G. Dellepiane, F. Speroni, C. Botta, and S. Luzzati. Optical properties and long-lived charged photoexcitations in polydiacetylenes. *Physical Review B*, **49** (12): 8059–8066, 1994.

[152] R. Österbacka, C. An, X. Jiang, and Z. Vardeny. Two-Dimensional Electronic Excitations in Self-Assembled Conjugated Polymer Nanocrystals. *Science*, **287** (5454): 839, 2000.

[153] Z. Wang, S. Mazumdar, and A. Shukla. Essential optical states in$\ pi$-conjugated polymer thin films. *Arxiv preprint arXiv:0712.1065*, 2007.

[154] G. Malliaras and R. Friend. An organic electronics primer. *Phys. Today*, **58** (5): 53, 2005.

[155] L. Rothberg. Relationship between conjugated polymer morphology and photophysics. In *Proceedings-International School of Physics Enrico Fermi*, volume 149, pages 299–316. IOS Press; Ohmsha; 1999, 2002.

[156] F. Babudri, A. Cardone, G. Farinola, C. Martinelli, R. Mendichi, F. Naso, and M. Striccoli. Synthesis of Poly (arylenevinylene) s with Fluorinated Vinylene Units. *European Journal of Organic Chemistry*, **11**: 1977, 2008.

[157] M. Piacenza, D. Comoretto, M. Burger, V. Morandi, F. Marabelli, G. M. Farinola, G. Gigli, and F. Della Sala. Raman spectra of fluorinated Poly(p-phenylenevinylene)s: evidence of inter-ring distortion. (submitted).

[158] M. Piacenza, F. Della Sala, G. Farinola, C. Martinelli, and G. Gigli. Large Blue-Shift in the Optical Spectra of Fluorinated Polyphenylenevinylenes. A Combined Theoretical and Experimental Study. *Journal of Physical Chemistry B*, **112** (10): 2996, 2008.

[159] T. Hrenar, R. Mitrić, Z. Meić, H. Meier, and U. Stalmach. Vibrational spectra and DFT calculations of PPV-oligomers. *Journal of Molecular Structure*, **661**: 33–40, 2003.

[160] M. Losurdo, M. Giangregorio, P. Capezzuto, G. Bruno, F. Babudri, A. Cardone, C. Martinelli, G. Farinola, F. Naso, and M. Büchel. Impact of fluorinated vinylene units on supramolecular organization and optical properties of poly (p-phenylenedifluorovinylene) thin films as a class of blue band gap conjugated polymers. *Polymer*, **49** (19): 4133–4140, 2008.

List of publications

- **V. Morandi**, J. Holt, Z. V. Vardeny, *Optical Probes of Poly(phenylene-vinylene) at High Hydrostatic Pressure*, submitted.
- M. Piacenza, D. Comoretto, M. Burger, **V. Morandi**, F. Marabelli, G. M. Farinola, G. Gigli and F. Della Sala, *Raman spectra of fluorinated Poly(p-phenylenevinylene)s: evidence of inter-ring distortion*, submitted.
- **V. Morandi**, M. Galli, F. Marabelli, D. Comoretto, *Highly Oriented Poly (p-phenylene Vinylene): Polarized Optical Spectroscopy Under Pressure*, Phys.Rev B, in press.
- **V. Morandi**, F. Marabelli, V. Amendola, M. Meneghetti, and D. Comoretto, *Light Localization Effect on the Optical Properties of Opals Doped with Gold Nanoparticles*, J. Phys. Chem. C, **112**, 6293 (2008).
- **V. Morandi**, F. Marabelli, V. Amendola, M. Meneghetti D. Comoretto, *Colloidal photonic crystals doped with gold nanoparticles: spectroscopy and optical switching properties*, Adv. Fun. Mat., **17**, 2779 (2007).
- **V. Morandi**, C. Soci, M. Galli,, F. Marabelli, , D. Comoretto , *Optical probes of electronic states in highly anisotropic polymeric semiconductors*, Conference Proceedings "Highlights on Spectroscopies of Semiconductors and Nanostructures", SIF, Bologna; **94**, 75 (2007).
- D. Comoretto, **V. Morandi**, F. Marabelli, V. Amendola, M. Meneghetti, *Optical effects in artificial opals infiltrated with gold nanoparticles*, Proc. of SPIE, Photonic Crystal Materials and Devices III, edited by Richard M. De La Rue, Pierre Viktorovitch, Ceferino Lopez, Michele Midrio, **6182**, 61820D (2006).